University of Southampton Research Repository

Thesis: Inés Moreno Jiménez (2016) "The chorioallantoic membrane assay as an *in vivo* model for the study of human bone and tissue engineering", University of Southampton, Faculty of Medicine, PhD Thesis, pagination.

Data: Inés Moreno Jiménez (2016) “The chorioallantoic membrane assay as an *in vivo* model for the study of human bone and tissue engineering”. URI [dataset]

UNIVERSITY OF SOUTHAMPTON

FACULTY OF MEDICINE

Human Development and Health

The chorioallantoic membrane assay as an *in vivo* model for the study of human bone and tissue engineering

By

Inés Moreno Jiménez

Thesis for the degree of Doctor of Philosophy

September 2016

UNIVERSITY OF SOUTHAMPTON

ABSTRACT

FACULTY OF MEDICINE

Thesis for the degree of Doctor of Philosophy

The chorioallantoic membrane assay as an *in vivo* model for the study of human bone and tissue engineering

Inés Moreno-Jiménez

Poor vascularization at the fracture site is one of the main limitations of successful bone healing. To improve vascularisation, new tissue engineering approaches aim to design scaffolds that allow not only osteogenesis but also stable capillary invasion: angiogenesis. Importantly, the efficacy and safety of novel bone tissue engineering constructs needs to be tested *in vivo* before the constructs can be used clinically, which typically involves invasive surgical procedures in murine hosts.

The present thesis proposes the use the chorioallantoic membrane (CAM) from the developing chick as a less sentient *in vivo* model to explore human bone healing, and the application of this system as a novel screening platform for biomaterials in tissue engineering. To test this model, human bone cylinders were extracted from fresh human femoral heads, stimulated with an injury using a drill-hole defect, and implanted on the CAM or cultured *in vitro* for a period of 7-9 days. Micro-computed tomography (µCT) was used to quantify the magnitude of bone volume changes together with histological analysis to follow bone repair.

Bone cylinders were vascularised by the CAM blood vessels and remained viable following implantation throughout the culture period. Histological evaluation showed formation of cell condensations in proximity to avian capillaries (immunocytochemistry positive for Sox9 and Runx2). New extracellular matrix (Collagen type II, X) deposition and osteoclast activity (Cathepsin K) on the CAM-implanted cylinders, correlated with a significant increase in bone volume as determined by µCT analysis ($p<0.01$). Visualisation of the structural changes was achieved by implementing 3D registration of the bone cylinders before and after incubation. These findings demonstrated the ability of the CAM to support bone formation as well as bone resorption; essential processes for tissue regeneration. In addition, the human-avian model was used to test different biomaterials containing growth factors (*i.e.* BMP, VEGF). The model was able to detect significant changes following treatment ($p<0.05$) and demonstrated the ability of the human-avian system as a test/screen for biomaterials.

In summary, the current studies demonstrate the potential of the CAM assay as a surrogate blood supply for viable human bone tissue. This human-avian system offers a simple refinement model for animal research and a step towards a humanized *in vivo* model not only for tissue engineering, but for many other disciplines.

Table of Contents

List of Tables

List of Figures

Supplementary Materials

Supplementary Figures

Supplementary Tables

DECLARATION OF AUTHORSHIP

I,... Inés Moreno-Jiménez declare that this thesis and the work presented in it are my own and has been generated by me as the result of my own original research.

"The chorioallantoic (CAM) assay for the study of human bone regeneration: an *in vivo* model for tissue engineering"

I confirm that:

1. This work was done wholly or mainly while in candidature for a research degree at this University;
2. Where any part of this thesis has previously been submitted for a degree or any other qualification at this University or any other institution, this has been clearly stated;
3. Where I have consulted the published work of others, this is always clearly attributed;
4. Where I have quoted from the work of others, the source is always given. With the exception of such quotations, this thesis is entirely my own work;
5. I have acknowledged all main sources of help;
6. Where the thesis is based on work done by myself jointly with others, I have made clear exactly what was done by others and what I have contributed myself;
7. Either none of this work has been published before submission, or parts of this work have been published as:
   Moreno-Jimenez, I. *et al.* The chorioallantoic membrane (CAM) assay for the study of human bone regeneration: a refinement animal model in tissue engineering. Sci. Rep. 6, 32168; doi: 10.1038/ srep32168 (2016).

Signed: ....

Date: 15th March 2017 ....

Acknowledgements

Firstly, I would like to thank my supervisors Professor Richard Oreffo and Dr Nicholas Evans for their guidance, constructive feedback and patience during this project. Their example, mentoring and support allowed me to achieve way more beyond science.

I am particularly thankful to Dr Janos Kanczler for adopting me as a student, always making me keep my head up and see the bright side of every unsuccessful experiment.

My sincere appreciation goes to my co-workers and, most of all, friends for their support: my great mentors May de Andrés and Gry Hulsart-Billstrom, and my fellows Edoardo Scarpa and Juan A. Númez for not allowing me to give up and stick with me during the ups and downs of this fantastic PhD.

Thanks to Dr. Stuart Lanham for his advice on μCT and generous help during this project.

I am thankful for all the team in the Bone and Joint Research Group for creating such enjoyable working atmosphere; it has been great fun to work within this team during these four years.

Finally, I am thankful to the National Centre of Reduction, Refinement and Replacements of Animals in Research (NC3Rs) for funding this project. As any PhD student, I have both suffered and greatly enjoyed my PhD. I shall take with me plenty of truly enriching and positive experiences, but most of all, I feel proud of being part of a 3Rs initiative.

Definitions and Abbreviations

AC	Articular cartilage
ALD	Alendronate
AS	Alcian blue and Sirius Red
bFGF	Basic fibroblast growth factor
BM	Bone marrow
BMD	Bone mineral density
BMP2	Bone morphogenetic protein 2
BTE	Bone tissue engineering
BV	Bone volume
CAM	Chorioallantoic membrane
CB	Cortical bone
CTG	Cell tracker green
CTR	Cell tracker red
Ec	Ectoderm
ECM	Extracellular matrix
ECs	Endothelial cells
Ed	Endoderm
EDD	Embryo development day
EDTA	Ethylene-diamine-tetra-acetate
EtH1	Ethidium Homodimer-1
FBS	Foetal bovine serum
FDA	Food and Drug Administration

GF	Growth factor
GFP	Green Fluorescent Protein
GT	Goldner’s Trichrome
Gy	Gray (X-ray dose unit)
HA	Hydroxyapatite
HC	Harvesian canal
HIF	Hypoxia inducible factor
HLA	Human leucocyte antigen
ID	Inner diameter
IOs	InductOs^{TM}
L&D	Live and dead staining
MT	Masson’s Tetrachrome
NOF#	Neck of femur fracture (osteoporotic)
OA	Osteoarthritic
OB	Osteoblast
OC	Osteoclast
OD	Outer diameter
OP	Osteoporotic
OP-1	Osteogenic protein 1; BMP7
PBS	Phosphate buffered saline
PDGF	Platelet-derived growth factor
PFA	Paraformaldehyde
PGL	Poly-glycolic acid
PLA	Poly-lactic acid

RT	Room temperature
S1P	Sphingosine-1-phosphate
SCB	Subchondral cortical bone
SD	Standard deviation
SSC	Skeletal stem cells
TB	Trabecular bone
TGFβ	Transforming growth factor β
VEGF	Vascular endothelial growth factor
vWF	von Willerbrand Factor
αMEM	Alpha minimum essential medium
β-TCP	β Tricalcium phosphate
μCT	Micro computed tomography

Chapter 1: General introduction

1.1 Overview

Bone fractures and large bone defects require an additional source of bone graft to encourage bone healing and regeneration. Current approaches in bone tissue engineering are focused on the development of scaffolds that mimic the osteogenic microenvironment and facilitate the regeneration of tissue. This is typically achieved by combining a biomaterial construct or scaffold with biological cues which are expressed during a tightly coordinated and orchestrated healing process. However, before these novel constructs can be translated into the clinic, their safety and efficacy needs to be tested *in vivo*.

Current *in vivo* models to test biomaterials are critical to provide information on the physiological response to the construct; however animal models safeguard important differences with respect the actual human response and raise important ethical concerns. In this context, the pipeline of preclinical testing in bone tissue engineering will be discussed as well as the potential alternatives in terms of reduction, replacement and refinement (3Rs) of animals in research. As a promising possibility, this PhD thesis examines an alternative model for *in vivo* testing using the chorioallantoic membrane of the chick embryo to culture human living bone tissue.

To set the scene, a concise description of the clinical problem, osteoporosis and bone fractures, will be provided in order to understand the clinical demand to find new biomaterials to aid bone healing. In further detail, the basics of bone biology, regeneration, and remodelling will be discussed, with particular emphasis on the importance of controlled mechanisms for growth factor release to achieve bone repair. The properties of an ideal biomaterial for bone tissue engineering will be introduced, together with a description of commonly used bone filling materials and developed strategies to design biomimetic scaffolds. From that perspective, the potential of a hydrogel construct to deliver growth factors will be detailed as a potential candidate to promote bone regeneration. Subsequently, the developed human-avian *in vivo* model will be used to examine two different biomaterials constructs. To justify the use and benefits of the CAM assay*, in vitro* models and alternatives *in vivo* models will be critically evaluated. The potential benefits and limitations of the chorioallantoic membrane as an *in vivo* model for bone tissue engineering testing will be disclosed, as well as a detailed list of its applications in regenerative medicine. Finally, the key points of the literature will be highlighted, setting the context for the aims and objectives of the project.

1.2 Osteoporosis and bone fractures – The clinical need

Osteoporosis is characterized by a significant loss of bone mass density, which weakens the strength of the skeleton (Figure 1.2.1). At the later stages of life, osteoporosis has a higher incident rate within the female population: one in two women over 50 will suffer a fracture, whereas the prediction for men at the same age is one in five (Van Staa *et al.* 2001). Osteoporosis is one of the main causes of large bone defects following trauma but not exclusively. Infection, osteotomy following tumour removal, osteonecrosis and other endocrine diseases can all result in an impaired bone mass balance as well (Calori *et al.* 2007; Macey *et al.* 1989).

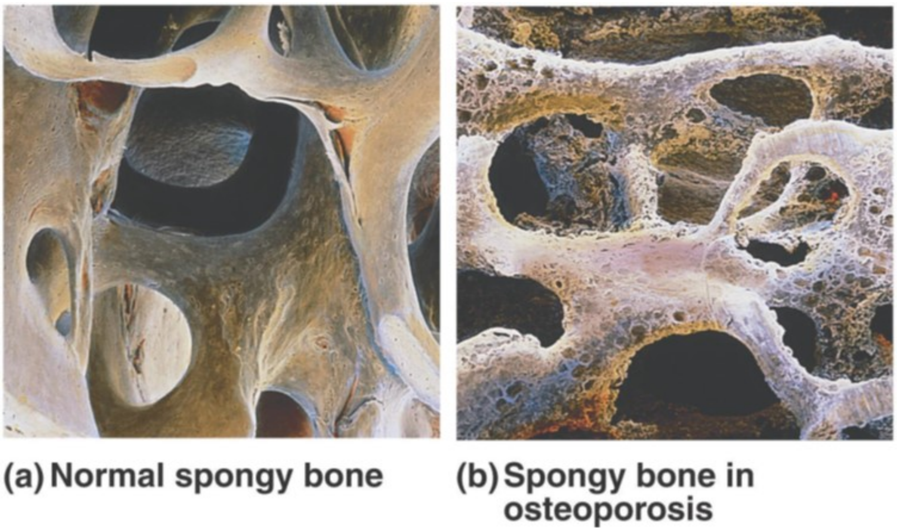

Figure 1.2.1: Structural differences in trabecular bone between normal (A) and osteoporotic bone (B). Note the differences in the density and porosity of bone (Marieb and Hoehn 2013). Copyright © 2009 Pearson Education, Inc., publishing as Pearson Benjamin Cummings.

Loss of skeletal tissue is a major socio-economic cost for an increasing ageing population. Life expectancy has doubled in the last 200 years and this is directly reflected in osteoporosis incidence. Just looking at hip fractures, the number has doubled between 1983 and 2010 (Boyce and Vessey 1985), and it is predicted that these numbers will triple by 2016 (Johnell and Kanis 2005). Not only has the incidence of fractures risen but also the associated costs: from 2001, the hospital and social care of an individual hip fracture has increased to £7,000 (Burge *et al.* 2008; Lawrence *et al.* 2005). Taking into account the number of hip fracture patients, the UK is spending approximately £2.3 billion on hip fracture treatment per year; approximately £6 million per day. Hence, there is a critical need to find novel bone augmentation strategies in order to effectively treat these clinical conditions.

Treatment of large bone defects requires bone graft material to fill the non-union gap. The gold standard in orthopaedic surgery is to harvest bone from the same patient, and re-insert the bone in the injury site: this is called autografting (Damien and Parsons 1991). However this option is not always available since not all the patients are eligible, particularly elderly people as their healing capacity is reduced. Additionally, autografts cause the patient donor site morbidity and extended surgical and recovery time. Another option is the use of allografts obtained from a human donor, usually from cadaveric sources. Allografts, however, have impaired osteoinductive properties as a result of the sterilization processes, and in some cases allografts can be a source of infection for the recipient and cause an immunogenic response (Bohner 2010; Holzmann *et al.* 2010). An alternative to the use of auto/allografts is the use of natural or synthetic biomaterials as bone substitutes. Bone tissue engineering has advanced significantly over the recent decades, bringing a plethora of biomaterials to the clinic (Calori *et al.* 2011). Nevertheless, there is still a long way to go to obtain bone graft substitutes which can fulfil all medical requirements and which are as effective as the natural bone.

Approximately 5 to 10 % of fractures fail to heal as a consequence of delayed union or non-union. Poor fracture healing is associated with metabolic disorders such as diabetes and obesity, and the increasing incidence of these conditions suggest a potential growth in the percentage of non-unions. These medical conditions also affect the vascular function, which has been highlighted as an important causal factor of bone healing failure (Calori *et al.* 2007). It is well-established that a stable invasion of vasculature at the implant site is critical for effective bone healing, in particular for open fractures which have a higher risk of non-union (Hankenson *et al.* 2011; Largo, Ramakrishnan, and Ehrbar 2010). In fact, patients with vascular conditions have a nearly 50 % unsuccessful rate of bone healing (Pountos *et al.* 2014). Hence, development of biomaterials that can serve as a scaffold for bone regeneration (osteogenesis) as well as promoting stable capillary invasion (angiogenesis) is a major bottleneck in tissue engineering strategies.

1.3 Bone biology – Tissue structure and repair mechanisms

Bone is the principal tissue that provides support and protection to vertebrates. Bone serves as a shield as well as a storage and metabolic regulator of elements such as calcium and phosphate. Bone also functions as a reservoir for the haematopoietic compartment, which controls the formation of blood cells in the bone marrow. The extracellular matrix (ECM) of bone is composed of an inorganic and an organic phase. The inorganic phase accounts for 60 % of the dry weight of bone tissue and it is composed of hydroxyapatite $Ca_{10}(PO_4)OH_2$, which provides the mineral component. The organic component of bone (40% dry weight) is composed primarily of collagen type I, and proteoglycans which provide tensile and compressive strength respectively (Sommerfeldt and Rubin 2001). The composition of organic (20 %), inorganic (60 %) and water (20 %) provides bone tissue with stability, stiffness, compression resistance and a relative elasticity as well (Sommerfeldt and Rubin 2001).

There are two types of bone: cortical and trabecular. Cortical or compact bone is solid and dense and provides the compartment for the trabecular bone. Trabecular or spongy bone has large spaces, named voids or trabecular separation, which contain the vascular component or bone marrow. Spongy bone is metabolically more active with a remodelling rate of 25%, compared to 2-3% of cortical per year (Clarke 2008). The internal surfaces of the trabecular bone are covered with a layer of connective tissue, endosteum, which contains progenitor cells (Figure 1.3.1). The cortical bone is also covered in a layer of periosteum, which is the external connective tissue around the compact bone.

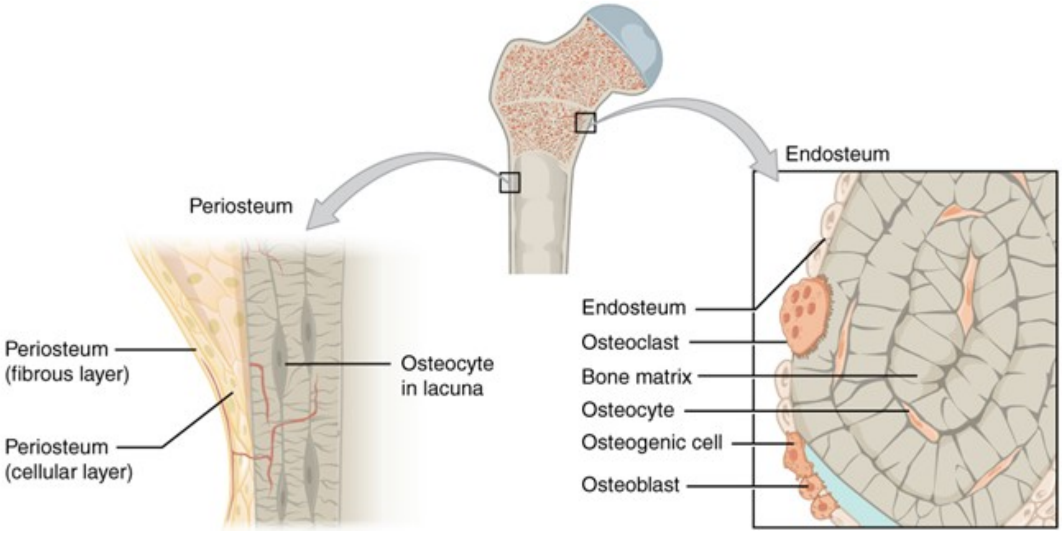

Figure 1.3.1: Location of endosteum and periosteum tissue in long bones. The connective tissue that surrounds the inner part of the bone is endosteum, while the periosteum covers the outer surface of bone. Osteocytes act as stress and strain sensors, and report to the bone remodelling cells (osteoclast and osteoblast) whether bone tissue needs to be resorbed or laid down. The space that osteocytes occupy once encased in bone matrix is called a lacuna. The channels between lacunas that allow communication between osteocytes are named canaliculi, forming a network in the bone tissue. Copyright © 2009 Pearson Education, Inc., publishing as Pearson Benjamin Cummings.

Bone is a dynamic tissue that is continuously remodelled through life, based on the destruction of old matrix and the *de novo* formation of bone tissue. The two cell types responsible for this remodelling process are osteoblasts (OB) and osteoclasts (OC). OB produce new collagen matrix (osteoid) that becomes mineralized, whereas the OC, large and multinucleated cells, resorb old and damaged bone matrix (Sommerfeldt and Rubin 2001). The process of osteoclastogenesis is coordinated by osteoclast through RANKL/RANK/MCSF signalling under the influence of a number of factors such as TNFa, IL-1b, parathyroid hormone and VitD$_3$ (Proff and Römer 2009) In the process of new matrix formation OBs become trapped in the mineralized osteoid and become osteocytes (Figure 1.3.1). Osteocytes are terminally differentiated OBs with extended cytoplasmic extensions that may provide mechanical sensing of bone homeostasis named canaliculi (Sommerfeldt and Rubin 2001). In the event of a physiological disruption, osteocytes are the first cells to detect and report changes in the bone by secreting signalling factors, hence acting as mechanosensors and endocrine cells. Another subset of OBs become flattened and cover all bone surfaces, known as bone lining cells (Kular *et al.* 2012). For many years bone lining cells have been considered 'inactive' cells, however bone lining cells serve to indicate the bone surfaces requiring remodelling, as well as coordinating the resorption/formation processes (Andersen *et al.* 2009).

An impairment in the OC-OB balanced activity results in the gain or loss of bone density, affecting the ability of the skeleton to sustain the weight of the body (Clarke 2008). OBs are derived from skeletal stem cells (SSC), whereas OCs are formed from the fusion of cells of hematopoietic origin, monocytes-macrophages (Udagawa *et al.* 1990). In the absence of a blood vessel (BV) supply, it would not be possible to maintain the OCs or OBs progenitors niche; consequently, bone remodelling cannot exist without angiogenesis.

1.3.1 Bone remodelling

Bone formation can occur as a single anabolic process (modelling) or coupled with a second catabolic process of bone resorption (bone remodelling). Modelling occurs to adapt the shape of the bones to their function whereas bone remodelling occurs to maintain homeostasis of the skeleton; this includes responding to changes in calcium metabolism, stress load stimulation and self-repair of damaged bone. Bone remodelling happens continuously throughout life, and the whole skeleton is remodelled every 10 years (Clarke 2008).

Bone remodelling implies a tight coordination between an initial bone resorption (osteoclast) followed by subsequent bone formation (osteoblast), known as bone remodelling unit. Bone resorption occurs first and takes approximately 2-4 weeks in each cycle, whereas (after the reversal phase) bone formation phase takes approximately 3-4 months to complete (Clarke 2008). Osteoclasts and osteoblasts work together in an enclosed compartment formed by a canopy formed by osteoblast and lining cells (Figure 1.3.2 A).

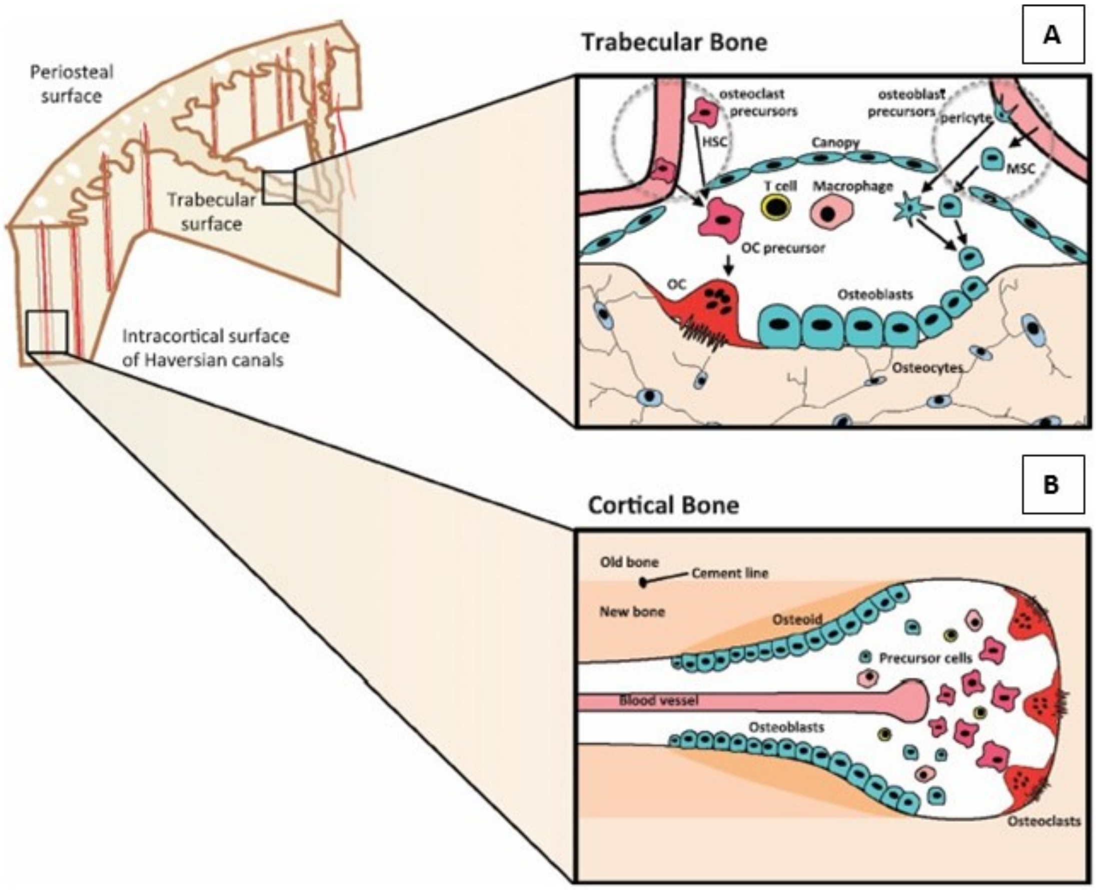

Figure 1.3.2: Bone remodelling in trabecular (A) and cortical bone (B). Blood vessels initiate the bone remodelling process in trabecular and cortical bone by recruiting SSC, pericytes (osteoblast precursors) and monocytes-macrophages (osteoclast precursors). The bone remodelling complex (A) is formed by a canopy of bone lining cells, creating a compartment in which communication between OC and OBs is facilitated. Reprinted with permission from Elsevier from (Sims and Martin 2014), Copyright.

This canopy-cell structure coordinates OC-OB communication and activity in space and time. At the initiation phase, osteocytes and lining cells at the bone surface express RANKL and CSF-1 to recruit osteoclasts which initiate the resorption process and release cytokines and signalling molecules from the resorbed bone matrix such as BMP, IGF and TBG-β (Centrella, McCarthy, and Canalis 1991; Hayden, Mohan, and Baylink 1995; Wozney *et al.* 1988). During the reversal phase, osteoclasts undergo apoptosis after completing their function and osteoblast precursors are recruited from the marrow space and/or neighbouring blood vessels to start the formation phase (Sims and Martin 2014).

1.3.2 Bone fracture healing

Bone tissue is able to heal without the formation of a fibrous scar, since this event would affect the ability of the skeleton to sustain body weight. Following bone injury, the damaged tissue initiates an acute inflammatory reaction by releasing cytokines such as TNF α, Il-1β and Il-6 and macrophage colony-stimulating factor (MCSF), which peak during the first 24 hours (Schmidt-Bleek *et al.* 2015). The secretion of these inflammatory cytokines results in the recruitment of blood cells and platelets which form a clot or hematoma between the two bone ends. A hypoxic environment is created due to the disrupted vascular supply, which results in the secretion of HIF1α and VEGF to initiate an angiogenic response during the next 3 days (Marsell and Einhorn 2011). In parallel, Il-10 and TGFβ are secreted as anti-inflammatory cytokines to control and arrest the initial inflammation burst. Skeletal stem cells (SSCs) are then recruited from the circulation, periosteum and bone marrow to aggregate in the granulation tissue that follows the hematoma (Dimitriou, Tsiridis, and Giannoudis 2005).

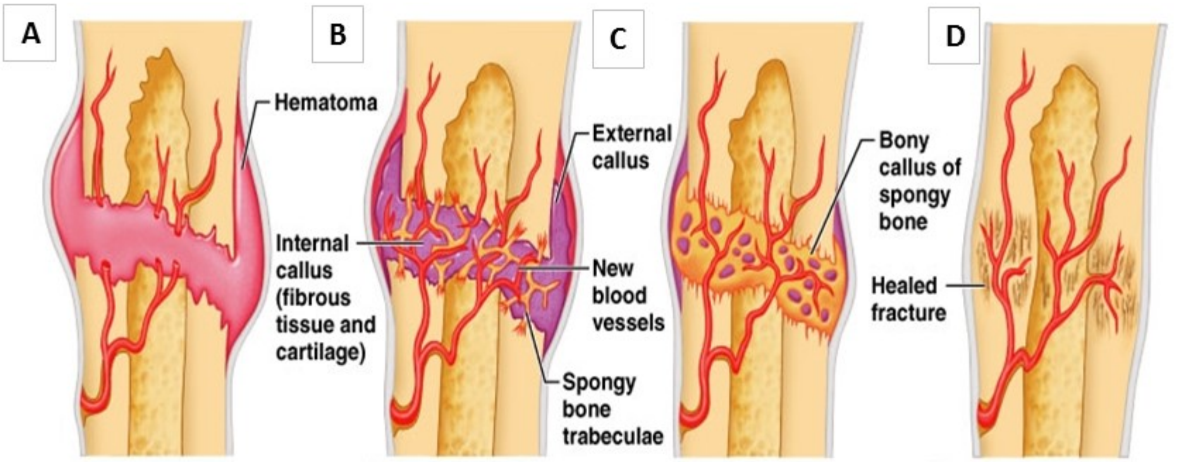

Figure 1.3.3: The different stages of bone repair. (A) Hematoma formation (B) Fibrocartilaginous callus formation (C) Bony callus formation: and (D) Bone remodelling. Intramembranous and endochondral bone formation differ in the transient formation of a cartilaginous callus (step C). (Marieb and Hoehn 2013). Copyright © 2009 Pearson Education, Inc., publishing as Pearson Benjamin Cummings

At this point, the ossification can continue with or without a cartilaginous phase, which will differentiate between endochondral or intramembranous bone formation, respectively (Kanczler and Oreffo 2008). Depending on the degree of fixation of the tissue at the fracture site, intramembranous or endochondral ossification occurs. In regions where there is poor mechanical support, an intermediate cartilaginous callus is formed by SSCs differentiating towards the chondrocyte lineage (endochondral pathway) during weeks 2 to 3 following injury (Dimitriou *et al.* 2005). Once chondrocytes cease proliferation and become hypertrophic, VEGF is secreted by the same cells to initiate a second angiogenic intervention. Blood vessel circulation results in monocytes-macrophages and SSCs which will differentiate into osteoclasts (bone resorption) and osteoblast cells (bone formation), respectively. Both cell types work in parallel to replace the soft cartilaginous callus by mineralized woven bone (Kanczler and Oreffo 2008). This woven bone is subsequently remodelled into lamellar bone and the callus returns to the original size.

A similar process occurs in intramembranous ossification, where SSCs differentiate directly towards an osteoblast lineage to form woven bone without an intermediate cartilaginous stage (Einhorn and Gerstenfeld 2015). The proliferation and differentiation of SSCs to osteoblasts is guided in part, by the Wnt proteins and the TGF β family of cytokines (Hughes *et al.* 2006). TGF β proteins are secreted by the recruited SSCs and also released by the extracellular matrix of bone during the next stages of repair; in particular from the TGF β family, bone morphogenetic proteins have a key role in differentiating SSCs towards the bone lineage (osteoinduction) (Marsell *et al.* 2014). Thus, both intramembranous and osteochondral bone formation require two sequential events of blood vessel invasion which are fundamental to achieve successful bone healing (Figure 1.3.3).

The section above has detailed the process by which bone repair occurs successfully, however in the clinical practice bone fractures commonly require surgical treatment to aid bone healing. Bone fractures in osteoporotic patients remain an area needing bone material substitutes; moreover severe high-impact trauma (*i.e.* military injuries) and tumour removal result in large volume defects with reduced treatment options and poor prognosis; hence also requiring material substitutes and therapeutic strategies. The next section will discuss current strategies developed in bone tissue engineering to find new bone material substitutes which attempt to fulfil the demands of the clinical situation.

1.4 Bone tissue engineering

Bone tissue engineering (BTE) is defined by an interdisciplinary approach that combines the principles of engineering, biology and materials science to regenerate or improve skeletal tissue function (Shrivats, McDermott, and Hollinger 2014). As described previously autograft and allograft are the traditional sources of bone graft substitutes, however autografts and allografts have several limitations such as donor site morbidity, limited availability and risk of contamination (Damien and Parsons 1991; Fages *et al.* 1998). Hence, the focus of BTE is to develop biomaterials that can provide the same results at the fracture site as the clinical gold standard: natural bone.

Regardless of the tissue that the implant aims to substitute, any scaffold should have some essential characteristics such as (1) biocompatibility to not elicit a toxic response, (2) porosity to allow the free diffusion of nutrients, oxygen and molecular waste, (3) provision of mechanical support and (4) biodegradability (substituted by the host tissue over time).

In particular, BTE scaffolds should ideally be osteoconductive and/or osteoinductive to resemble as much as possible natural bone. Osteoconduction refers to the capacity of the scaffold to sustain (*conduct*) the growth of native tissue and vascular invasion, whereas osteoinduction refers to the ability of the scaffold to trigger (*induce*) the differentiation of progenitor cells into the osteo-lineage (Damien and Parsons 1991). The osteoconduction depends on the type of biomaterial itself (extracellular matrix composition, porosity, mechanical properties) and osteoinduction refers to the addition of osteogenic factors (*e.g.* BMP) which induce osteodifferentiation (Kolk *et al.* 2012).

In fact, these properties reflect to some degree the essential hallmarks of the natural healing process, which are (1) the recruitment and agglomeration of SSC, (2) hematoma formation and release of signalling molecules to recruit progenitor cells and neovascularization, (3) formation of the ECM as a natural scaffold and (4) the mechanical stability at the callus site to fill the gap between the two fractures edges. This is the diamond concept of Giannoudis *et al.* which describes the properties of an ideal bone graft substitute as an integration of biological and mechanical aspects tailored for the purpose of the targeted bone. (Giannoudis, Einhorn, and Marsh 2007). For example, properties such as porosity to allow for cell and blood vessel invasion, transitionary/permanent mechanical strength, degree of resorbability/incorporation rate should be tailored for specific bone sites (*i.e.* load-bearing bones vs flat bones). Hence, biomaterials need to resemble the properties of the original tissue before injury.

1.4.1 Biomaterials for bone tissue engineering

Ideally, bone scaffolds should be biocompatible, biodegradable and have an appropriate porosity and density (Salgado, Coutinho, and Reis 2004). Non-resorbing materials such as metal substrates are used as joint prostheses, screws and plates to provide long-term mechanical and weight-bearing capacity. Resorbable, natural materials such as hydroxyapatite (HA) and β-tricalcium phosphate (β-TCP) have been used as scaffolds for bone regeneration given their excellent compressive strength and wear resistance. The fast degradation of β-TCP as a hard tissue replacement material is often compensated by combining different ratios of β-TCP with HA, a more stable ceramic. However, these materials have the disadvantages of low tensile strength, toughness, low porosity and brittleness (Devin, Attawia, and Laurencin 1996). Bioglass is another natural bone filling material and it is composed of silica and HA. Different forms of bioglass exist with various porosity and mechanical properties, and hence a more stable/reactive profile (Kolk *et al.* 2012). There is a wide range of synthetic materials for BTE: polymers such as poly-lactic acid (PLA), polyglycolic acid (PGA) and their co-polymers are FDA-approved for medical applications. The advantages of these synthetic polymers are good biocompatibility and adaptability in terms of design and manufacturing. However synthetic polymers have poor structural properties, can degrade rapidly into acidic products and absorb excess of water from the body (Hutmacher and Schantz 2007).

While plain biomaterials have been traditionally used as bone filler materials, current trends in BTE are moving towards a more biomimetic approach. An effort has been made to try to develop extracellular matrix that resembles the bone microenvironment rather than an inert load-bearing support. Strategies to functionalise materials with biological cues include incorporation of molecules from the extracellular matrix (collagen, proteoglycans, fibronectin, etc.), binding cues (integrins, RGD sequences) and signalling molecules (BMP, VEGF, Wnt) (Peng *et al.* 2002; Schönmeyr *et al.* 2010; Sukul *et al.* 2015). Importantly, these different approaches can be applied jointly into a single scaffold, developing more complex but effective, smart biomaterials. For instance, the combined effect of dual delivery of angiogenic and osteogenic growth factors has been well-established in the literature. As an example, the synergy between growth factors (VEGF, BMP2) and progenitor cells (skeletal stem cells) in bone repair has been demonstrated in several studies. Peng *et al.* implanted BMP4 genetically modified cells with or without a VEGF inhibitor in a calvarial defect model, demonstrating that lack of VEGF delayed bone formation (Peng *et al.* 2002). The same authors applied a BMP2 gel-foam with VEGF in mouse calvarial defect reporting significant capillary density and bone formation following 6 weeks implantation (Peng *et al.* 2005). Importantly, Peng *et al.* showed that the synergistic BMP2-VEGF effect on both studies was dependent on the ratio between growth factors (Peng *et al.* 2002, 2005). Another study combined a calcium phosphate scaffold with BMP2, VEGF and bone marrow stromal cells and both ectopic and orthotopic implants showed enhanced bone formation compared to control (Sukul *et al.* 2015). Patel *et al.* applied VEGF-BMP2 gelatin microparticles within the pores of a polymer scaffold (poly(propylene fumarate) showing their regenerative potential in a in critical-sized defect (Patel *et al.* 2008). Hence, biomaterials combining tuning both at the macro and at the microscale can provide the mechanical support required at the injury site while at the same time boosting the healing process with biological cues.

Gene therapy has also been combined with biomaterials as a treatment targeted to the host cells via the incorporation of coding sequences (adenoviral vectors, plasmids), aiming to stimulate the local environment to aid tissue regeneration (Keramaris *et al.* 2008; Peng *et al.* 2005; Schönmeyr *et al.* 2010). Scaffolds with pre-seeded stem cells or biomaterials encapsulating the progenitor cells for delivery at the injury site are additional approaches used in BTE (Kanczler *et al.* 2008; Lenze *et al.* 2014; Steffens *et al.* 2009).

The previous section has detailed various possibilities to implement the biology occurring during fracture healing in the BTE scaffolds. From these strategies, one of the most commonly used is the delivery of growth factors. The next section will discuss in detail the potential and caveats of these types of approaches in BTE.

1.4.2 Growth factor strategies in bone tissue engineering

The previous section 1.3.2 explained the tight coordination of events during fracture healing, coordinated by multiple signalling molecules and growth factors. From the array of cytokines involved in this process, VEGF and BMP2 are amongst the most commonly studied factors given their essential role in bone formation (Carmeliet *et al.* 1996; Peng *et al.* 2005; Zelzer *et al.* 2002). The next section will discuss the role of these growth factors in bone formation, repair and tissue engineering strategies.

1.4.2.1 Vascular endothelial growth factor in bone healing

The VEGF family includes six different subtypes (A, B, C, D, E and F) and Placental growth factor, though the most abundant form and indeed the most widely studied by the scientific community is VEGF-A, commonly referred to as VEGF. The VEGF gene has 8 exons, and depending on the alternative splicing there are four isoforms named after the number of amino acids present

($VEGF_{121}$,$VEGF_{165}$, $VEGF_{189}$, $VEGF_{206}$) from which $VEGF_{165}$ is the principal isoform (Ferrara, Gerber, and LeCouter 2003). The VEGF ligand and the VEGF receptors have been shown to have an important role in signal transduction for angiogenesis. The main VEGF receptors are VEGFR-1 (Flt-1) and VEGFR-2 (Flk-1 or KDR). The expression of these receptors has been shown to be dependent on bone formation in various models of distraction osteogenesis in which mechanical strains are used to prolong bone growth (Ai-Aql *et al.* 2008; Eckardt *et al.* 2003; Fang *et al.* 2005).

The essential role of VEGF in bone healing is also recapitulated during embryonic skeletogenesis. In evidence of that, in 1996 two studies developed genetically modified VEGF knockout murine strains, resulting in mortality of the embryos (Carmeliet *et al.* 1996; Ferrara *et al.* 1996). Heterozygous $VEGF^{+/-}$ mouse embryos were studied before embryo lethality and exhibited significantly impaired bone development (Zelzer *et al.* 2002). The previous studies demonstrated the crucial role of VEGF during embryo development. In models of osteoporosis using ovariectomised mice, reduced bone mass was coupled with a reduction in VEGF expression and blood vessels in the bone tissue (Ding, Wei, and Liu 2011). As fracture healing also recapitulates several aspects of embryonic skeletogenesis (endochondral bone formation), VEGF is one of the key regulators of fracture repair. A clinical study collecting plasma from patients 24 hours after fracture injury showed a significant upregulation of VEGF levels (15x) compared to control subjects (Street *et al.* 2000). At the fracture local microenvironment, VEGF is expressed by hypertrophic chondrocytes, OBs, OCs and ECs which recruit vessel invasion at different stages of the healing process such as chondrocyte apoptosis, callus vascularisation and remodelling (Clarkin and Gerstenfeld 2013). Further evidence of the important role of VEGF in osteogenesis was shown by Fang *et al.* in a distraction osteogenesis model: the addition of a VEGF antagonist resulted in the formation of fibrous scars compared to the successfully healed control (Fang *et al.* 2005). Similar outcomes have been reported in other studies which disturb the signalling pathway of VEGF, failing to achieve bone regeneration (Ding *et al.* 2011; Fang *et al.* 2005; Street *et al.* 2002).

1.4.2.2 Bone morphogenetic proteins – BMP2

The bone morphogenetic proteins (BMP) belong to the superfamily of transforming growth factor β and play a crucial role during embryo skeletal development as well as during adulthood to maintain bone homeostasis and initiate bone repair (Rosen 2009). Transgenic animal models showed that impaired skeletogenesis occurs when various BMP genes were knocked out independently or together (Bandyopadhyay *et al.* 2006). From the broad family of BMPs, specific deletion of BMP2 in the post-natal skeleton resulted in severe developmental effects due to a delay in endochondral bone formation in the limbs, as well as an osteoarthritic phenotype in the cartilage (Rountree *et al.* 2004; Tsuji *et al.* 2006). Several developmental *in vivo* models have shown the crucial role of BMP2 in aggregating skeletal (Sox9+) cells to produce a cartilage template (Barna and Niswander 2007), as well as in the differentiation of hypertrophic chondrocytes and osteoblasts (Enomoto-Iwamoto *et al.* 1998), and even a role in modulating osteoclast function (Okamoto *et al.* 2006). Hence, BMP2 is crucial to initiate bone fracture healing as it recapitulates the process of endochondral bone formation.

Since 1965, when Urist first described the ability of demineralised bone matrix to induce bone formation in ectopic locations in a rabbit model (Urist and Daly 1965), the term *bone morphogenesis* has been used to describe the newly formed bone and *bone morphogenetic protein* the specific factor within the decellularised bone matrix that caused bone formation. Thereafter, a multitude of studies have examined the effects of the BMP family, and in particular BMP2 to induce ectopic bone formation and validate its osteoinductive properties (Cai *et al.* 2014; Kempen *et al.* 2009; Peng *et al.* 2002; Wang *et al.* 1990).

Wang *et al.* reported in 1990 the formation of ectopic bone following the implantation of a demineralised, acellular collagen sponge (ACS) impregnated in BMP2 in a rat subcutaneous implant model (Wang *et al.* 1990). The authors examined the effect of various BMP2 dosages over the course of 21 days and provided histological images to score bone and/or cartilage formation. Bone formation was described as early as 5 days on the highest doses of BMP2 (115 µg), whereas cartilage formation was seen from much lower doses (18.2 µg) for the same time-point. More recent studies from Kempen *et al.* tested the implantation of 6.6 µg BMP2 on a rat ectopic model and showed significant bone formation following 8 weeks implantation (Kempen *et al.* 2009). Another study examined the effect of a fibrin matrix containing 125 µg of BMP2 implanted on the femoral vessel bundle, which was separated from the skeletal tissues by a surgical membrane. Heterotopic bone formation was significantly higher following the BMP2 implantation, and further enhanced by VEGF co-delivery (Cai *et al.* 2014).

The osteoinductive properties of BMP2 have been extensively studied, and following FDA approval in 2002, human recombinant BMP2 has been commonly used in the clinic for spinal fusion and open tibia fracture, as well as for maxillofacial reconstructions (Govender *et al.* 2002; Poynton and Lane 2002); however BMP2 delivery has also been associated with severe side effects post-surgery. Two systematic reviews evaluated data from over 10 randomised controlled clinical trials examining the effectiveness and safety of BMP2 compared to the gold standard (autograft) in spinal fusion (Fu *et al.* 2013; Simmonds *et al.* 2013). Clinically there was not a relevant difference since both options were associated with similar frequency of complications, however there was an apparent association of BMP2 with ectopic bone formation (Resnick and

Bozic 2013). Additional adverse effects reported in the literature include inflammation, infection, nervous system effect (retrograde ejaculation), and osteolysis (Carragee, Hurwitz, and Weiner 2011; Poynton and Lane 2002). Therefore, these previous studies demonstrate that the use of potent growth factors can also causes important side-effects, which require additional consideration.

1.4.2.3 Role of cytokines in bone tissue engineering

Angiogenesis and osteogenesis are mediated by the secretion of signalling molecules which trigger a spatio-temporal regulated series of events. The previous section has highlighted the importance of two cytokines, VEGF and BMP2, to trigger blood vessel invasion and new bone formation. However, even if their role in bone repair has been extensively demonstrated, their effects can be reversed in the context of inappropriate dosage or temporal application. For instance, continuous administration of VEGF results in unstable and leaky blood vessels (Davies *et al.* 2008; Greenberg *et al.* 2009). Moreover, while VEGF-expressing bone marrow stromal cells can improve vascularisation, these cells can also impair bone formation due to excessive osteoclast activity (Helmrich *et al.* 2013). The synergistic effect of VEGF and BMP2 has been proven to depend significantly on the ratio dose between both factors as well as their temporal release (Kempen *et al.* 2009; Peng *et al.* 2002). Again, demonstrating the tight coordination of the signalling cascade that exists during bone repair.

Although BMP2 was shown to have great potential in the induction of bone formation, BMP2 has also been associated with adverse reactions: inflammation, ectopic bone formation and other complications (Resnick and Bozic 2013). To overcome the issues mentioned above, several strategies have been developed in the field of drug delivery. In order to mimic the physiological conditions in which growth factors are released following injury, cytokines (VEGF, BMP2, etc.) can be combined with biomaterials that will; i) protect their half-life effect, ii) shield from the blood torrent clearance and iii) localize to the area of treatment. Controlled and sustained release of growth factors over time avoids the effect associated with bolus injection of growth factors (supraphysiological dose in a single administration) and hence its unwanted side effects. A multitude of studies have proven the osteogenic potential of a low, controlled release BMP2 (Chappuis *et al.* 2012; Gibbs *et al.* 2016), in combination with other angiogenic growth factors (Kanczler *et al.* 2010; Kempen *et al.* 2009; Patel *et al.* 2008) and anti-resorptive drugs such as alendronate (Shah *et al.* 2014).

Given that the functionalisation of biomaterials has to preserve the bioactivity of growth factors while at the same time deliver a dose within a pharmacologically effective window, the range of biomaterials compatible with physiological conditions narrows down significantly. Hydrogels would be potential candidates, as these materials can provide a matrix to encapsulate growth factors and/or cells, and be directly injected *in situ* in the operating theatre, thus providing a minimally invasive mechanism to deliver pro-osteogenic factors at the fracture site (Dawson et al. 2012; Saul and Williams 2013)

1.4.3 Hydrogels for bone tissue engineering

Hydrogels have gained attention in the field of tissue engineering because of their similarities with the natural ECM: high water content, three-dimensional network and efficient mass transfer. In addition hydrogels offer biocompatibility, tailored mechanical properties, and easy manipulation (Saul and Williams 2013). Combination of hydrogels with target anchoring moieties, cell-cell interaction peptides, growth factors and/or cell encapsulation makes them excellent candidates for developing smart materials.

Natural materials such as collagen, chitosan, hyaluronic acid and alginate have been used in BTE due to their similarities to ECM matrix and their excellent biocompatibility. However, natural materials are limited, have a relative risk of disease contamination and are difficult to process and standardise (Bai *et al.* 2013). Synthetic hydrogels such as poly-lactic acid (PLA), poly-glycolic acid (PGA) and polyethylene glycol (PEG) offer several advantages over natural polymers given their tuneable properties, ease to scale up and reproducible production. Generally, polymeric (PLA, PGA, PEG) biomaterials show good integration due to their biocompatibility with host tissue (Lutolf *et al.* 2003; Suzuki *et al.* 2000), and are commonly used as carriers for biomolecules and growth factors to aid bone repair. Yet, synthetic polymers are naturally inert due to the lack of anchoring moieties present in natural ECM, hence requiring subsequent bio-functionalisation. In addition, their cross-linking conditions are not always compatible with physiological conditions, thus limiting their potential for minimally invasive surgeries. Current research is focusing on developing free-radical crosslinking, thermal (37 degrees) gelation and self-assembling hydrogels as alternative strategies to produce injectable scaffolds (Liu *et al.* 2012; Saul and Williams 2013; Seo *et al.* 2015).

Alginate based hydrogels have been used to evaluate the dose response of BMP2, showing beneficial effect in bone healing up to 5 µg at the fracture site in a murine model (Ribeiro *et al.* 2015). Another study combined BMP2-loaded chitosan hydrogels with calcium phosphate particles in an ectopic model to optimise dose, and then in an orthotopic rabbit radius model, showing significant bone repair (Luca *et al.* 2011). Other growth factors such as matrix metaloproteases (MMP) were cross-linked with synthetic (RGD-PEG) hydrogels with the objective of tuning the degradation rate of the biomaterial *in vivo* (Lutolf *et al.* 2003). Hydroxyapatite particles have also been combined with collagen-fibrinogen hydrogel, reporting good biocompatibility both *in vitro* and *in vivo* (Rao *et al.* 2014). In our laboratory, PLGA hydrogels were combined with several growth factors to seed an alginate/bovine ECM scaffold and the multiple biomaterials variables were tested in the organotypic (*in vitro*) chick femur defect model. This hydrogel matrix allowed the study of the osteogenic or chondrogenic effects of VEGF, BMP2, TGFβ together with human primary Stro-1$^+$ cells (Smith *et al.* 2014b). Other studies have used the combination of two different polymeric nanoparticles with water to achieve thermal gelation into a hydrogel (Seo *et al.* 2015). The previous study incorporated BMP2 on the hydrogel and after testing it ectopically, implanted into a mouse bone defect showing significant bone regeneration (Seo *et al.* 2015). The regenerative effect of sustained release strategies was further validated by Lienemann *et al.* who monitored the formation of HA crystals in a calvariall defect using SPECT and PET techniques following the application of BMP2-controlled-release PEG hydrogel (Lienemann *et al.* 2015).

1.4.3.1 Laponite as a hydrogel for bone tissue engineering

In an ideal situation, the hydrogel employed in BTE should be easy to manufacture and to combine with bio-factors, with controllable gelling parameters. Their mechanical strength should be sufficient to remain stable following injection but at the same time degrade upon tissue in-growth (Tan and Marra 2010). It is likely that these properties can be tailored in Laponite, a synthetic smectite clay hydrogel with a composition and structure similar to natural clay (Thompson and Butterworth 1992).

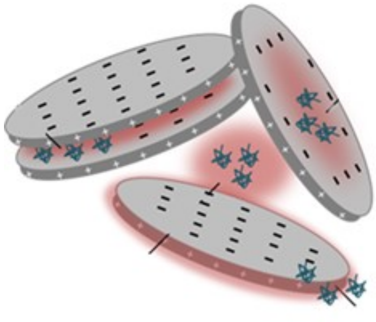

Figure 1.4.1: Illustration of Laponite nanodiscs structure. Laponite nanodiscs have weak negative charge that allows electrostatic interaction with organic molecules such as nucleic acids, peptides and proteins. The figure illustrates the multiple interactions sites that these silica nanoparticles provide: surface, edges, inter-articles and interlayer sites. Reprinted with permission from Elsevier from (Dawson and Oreffo 2013), Copyright.

Laponite is composed of nanodiscs, 30 nm in diameter and 1 nm in thickness (30:1 aspect ratio), negatively charged on the surface and positively charged on the sides (Figure 1.4.1). The unit structure of smectites consist of two silica layers with a metal ion layer in between (Al^{3+} and Mg^{2+}), which provides a net negative charge (Dawson and Oreffo 2013). However, this negative net charge is relatively weak, allowing electrostatic interactions between the nanodiscs as they agglomerate. This synthetic smectite material starts to self-assemble upon contact with the surrounding buffer, forming a colloidal suspension and upon rapid agitation, a gel. Hence, the gelation mechanism of this hydrogel is compatible with physiological conditions (Bonn *et al.* 1999).

The swelling ability of the charged smectite particles is key for the interaction of the clay with organic molecules, which provides a unique adsorption capacity when forming a hydrogel (Dawson and Oreffo 2013). Laponite is able to adsorb proteins such as VEGF from the surrounding media, with negligible remaining VEGF in the media after two hours incubation (Dawson *et al.* 2011). Following VEGF-binding to Laponite, the clay gel was washed repeatedly and an *in vitro* angiogenesis test (HUVEC tubule formation assay) showed the retention of growth factor bioactivity over the next 48 hours culture (Dawson *et al.* 2011). The previous investigation demonstrated the simplicity of the conjugation process of Laponite, based on its natural adsorption capacity.

Smectite materials have been used as a cell culture supplement, with no indications of cell toxicity (Dawson *et al.* 2012; Depan, Kumar, and Singh 2009; Fisichella *et al.* 2009; Mihaila *et al.* 2014) or toxic degradation products *in vitro* (Sharifi *et al.* 2012). Baek *et al.* studied the oral drug administration of smectite nanocomposites, reporting no acute or long term negative effect *in vivo* (Baek and Choi 2012). Laponite has been used to deliver Doxorubicin to cancer cells, improving drug efficiency because of the improved release profile. In the earlier study, the combination of PLGA with Laponite provided a sustained release over time of the drug in a pH dependent manner, important for cancer therapy (Wang, Zheng, *et al.* 2012). Wang *et al.* combined PLGA with Laponite to encapsulate Amoxicilin in a nanofiber scaffold, successfully inhibiting the growth of bacteria (Wang, Zheng, *et al.* 2012). In the same study, the release profile was examined, and again Laponite resulted in a controlled release over a longer period compared to control composite (Wang, Zheng, *et al.* 2012).

There are few references in the literature that have used Laponite in an osteogenic context. Mihaila *et al.* used Laponite as a media supplement to trigger osteogenic differentiation of primary human adipose stem cells (Mihaila *et al.* 2014). Wang *et al.* used hybrid Laponite-doped electro-spun PLGA nanofibers to study the cellular response of human SSC, reporting again a significant increase in osteogenic markers (osteocalcin and alkaline phosphatase) as well as mineral deposition (Wang, Castro, *et al.* 2012). Following from the *in vitro* examination of Laponite, there remain a paucity of studies in which Laponite was used to treat bone defects *in vivo*. In 2011, Dawson *et al.* published a study in which VEGF and BMP2 were delivered using a Laponite-collagen scaffold in a murine critically sized femur defect (Dawson *et al.* 2011). µCT analysis showed a significant increase in vessel density, though no significant bone formation was achieved (Dawson *et al.* 2011). The same paper showed the ability of Laponite to support the encapsulation and survival of skeletal stem cells, displaying differentiation towards the three stromal lineages after 28 days culture (Dawson *et al.* 2011).

In 2014, Wang *et al.* used Laponite bioceramics to treat a critically sized bone defect in a porcine tibia; 24 weeks after, radiologic examination showed that Laponite treatment healed the defect while the control did not (Wang *et al.* 2014). However, the study was conducted on a small animal cohort (n=2), and there was no quantification of bone formation over time (histomorphometric or high resolution X-ray µCT) to assess how bone was unified (Wang *et al.* 2014). The same study examined the biosafety of Laponite ceramics in an acute systemic toxicity and intramuscular stimulation test in rats, with no reported symptoms of irritation or toxicity (Wang *et al.* 2014). More recently, Gibbs *et al.* used Laponite-coated allograft bone to localise BMP2 in a subcutaneous mouse implant, demonstrating that the sustain release of lower doses of BMP2 (40 ng *versus* 500 ng) improved the formation of bone tissue (Gibbs *et al.* 2016). This data demonstrate that hydrogels in general, and Laponite in particular, are strong candidates as a biomaterial and drug delivery carrier for BTE.

1.4.4 μCT and bone imaging for construct evaluation

Micro computed tomography (μCT) is a high resolution imaging technology that utilizes non-invasive, non-destructive X-rays to obtain cross-sectional images through the sample (tomography). As a basic description of the μCT mechanism, the energy source produces an X-ray beam that passes through the sample and is collected or registered on the other side of the sample by a detector (Figure 1.4.2). Depending on the radiodensity of the sample, the X-rays are attenuated or absorbed (attenuation coefficient), creating a cross-sectional image or projection (Figure 1.4.2). An entire scan is composed of multiple images of each of those cross-sectional images or “slices”. Similar to the clinical devices, the SkyScan 1176 system used in this study employs a rotating X-rays source and detector while the sample is maintained stationary (Figure 1.4.2). The filter between the X-ray source and X-ray detection serves to adsorb low energy X-rays, passing through high energy X-rays only. The use of filters allows adapting the energy source to the density of the scanning object, hence high density materials require high energy beams which can actually pass through the object, however not high enough to generate saturated (white) pixels.

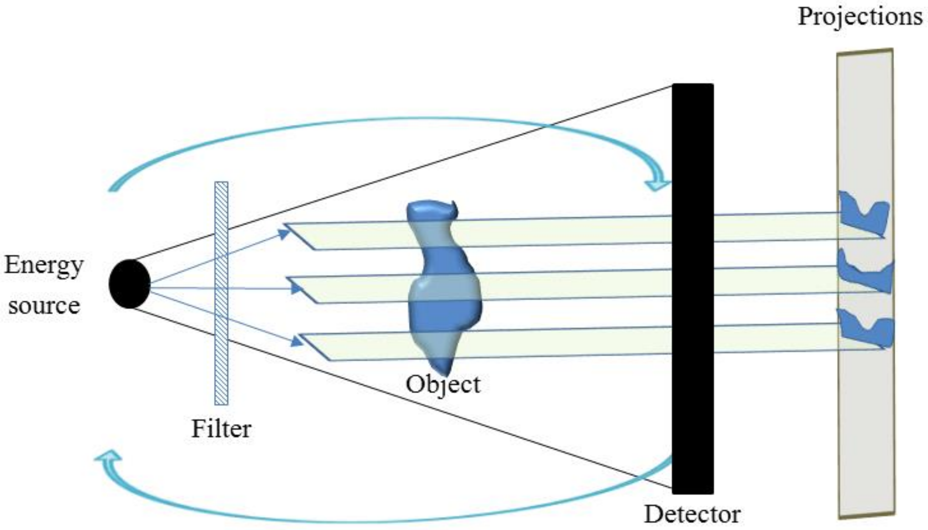

Figure 1.4.2: Diagram of the *in vivo* scanning system, SkyScan 1179 (Bruker, Belgium). The energy source and the detector rotate around the sample, which remains static.

Optimisation of CT parameters such as X-ray energy (kV, (μA), exposure time (ms) and resolution are critical for the quality of the scan and should be tailored for samples of different sizes, compositions and densities. In particular for *in vivo* scanning, additional parameters such as exposure time and X-ray dose (Grays; Gy) should be carefully considered so as not to compromise viability of the animal. CT scanners are commonly used to irradiate animals to create immune-compromised phenotype (10-15 Gy); however X-rays exposition under 1 Gy do not show biological relevant effects on living mouse , and under 400 Gy on *in vitro* cultured cells (Kanno *et al.* 2015; Mitchel 2007; J. H. Waarsing *et al.* 2004)

The µCT scan allows the generation of X-ray images of the sample from different perspectives or projections at a certain resolution or voxel size. The higher the resolution, the highest the signal-to-noise ratio on the projections (Figure 1.4.3).

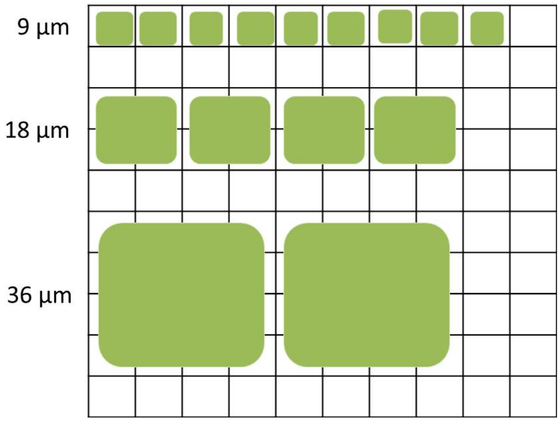

Figure 1.4.3: Diagram illustrating the scanning resolutions available (9, 18, 36 µm) in the *in vivo* 1179 SkyScan system.

These projections need to be reconstructed using computer software (NRecon) to build up a 3D image stack of cross-sectional slices in 8 bit format (0-255 greyscale) from the original projection images (16 bit format). The greyscale images will then need to be segmented to separate the foreground (X-ray attenuating tissue) from the background (soft tissue, fat, water and air). Segmentation is commonly conducted using a thresholding method based on different algorithms (automatic, global, adaptive, etc.). In general, the function of the threshold is to achieve minimal error in the process of classification of pixels to foreground and background, respectively (Hara *et al.* 2002; Kothari *et al.* 1998; Jan H Waarsing, Day, and Weinans 2004). Following the application of a threshold, a binarised dataset is created which can be then analysed to obtain quantitative and structural measurements such as bone volume, trabecular number, thickness, separation and additional parameters (Figure 1.4.4). By scanning under the same X-rays parameters specials rods with a known concentration of hydroxyapatite (calibration phantoms), the bone mineral density of the tissue can be estimated or inferred as well.

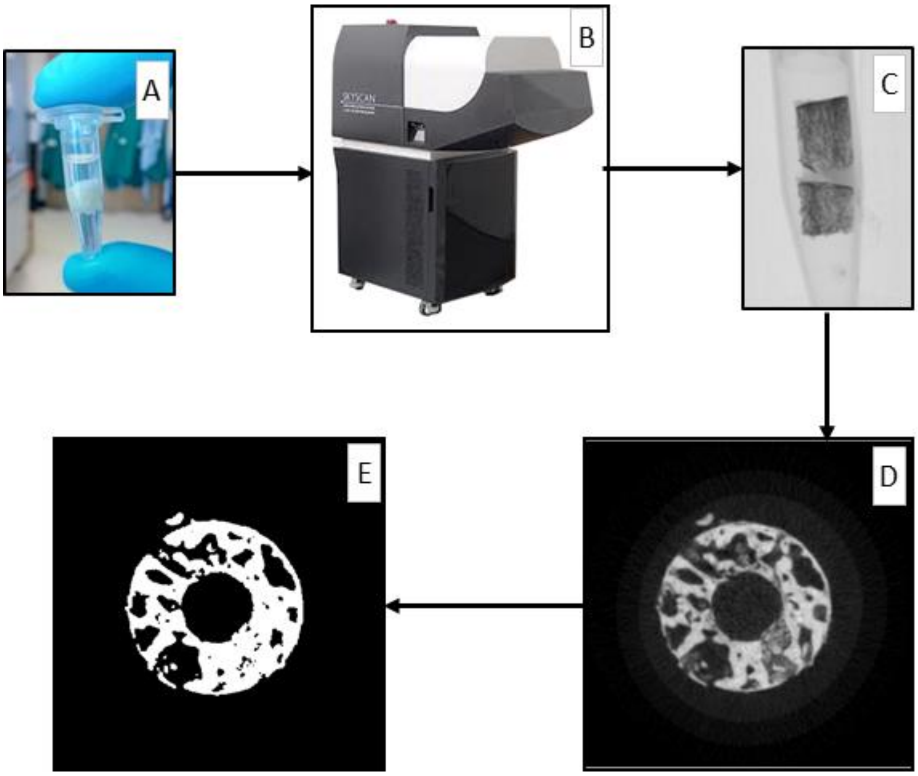

Figure 1.4.4: Schematic process of µCT analysis. Bone cylinders were scanned in plastic tubes (A) in an *in vivo* SkyScan 1176 system (B) to obtain X-ray projections (C). Following reconstruction of the dataset, the greyscale stack of images (D) was thresholded (binarised) to allow for image analysis (E).

Depending on the research question, different parameters can be measured using µCT analysis. Generally, studies focused on assessing new tissue formation account for more global parameters such as bone volume (Cai *et al.* 2014; De la Riva *et al.* 2010) or bone mineral density (Deng *et al.* 2014). Hence, most *in vivo* studies implement µCT technology to evaluate the success of the scaffold- biomaterial by measuring bone volume on the implant site (Davies *et al.* 2006; Dawson *et al.* 2011; Fang *et al.* 2005; Kanczler *et al.* 2008) For developmental studies, additional parameters to examine the architecture and composition are required (*i.e.* cortical thickness, trabecular thickness number and separation, etc.)(Davies *et al.* 2006).

As well as measuring bone architecture and new tissue formation, µCT can be used to quantify functional blood vessels (angiogenesis). In *in vivo* studies, the animal vascular system can be perfused with a radio-opaque contrast dye prior to performing the scan. This method can also be applied to mineralized tissue or scaffolds by including a demineralization treatment before the µCT scan, ensuring that only the contrast dye is visualized in the scan (Bolland *et al.* 2008; Dawson *et al.* 2011). However, this implies that bone tissue examination is not available in parallel and hence a limitation for the comparison of bone formation and vessel formation on the same scan.

In order to assess the potential of biomaterials to induce bone formation *in vivo*, common preclinical tests involve the implantation of the biomaterial under the skin of a murine host (subcutaneous implant) or, in the next stage of testing, into a critically sized bone defect.

Evaluation of bone formation is typically assessed using X-ray analysis for mineral deposition, followed by histological analysis. 3D X-ray imaging (*i.e.* μCT) is superior to 2D imaging (*i.e.* Faxitron) for analysis of bone tissue healing given that the contrast resolution of μCT allows detection of small changes in tissue type, architecture and composition. In terms of bone regeneration, traditional X-ray would identify tissue formation in a fracture, whereas μCT imaging would give added depth of detail to assess whether tissue has been formed in union or non-union, and whether is mineralized or non-functional fibrotic tissue. Hence, micro-computed tomography (μCT) is the current gold standard to evaluate tissue regeneration and bone microstructure (Bouxsein *et al.* 2010). Due to the rapid advances in the field of X-ray imaging analysis, the technology has moved from millimetre resolution in clinical CT, to very high resolution (synchrotron at the nanoscale), permitting even the visualisation of osteocyte lacunae (van Lenthe *et al.* 2007).

In summary, this past section of bone tissue engineering (1.4) has described the current bone filling materials together with the available biological strategies to design smart biomaterials, as well as the important tools (*i.e.* μCT) for construct evaluation. Ideally, these strategies should translate into the clinic to achieve patient applications, implying extensive and thorough preclinical testing. Hence, the next section will discuss in the detail the importance of appropriate animal research in BTE, highlighting the limitations and potential alternatives.

1.5 The use of animals in research

Animal research has a critical and crucial role in aiding advances in the biomedical field. The use of animal models provides an unrivalled approach to understand biological processes and diseases. *In vivo* testing is crucial for the development of novel drugs and devices that can improve the lives of millions of people worldwide. In particular for BTE; the previous section 1.4.1 detailed the numerous combinations and design options available to construct smart biomaterials, illustrating the large number of scaffold-strategies developed. The number of biomaterials-scaffolds for tissue engineering publications have increased significantly over the last 15 years, currently reaching over 400 per year (Figure 1.5.1). More importantly, the number of studies involving *in vivo* testing of these biomaterials increased proportionately (Figure 1.5.1). Hence, the development of alternative methods to determine data of equivalent quality and relevance remains a constant research objective, with the ultimate view to reduce, or even eliminate, the use of *in vivo* models.

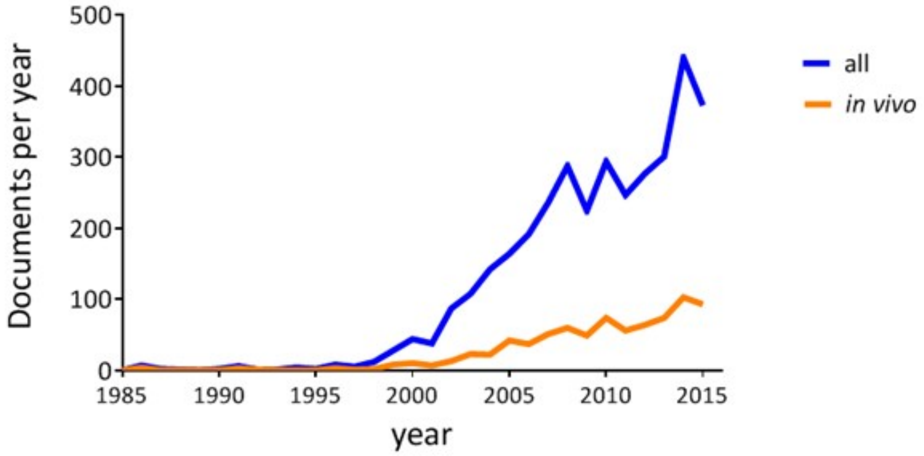

Figure 1.5.1: Evolution of number of publications in tissue engineering from 1985 until 2015. Number of research articles published from 1985 until 2015 under the keyword search of "tissue engineering" and "biomaterial" (blue line), and "*in vivo*" (orange line) on Web of Knowledge database.

Critically, public opinion on the use of animals in research remains positive, with the understanding that such research is performed within a strictly humane context (68% of acceptance in 2014 in the UK (Leaman, Latter, and Clemence 2014). This is accomplished by minimizing the amount of animals in research as well as improving their life quality within research laboratory facilities. It is clear that enhanced understanding of animal behaviour allows for improved animal welfare and provides additional information to the reaction of animals to certain treatments (mobility, activity, etc.). For instance, facial recognition in mice has been used to examine response to pain and distress of new treatments (Langford *et al.* 2010).

The principle that each individual animal in research is important is enshrined in the 3R's concept, first described in 1959 by Russel and Burch (Russel, W. M. S and Burch 1959):

- Reduction of the number of animals employed in each experiment to the minimum essential to obtain comparable levels of information.
- Refinement - the improvement of the conditions for animals not only at the husbandry level but also during the experimental procedure to try to minimize as much as possible potential distress, pain or stress to the animal.
- Replacement - the development and use of alternative methods which will still provide significant information and at the same time avoid the use of experimental animals. Immature vertebrates (embryos), computer modelling and *in vitro* techniques are example of replacement models.

Current efforts within animal research are centred on producing high quality science while decreasing the use of animals and improving the wellbeing for all laboratory animals. This is paramount not only from an ethical perspective but also given the costs involved and requisite time typically required for such studies. *In vivo* studies are generally a final step/option in the research pathway, having optimized experimental parameters as far as possible *in vitro*. Moreover, regulatory bodies such as the U.S Food and Drug Administration (FDA) consider the implementation of the 3Rs essential policy on their preclinical design (*i.e.* choice of animal model, age, delivery route, dose, etc.) while reviewing new applications from sponsors and investigators (Robinson 2011). It is within the FDA scope to assess the suitability of preclinical studies as it represents a critical component to provide the adequate and relevant data to support the successful development of the subsequent clinical trials (Robinson 2011). In fact, since 1998 the FDA has approved the use of 42 alternative safety testing methods, of which half of them do not require *in vivo* studies (Robinson 2011).

1.5.1 *In vitro* models for tissue engineering

Current efforts towards developing *replacement* alternatives are mainly based on *in vitro* studies among others (immature forms of vertebrates, human tissue, computational modelling of biological systems, etc.). Isolation of primary cells from human tissue provides more clinically relevant information of the cell response in terms of biocompatibility (proliferation, cytotoxicity), characterisation (gene/protein expression) and functional (differentiation) assays, compared to cell lines (Czekanska *et al.* 2014; Tuli *et al.* 2003). Hence, *in vitro* studies such as simple incubation in cell monolayer is often sufficient to study the response of the cell to diverse stimuli such as different topographies, growth factors and culture conditions such as hypoxia (Cooley *et al.* 2010; Mirmalek-Sani *et al.* 2006; Stoddart *et al.* 2006).

Co-culture studies involving skeletal stem cells (SSC), osteoblasts (OBs) and endothelial cells (ECs) have provided information concerning the interactions between cell types, significantly contributing to the biological relationship of angiogenesis and osteogenesis (Clarkin *et al.* 2008; Pedersen *et al.* 2012; Steiner *et al.* 2012; Udagawa *et al.* 1990; Villars *et al.* 2002). More complex culture conditions have been developed using three dimensional (3D) sphere mono or co-cultures of different cell types to study cell-cell interaction and cell-environment interactions which mimic more closely their natural niche (Hadjizadeh and Doillon 2010; Rao and Stegemann 2013; Saleh, Whyte, and Genever 2011). As an example, 3D cultures have been used in drug delivery research as a high throughput screening method (Hofstaedter and Ebner 2004). In addition, *in vitro* bioreactors have been developed for the culture and differentiation of SSC by modifying their culture and mechanical conditions (David *et al.* 2008; Haycock 2011; Liu *et al.* 2013; Stevens *et al.* 2005). Perfusion bioreactors can be used to mimic the physiological conditions of mass transfer within the cell culture (Liu *et al.* 2013). More intricate bioreactors including cyclic compressions have shown improved osteogenesis in co-culture studies (David *et al.* 2008; Davies *et al.* 2006; Vivanco *et al.* 2013). However it is important to consider that despite the large variety of *in vitro* tests available, these tests do not fully predict *in vivo* outcomes (Hulsart-Billström *et al.* 2016). Hulsart-Billström *et al.* recently examined the correlation between 47 *in vitro* and 36 *in vivo* experiments scoring 93 biomaterials variables across eight European laboratories, reporting no significant association between the outcomes (Hulsart-Billström *et al.* 2016). Importantly, only when examining two different categories of *in vitro* assays involving biocompatibility and functional assays (*i.e.* alkaline phosphatase activity) the correlation proved to be significant (Hulsart-Billström *et al.* 2016). Hence the previous study demonstrates the need to improve and develop new strategies to link the *in vitro* and the *in vivo* data towards translation.

Following a more biologically relevant approach, organotypic cultures have been used to incubate a living organ *in vitro* at a controlled air/liquid interface while maintaining the original 3D structure of the tissue (Figure 1.5.2). Studies conducted implementing organotypic culture of bone have provided an *in vitro* system to study tissue regeneration and repair (Saunders *et al.* 2010) as well as insights into the skeletal tissue development of the chick embryo (Kanczler *et al.* 2012). In particular, Kanczler *et al.* developed a critically sized chick femur defect model for organotypic culture which has been used to evaluate more than fourteen biomaterial combinations for tissue engineering (Kanczler *et al.* 2012; Smith *et al.* 2014a, 2014b; Smith, Kanczler, and Oreffo 2013).

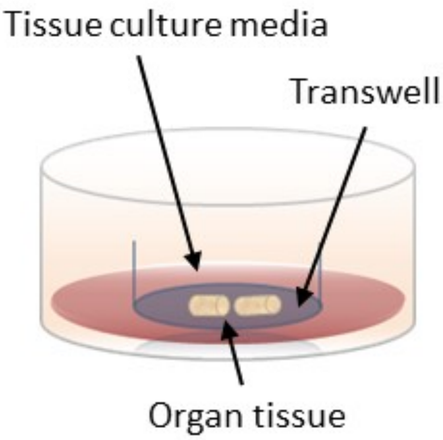

Figure 1.5.2: Organotypic culture of bone tissue. Transwell insert for a 6-well-plate well made of a semi-permeable membrane provides an air-liquid interface for 3D organ culture.

The air-liquid interface in which the bone is cultured has been shown to increase the oxygen tension, which resulted in improved cell viability and bone formation (Smith *et al.* 2013). In organotypic culture, chick femurs can be maintained up to 18 days *ex vivo*, however after the initial 10 days, the femur starts to deteriorate resulting in tissue necrosis. Given the optimal stage for cell proliferation and cartilage and bone growth is between day 3 and day 9, organotypic culture is standardly performed up to 8-10 days (Smith *et al.* 2013). During that incubation time, the femur can respond to exogenous stimuli and the effects can be measured as a result of femur growth in length (mm), mineralization (μCT) and collagen deposition (Kanczler *et al.* 2012; Smith *et al.* 2014a, 2014b). Hence the organotypic model offers a number of advantages as *in vitro* model for the study of bone and cartilage repair and as a relatively high throughput system to test biomaterials *in vitro*. However, even if this models provides a refinement alternative for animal research, lack of complete animal physiology (vasculature, inflammatory and immune system) remains a crucial aspect of preclinical research which still remains to be addressed. In addition, the fact that bone graft vascularization is a major bottleneck in skeletal tissue engineering strategies further demands the use of a vascular bed for the evaluation of bone regeneration.

1.5.2 *In vivo* models for bone tissue engineering

Despite the variety of *in vitro* models offering an alternative to animal testing, novel biomaterials still need to be tested in the context of a full animal physiology to assess their safety and efficacy. In addition, these are a mandatory requisite for the regulatory steps/hurdles prior to clinical evaluation. Preclinical testing of biomaterials is commonly evaluated following different stages or steps; initially, a subcutaneous implant model is used to assess biocompatibility, followed by a bone fracture or orthopaedic defect to examine the ability of the biomaterial to boost bone repair. These studies are normally conducted in small animal models before the ultimate evaluation in larger animals such as the sheep and goat, as those provide a more similar mechanical and physiological context to the human response (Muschler *et al.* 2010). In particular, small animal models account for approximately 50 % of studies examining *in vivo* bone fractures (mouse 15 %, rat 38 %), followed by the rabbit model (19 %) and then larger animals such as goat, sheep and dog account for approximately 25 % of the cases (O'Loughlin 2008).

Most studies describing novel constructs for bone repair employed subcutaneous models to optimise (*i.e.* dose) and characterise (*i.e.* drug release profile) construct variables before application onto actual bone defects (see section 1.4.1). Subcutaneous implants in mice are typically used to test whether the constructs are biocompatible and able to form bone ectopically in the context of vascular supply (Davies *et al.* 2008; Wang *et al.* 2014; Yang *et al.* 2004). Hence the previous model serves as a screening tool prior to assessment within an orthopaedic defect model. This process commonly requires the use of immunodeficient mice and a surgical procedure to implant the construct, maintained approximately over 28-56 days (Scott *et al.* 2012). Following that, a critically sized (not capable of self-repair) bone defect will be used to evaluate the construct (Reichert *et al.* 2009). A multitude of bone defect models have been described in the literature, including different animal species, age, defect size and location; hence preventing the unanimous use of a gold standard *in vivo* model in BTE (Reichert *et al.* 2009).

1.5.3 Development of translational *in vivo* models

There is evidence that animal models have limited potential to predict the human response to drugs and disease given the evolutionary biology differences between species (Greek and Menache 2013).

While animal models provide crucial insights on fundamental biological and physiological research, the understanding of human specific response go beyond the limits of any *in vivo* model. Hence, the use of appropriate and suitable animal models which resemble a human response scenario as much as possible is essential, and a mandatory requirement for FDA application approval (Robinson 2011). Advances in the genetic engineering field have allowed the generation of diversity of mutant animals to resemble human diseases and phenotypes, typically employing genetically modified mice strains. However, the ability of these models to efficiently simulate the response on humans has been challenged in several studies (McGonigle and Ruggeri 2014). Indeed, it is important to consider that human and rodents have a different life-span and their gene regulation diverges significantly, even at the tissue-specific level (Odom *et al.* 2007).

Hence it is not surprising that genetically modified animals fail to recapitulate the human symptoms of the same disease (Wall and Shani 2008). A study examining the similarities between animal toxicology studies and human toxicity of more than 150 compounds found that non-rodent models could effectively predict 63 % of the cases, while rodent models where predictive in only 43 % of cases (Olson *et al.* 2000). Moreover, discrepancies in drug doses, regimen, follow-up length and delivery route of administration between animal studies and clinical trials contribute as additional sources of divergence (Greek and Menache 2013). This is why FDA approval of clinical studies requires testing in at least two different animal species, from one of which to be non-rodent (Robinson 2011). Finally, another common reason for animal studies to fail to translate is related to the lack of appropriate experimental design and outcome reporting (McGonigle and Ruggeri 2014; Song *et al.* 2010). To overcome those issues, a comprehensive list of reporting guidelines “Animal research: Reporting *in vivo* experiments: ARRIVE guidelines” was published in 2010 to standardise across journals and improve the quality of reporting (Kilkenny *et al.* 2010, 2013).

Within the 3Rs paradigm, a central approach has been the development of replacement strategies to develop better models and tools which specifically mimic human biology and physiology. This aims to improve translational studies by improving the prediction efficacy and safety of drugs and therapies. Strategies moving towards humanised models include the implantation of human tumour grafts into immunodeficient mice, as those studies have been proven to reflect tumour growth, metastasis and predict drug responses (DeRose *et al.* 2011). In a similar manner, the chorioallantoic membrane (CAM) of the developing chick embryo could be used for the culture of human tissue, as it would provide a comparable physiological environment to the subcutaneous implant. In addition, the CAM is a simple and painless system that provides a vascular test-bed to examine the angiogenic component, hence providing a refinement model for animal research. Importantly, the use of the CAM to culture skeletal tissue freshly derived from patients may offer a more appropriate tool to predict the human physiological response compared to animals models which do not implement human xenografts. The next section will discuss in more detail the principle of the CAM assay, with particular focus in tissue engineering applications.

1.6 The chorioallantoic membrane (CAM) assay

From the moment of fertilisation the chick embryo develops over 21 days before hatching, staged and named by Hamilton and Hamburger as embryo development day (EDD) (V. Hamburger 1951). The chick embryo is surrounded by four extra-embryonic membranes: i) the yolk sac ii) the amnion iii) the allantois and, iv) the chorion. The functions of these membranes are to protect and nourish the embryo during its development. The CAM is formed around EDD 4 by the fusion of the mesoderm tissue of the allantois and chorion membranes, and it is fully developed by EDD 14, growing exponentially from 6 cm^2 up to 65 cm^2 in 10 days (Figure 1.6.1) (Nowak-Sliwinska, Segura, and Iruela-Arispe 2014). After EDD 14, the capillary plexus of the CAM becomes attached to the eggshell membrane (Figure 1.6.2 B).

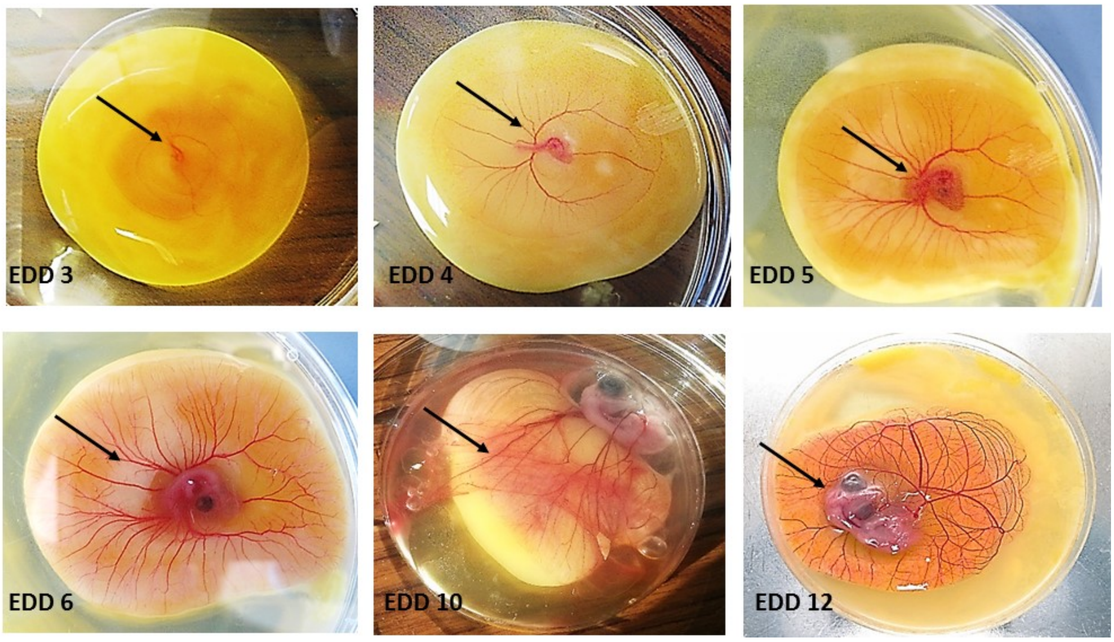

Figure 1.6.1: *In vitro* culture of chick embryos from EDD 3 until EDD 13. Fertilized eggs were incubated until EDD 3 to transfer the chick embryo into a petri dish and resume incubation in vitro. Shell-less culture was maintained up to EDD 12 and images of the chick embryo (see arrows) were taken at EDD 3, 4, 5, 6, 10 and 12. Embryo developmental day (EDD).

This fused, non-innervated membrane works as a respiratory organ facilitating the gas exchange of O_2 and CO_2 between the eggshell pores and the embryo as well as serving as a nutrient-waste interchange. In addition, the CAM contributes in ion transport as well as incorporating calcium from the eggshell to allow bone mineralization (Tuan and Lynch 1983; Tuan 1980). The CAM is located between the eggshell and the allantois, surrounding all the embryo structures where the allantois serves as a deposit for the waste material such as urea and uric acid (Figure 1.6.2 A).

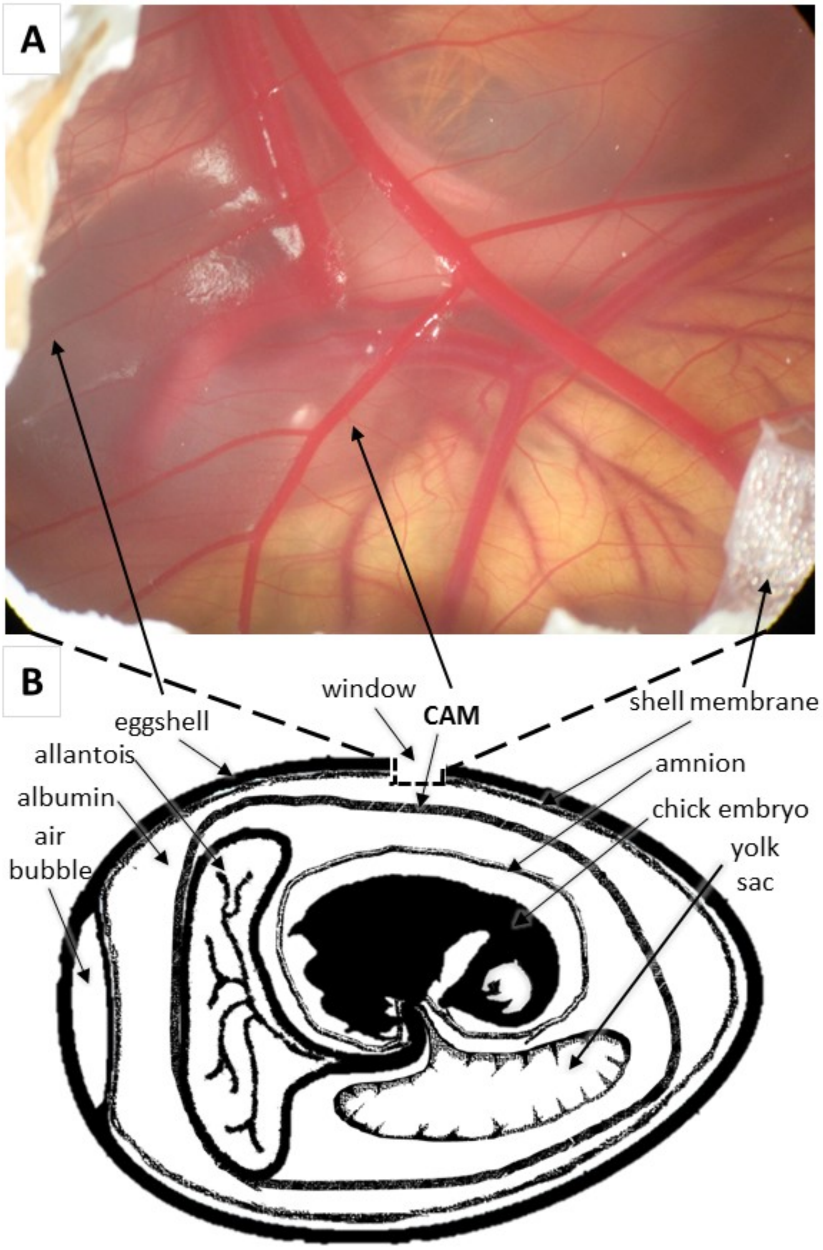

Figure 1.6.2: Illustration of the chick embryo and extraembryonic membranes anatomy for CAM assay. (A) View of the CAM window. Vascular tree with arteries and veins in the chorioallantoic membrane. (B) Schematic representation of the chick embryo egg, extraembryonic membranes and CAM window. The chick embryo is surrounded by the *amniotic* membrane containing amniotic fluid. The embryo is also connected to the yolk sac and to the allantois membrane. The allantois membrane which fuses with the chorion forming the *chorioallantoic* membrane (CAM) which surrounds the chick embryo. The *yolk sac* is contained within a vascular viteline membrane providing the nutrients for embryo development. The *shell membrane* or cuticule surrounds the eggshell as a defensive mechanism to prevent entry of bacteria. The eggshell is composed of porous $CaCO_3$ to facilitate gas exchange between the CAM and the atmosphere. During windowing the eggshell and shell membrane (cuticule) are perforated to access the CAM beneath. Arrows point at the structures shown in the macroscopic image (A) and in the cartoon representation (B).

Due to the rapidly developing vascular system in the CAM the chick embryo is commonly used to perform (anti)angiogenic studies as well as cancer research (Kilarski *et al.* 2012; Lokman *et al.* 2012; Ribatti 2010). In short, the CAM assay consists of assessing whether the tested compound promotes or repeals the angiogenic response from the extraembryonic membrane. This is achieved by placing the treatment substance on the CAM surface, approximately between EDD 4 and EDD 10, to observe its angiogenic response over the rest of the chick embryo incubation period (Ribatti *et al.* 2006).

1.6.1 The chick embryo (pseudo) immune response

While the chick embryo is conventionally considered an immunodeficient host for graft implantation, some studies indicate that the chick embryo is able to elicit a primitive immune response (Klueh, Dorskty, and Moussy 2003; Lafferty and Jones 1969; Sys *et al.* 2012; Valdes, Kreutzer, and Moussy 2002). It is known that as early as EDD 7, the chick thymus starts the process of recruiting lymphocyte precursors (Bellairs and Osmond, 2005). Lymphocytes T develop in the chick thymus around EDD 11, while lymphocytes B develop from the bursa of Fabricius (the equivalent organ to the bone marrow in mammalian) around EDD 12. Both lymphocytes B and T cells start to circulate through the blood stream from EDD 12, together with monocytes and heterophils, the latter acting as a mammalian version of neutrophils (Janse and Jeurissen, 1991). Lymphocytes T and B and monocytes cells do not became mature until EDD 18, and hence this is why the chick is considered an immunocompromised host (Lafferty and Jones 1969). However, no differences were observed between day 14 chick embryos and 16 week old adults in macrophage function (Friend *et al.* 1990).

In fact, there are several studies which have reported an immune response following the implantation of (xeno)graft material on the CAM (Lafferty and Jones, 1969; Valdes *et al.* 2002a; Klueh *et al.* 2003; Sys *et al.* 2012). One study implanted lymphocytes cells from various animal species (pigeon, duck, sheep, rat and guinea pigs) on CAM and reported swelling of the chick embryo spleen (Lafferty and Jones, 1969). Another study implanted human osteosarcoma biopsies on the CAM to study their tumorigenic potential and described an inflammatory response together with fibrous deposition and CAM hyperplasia (Sys *et al.* 2012). In a similar manner, the CAM produced significant fibrous deposition after implantation of bacterial endotoxins and cotton threads (Valdes *et al.* 2002a). The same study also reported the presence of leukocytes and macrophages at histological analysis, which the authors described as an acute inflammatory response comparable to the mammalians (Valdes *et al.* 2002a). Other investigations testing the similarities between mammalian and CAM immune system showed biocompatibility to nylon and silicone: commonly used surgical materials in the clinic (Klueh *et al.* 2003). The previous studies demonstrate that the chick embryo does have a primitive immune response, which matures upon the end of the gestational process. Depending on the research question, this could become a positive or a negative factor when performing the CAM assay. Indeed, the culture of tissue from different species (xenograft) requires a suppressed immune response; however it is the initial inflammatory response which triggers the healing process of the grafted tissue. The second observation becomes particularly important in the context of biomaterials screening, as information about the physiological immune response would be relevant to assess construct performance.

1.6.2 CAM assay: *in ovo versus ex ovo*

There are two forms of the CAM assay depending on whether the chick embryo continues developing in the eggshell or alternatively in a petri dish (shell-less culture), respectively termed *ex ovo* and *in ovo* culture. The *ex ovo* assay permits direct continuous visualization of the implant during the incubation period, even so it also causes a reduction of the chick embryo death rate of 50-70 % during the initial five days of culture, reaching 90% around EDD 14 (Klueh *et al.* 2003; Lokman *et al.* 2012). Maintaining the eggshell is important since the CAM regulates the transport of calcium required for the normal mineralization of the chicken skeleton (Gabrielli and Accili 2010). As a result, in the context of an *ex ovo* assay the CAM can uptake mineral from the implant to compensate for the absence of eggshell. Vargas *et al.* proved the ability of the CAM to completely resorb bioglass-ceramic scaffold which resulted in significant mineralization of the chick skeleton compared to control embryos (Vargas *et al.* 2009).

Since the embryo is allowed to develop normally prior to the moment of graft implantation, lesser numbers of animals are required when doing the assay *in ovo*; hence implementing the 3Rs policy. For an *in ovo* approach, the shell of the egg is carefully pierced to open a small window which allows to place the implant on top of the CAM. Following that, the eggshell window is sealed to preserve sterility and the chick egg is placed in the incubator to resume incubation (for a detailed description of the procedure see section 2.3.2). The termination date and procedure of the protocol should be determined following the local ethics committee guidelines and approval. It is worth noting that many countries such as the UK and the US, the chick embryo becomes a legally ‘protected’ animal on the last third of the gestational period (EDD 14), hence requiring a license to conduct any regulated procedure (Animals Scientific Procedures Act (ASPA) 1986, amended 2012; Policy on the Humane Care and Use of Laboratory Animals. As an example to illustrate the steps of the CAM assay, Figure 1.6.3 shows the setup for organ culture from EDD 10 until EDD 18.

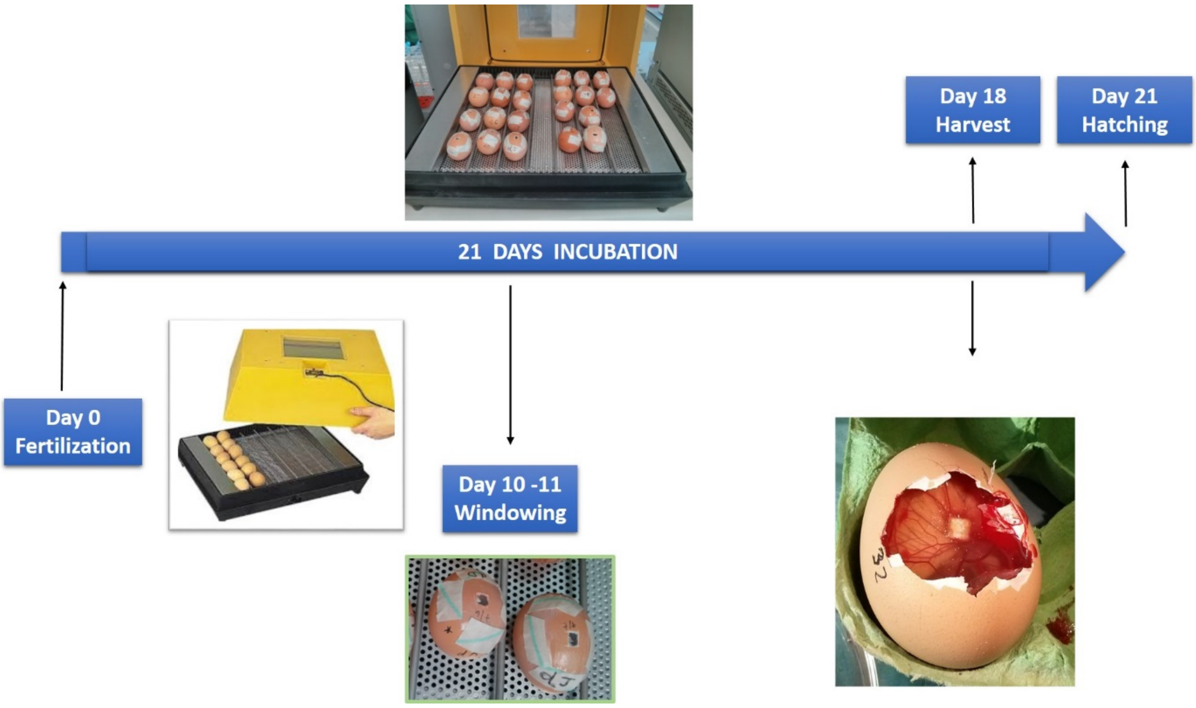

Figure 1.6.3: CAM assay experimental set up for tissue culture. Fertilized eggs are incubated in a Hatchmaster in a humidified atmosphere at 37 ˚C until EDD 10-11. At this point, a square window is opened on the eggshell to place the compound or graft on top of the CAM. The window is sealed under sterile conditions and the eggs continue incubating till EDD 18, when the grafts are harvested and the chick embryo is sacrificed according to the Home Office, UK guidelines.

Other variations of the CAM assay have been explored, such as graft implantation beneath the CAM as opposed to the standard form of graft deposited on top of the membrane (Martinez-Madrid *et al.* 2009). The previous study described that the altered CAM assay slightly reduced the viability of chick embryos as well as the integration of the grafted tissue on the membrane (Martinez-Madrid *et al.* 2009). An innovative design by Borges *et al.* involved the use of a plastic cylinder with a semi-permeable membrane to sustain the graft while implanted *in ovo* to allow for construct continuous localisation (Borges *et al.* 2003). Additional CAM approaches include the ‘egg-in-cube’, which consisted on the *ex ovo* culture of chick embryos using an artificial eggshell made of porous polycarbonate to facilitate graft visualisation while mimicking physiological environment of the chick egg (Huang, Arai, and Kawahara 2015).

Typically, the implant becomes integrated by the CAM in the following 24-48h (Ausprunk, Knighton, and Folkman 1975), and the angiogenic response can be evaluated as early as 48-72 hours post implantation (Baiguera *et al.* 2012). The CAM assay start-point can range from EDD 4 to EDD 11, depending on the size and weight of the sample and the scope of the experiment (angiogenesis *versus in vivo* culture). It is important to consider that the CAM develops promptly from EDD 4 to EDD 14, and thus the application of the same compound on CAM can elicit a different response depending on the CAM developmental stage (EDD). As an example, Bai *et al.* studied the angiogenic effect of BMP2 in combination with VEGF and FGF-2 at different time-points on the membrane (Bai *et al.* 2014). The peak response from the CAM was observed to be from day 10 until day 12 (3 days), even compared to extended implantation times (up to 6 days) at different start-point (Bai *et al.* 2014). In agreement, a study measuring the relative expression of VEGF, VEGFR2 and HIF-1a from the CAM showed an expression peak at EDD 11, however the study did not include earlier time-points than EDD 8 (Makanya, Dimova, and Koller 2016). Even so, a multitude of studies employing the CAM assay have described different start-points with, again, variable duration of the incubation period (Supplementary Table 7.1.1).

Importantly, the CAM assay is not suitable to evaluate long-term effects given the incubation time of any implant is limited to 7-10 days (period available between the CAM formation and the end of the chick embryo gestation). Another limitation of the CAM assay is the difficulty to differentiate between pre-existing and newly formed blood vessels (Ribatti *et al.* 2001; Richardson *et al.* 2005). Moreover most antibodies cross react with avian species, hence requiring to perform parallel immunohistochemistry for the antigen of interest as well as a specie specific markers (*i.e.* human leucocyte antigen; HLA) to confirm no cross-reactivity (Kunzi-Rapp, Rück, and Kaufmann 1999).

Several studies have evaluated the same constructs on the CAM as well as in rodents (subcutaneous implant), and even compared the outcome from both models (Deryugina and Quigley 2008; Edwards *et al.* 2014; Ling *et al.* 2014; Shivani. 2013; Steffens *et al.* 2009). Steffens *et al.* used the CAM assay to examine the effect of cell-seeded bovine cancellous bone scaffolds on the CAM for 8 days or on a mouse subcutaneous model for 21 days (Steffens *et al.* 2009). The results of the previous study showed that the vascular response from the CAM was comparable, if not higher, to the one from the mouse model (Steffens *et al.* 2009). Cellularised gelatin scaffolds were evaluated on the CAM assay for 7-9 days, as well as up to 28 days in a dorsal subcutaneous SCID mouse implant, reporting as well similar results between both models in terms of vascularisation (Ling *et al.* 2014). These studies provided evidence of the significant angiogenic response from the extraembryonic membrane even for a short incubation time frame.

A number of authors have already employed the CAM assay as a substitute for the subcutaneous murine model. Martinez-Madrid *et al.* investigated the effect of cryopreservation as a method to preserve fertility after aggressive chemotherapy on patients; the authors used the CAM for transplantation of human ovarian tissue and proved it was possible to obtain equivalent results, validating the CAM as an alternative for the traditionally used immunodeficient mice (Martinez-Madrid *et al.* 2009). Furthermore, the CAM assay has already replaced the use of the eye irritation test on rabbits, being now the Hen's egg CAM test a mandatory assay based on a scoring system which measures hyperaemia, haemorrhage and clotting (Debbasch *et al.* 2005; Luepke 1985). Moreover, over 10 FDA-approved anti-cancer drugs have been tested on the CAM and compared retrospectively with the preclinical data obtained employing mouse and rats models (Kue *et al.* 2015). The correlation demonstrated that the CAM was predictive of the results shown in preclinical studies. Hence this data demonstrate the growing potential of the CAM to be used as a less-sentient replacement/refinement alternative for currently used *in vivo* models.

1.6.3 The CAM assay in biomedicine

The first use of the CAM was documented as early as 1911 by Rous and Murphy, who described the culture of chicken sarcoma in the CAM (Rous and Murphy 1911). One year later the authors published similar studies with xenotransplants from rats tumours (Murphy 1913, 1914a, 1914b). From those early studies, the use of the CAM has evolved into multiple applications, mainly related to cancer research (Ausprunk *et al.* 1975; Balke *et al.* 2011; Lokman *et al.* 2012; Vacca *et al.* 1999) and development of viral vaccines (Durupt *et al.* 2012; Hardy *et al.* 1995). In recent times the CAM has been mainly used as a highly reactive vascular bed, where the CAM assay has been used for the study of the angiogenic properties of a variety of compounds such as VEGF, BMP2, FGF2 and endothelin (Anderson, Siegman, and Segura 2011; Bai *et al.* 2014; Cruz *et al.* 2001). Other cytokines and growth factors such as osteogenic protein 1 (BMP7), thrombin peptide, osteocalcin, Vitamin D and human angiotensin have been examined as well (Neve *et al.* 2013; Norfleet, Bergmann, and Carney 2000; Ramoshebi and Ripamonti 2000; Ribatti *et al.* 2001).

Additional applications of the CAM include testing of drug delivery systems, dosage and toxicity (Kue *et al.* 2015; Vargas *et al.* 2007). Other studies have examined the effect of applying X-rays on the CAM as a model to determine the side-effects in blood vessels after radiotherapy (Polytarchou *et al.* 2004) or following hyperglycaemia for diabetes research (Larger *et al.* 2004). The CAM has also been used to evaluate novel surgical tools for retina vascularization (Kilarski *et al.* 2009; Leng *et al.* 2004), glucose biosensors (Klueh *et al.* 2003; Klueh, Dorsky, and Kreutzer 2005) and Doppler tomography measurements of blood flow rate (Chen *et al.* 1997).

1.6.3.1 Biomaterial testing on the CAM assay

The CAM assay has been used for a number of years now as a screening platform for biomaterials. A variety of constructs with growth factors and/or cells have been implanted onto the CAM over the last 40 years (Supplementary Table 7.1.1). Supplementary Table 7.1.1 contains a detailed summary from a variety of studies implanting biomaterials on the CAM, demonstrating the large diversity in start-points, choice of *in ovo versus ex ovo* approach, output measurements and incubation length (Supplementary Table 7.1.1). Generally, most studies use the CAM to assess the angiogenic response of the biomaterial based on macroscopic evaluation of vessel formation at the implant site (vascular density, vessel branching points/mm^2 or blood vessel length) and/or histomorphometric analysis such as immunohistochemistry for CD31, an endothelial marker. Alternative methods to quantify angiogenesis include injection of a contrast dye for vessel perfusion and biochemical assays to measure haemoglobin at the implant site (Supplementary Table 7.1.1).

In 2001, Valdes *et al.* used the CAM to test the effect of a variety of biomaterials regularly used in operating theatres, showing comparable results to the mammalian response (Valdes *et al.* 2002). Naturally derived materials such as small intestine submucosa as well as polymer derived materials such as polyglycolic acid (PGA) and PGA modified with poly(lactic-co-glycolic acid) (PLGA) with and without growth factors have been tested on CAM as well (Azzarello *et al.* 2007; Kanczler *et al.* 2007). Covalent immobilisation of angiogenic growth factors (VEGF, Ang-1) on collagen scaffolds for cardiac repair has been examined on CAM, improving performance over growth factor conjugation (Chiu and Radisic 2010). Additional collagen-based scaffolds composed of microporous spheres proved to induce greater angiogenic response compared to polycaprolactone (PCL) ones (Keshaw *et al.* 2010).

The CAM assay has also been used to evaluate constructs for BTE applications. Composite materials such as bioactive glass nanoparticles with collagen scaffolds (Vargas *et al.* 2013) and PLGA combined with amorphous calcium phosphate have been tested on the CAM to observe a potential angiogenic response (Buschmann *et al.* 2012). In 2009, Vargas *et al.* examined the biocompatibility and bone mineralization potential of 45S5 Bioglass® using an *ex ovo* approach where the authors used the embryo survival rate as an indicator of biocompatibility (Vargas *et al.* 2009). Buschmann *et al.* seeded adipose-derived stem cells in electrospun nanocomposites PLGA-calcium phosphate scaffolds and achieved complete infiltration of blood vessels throughout the scaffold (Buschmann *et al.* 2012). Following a slightly more complex approach, Yang *et al.* used the CAM as a vascular bed for the culture of chick femurs from a chick donor containing a bone wedge-defect on the diaphysis (Yang *et al.* 2004). The implanted chick femurs were used to examine the effect of a BMP2-PLA scaffold seeded with patient derived cells, showing for the first time the ability of the chick femur to heal and bridge the gap following CAM-implantation (Yang *et al.* 2004).Thus, the CAM can serve not only as an angiogenic assay, but also as a 'bioreactor' capable of vascular and nutrient supply for the grafted tissue.

1.6.3.2 The CAM for the culture of graft tissue

As the CAM has a poorly developed immune system, the CAM has been used to implant living and allograft tissue from other species (xenografts). Skin transplants have also successfully engrafted; Kunzi *et al.* described blood vessel formation and infiltration of chick erythrocytes in the pre-existing capillaries of a human skin graft and preservation of human specific markers after culture (Kunzi-Rapp *et al.* 1999). Healthy mouse fetal skin was CAM-implanted and vascularised to be used as a model of wound healing (Carre *et al.* 2012). Other studies by Ribatti *et al.* studied the effect of decellularised brain and aorta tissue from rats on the CAM to serve as extracellular matrix scaffolds (Coconi *et al.* 2005; Ribatti *et al.* 2003). In a similar manner, bio-engineered allograft tracheas from human donors have also been tested on the CAM and showed an up-regulation of various angiogenic factors from the CAM (Baiguera *et al.* 2010). In contrast, freshly collected human placenta after delivery appeared to repel blood vessel formation from the CAM (Stallmach *et al.* 2001). Additional studies implanting living human tissue on the CAM include cryopreserved ovarian tissue (Martinez-Madrid *et al.* 2009) and patient derived tumours (Sys *et al.* 2012).

There is limited evidence in the literature on human bone tissue cultured in the CAM; it would appear only two investigations have implanted human living bone tissue on the CAM (Holzmann *et al.* 2010; Sys *et al.* 2012). In 2010 Holzmann *et al.* studied the effects of the bone banking procedures on human allograft bone tissue, assessing their ability to induce CAM angiogenesis (Holzmann *et al.* 2010). To evaluate the angiogenic properties of the allografts, samples were collected at different banking stages and incubated on an *ex ovo* CAM for 48 hours, employing fresh human femoral head bone chips as a control (Holzmann *et al.* 2010). The vascular reaction of the CAM was significantly higher for the control bone chips compared to the allograft samples, however no attempt was made to measure tissue repair (Holzmann *et al.* 2010). Another investigation conducted in 2012 by Sys *et al.* used the chick embryo to culture patient-derived biopsies from osteosarcoma tumours. The analysis, based on immunohistomorphometry, showed the ability of the CAM to maintain the original features of the tumours after culture (Sys *et al.* 2012). Importantly, the viability of the grafts upon CAM-implantation was proportional to the cancer stage and, ultimately, patient death (Sys *et al.* 2012). Overall, these studies demonstrated the potential of the CAM to answer their respective research questions, however neither of them aimed to evaluate tissue regeneration and repair of living human tissue.

1.7 Summary, scope and hypothesis

Due to an increasing ageing population, and thus the escalation in number of bone fractures, there is an urgent need to find alternative biomaterials that can aid bone regeneration. These bone graft substitutes need to be osteoconductive and, ideally, osteoinductive to allow tissue ingrowth and induce bone formation. To achieve this goal, current BTE strategies have sought to mimic the spatio-temporal cascade of events occurring naturally during bone healing. Thus, bone filling materials are combined with signalling molecules, cells and components of the extracellular matrix; hence increasing the number of biomaterial variables to test prior to clinical translation.

Preclinical testing typically involves a surgical procedure to implant the biomaterial subcutaneously in rodents for a period of 21-28 days. These *in vivo* studies permit to evaluate the biocompatibility of the construct and potentially the ability to form bone ectopically; however those studies are also expensive, time consuming, technically demanding and, critically, raise ethical concerns. While animal models can predict the human reaction to the biomaterial, those models are incapable of reproducing the clinical response. Hence it is necessary to develop better alternatives for preclinical testing which implement the 3Rs policy (reduction, refinement and replacement of animals in research).

To date, no study has described the use of the CAM to culture living human bone tissue as a framework for the study and examination of skeletal regeneration. Thus a human-avian model would offer a more clinically relevant osteogenic microenvironment to examine novel BTE strategies. In addition, the use of the non-innervated CAM as a surrogate blood supply would permit the *in vivo* study of bone regeneration in the context of angiogenesis, a major bottleneck in tissue engineering. This would have a critical impact as it would provide a refinement for the traditional murine subcutaneous implant model, an ethical obligation in animal research.

In particular, the development of the CAM assay for the culture of living human tissue would allow to test the effect of BMP2, a potent osteoinductive factor FDA-approved for clinical applications. It is well-known that supraphysiological doses of BMP2 can result in ectopic bone formation and additional side-effects hence requiring the use of controlled and sustain release of this growth factor. From that perspective, hydrogels can be used as a delivery vehicle for growth factors and cells directly at the fracture site (*in situ*). In that context, Laponite offers a significant advantage given its natural capacity to sequester and absorb proteins in solution, avoiding the expensive and time-consuming conjugation techniques and providing a potential candidate for BTE applications.

The ultimate aim of the present thesis is to develop a less sentient *in vivo* model for preclinical research in bone tissue engineering. To achieve this, this investigation aims to use the CAM assay as a surrogate blood supply to maintain the viability of human living bone, collected from surgical waste material following total hip replacement procedures. Hence this projects aims to study and examine bone regeneration in the context of i) vascular supply and ii) a human-like microenvironment. To validate this model as a tool to evaluate constructs in tissue engineering, this human-avian system will be examined in the context of a well-established, FDA-approved osteoinductive factor (BMP2) in addition to a novel, clay-based hydrogel (Laponite) for growth factor and cell delivery.

Hypothesis:

Human living bone can be cultured in the CAM assay to study bone healing and repair, and that this tissue regeneration can be measured/quantified by µCT and histological analysis.

Thus, the main aims of this thesis are:

- Develop the CAM assay as an *in vivo* model for the culture of living human bone

    - To standardise and optimise the production of bone grafts for the CAM assay
    - To overcome the technical challenges associated with histological processing and to familiarise with the regular features of both the CAM and bone tissue
    - To optimise and validate the use of µCT to measure changes in the human bone grafts
    - To develop fluorescent viability stains to assess bone tissue viability.
    - To implement the use of transgenic chick embryos in this model

- To examine the ability of the CAM to culture human bone and facilitate tissue growth:

    - To understand the interaction between the human and avian tissues
    - To assess the infiltration of avian blood vessels in the human bone tissue
    - To examine the viability of the bone tissue following CAM-implantation
    - To quantify the structural changes after CAM-implantation using µCT
    - To validate the observed structural changes by implementing histological analysis

- Examine the potential of this avian-human model as an assay to test biomaterials and develop the suitable techniques for its analysis.

    - To visualise the structural changes following incubation by implementing the 3D registration to superpose consecutive scans from the same bone cylinder.
    - To identify the bone mineral density of the newly formed bone following CAM-implantation.
    - To assess the role of the human autologous cells on the process of bone formation.
    - To examine whether the CAM can be utilised as a model of ectopic bone formation
    - To test the effects of BMP2 in the human-avian model using two biomaterials: an FDA-approved acellular collagen sponge and a clay-based hydrogel (Laponite)
    - To examine the effects of a clay-based hydrogel-vehicle of growth factors (*i.e.* BMP2, VEGF) and primary cells.

Chapter 2: Materials and Methods

2.1 Experimental design

Bone cylinders were extracted from freshly collected human femoral head and a concentric drill defect was introduced on the cylinders (see more details in section 2.2.1). The defect region was perfused with the biomaterial to be evaluated (see section 2.4) or left as blank (bone cylinders with empty bone defect). A number of 8-10 bone cylinders were used for each treatment group for *in vivo* implantation (Figure 2.1.1 D-i), and 2-6 cylinders for *in vitro* culture (Figure 2.1.1 D-ii) during a 7-9 day period. Specific protocol for the CAM assay and the *in vitro* culture are detailed in sections 2.3.2 and 2.3.1, respectively. Bone cylinders were µCT-scanned before and after incubation as detailed in section 2.5.1.

Only bone cylinders from successful CAM-assay (viable chick embryo, CAM-integrated samples) were included in the µCT analysis. Representative samples (n=3) were processed for histology.

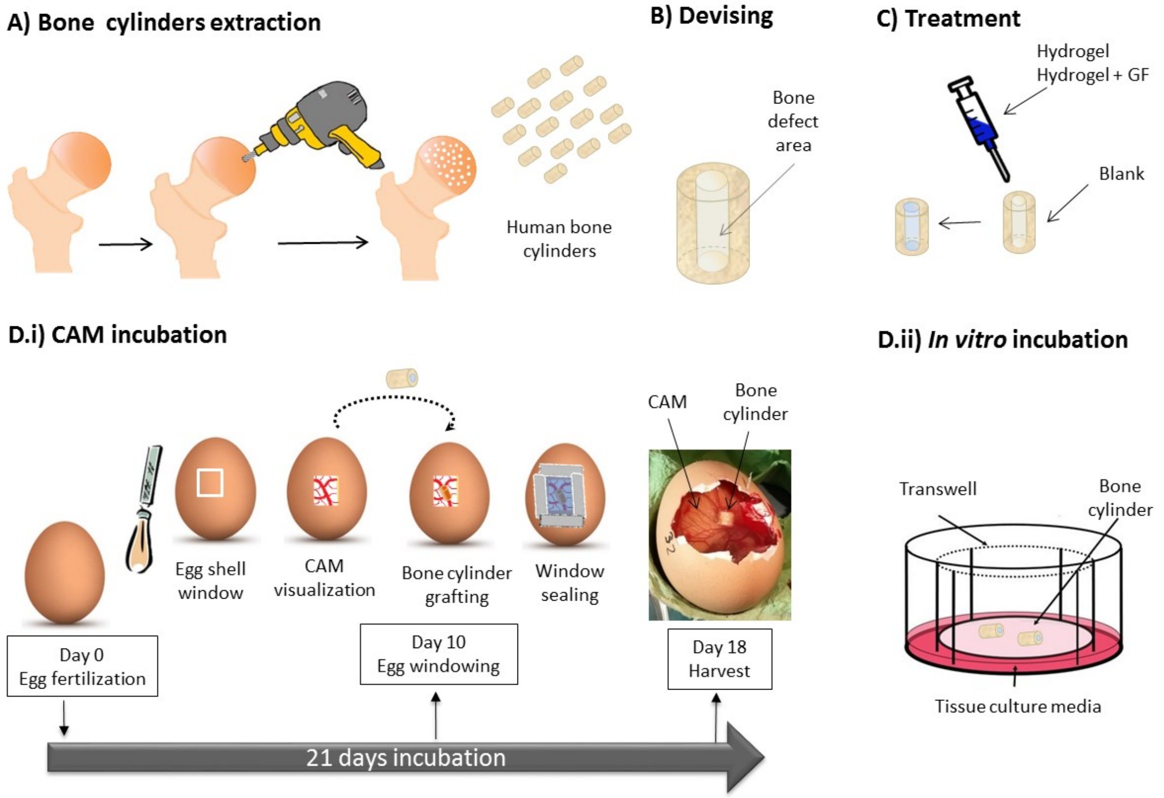

Figure 2.1.1: Schematic of the experimental design. A-B) Extraction and devising of the bone cylinders with a concentric bone defect, (C) Bone cylinder defect was perfused with the evaluated biomaterial (i.e. collagen sponge, hydrogel), (D-i) *in vivo* implantation on the CAM and (D-ii) organotypic *in vitro* culture for a period of 7-9 days.

2.2 Bone cylinders extraction, processing and culture

Tissue was obtained from adult femoral heads and bone marrow collected from haematologically normal patients undergoing routine elective hip replacement surgery. Only tissue samples that would have been discarded were used following informed patient consent. All protocols were conducted in accordance with the Southampton & South West Hampshire Local Research Ethics Committee (194/99/w).

Unless otherwise stated, all reagents were obtained from Sigma-Aldrich (UK); full list of reagents detailed in section 7.2

2.2.1 Bone cylinder extraction and devising

Bone cylinders were isolated from human femoral heads by first drilling with a guided-pilot drill (2 mm) followed by making a second, concentric incision with an empty-core cylindrical drill (6 mm). using a dentist surgical drill (Osteomed, USA). See section 3.2.3.3 for more technical detail. Sterile saline was perfused throughout. The articular cartilage was removed and PBS perfused through the defect area to remove any debris. Bone cylinders were then cultured in plain media (see section 7.2.1 for media description) in 5% CO_2 at 37 °C until the next day.

2.2.2 Processing of cylinders

2.2.2.1 Decellularised bone cylinders

To destroy endogenous cells in the bone tissue, the cylinders were i) fixed overnight in paraformaldehyde (PFA) 4% in PBS, ii) maintained at 121 °C for 20 minutes, or iii) submerged in 30 % hydrogen peroxide with repeated changes for 3 days. Thereafter, bone cylinders were thoroughly washed in PBS for 2 hours in rotation (3x) before resuming CAM protocol.

2.2.3 Bone cylinder viability stains

2.2.3.1 Live and dead staining

Two different molecular probes were used to label live and dead cells: Cell Tracker Green (CTG) and Ethidium Homodimer 1 (EtH1) respectively. CTG is composed of 5-chloromethylfluorescein diacetate (CMFDA) which is a non-toxic fluorescent dye that diffuses through the mammalian cell membranes. Once inside the cell the dye becomes transformed into a non-membrane permanent product through a transferase-mediated reaction. Cells labelled with CTG retain fluorescence and transfer it to the daughter cells for a number of generations, but not to the adjacent cells. The excitation/emission spectra was 492/517 nm. EtH1 is a molecular probe that becomes strongly fluorescent upon binding to DNA. In dead or dying cells with a disrupted cell membrane, EtH1 can enter and bind the DNA resulting in a positive signal. The excitation/emission spectra for EtH1 was 528/617 nm.

Freshly isolated bone cylinders were stained using the Live and Dead kit by incubating the bone cylinders in plain media (see section 7.2.1 for media description) with 10 µg/ml of CTG (C7025, Molecular Probes) and 5 µg/ml of EtH1 (E1169, Molecular Probes) prepared following the manufactures instructions. Each bone core was submerged in 1 ml of the staining solution and then incubated for 3 hours at 5 % CO_2 at 37 ˚C. Afterwards bone grafts were washed with sterile PBS (3x for 5 minutes each) and fixed overnight at 4 ˚C in 4 % (w/v) paraformaldehyde (PFA) in PBS. Non-stained control were extracted from the same femoral head and fixed as described before.

2.2.3.2 Cell Tracker Red staining

Cell Tracker Red (CTR) is a fluorescent probe that works in the same way as Cell Tracker Green though it does not need the enzymatic cleavage step to be active. The excitation/emission spectra of CTR is 577/602 nm (red). Freshly isolated bone cylinders stained using CTR were washed in PBS and incubated in plain media (see section 7.2.1 for media description) with 10 µg/ml of CTR (C34552, Molecular Probes) prepared according to the manufacturer's instructions. Each bone core was submerged in 1 ml of the stain solution and then incubated for 3 hours at 5 % CO_2 at 37 ˚C. Afterwards bone grafts were incubated with fresh complete media to resume the incubation. Alternatively, the bone cores were washed in PBS and fixed overnight at 4 ˚C in 4 % (w/v) PFA in PBS as non-stained control.

2.3 Tissue culture

2.3.1 Organotypic (*in vitro*) culture of bone cylinders

Bone cylinders were placed on top of Millicell inserts (0.4 µm pore size, 30mm diameter, Millipore UK) in 6-well tissue culture plates (Greiner Bio-One Ltd, UK) containing with 1 ml of plain media (see section for details 7.2.1) contacting the basal surface of the well insert. Media was supplemented with fetal bovine serum (FBS) for the experiments which did not examine the effects of growth factors (*i.e.* VEGF, BMP2). Each sample was placed on a transwell of a 6 well plate, and the plate was incubated in 5% CO_2 at 37 ˚C. Media was replaced every other day for the culture period.

2.3.2 CAM assay

Fertilized wild type eggs were obtained from Henry Stewart & Co, Norfolk, England. Genetically modified chick embryos expressing green fluorescent protein (GFP) were kindly donated by the Dr Adrian Sherman from the Transgenic Chicken Facility at the Roslin Institute (Edinburgh, UK). The eggs were incubated for 9-10 days at 37 ˚C in a 60 % humidified atmosphere, rotation was programmed every hour in a hatchmaster incubator. At day 9-10 of incubation a 0.5 cm^2 window was cut in the eggshell, and the implant was carefully placed on the CAM (Figure 2.3.1). Sterile parafilm was used to seal the eggshell window and the eggs incubated for another 7-9 days without rotation. Parafilm was sterilized by submerging in 70% ethanol for 5 minutes, followed by a PBS wash for 10 minutes.

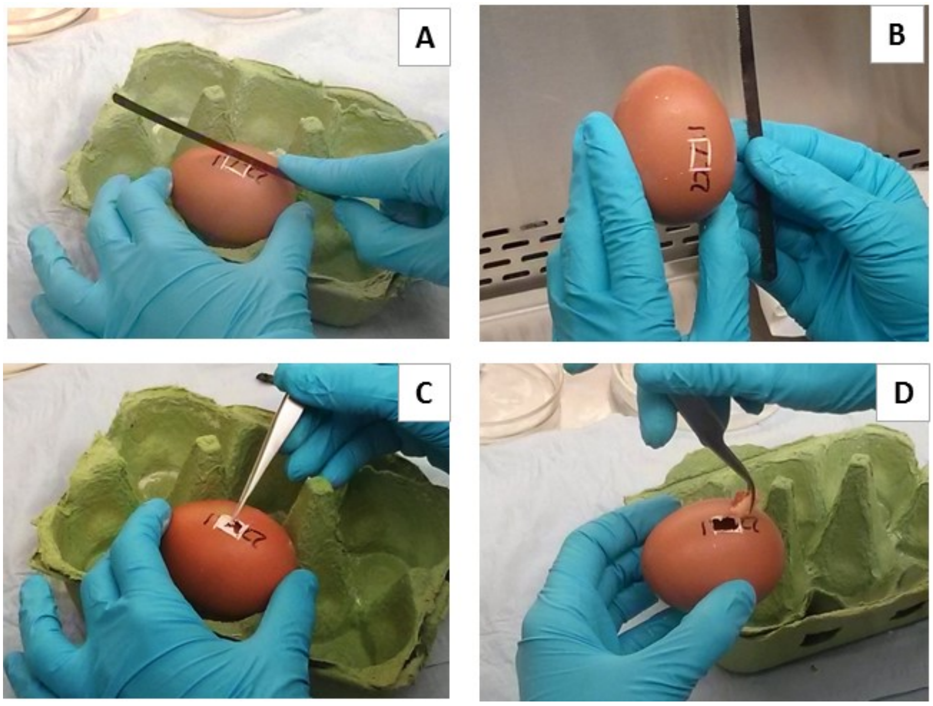

Figure 2.3.1: Eggshell windowing and graft implantation on EDD 10-11 chick embryos. (A-B) File-saw to indent the eggshell square (C) forceps to open the window and (D) implantation of bone cylinders.

At day 18-19 the samples were harvested from the eggs and the chick embryos were sacrificed in accordance to schedule 1 protocol under Home Office (UK) guidelines. The number of fully developed chick embryos according to Hamburger and Hamilton was recorded (V. Hamburger 1951). All animal procedures were carried out in accordance with the guidelines and regulations laid down in the Animals (Scientific Procedures) Act 1986, UK and chick embryo chorioallantoic membrane experimental protocols were approved and conducted under Home Office Approval UK (Project licence – PPL 30/2762) approved at the University of Southampton.

2.3.3 Cell outgrowth from explant culture of bone cylinders

After incubation, bone cylinders and CAM tissue were collected under sterile conditions and sliced into small fragments (2-3 mm) using a scalpel. Bone fragments were evenly distributed through the surface area of a well of a 6-well-plate containing minimum amount of complete media (see section 7.2.1 for media description) to cover the surface. The plate was maintained at 5% CO_2 at 37 ˚C, and the media were replaced every 5 days for the first 10 days. After 10 days, the tissue fragments were removed from the well using sterile forceps, followed by repeated 1x PBS wash to remove remaining tissue. The cultures were further incubated for 10 more days with media changes every other day. Cells were trypsinised at 90% confluency and prepared for fluorescence-activated cell sorting (FACS) analysis.

2.3.3.1 Human Leukocyte Antigen (HLA) detection by FACS

Cells suspensions were washed (2x) in FACS buffer (2% foetal bovine serum and 0.1% sodium azide in PBS) before incubating with W6/32 mouse anti-human HLA-A-B-C monoclonal antibody (kindly provided by Prof. Tim Elliot, CSU, University of Southampton, UK) at 10 µg/ml, for 30 minutes at 4 °C. Following FACS buffer washes (2x), goat anti-mouse IgG (H+L)-AF647 (A-21237, Life Technologies, UK) was used for the secondary antibody incubation (1:2000 dilution) at 4 °C for 30 minutes and the cells were further washed (2x) with FACS buffer. Cells stained with secondary antibody only and non-stained cells were used as controls for non-specific antibody binding and autofluoresence, respectively. Sample controls were used for appropriate gating, together with test samples on a FACS Canto I Flow cytometer (BD Biosciences, San Jose, USA) and data were analysed using FlowJo v10 software (Ashland, USA).

2.3.4 Extraction and culture of human bone marrow stromal cells (hBMSC)

Human bone marrow aspirates were obtained under sterile conditions from patients undergoing routine total hip replacement surgery at Southampton General Hospital with Southampton & South West Hampshire Local Research Ethics Committee approval and full patient consent (LREC 194/99/w). BMSCs were obtained from the mononuclear fraction after density gradient separation (Lymphoprep, Axis-Shield), seeded in a flask with complete media (see section 7.2.1 for media description) and incubated in 5 % CO_2 at 37 ˚C. After a week, cells adhered to the flask and complete media was replaced every 2-3 days. At 90 % confluency, cells were passaged using 0.05 % (w/v) trypsin / 0.5 mM EDTA (Lonza, Switzerland).

2.3.5 Extraction and culture of human umbilical vein endothelial cells (HUVEC)

Umbilical cords were obtained from Princess Anne Hospital (Southampton) from consented, healthy mothers after normal, full-term deliveries under ethical approval from Southampton & South West Hampshire Local Research Ethics Committee (LREC 05/Q1702/102). The umbilical cord was clamped at one end, and on the other end perfused with 0.05 g collagenase B (Roche) in 10 ml PBS using a syringe. Following incubation with collagenase for 1 hour, the clamped end was released to collect the collagenase, and additional PBS washes were passed through the cord to collect all the released cells in a falcon tube. Released cells were then collected in the same tube, which was centrifuged at 800 g for 5 minute and the pellet was resuspended in EC media (see section 7.2.1 for media description) and incubated in a flask in 5 % CO_2 at 37 ˚C. Once cells adhered to the tissue culture plastic, EC media was replaced every 2-3 days, and cells were passaged at 80 % confluence using 0.05 % trypsin (w/v) /0.5 mM EDTA (Lonza, Switzerland).

2.4 Biomaterial preparation

Generally, the bone cylinder defect region was perfused with the following groups before resuming incubation.

- Group 1: Biomaterial (*i.e.* collagen sponge, hydrogel) containing biomolecules (*i.e.* BMP2, VEGF, cells)
- Group 2: Biomaterial (*i.e.* collagen sponge, hydrogel) containing plain buffer solution (vehicle control).
- Group 3: Blank group (bone cylinders with empty bone defect) as a control for the base-line response of individual patient-donors in each independent experiment.

Each of the previous groups were used for CAM-implantation (n= 8-10), and the same treatments were also cultured *in vitro* (n=4-6). Following a similar approach to the treatment of bone defects in the clinic, the growth factor delivered dose was proportional to the bone defect size, which generally was between 4-6 mm in length.

2.4.1 Collagen sponges-InductOs

Lyophilised rhBMP2 (dibotermin alfa, InductOs^{TM}, Medtronics, USA) was reconstituted to a stock concentration of 1500 µg/ml BMP2. Two working concentrations, 150 µg/ml and 7.85 µg/ml protein solution were prepared in formulation buffer (2.5% glycine, 0.5% sucrose, 0.01% Polysorbate 80, 5 mM sodium chloride and 5 mM L-glutamic acid, pH 4.5), in low-protein binding Eppendorf tubes at 4 °C to preserve bioactivity. Vehicle control (solution buffer) was used as 0 µg/ml (Blank control).

2.4.1.1 Collagen sponges applied to bone cylinder defect

Collagen sponge were cut in rectangles of standard width (2 mm approximately) and length proportional to the bone cylinder (see Table 2.4.1). Collagen sponges were applied with the corresponding volume of BMP2 buffer for the three respective doses (see Table 2.4.1) and incubated for 15 minutes at room temperature before being applied into the bone cylinder defect region. Immediately after application of the biomaterial, bone cylinders were CAM-implanted (n=8-10) or *in vitro* cultured (n= 4-6) for a period of 7-9 days.

Table 2.4.1: BMP2 InductOs dose and biomaterial volume delivered was proportional to defect size. Volume calculated based on bone cylinder formula = π r^2 h, and bone defect radius = 1 mm. BMP2 high dose (150 µg/ml), BMP2 low dose (7.85 µg/ml) and Blank (0 µg/ml; vehicle control).

Cylinder length	Defect size	Volume applied	Blank	BMP2 low dose	BMP2 high dose
h = 3.5 mm	10.99 mm^3	11 µl	0 ng	86.35 ng	1650 ng
h = 4 mm	12.56 mm^3	13 µl	0 ng	102.05 ng	1950 ng
h = 4.5 mm	14.14 mm^3	14 µl	0 ng	109.9 ng	2100 ng
h = 5 mm	15.70 mm^3	16 µl	0 ng	125.6 ng	2400 ng
h = 5.5 mm	17.28 mm^3	17 µl	0 ng	133.45 ng	2550 ng
h = 6 mm	18.85 mm^3	19 µl	0 ng	149.15 ng	2850 ng

2.4.1.2 Collagen sponges alone

Standard size collagen sponges were canulated and impregnated with 16 µl of the BMP2 working solutions (2.4 µg high dose, 0.125 µg low dose BMP2 and 0 µg blank) and incubated for 15 minutes at room temperature before implantation on CAM or *in vitro* culture for 9 days. *In vitro* culture was conducted in transwells with serum-free media (see section 7.2.1 for media description), maintained in 5 % CO_2 at 37 ˚C, and media was replaced every other day.

2.4.2 Alendronate (ALD) preparation

Alendronate powder (A4978, Sigma) was solubilised to a stock concentration of 10 mg/ml in ddH_2O. An intermediate working solution of 0.03 M ALD was prepared and sterilised using a 22 µm filter, to produce 100 µM and 1µM ALD solutions in plain media (see section 7.2.1 for media description). Bone cylinders were incubated overnight in the previous ALD concentrations, and the excess ALD removed by washing in PBS first and then in plain media (x2 PBS 1h in 5 % CO_2 at 37 ˚C; x1 basal media 1h in 5 % CO_2 at 37 ˚C).

2.4.3 Laponite

Laponite (Rockwood Additives Ltd, UK) at a 2.7 % (w/v) concentration was prepared using ultrapure water and stirred until the solution was clear and transparent (approximately 2 hours). The Laponite hydrogel was then autoclaved, and once it reached room temperature was ready to be mixed with biomolecules. Plain Laponite control was prepared by adding the buffer solution without the biomolecules (growth factor or cells). Immediately after application of the biomaterial, bone cylinders were CAM-implanted (n=8-10) or *in vitro* cultured (n= 4-6) for a period of 7-9 days.

2.4.3.1 Laponite - BMP2

A 1000 µg/mL rhBMP2 stock solution (hydridoma in-house produced) was used to prepare an intermediate BMP2 solution of 78.5 ng/µl BMP2. From this working solution, 100 µl were added to 900 µl of Laponite 2.7 % and mixed using a vortex to make up a final concentration of 7.85ng/µl BMP2 and 0 ng/µl (vehicle control) in 2.5 % Laponite hydrogel. Each bone core was perfused with a biomaterial volume proportional to the cylinder length; details of the volume applied and growth factor dose are detailed in Table 2.4.2.

Table 2.4.2: BMP2 dose and delivered biomaterial volume. Volume calculated based on bone cylinder formula = π r^2 h, and bone defect radius = 1 mm. Laponite (Lap) Biomaterial volume delivered was proportional to defect size.

Cylinder length	Defect size	Volume applied	Lap BMP2 (BMP2 dose)	Lap (BMP2 dose)
h = 3.5 mm	10.99 mm^3	11 µl	86.35 ng	0 ng
h = 4 mm	12.56 mm^3	13 µl	102.05 ng	0 ng
h = 4.5 mm	14.14 mm^3	14 µl	109.9 ng	0 ng
h = 5 mm	15.70 mm^3	16 µl	125.6 ng	0 ng
h = 5.5 mm	17.28 mm^3	17 µl	133.45 ng	0 ng
h = 6 mm	18.85 mm^3	19 µl	149.15 ng	0 ng

2.4.3.2 Laponite - VEGF

A 10 µg/mL rhVEGF$_{165}$ solution (Peprotech, USA) was prepared in sterile ultrapure dH$_2$0. From this stock solution, 100 µl was added to 900 µl of Laponite 2.7 % and mixed using a vortex to make up a final concentration of 0.15 ng/µl rhVEGF$_{165}$ and 0 ng/µl (vehicle control) in 2.5 % Laponite hydrogel. Each bone core was perfused with a biomaterial volume proportional to the cylinder length; details of the volume applied and growth factor dose are detailed in Table 2.4.3.

Table 2.4.3: VEGF dose and delivered biomaterial volume.. Volume calculated based on bone cylinder formula = π r^2 h, and bone defect radius = 1 mm. Biomaterial volume delivered was proportional to defect size.

Cylinder length	Defect size	Volume applied	Lap VEGF (total dose)	Lap (total dose)
h = 3.5 mm	10.99 mm^3	11 µl	1.65 ng	0 ng
h = 4 mm	12.56 mm^3	13 µl	1.95 ng	0 ng
h = 4.5 mm	14.14 mm^3	14 µl	2.1 ng	0 ng
h = 5 mm	15.70 mm^3	16 µl	2.4 ng	0 ng
h = 5.5 mm	17.28 mm^3	17 µl	2.55 ng	0 ng
h = 6 mm	18.85 mm^3	19 µl	2.85 ng	0 ng

2.4.3.3 Laponite - Cells

Primary hBMSC passage 1 (SSCs) and primary human umbilical vein endothelial cells passage 4 (ECs) were obtained as isolated and cultured as described in sections 2.3.4 and 2.3.5. Upon confluence, cells were resuspended either separately or in combination (1 SSCs : 6 ECs) in 20 µl final volume containing 500 µg/ml of fibronectin and 2.5M sucrose in dH_2O. Each of these cell suspensions was added to 180 µl of 2.7 % Laponite, and gently pipette-mixed to make up a final 2.5 % Laponite hydrogel containing 50 µg/ml of fibronectin and 0.25 M sucrose in dH_2O and the following cell concentrations (see below), or combined with 0 cells/µl as vehicle control (Laponite group). Volume applied was proportional to the bone cylinder defect (Table 2.4.4).

- SSCs 2,800 cells/µl; 28,000 cells approximately per bone cylinder
- SSCs:ECs 2,800 cells/µl + 16,715 cells/µl; 195,150 cells approximately per bone cylinder
- ECs 16,715 cells/µl: 167,150 cells approximately per bone cylinder

Table 2.4.4: Volume of hydrogel containing SSCs, ECs and SSCs:ECs cells applied in proportion to the defect site. Volume calculated based on bone cylinder formula = π r^2 h, and bone defect radius = 1 mm.

Cylinder length	Defect size	Volume applied
h = 3.5 mm	10.99 mm^3	11 µl
h = 4 mm	12.56 mm^3	13 µl
h = 4.5 mm	14.14 mm^3	14 µl
h = 5 mm	15.70 mm^3	16 µl
h = 5.5 mm	17.28 mm^3	17 µl
h = 6 mm	18.85 mm^3	19 µl

2.5 Micro Computed Tomography (µCT) scanning

2.5.1 Scanning settings, reconstruction and analysis of human bone cylinders

Bone cylinders were scanned before and after incubation using the same parameters. The cylinders were scanned in plastic Eppendorf tubes using *in vivo* an high resolution computed tomography SkyScan 1176 scanner and analysed using the SkyScan own software (Bruker, Belgium). Scans were conducted using the following settings: X-ray source 50 kV, 500 µA, rotation step 0.55°, exposure time 496 ms, averaging (1) and an isotropic voxel size of 18 µm. The estimated radiation dose for these scanning conditions was 100 mGy. Once the scans were completed, the raw data was reconstructed using NRcon software (version 1.7.0.4) with correction for misalignment, ring artefacts (6), smoothing (3) and beam hardening (30%). The reconstructed datasets were orientated in the same position using DataViewer software (version 1.5.2.4) to match the pre and post scans of the same bone cylinder. Binarisation of each image dataset was achieved through a global threshold, decided according to visual inspection of the samples, and the same threshold was applied in the pre and post scans. Finally, CTan software (version 1.16) analysis provided the bone volume of the whole bone grafts, and the percentage of change was calculated with respect to the pre scan. 3D rendering of the bone cylinders was generated using CTVox software (version 3.2). All the software was from SkyScan, Bruker, Kontich, Belgium

2.5.2 Scanning settings, reconstruction and analysis of collagen sponges

Collagen sponges were scanned after incubation and fixed in 4 % paraformaldehyde in plastic Eppendorf tubes using *in vivo* high resolution computed tomography SkyScan 1176 and analysed using SkyScan software (Bruker, Belgium). Scans were conducted using the following settings: X-ray source 40 kV, 600 µA, (Aluminium 0.5mm filter) exposure time 496 ms, averaging of 3, rotation step 0.5° and an average voxel size of 18 µm. The estimated radiation dose for these scanning conditions was 100 mGy. Once the scans were completed, the raw data was reconstructed using NRcon software with correction for misalignment, smoothing (Gaussian, 2), ring artefacts (6) and beam hardening (30%). The image dataset was binarized applying a global threshold, decided according to visual inspection though the samples and CTan software analysis provided the bone volume (mm^3). All the software was from SkyScan, Bruker, Kontich, Belgium.

2.5.3 Registration of sequential scans

As previously described, pre and post (Figure 2.5.1 A-B) scans of the same sample were loaded for 3D registration. This 3D plug-in loads the reference (pre) and target (post) datasets before registration, and then inverts the original greyscale of the post scan dataset (Figure 2.5.1 C) so that high density material (*i.e.* bone) in the pre dataset appears black, and bone in the pre dataset appears white (Figure 2.5.1 A-C). Thus, the registration of structures occurs by superposing the post scan (black) over the pre scan (white), resulting in a grey colour for the successful matches on the registered image, also named 'difference' image (Figure 2.5.1 D). Besides the registered structures in grey, the software also displayed non-registered areas in black if present in the post dataset and in white if present in the pre dataset (Figure 2.5.1 D).

The difference dataset obtained following 3D registration was saved and then loaded in CTAn to plot the histogram of pixels of the dataset under each greyscale value, ranging from 0 to 255 (Figure 2.5.1 E).

As opposed to the regular histogram distribution where greyscale value reflects density of the object, the greyscale of the difference image indicates the certainty of the 3D registration software to categorise as match (90-170), or mismatch (0-89, 171-255). This histogram, in logarithmic scale, showed a Gaussian distribution of pixels with the peak of the curve located within the 100-180 greyscale values, which corresponds to the grey colour of the registered structures. The two tails of the curve relate to the non-registered pixels, located between 0 and 90 for the pre-difference, and 170 to 255 for the post-difference, approximately (Figure 2.5.1 E).

The difference image was thresholded conservatively to select specifically the structures that the 3D registration software was more confident belonged to the pre-difference and post-difference (Figure 2.5.1 E). An arbitrary number of 60 pixels was used to select the pre-difference (0-60) as shown by the foreground selection in pink over background in green (Figure 2.5.1 F), and saving the thresholded dataset as a binary image (Figure 2.5.1 H). The same process was repeated to obtain the post-difference by loading the registered dataset (Figure 2.5.1 E), applying a 195-255 threshold to select the post-difference (Figure 2.5.1 G), and saving the binary image (Figure 2.5.1 I).

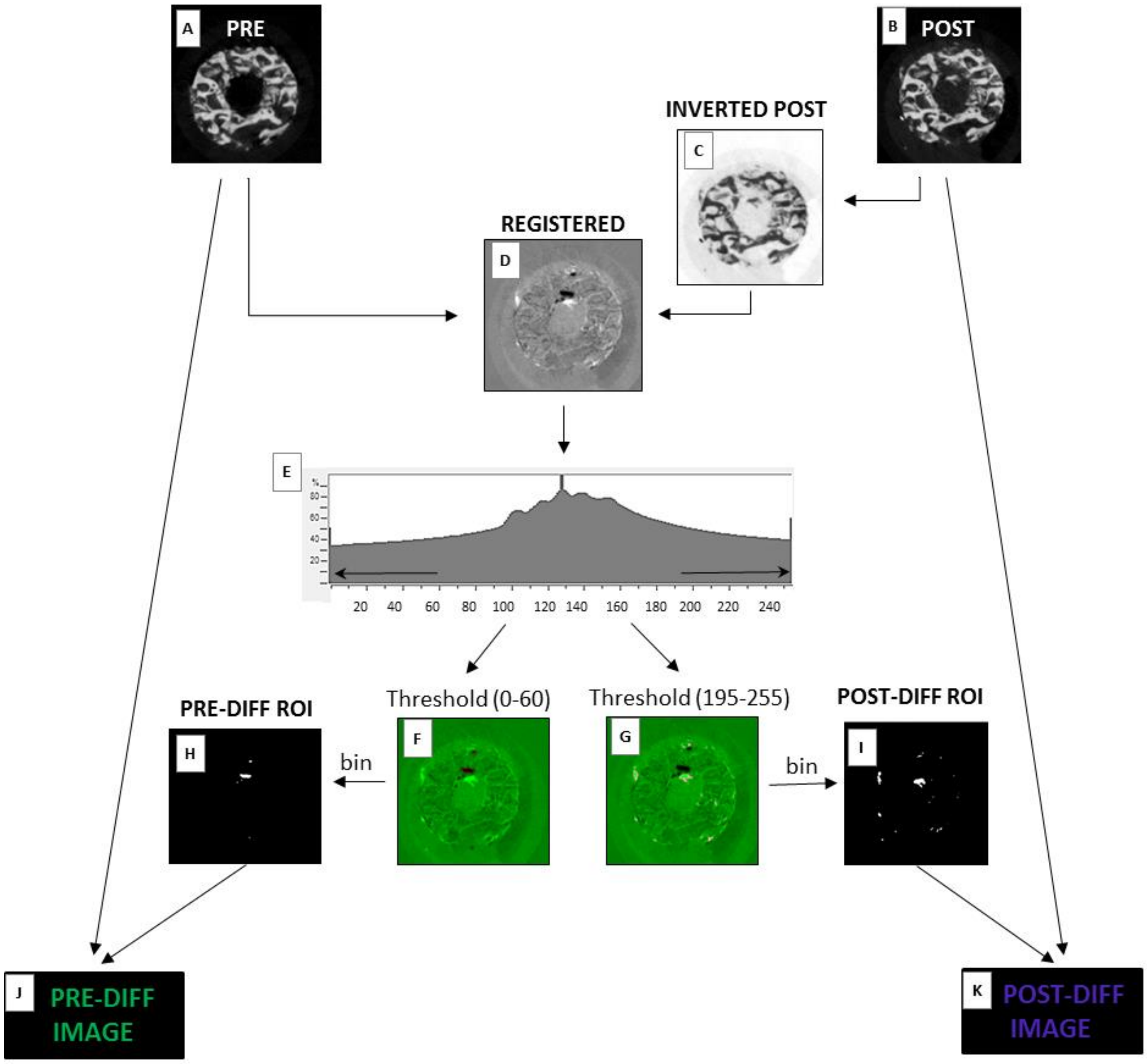

Figure 2.5.1: Image analysis pipeline to obtain the greyscale image of the mismatch regions from pre and post datasets. After registration (D), the difference image dataset was saved (E) and binarised in two occasions (F, G) to generate the difference ROI or masks (H, I). The previous masks were then loaded on top of the original and respective scans, to obtain the pre-diff (J) and post-diff (K) datasets, in greyscale.

Those two binary datasets were used as ROI or masks corresponding to the pre-difference and post-difference, respectively (Figure 2.5.1 H and I); pre-difference mask was loaded as an ROI on the original pre-scan (in regular greyscale), and the image within the ROI was saved as a new dataset, named '*pre-diff*' (Figure 2.5.1 J). Post-difference mask was loaded as an ROI on the original post-scan (in regular greyscale), and the image within the ROI was saved as a new dataset, named '*post-diff*' (Figure 2.5.1 K).

This image processing pipeline was applied to obtain Figure 5.2.2, which shows the 3D rendering of pre-diff and post-diff on the same image. Pre-diff displayed the mismatched structures corresponding to the pre-scan only, in green colour. Post-diff displayed the mismatched structures corresponding to the post-scan only, in purple colour. From the biological perspective, pre-diff and post-diff identify potential bone resorption and bone formation regions; however not exclusively due to the intrinsic error of the 3D registration process.

To assess the reproducibility of the 3D registration method, control bone cylinders were maintained at four degrees for the same incubation period, and repositioned between scans.

2.6 **Histology**

All bone grafts were collected and processed for histology at the same time for each experiment. The bone fragments were fixed in 10 times their volume of 4% PFA in PBS overnight at 4 ˚C and then washed in PBS for an additional 16h.

Samples were submerged in acid decalcifying solution (Histoline, Milan, Italy) in 10 times their volume and maintained at 4 ˚C for 24 hours. Complete demineralization was confirmed using X-ray imaging (Faxitron). Samples were dehydrated in increasing concentrations of alcohol (50, 90, 100 and 100 %) and then immersed in histoclear to ensure the samples were miscible with the wax (for details see Supplementary Table 7.2.1). Afterwards the grafts were infiltrated embedded in paraffin wax. Microtome sectioning was performed to obtain 5 µm in thickness sections.

2.6.1 Histological stains

2.6.1.1 Alcian blue and Sirius red staining (AS)

Histological sections were de-waxed and re-hydrated, incubated with 0.16 M haematoxylin Weigerts (Fisher) for 10 minutes and submerged in the water bath. To remove excess stain, the slides were dipped in acid alcohol and back into the water bath. Slides were then immersed in 0.5 % (w/v) Alcian blue 8GX staining solution (Fisher, Hampton, USA) for 10 minutes, rinsed in the water bath and submerged in molybdophosphoric acid 1 % (w/v) for 10-20 minutes. After a quick dip in water, the slides were maintained in 1 % (w/v) Sirius red F3B for 45-60 min, rinsed in water, de-hydrated and mounted in DPX.

Colour legend: Alcian blue stains cartilage matrix (proteoglycans) blue and Sirius red stains collagens pink-red. (See Table 2.6.1).

2.6.1.2 Goldner's Trichrome (GT)

Histological sections were stained for haematoxylin as detailed in Methods Section 2.6.1.1. The slides were then immersed in Ponceau-fuchsin-azopholin 1 % (w/v) solution (Fisher, Hampton, USA) for 5 minutes and rinsed in the acid acetic 1 % (v/v) and stained in molybdophosphoric acid/Orange G solution 1 % (w/v) solution (Acros Organics, Fisher, UK) for 20 minutes. After rinsing in acid acetic 1 %, the slides left in Light Green 1 % (w/v) solution for 5 minutes and washed again. Finally the slides were de-hydrated and mounted in hydromount.

Colour legend: Light green stains collagen, cytoplasm in bright red, nuclei in black, mineralized tissue stains pink-red. (See Table 2.6.1).

2.6.1.3 Masson's Tetrachrome (MT)

The staining was conducted following protocols as detailed by Ralis and Watkins (Ralis and Watkins 1992). In brief, Histological sections were stained for haematoxylin as detailed in Methods Section 2.6.1.1. Then the slides were immersed in 90 % ethanol solution for 2 min, and immediately applied with phosphotungstic acid 1 % (w/v) for 5 minutes, dipped in water for immersion in aniline blue 0.1 % (v/v) in acetic acid for 8 minutes at RT. Sections were washed thoroughly in water before staining in 0.1 % (w/v) Orange G (Acros Organics, UK) in saturated picric acid at RT for 3 minutes. After 2-3 dips in water, Ponceau Mixture (4 ponceau 2R : 1 crystal ponceau in 1 % (w/v) acetic acid in water) was added to the sections and incubated at RT for 6 minutes followed by a wash in water. Finally the slides were dehydrated and mounted in DPX.

Colour legend: Deep blue staining indicated osteoid, bright red/orange staining lamellar bone, yellow/orange staining red blood cells and cell nuclei in black. (See Table 2.6.1).

2.6.1.4 von Kossa staining

Histological sections from non-decalcified specimens were stained for haematoxylin as detailed in Methods Section 2.6.1.1. Sections were stained with 1 % (w/v) $AgNO_3$ under ultraviolet light for 30 min followed by water wash. The staining was fixed with 2.5 % (w/v) sodium thiosulphate and counterstained with Alcian blue (0.5 w/v) and van Gieson stain 1.8 % (w/v). Finally the slides were de-hydrated and mounted in DPX.

Colour legend: Black colour staining indicates deposited mineral, pink staining indicates cellular component and blue staining proteoglycan content. (See Table 2.6.1). See example of staining in Supplementary Figure 7.2.4, page 200.

2.6.1.5 Summary colour legend from histochemical stains (AS, GT, MT and VK)

Table 2.6.1: Colour legend for histochemical stains.

Tissue component	***Alcian blue and Sirius red staining (AS)***	***Goldner's Trichrome (GT)***	***Masson's Tetrachrome (MT)***	***von Kossa (VK)***
Collagen	pink	green	pink/orange	pink
Osteoid	pink	Pink/orange	deep blue	pink
Mineralised tissue	pink	green	pink/orange	black
Cell cytosol	---	bright red	bright red	pink
Nuclei	black	black	black	black
Cartilage	Blue	---	---	blue

2.6.2 Immunohistochemisty

After the slides were de-waxed and re-hydrated, antigen retrieval steps were optimised for each antibody (see for details Table 2.6.2). Following antigen retrieval, sections were then incubated with 3 % (v/v) H_2O_2 for 5 minutes to quench endogenous hydrogen peroxide activity, and then in 1 % (w/v) BSA in PBS for 5 minutes to block non-specific staining, with wash (3x for 5 minutes) in between. Primary antibody (see Table 2.6.2) was diluted in 1 % (w/v) BSA in PBS and applied to the sections in a humidified chamber overnight at 4 °C. After washes (3 steps of 0.05 % (v/v) Tween/PBS for 5 minutes), the secondary antibody (Table 2.6.2) was applied to the sections during 1 hour at RT, followed by PBS/Tween washes (3x for 5 minutes). Sections were then covered with Streptavidin-Peroxidase solution (1:50, DAKO) for 30 min at RT. After the washes (3 steps of 0.05% Tween/PBS for 5 minutes), the substrate mixture (DAKO) was applied to the sections at RT for 3-10 minutes, depending on antibody (see Table 2.6.2). The reaction was stopped by submerging the slides in water. Counterstains were Alcian Blue and Light Green for 1 minute each with washes in between. Finally, the slides were mounted in glycerol media. Positive and negative (isotype) controls were stained in parallel for each experiment (see controls in section 7.2.2).

Colour legend: Positive immunostaining for the antigen of interest appeared dark red-brown while proteoglycan (matrix) counterstain appeared light blue.

Table 2.6.2: List of primary antibody and their respective protocols. . Heat-induced antigen retrieval (HIER) with citrate buffer 0.1 M was performed as (A) boiling temperature for 10 minutes, sub-boiling temperature for another 10 minutes and cool down at room temperature an additional 10 minutes or (B) 30 min at 70 °C in the oven. Enzymatic digestion retrieval was performed with hyaluronidase enzyme at a concentration of 520 U/ml at 37 °C for 20 minutes. Permeabilisation was done using 0.1 % (v/v) Triton X in PBS for 15 minutes at RT.

Primary antibody	Details	Antigen Retrieval	Secondary antibody	Colour development	Control images
Cathepsin K (ab66237) Abcam	Mouse anti-human (1:50)	HIER (A) +digestion +Permeab.	SignalStain® Boost (8114P, Cell Signalling)	8-9 min	Supplementary Figure 7.2.2
Sox9 (AB5535) Merck Millipore	Rabbit anti-human, (1:150)	HIER (B) +digestion	Goat anti-rabbit biotinylated (1:100, DAKO)	8-10 min	Supplementary Figure 7.2.1
Runx2 (ab23981) Abcam	Mouse anti-human, (1:100)	HIER (B) *Blocking for 30 min	Goat anti-mouse biotinylated (1:100, DAKO)	4 min	Supplementary Figure 7.2.1
GFP (2555) Cell Signalling	Rabbit (1:100)	HIER (A) +digestion +Permeab.	SignalStain® Boost (8114P, Cell Signalling)	8-10 min	Figure 3.2.19
Collagen type I LF68 from Dr Larry Fisher, NIH, USA)	Rabbit anti-human (1:1000)	+digestion	Goat anti-rabbit biotinylated (1:100, DAKO)	3-4 min	Supplementary Figure 7.2.3
Collagen type II (234187) Merk Millipore	Rabbit anti-human (1:500)	+digestion	Goat anti-rabbit biotinylated (1:100, DAKO)	3-4 min	Supplementary Figure 7.2.3
Collagen type X (234196) Merk Millipore	Rabbit anti-human, (1:00)	+digestion	Goat anti-rabbit biotinylated (1:100, DAKO)	3-4 min	Supplementary Figure 7.2.3

Images of all immunohistochemical and histochemical stains were captured with an Olympus BX-51/22 dotSlide digital microscope, and created using OlyVIA 2.1 software (Olympus Soft Imaging Solutions, GmBH).

2.7 Statistical Analysis

All experimental data was analysed using Statistical Analysis SPSS Base 16.0 software for Windows. Results were expressed as the mean ± SD and plotted using GraphPad Prism. Data distribution was examined using Kolmogorov-Smirnov test to determine normality. A minimum of 8-10 samples per group for CAM assay (*in vivo*) and a minimum of 2-8 samples for *in vitro* groups were included in each independent experiment. Only data from viable, integrated implants (bone cylinders, collagen sponges) were included for analysis. Comparisons between two treatments were performed using student t-test. Comparisons between more than 2 treatments were performed using the one-way ANOVA test including Tukey post-hoc test. Values of $p<0.05$ were considered statistically significant.

Chapter 3: Results Part I

Development of the CAM assay for the culture of human bone

3.1 Introduction

The aim of the present chapter was to establish the suitable methodology to develop the CAM assay for the culture of human bone as well as optimise the analytical techniques (µCT, histology) to assess the effects following incubation. A common limitation in the use of the CAM assay for xenograft culture (*i.e.* human bone) is the inability to differentiate between host and graft tissue due to antibody cross-reactivity between species (Ramos-Vara and Miller 2014; Yang *et al.* 2003). To circumvent this issue, genetically modified chick embryos constitutively expressing green florescent protein (GFP) were used in the present study. The GFP chick embryos were originally developed by McGrew *et al.* with the central objective to generate therapeutic proteins in chick eggs, given advantage of post-translational modifications such as glycosylation (Simon G. Lillico, Michael J. McGrew 2005). The production of transgenic chick embryos was achieved by using a lentiviral vector carrying a reporter transgene (GFP) followed by cross-mating to identify homozygous GFP+/GFP+ birds (Simon G. Lillico, Michael J. McGrew 2005). GFP transgenic chickens have been used to examine gene expression regulation patterns in different tissues (McGrew *et al.* 2010) as well as to substitute neural tube grafts in wild type chickens for the study of nervous and vascular system (Delalande *et al.* 2014). Following a similar approach, in the present investigation we aimed to use the GFP labelling to differentiate human cells and tissue from chicken. Thereby, the use of GFP CAM was compared with wild type CAM tissue and the suitable signal detection methods before and after histological processing examined accordingly.

Another important requirement to set up the bases of the CAM assay was to obtain small, standard size bone graft tissue to achieve successful CAM-implantation. Thus, initial efforts were focused on evaluating different sectioning/drilling methods to generate sufficient number of homogenously sized bone grafts from a human femoral head. Moreover, fluorescent viability stains traditionally applied in cell culture (2D) were examined to assess tissue viability on the human bone cylinders (El-Serafi *et al.* 2011; Saleh *et al.* 2011).

In this thesis, micro computed tomography (µCT) analysis was used to quantify the changes in the bone structure, followed by histological analysis to validate at the morphological level the µCT findings. µCT is a well-established non-destructive, non-invasive technique that enables the generation of three dimension (3D) high resolution images of X-ray dense material, and hence µCT was used to measure the variations on the bone microstructure before and after CAM-implantation. Commonly used to monitor the progress of bone fracture healing over time, µCT has been used to quantify basic parameters such as callus volume and bone volume in many *in vivo* studies (Kanczler *et al.* 2008, 2010; Yuasa *et al.* 2014), as well as additional parameters (trabecular number, thickness, separation and rode to plate ratio) (Wang *et al.* 2015). Considering a similar approach, the experiments of the present chapter aim to test the potential of µCT analysis as a tool to evaluate changes in cultured bone cylinders, including the optimisation of crucial parameters such as pixel resolution and threshold methodology (Bouxsein *et al.* 2010).

Following µCT analysis, paraffin histology processing was conducted to determine the interaction of CAM and bone tissues at the histological level using (immuno)histochemistry. However, paraffin processing requires a critical step to remove the mineral content to allow for wax penetration and sample sectioning. This process of decalcification or demineralization typically involves submerging the sample in an acidic solution to dissolve the hydroxyapatite $Ca_5(PO_4)_3(OH)$ generating Ca^{2+} and OH^- ions (Callis and Sterchi 1998). Alternatively, a chelating agent such as ethylene-diamine-tetra-acetate (EDTA) can be used to sequester metal ions, in this case calcium (Callis and Sterchi 1998). Decalcification of adult mouse bones can take as long as several weeks using a conventional method such as EDTA (Cho 2010). On extrapolation to human mature bone from femoral heads, this period may extend and consequently, significantly delay histological processing. As an alternative, rapid demineralization solutions primarily composed of strong and concentrated acids can be employed (Cho 2010; Cunningham *et al.* 2001). However, use of such agents is also typically associated with tissue morphology degradation, loss of antigenic sites and enzyme reactivity. For that reason, it was important to find the appropriate decalcification method that allowed reducing the duration of the process without compromising the histological properties of the tissue. To do so, different commercial and in-house made decalcification solutions were tested in this investigation (Callis and Sterchi 1998). Successful optimisation of decalcification was then used to process bone and CAM tissue individually with the aim to examine their particular features separately, and hence facilitate the subsequent study of the CAM-implanted bone tissue in the following thesis chapters.

While µCT and histology offer core techniques for sample analysis (in this section), the reaction of the chick embryo following sample implantation provides a biocompatibility test, essential for biomaterial testing. The reaction of the CAM (host) to the implanted tissue (graft) has been extensively used in cancer research to assess tumour angiogenesis and metastasis potential, commonly based on chick embryo survival (Balke *et al.* 2011; Sys *et al.* 2012). Moreover the CAM assay has been recently used to examine scaffold and construct biocompatibility in tissue engineering based on immune reaction and construct vascularisation (Baiguera *et al.* 2012; Vargas *et al.* 2007). The current work has adopted a similar approach to evaluate the success of the CAM for human bone tissue implantation. Parameters such as chick embryo viability and graft integration were evaluated, as well as viability assessment of the tissue based on florescent dyes.

In summary, the aim of the work in this chapter was to establish the basis of the CAM assay for the culture of living human bone, and the hypothesis was that micro computed tomography combined with histological analysis can be used to measure the outcome of the *in vivo* incubation of human bone on the CAM. Hence, the specific objectives of this chapter were:

- To obtain standard sized bone grafts from a human femoral head
- To overcome the technical challenges associated with histological processing
- To develop fluorescent viability stains to assess bone tissue viability.
- To optimise µCT parameters for the analysis of bone tissue, and validate the use of µCT to examine tissue regeneration.
- To familiarise with the regular features of both the CAM and bone tissue.
- To identify the outcome of a successful CAM assay for the culture of human bone.
- To implement the use of genetically modified chick embryos in the CAM assay

3.2 Results

3.2.1 Extraction and processing of human bone cylinders

The first objective of this chapter was to obtain bone grafts from human femoral heads while preserving their original structure and cellular components. In order to generate sufficient bone grafts for a single experiment, between 50 to 60 samples from the same femoral head were required. Two different methods to extract bone grafts from human femoral heads were tested: a circular saw and a dentist drill (Figure 3.2.1).

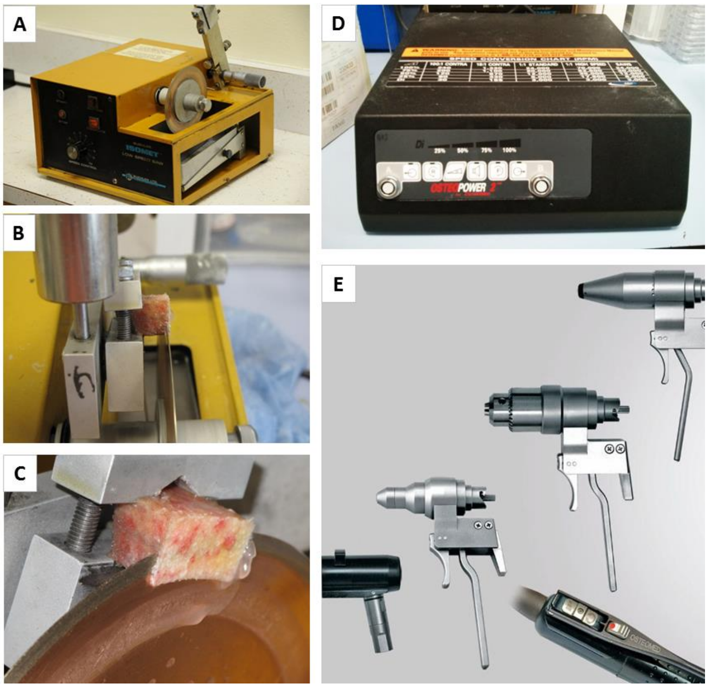

Figure 3.2.1: Equipment to generate bone grafts from human femoral heads. Isomet circular water-cooled diamond saw (Isomet) to cut bone slices (A-C) and Osteomed surgical dentist drill box and handset (D-E). Diamond saw set up (A): The bone sample is clamped with a light weight applied to force the bone sample onto the blade. (B). The low speed saw is further cooled by the water bath in the lower compartment (C). Osteopower modular surgical handpiece system (Osteomed). The surgical borer is connected to the modulator box (D) which allows drilling over a number of power outputs (0-25-75-100%). The handpiece motor-unit (E) can be configured with different attachments components (drills) (autoclavable). For the purpose of this project, the surgical borer was coupled to an empty-core tooth drill bit.

The circular saw method enabled minimal abrasion of the sample due to the application of a water-cooled system while cutting through the femoral head. Although, scaling down the size of the generated bone slices using the previous approach proved challenging and time consuming (Figure 3.2.1 A-C). In order to generate standard shaped bone grafts of a relatively small size, a dentist surgical drill was used (Figure 3.2.1 D-E). The surgical drill was attached to a trephine bit of

6 mm in diameter, which allowed obtaining standard size bone grafts of 6 mm in diameter. In addition, the surgical drill allowed reducing the dimensions of the bone grafts compared to the diamond saw method, hence obtaining greater number of samples from a single femoral head. Details of the extraction procedure shown in Figure 3.2.2.

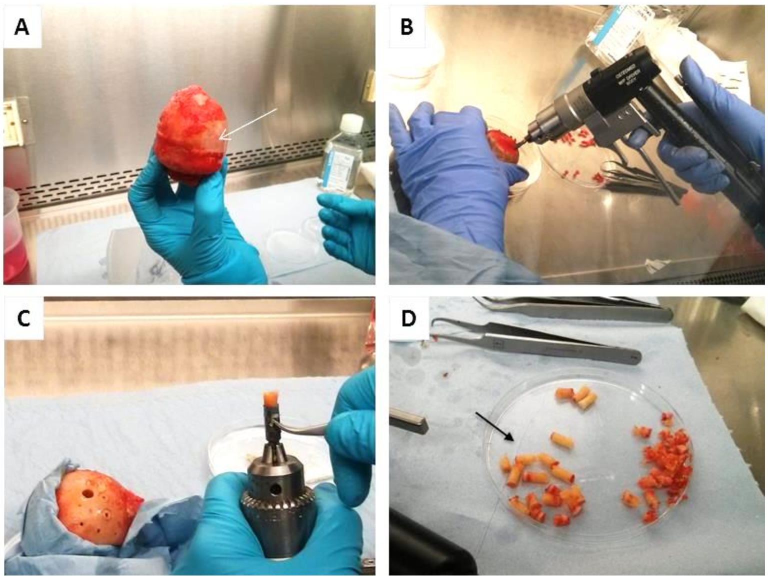

Figure 3.2.2: Osteoarthritic femoral head processing and collection of bone fragments from a patient. (A) Femoral head from osteoarthritic patient was freshly collected from surgery; white arrow indicates region without articular cartilage on the right side of the head. (B) Handpiece attached to the empty-core tooth drill, 6 mm outer diameter. The femoral head was pierced from the articular cartilage towards the trabecular bone. (C) Forceps were used to collect the bone piece from the drill core and (D) select the suitable fragments for the CAM assay (solid arrow) from the rest of the bone debris.

In order to understand the interaction between the CAM and the bone cylinders following *in vivo* implantation, samples were processed for paraffin histology and (immuno)histochemistry. Processing for paraffin sectioning required several steps (fixation, decalcification, dehydration through alcohols and paraffin embedding); however decalcification proved the most time consuming and hence the limiting step. To optimise and shorten the preparation time for histology, several in-house (EDTA and formic acid) and commercially available (Decal Stat and Histoline) decalcifying solutions were tested, in parallel to control (PBS buffer). The demineralization process was monitored after 2 and 24 hours using X-rays which showed the progression of mineral content, followed by paraffin processing, sectioning and immunohistochemistry to assess cellular integrity (Figure 3.2.3).

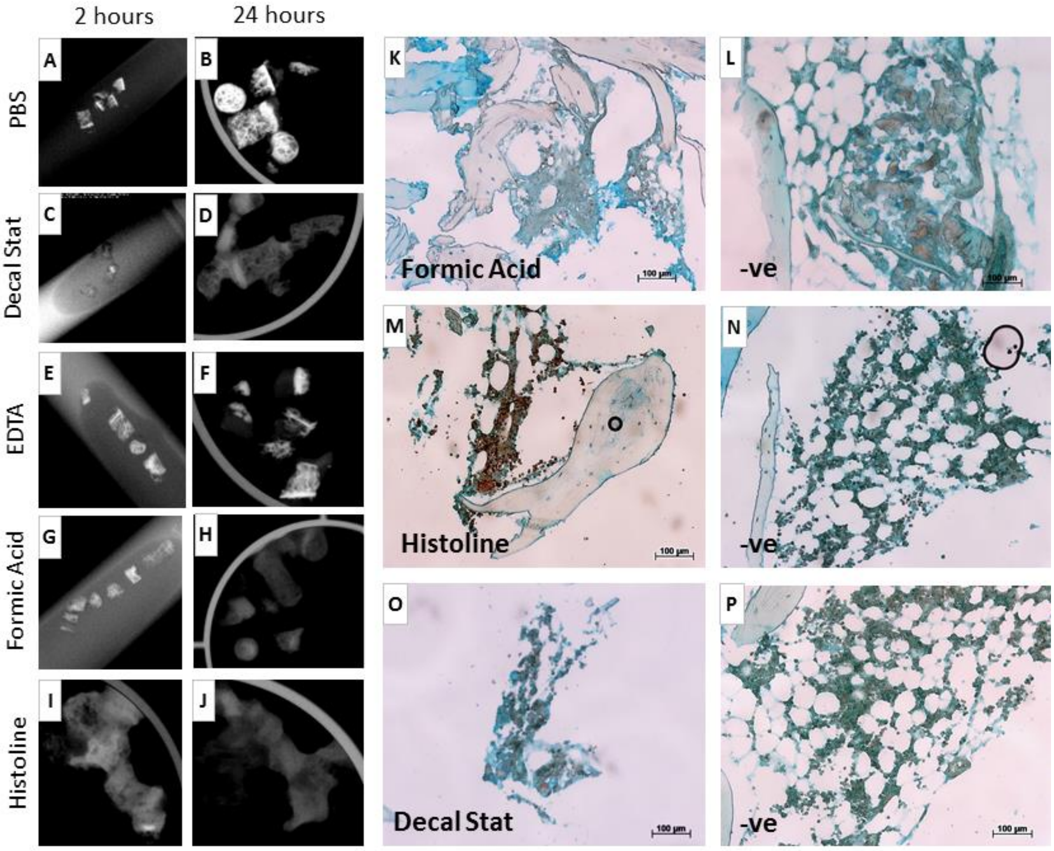

Figure 3.2.3: Optimisation of bone decalcification method. Bone grafts were X-ray scanned at 2 (A, C, E, G and I) and 24 hours (B, D, F, H and J) following demineralisation in different solutions: Decal stat (C, D), Histoline (I, J), Formic acid (G, H), EDTA (E, F) and PBS (A, B) as control. Following decalcification, samples were processed for histology to examine the cellular integrity: immunohistochemistry to detect a nuclear proliferation marker, Ki67 (K-P), and negative controls (L, N, P). Red/brown colour shows positive staining of dividing cells, matrix stain in blue was used as a counterstain (Alcian Blue). Scale bar = 100 µm.

After 2 hours, both Histoline (Figure 3.2.3 I) and Decal Stat (Figure 3.2.3 C) showed significantly less mineral compared to other conditions examined (Figure 3.2.3 A, E, G). Following 24 hours decalcification, formic acid, Histoline and Decal Stat showed complete demineralisation by X ray assessment (Figure 3.2.3 D, H and J), and were processed for paraffin histology. Sectioning proved challenging for the cylinders decalcified in formic acid, indicative of incomplete demineralisation. Immunostaining for a proliferation marker showed minimal staining on the formic acid and decal stat samples (Figure 3.2.3 K, O), whereas Histoline preserved the clear nuclear staining on the bone marrow of the human tissue (Figure 3.2.3 M).

3.2.1.1 Viability assessment of the extracted bone cylinders

An important consideration for the development of the CAM assay as a bioreactor for human bone culture was the ability of the CAM to maintain bone viability. To examine alternative methods to assess cell viability, Live (Cell tracker Green) and Dead (Ethidium Homodimer 1; red signal) staining was explored as a method to evaluate the viability of the whole-tissue samples. Figure 3.2.4 shows Live / Dead staining of freshly isolated bone cylinders (Figure 3.2.4 A, B) or bone cylinders maintained at -20 ˚C to impair cell viability (Figure 3.2.4 C, D). Green emission filter did not allow seeing clear living cells due to the bone autofluorescence, as shown in the non-stained controls (Figure 3.2.4 E); however lower autofluorecence was observer in the red emission filter for the same group (Figure 3.2.4 F).

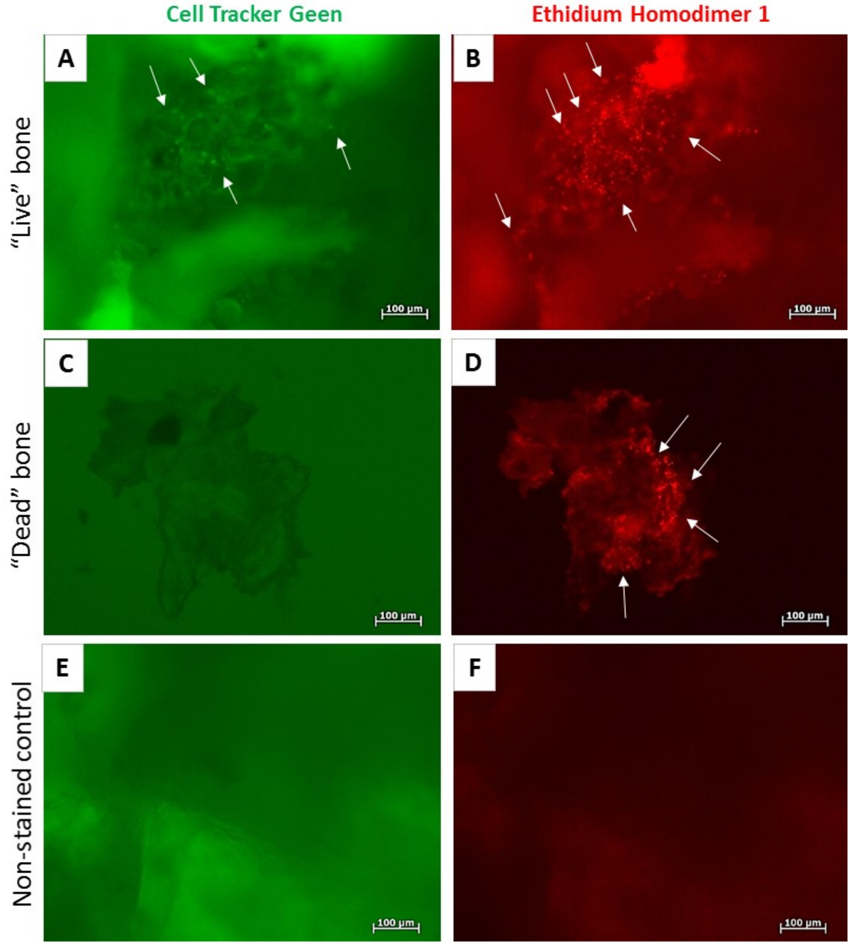

Figure 3.2.4: Green fluorescence signal masked by bone autofluorescence. Freshly isolated bone cylinders from the same femoral head were cultured *in vitro* ('live bone') (A-B) or maintained at -20 ˚C for 4 hours to impair viability ('dead control') (C-D), followed by Live (Cell Tracker Green: green emission) and Dead (Ethidium Homodimer; red emission) staining. Non-stained bone cylinders were used as control (E-F). Images for the same exposure time under the green (A, C and E) and red (B, D and F) emission fluorescence images. Arrows indicate stained cells. Scale bar equal to 100 µm.

After processing and sectioning of samples, Live and Dead fluorescence staining was still observed (Figure 3.2.5), however bone collagen autofluorescence masked identification of individual cells (Figure 3.2.5 A, D).

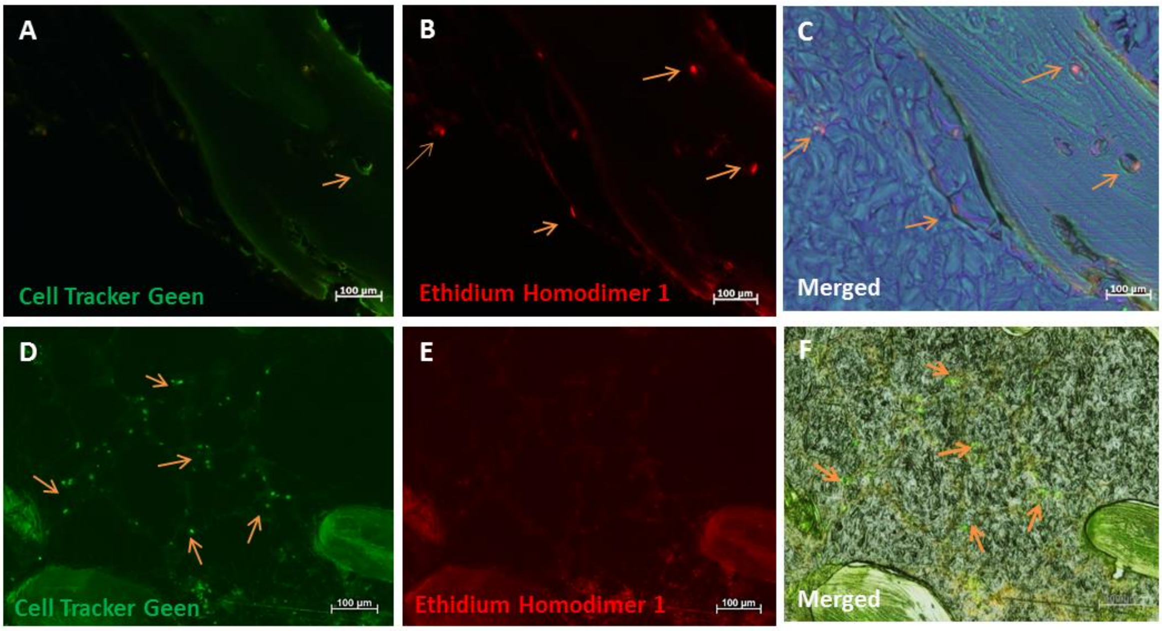

Figure 3.2.5: Live and dead staining fluorescence remains following paraffin tissue processing. Freshly isolated bone cylinders were stained for Cell Tracker Green (A, D) and Ethidium Homodimer 1 (D, E), processed for paraffin sections and imaged using a fluorescence microscope. Arrows indicate individual cells. Merged images with bright field (C, F). Scale bar equivalent to 100 µm.

To try and circumvent the natural bone autofluorescence observed using the green filter, an alternative fluorescent probe was employed: Cell Tracker Red. Figure 3.2.6 shows freshly isolated bone cylinders stained with either Live and Dead staining (Figure 3.2.6 A-D) or Cell Tracker Red (Figure 3.2.6 E-H) for comparison.

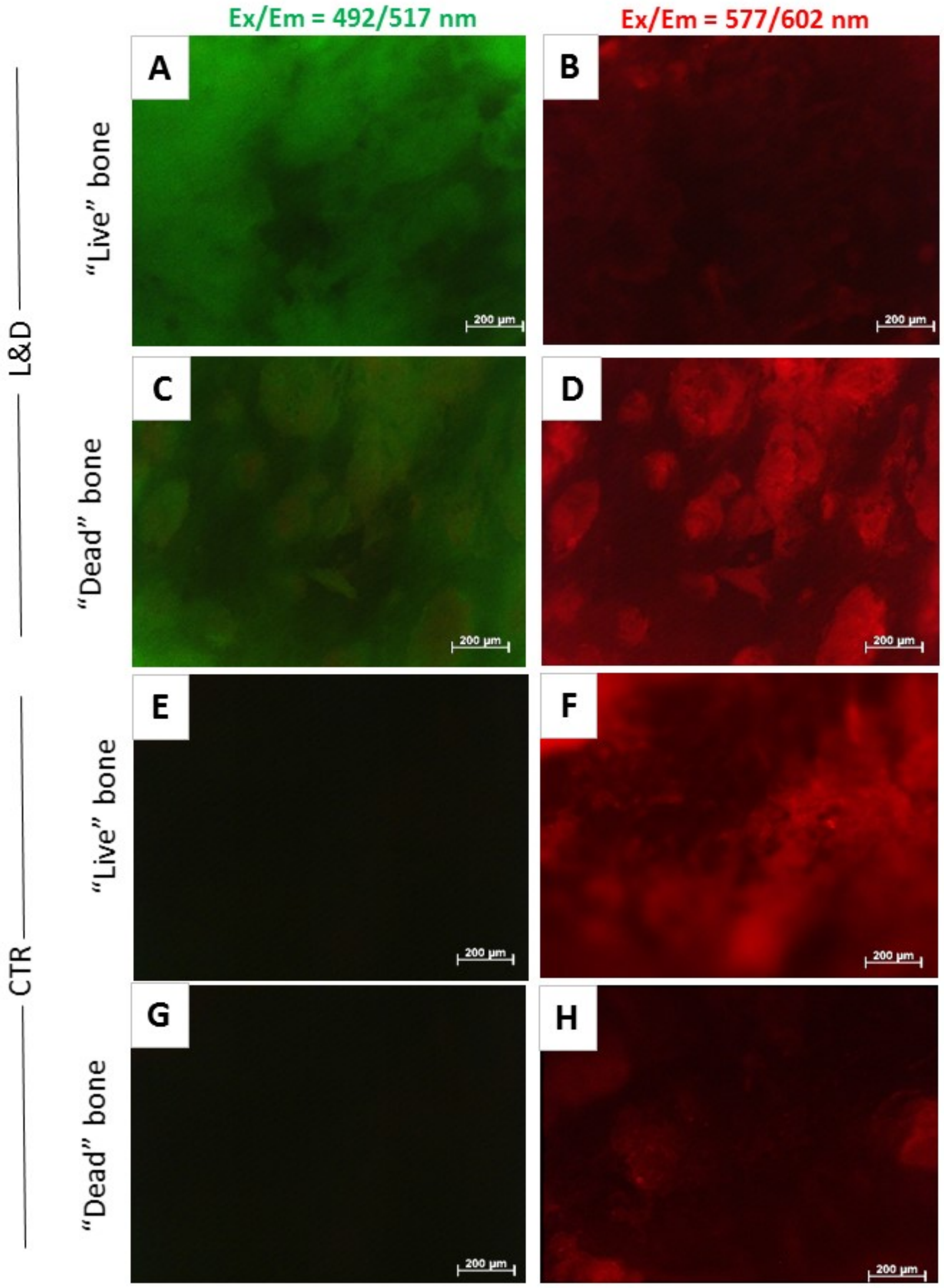

Figure 3.2.6: Red fluorescence emission significantly reduced bone autofluorescence compared to the green emission filter. Freshly isolated bone cylinders were maintained under standard culture conditions 'live bone' (A, B, E and F) or maintained at -20 ˚C (C, D, G and H) before Live and Dead staining (A-D) or Cell Tracker Red staining (E-H). Images taken under the same exposer time under green fluorescence filter 490/517nm (A-D) and red filter 577/602nm (E-H). Scale bar equivalent to 200 µm.

As observed previously, natural bone autofluorescence prevented specific visualisation of live cells using the green emission filter (Figure 3.2.6 A), however the live signal under Cell Tracker Red staining was more clealry evident when comparing 'live' *versus* 'dead bone (Figure 3.2.6 F, H respectively). Hence this indicates that Cell Tracker Red was a more suitable candidate to assess viability of bone cylinders following CAM-implantation.

3.2.2 Validation of µCT to quantify changes in bone cylinders

In the present thesis, µCT was used to measure the outcome of the treatment, such as *in vivo versus in vitro* incubation of bone cylinders. An important parameter to define in the µCT analysis was the segmentation method which separates the foreground (mineralised tissue) from background (non-mineralised tissue). To evaluate which threshold method was more suitable, two samples (A and B) were scanned using the same X-rays settings at three different resolutions (9, 18 and 36 µm) and the bone volume was quantify accordingly (Figure 3.2.7). The relative difference in bone volume of the three measurements (9, 18 and 36 µm) was calculated with respect the 9 µm measurement, as this one was the highest resolution available and therefore the most accurate measurement (indicated by % diff in Figure 3.2.7).

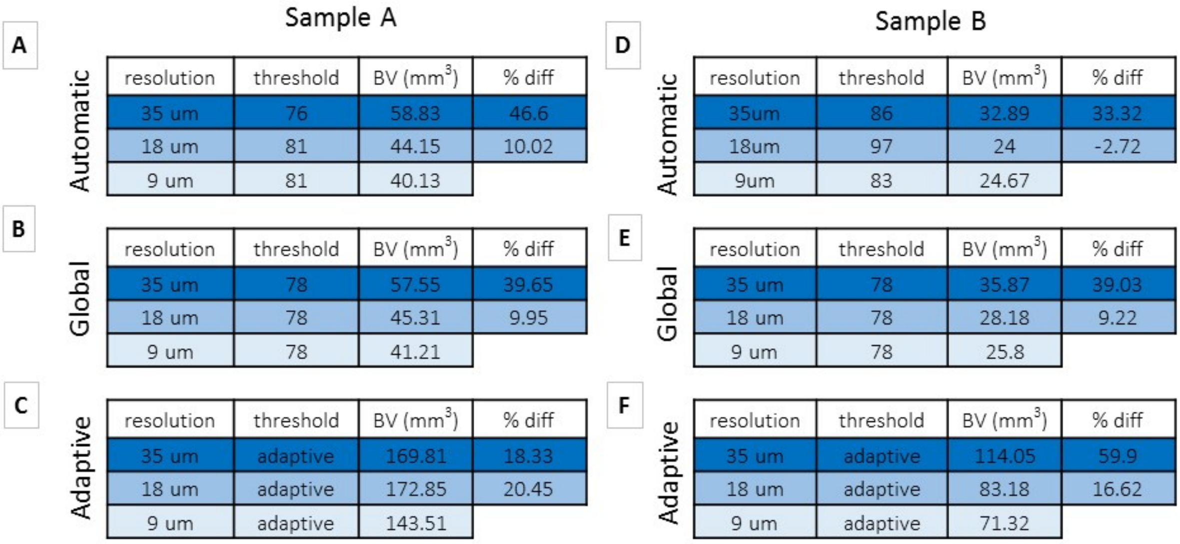

Sample A

A Automatic

resolution	threshold	BV (mm^3)	% diff
35 um	76	58.83	46.6
18 um	81	44.15	10.02
9 um	81	40.13	

B Global

resolution	threshold	BV (mm^3)	% diff
35 um	78	57.55	39.65
18 um	78	45.31	9.95
9 um	78	41.21	

C Adaptive

resolution	threshold	BV (mm^3)	% diff
35 um	adaptive	169.81	18.33
18 um	adaptive	172.85	20.45
9 um	adaptive	143.51	

Sample B

D Automatic

resolution	threshold	BV (mm^3)	% diff
35um	86	32.89	33.32
18um	97	24	-2.72
9um	83	24.67	

E Global

resolution	threshold	BV (mm^3)	% diff
35 um	78	35.87	39.03
18 um	78	28.18	9.22
9 um	78	25.8	

F Adaptive

resolution	threshold	BV (mm^3)	% diff
35 um	adaptive	114.05	59.9
18 um	adaptive	83.18	16.62
9 um	adaptive	71.32	

Figure 3.2.7: Evaluation of Global, Adaptive and Automatic thresholding to quantify bone volume on the human bone cylinders. Sample A (A-C) and Sample B (D-F) were scanned using the same X-ray settings at different resolutions 9 µm, 18 µm and 36 µm, and bone volume was quantified applying automatic (A, D), Global (B, E) and Adaptive (C, F) thresholding. The relative difference in bone volume (% diff) with respect the highest resolution was calculated.

Regardless of the threshold methodology employed, the difference with respect 36 µm to 9 µm measurements was almost 4 times higher than the difference between 18 µm to 9 µm (Figure 3.2.7). With respect the individual threshold methods, Automatic threshold was not consistent between the three scanning resolutions or between samples from the same femoral head, and the differences with respect the highest resolution were variable and greater compared to Global threshold implementation (Figure 3.2.7 A, D). Adaptive thresholding appeared to overestimate the amount of mineralised tissue compared to the other thresholds, and again it appeared to be variable (Figure 3.2.7 C, F). Visual inspection of the samples indicated that 78 was a suitable threshold for global analysis, resulting in approximately 10 % difference on the measurement at 18 µm compared to 9 µm, consistently in both samples A and B (Figure 3.2.7 B, E). Hence, global thresholding assessed by visual inspection was determined as a suitable method to quantify bone volume.

To assess whether µCT provided a method to determine differences in the mineral content of the bone cylinders over time, a study was designed to monitor the decalcification of bone cylinders in EDTA for a period of 5 days (Figure 3.2.8 A-C). Identical scanning and reconstruction settings were used for the bone cylinders (n=4; A-D) and bone volume quantified using a constant global threshold. As expected, the bone volume of the bone cylinders was reduced following decalcification over time (Figure 3.2.8 D), and this difference was also visible in the flat X-rays (Figure 3.2.8 A-C). The relative bone volume change with respect day 0 was greater for the samples that were larger in size, reaching a minimum of 38 % bone volume loss after 2 days, and a maximum of 85 % loss following 5 days in EDTA treatment (Figure 3.2.8 E).

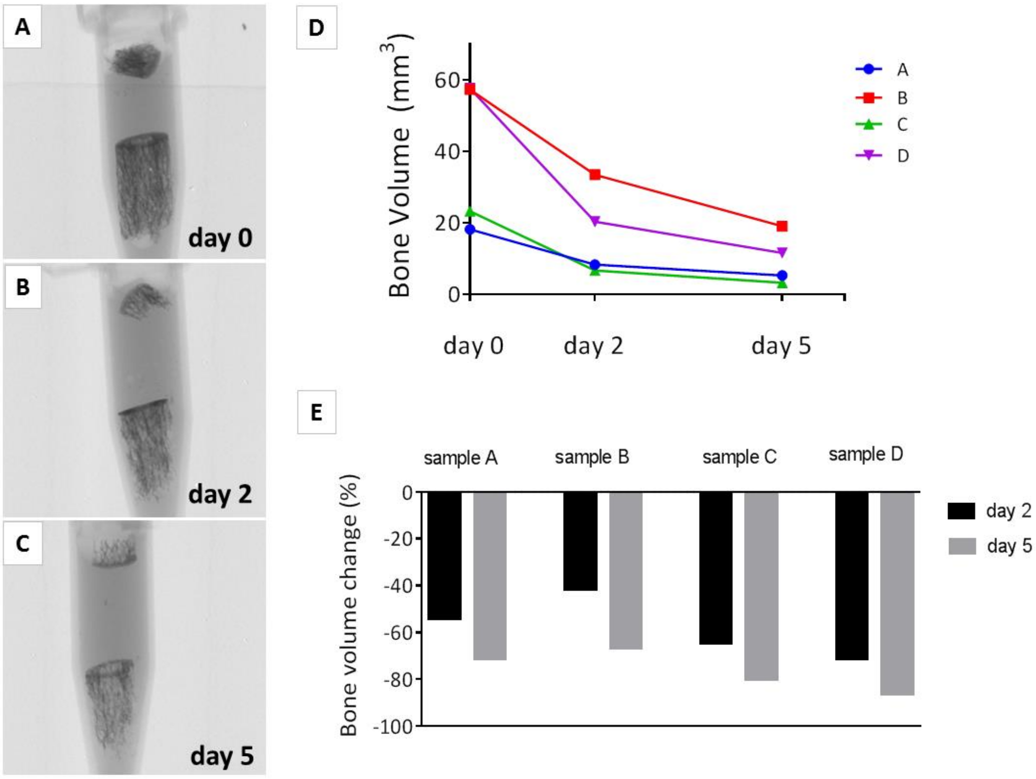

Figure 3.2.8: Sequential µCT scans allow quantifying a reduction in bone volume following decalcification. Bone cylinders were extracted from a human femoral head (n=4; A-D), demineralised using EDTA solution and µCT scanned at day 0 (A), day 2 (B) and day 5 (C) using identical settings. Decalcification was conducting in rotation at 4 °C, 15 ml solution per sample was replaced every other day. Bone volume was quantified (D) and the relative change with respect day 0 was calculated (E).

The previous experiment demonstrates that µCT allows quantification of bone volume changes in human bone cylinders following alterations on their mineral content over time (*i.e.* demineralisation with EDTA solution). In addition, it was important to examine the reproducibility of consecutive scans as a reference of the measurement error from batch-to-batch scan. Bone cylinders were extracted from the same femoral head and maintained in PBS or in fixative solution (paraformaldehyde, PFA) and scanned at different time-points under the same X-ray and image processing settings to quantify bone volume (Figure 3.2.9). As a control, a phantom (internal µCT standard) was scanned in parallel. In general for PFA and PBS-treated samples, bone volume showed negligible changes following 30 min, 1 day, and 7 days (Figure 3.2.9).

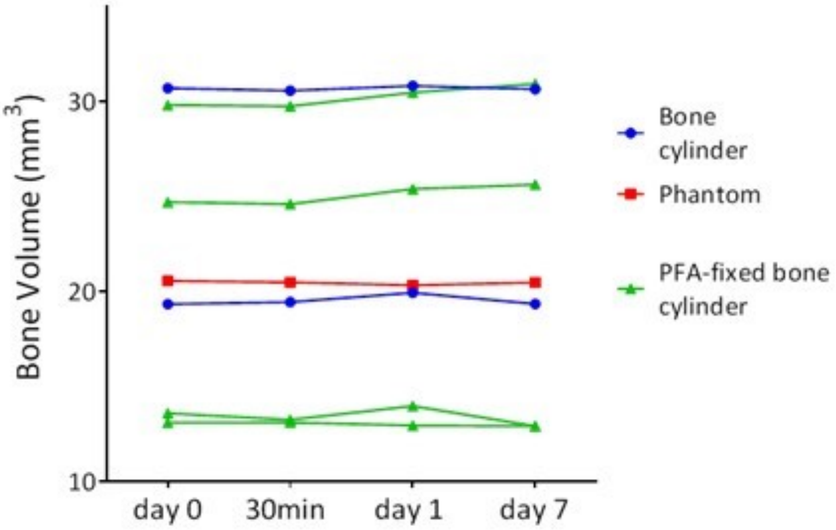

Figure 3.2.9: Minimal variance between consecutive μCT scans on the same bone cylinders. Bone grafts were freshly extracted and maintained in PBS (n=2) or PFA (n=4) over 7 days. After 30min, 1 day and 7 days samples were scanned using identical μCT settings to measure their bone volume (mm^3). In parallel to the human bone grafts, the internal control of the μCT machine (phantom) was scanned. Phosphate buffered solution (PBS), paraformaldehyde (PFA).

Bone volume differences within samples were due to the variability in size, femoral head location and mineral of the extracted bone cylinders (Figure 3.2.9). The data indicate the precision of μCT measurements conducted under the same scanning and analysis settings, at a resolution of 18 μm.

3.2.3 Insights into histology: CAM and bone tissue analysis

To be able to assess the effect of the *in vivo* implantation of human bone cylinders in the CAM, it was necessary to first examine the histological features of both tissues (human and avian) as the samples would display in original conditions independently. The following section details bone and CAM tissue histological features and characteristics.

3.2.3.1 CAM histology

The avian extraembryonic membrane sample was observed to be composed of numerous capillaries contained in the stromal space, enveloped by the endoderm and ectoderm layers (see arrows Figure 3.2.10). Depending on the size of the capillaries in the stroma of the CAM, the thickness of the membrane varied between 100-200 μm. The stromal space between endoderm and ectoderm layers was naturally rich in collagen, as indicated by the pink colouration in the

Alcian Blue and Sirius Red (AS) staining (Figure 3.2.10 B) and the green colouration on the Goldner's Trichrome (GT) staining (Figure 3.2.10 A). The proteoglycan content of the endoderm layer was highlighted in blue in the AS staining (Figure 3.2.10 B), whereas the high cellularity of the ectoderm was emphasized on the GT given the intense nuclear staining (Figure 3.2.10 A). In addition, the GT staining allowed distinguishing erythrocytes of avian origin because of their fusiform morphology, the bright red cytoplasm and, in particular, the dark black of their nuclei (Figure 3.2.10 A).

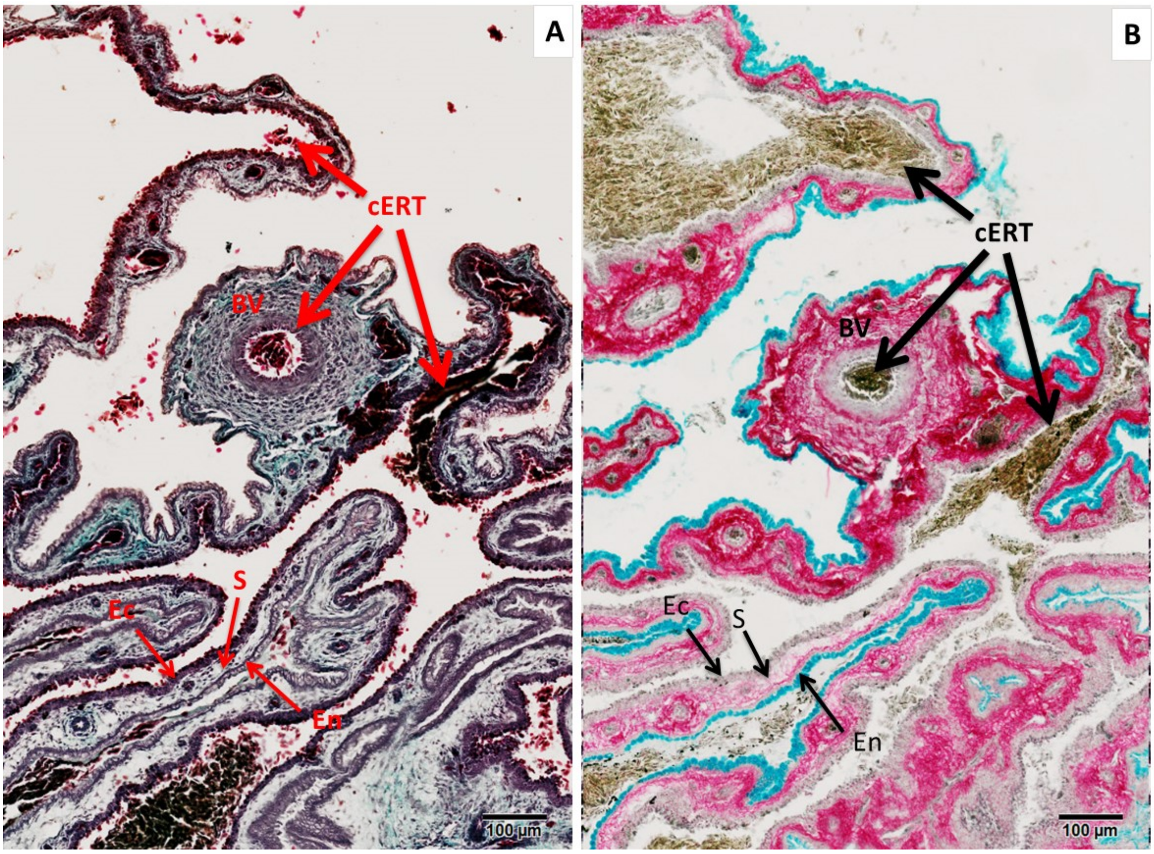

Figure 3.2.10: Characteristic features of EDD 18 CAM. CAM tissue was collected from a non-intervened chick embryo at day 18 of gestation, and processed for histology. Representative images from consecutive sections stained for GT (A) and AS (B). Arrows indicate the three different layers of the CAM: mesoderm (stroma S), endoderm (En) and the ectoderm (Ec) layers, and nucleated chick erythrocytes from the embryo (cERT). Alcian Blue and Sirius Red (AS), Goldner's Trichrome (GT). See colour legend in Table 2.6.1. Scale bar equivalent to 100 µm.

The nucleation of the avian red blood cells provided a key feature to distinguish between CAM and human erythrocytes, given that mammalian erythrocytes do not possess nuclei. The difference between both types of erythrocytes is exemplified in Figure 3.2.11, with dashed arrows indicating human blood vessels in the normal bone marrow, and solid arrows indicate nucleated chick erythrocytes from the CAM.

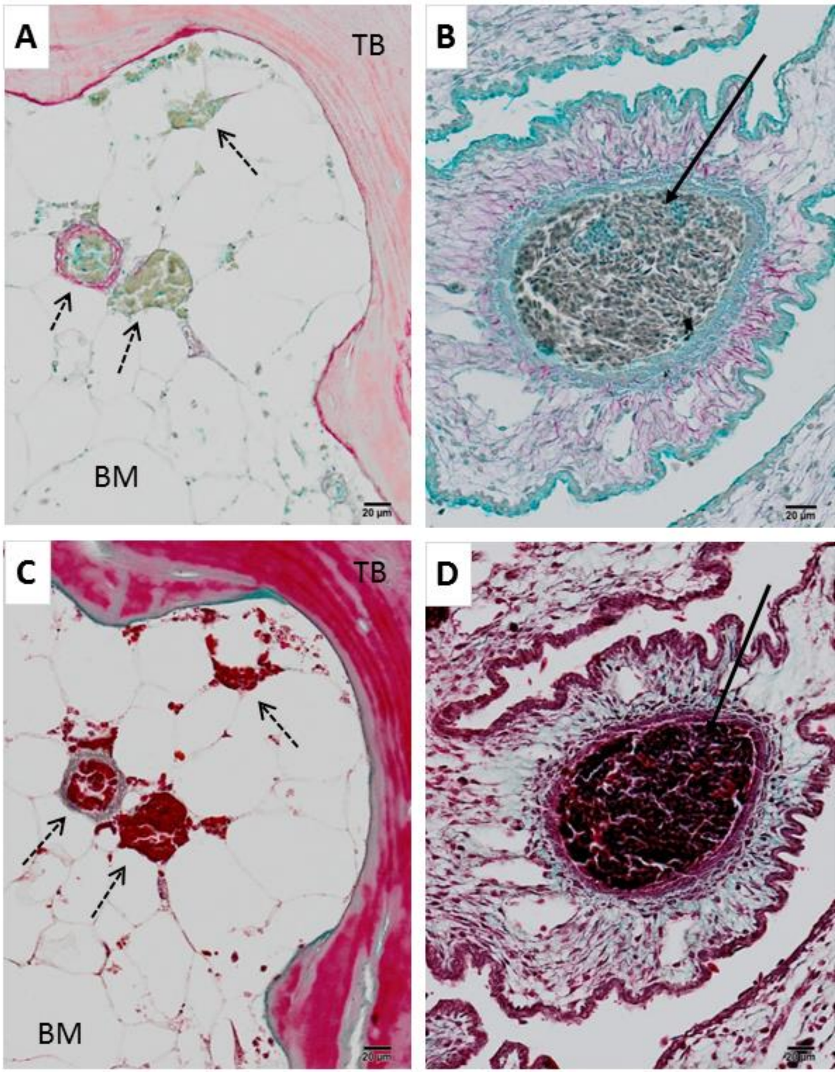

Figure 3.2.11: Histological differences between human and avian erythrocytes. Paraffin sections of freshly isolated human bone (A and C) and CAM tissue (B and D) stained for AS (A-B) and parallel section for GT (C-D). Dashed arrows indicate round and enucleated human erythrocytes in the bone marrow. Solid arrows indicate chick erythrocytes within a CAM blood vessel. Alcian Blue and Sirius Red (AS), Goldner's Trichrome (GT), trabecular bone (TB). See colour legend in Table 2.6.1. Scale bar equivalent to 20 µm.

The differences between chick and human erythrocytes were more evident in the GT staining given the intense colour of the cytosol and the nuclei (Figure 3.2.11 C, D).

3.2.3.2 Human bone cylinders histological features.

Bone cylinders were extracted from human femoral heads, with standard dimensions of 6 mm in diameter and 4-6 mm in length. The bone cylinders were composed of articular cartilage and subchondral cortical bone (Figure 3.2.12 A, B) followed by the main body: trabecular bone and bone marrow (Figure 3.2.12 C, D).

The articular cartilage within the samples was typically around 3 mm in thickness, and the superficial layer (articular surface) was followed by a transitional zone containing round chondrocytes alone or in group, and a mixed orientation of the collagenous fibres (see arrows Figure 3.2.12). The deep zone displayed radial columns of chondrocytes, with collagen distribution parallel to the same orientation. Finally, the tidemark indicated the interface between cartilage and calcified cartilage (see arrows Figure 3.2.12).

Below the subchondral bone, the femoral head bone contained trabecular bone. The trabecular bone was composed of bone spicules with marrow space in between, containing blood vessels as well as a heterogeneous population of haematopoietic tissue islands and adipose cells (Figure 3.2.12 C, D). Erythrocytes within the blood vessels were small round and enucleated (see arrows Figure 3.2.12 C, D).

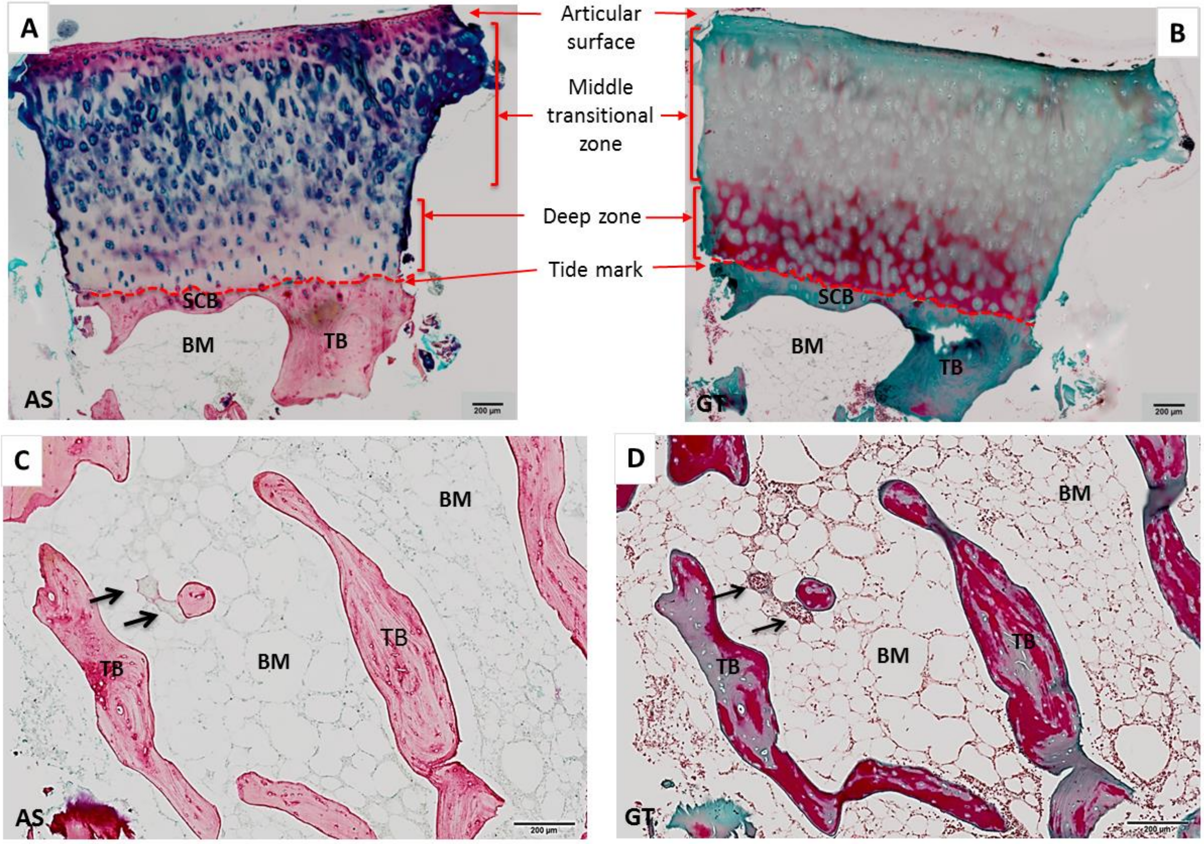

Figure 3.2.12: Histology of the normal bone tissue from freshly collected femoral heads. Articular cartilage (A-B) and bone marrow (C-D). Bone cylinders were extracted from a human femoral head and immediately processed for paraffin. Consecutive sections were stained AS (A, C) and GT (B, D). Red arrows indicate different regions of the articular cartilage. Black arrows indicate human blood vessels. See colour legend in Table 2.6.1. Trabecular bone (TB), bone marrow (BM), subchondral bone (SCB). Alcian Blue and Sirius Red (AS), Goldner's Trichrome (GT), trabecular bone (TB). Scale bar equivalent to 200 µm.

In this study, femoral heads were obtained following routine total hip replacement surgery form osteoarthritic patients (OA) and a smaller number form patients presenting as a as a consequence of bone fracture (osteoporotic patients; OP). Thus, most of the femoral heads displayed a certain degree of osteoarthritis and/or osteoporosis, respectively. To illustrate the differences between OA and OP femoral heads, Figure 3.2.13 shows longitudinal sections of the bone cylinders following extraction from the femoral heads.

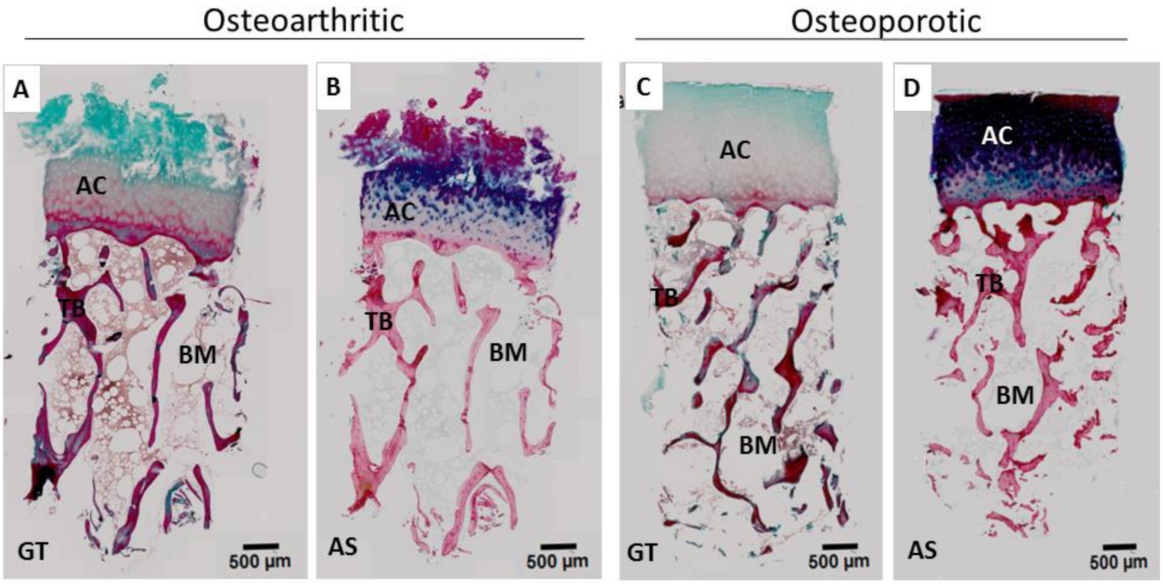

Figure 3.2.13: Histological features of osteoarthritic and osteoporotic graft tissue from human femoral heads. Freshly collected osteoarthritic (A-B) and osteoporotic (C-D) femoral heads were drilled to extract bone cylinders and then processed for paraffin sectioning. Consecutive representative sections were stained for AS (B, D) and GT (A, C). See colour legend in Table 2.6.1. Articular cartilage (AC), Trabecular bone (TB), bone marrow (BM). Alcian Blue and Sirius Red (AS), Goldner's Trichrome (GT), trabecular bone (TB). Scale bar equivalent to 500 µm.

The main difference between OA and OP patients resided in the quality of the articular cartilage, with OA samples displaying fissures and damaged areas on the superficial zone (Figure 3.2.13 A, B), compared to healthy cartilage (Figure 3.2.13 C, D). In addition, OA patient samples displayed, typically, a thicker cartilage due to the formation of non-functional fibrocartilage (Figure 3.2.13 A, B). The bone quality of osteoporotic patients was evident during the femoral head extraction procedure, indicated by the brittle composition of bone cylinders. In contrast, osteoarthritic patient samples proved harder to perforate, due to the excessive remodelling caused by the lack of cartilage.

3.2.3.3 Design and development of the bone injury model

The ultimate aim of culture of human bone on the CAM was to develop a bioreactor for biomaterial testing *in vivo*. To facilitate a constant and standard size region of interest, a concentric drill defect was introduced into the bone cylinders. This resulted in a simulation of a bone fracture environment while at the same time creating a specific region within which to apply the biomaterial of interest. To create the bone cylinders, the articular cartilage was removed from the cylinder surface, and the bottom end of the cylinder was trimmed using a scalpel to create a uniform cylinder size between samples of 4-6 mm in length. The subchondral bone of the cylinders was maintained, providing a reference point on the X-ray scan due to its higher mineral density. Next, the bone cylinders were engineered to have a 2 mm inner diameter cavity (#), concentric to the 6 mm outer diameter.

After bone cylinder extraction, the defect region was perfused with sterile saline to avoid interference with any residual bone debris. Representative images of the 3D rendering from a bone cylinder µCT scan following the devising procedure is shown in Figure 3.2.14. Note the cylindrical defect of 2 mm in the bone cylinder, clear from bone debris (Figure 3.2.14 A).

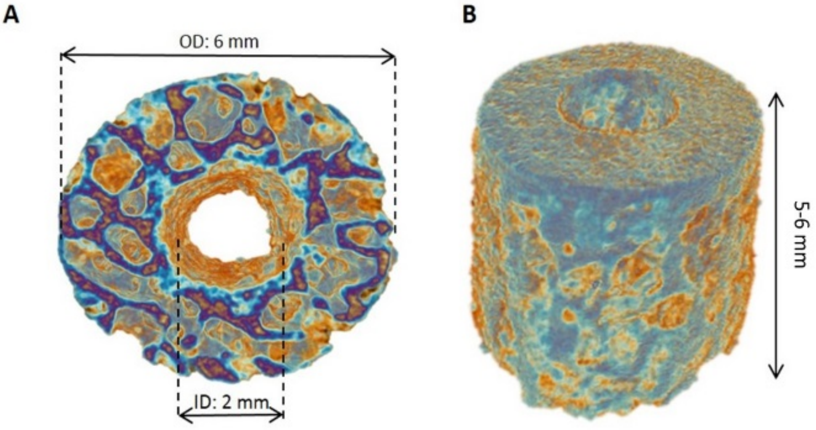

Figure 3.2.14: 3D image from a µCT scan of an engineered human bone cylinder injury model. (A) Top and (B) lateral view. Human bone grafts were extracted following a two-step drilling protocol. A 2mm diameter trephine was used to drill the surface of the femoral head. Then, a hollow saw (6 mm) with a pilot drill (2 mm) attached was used to drill the outer diameter of the graft. The length of the bone graft varied between 5-6 mm. Purple colour indicates low density tissue, orange colour indicates high density tissue. Inner diameter (ID), outer diameter (OD).

Figure 3.2.15 A-B shows example of the histological features of human bone cylinders with and without the bone defect. The cross section of the cylinders allowed determination of the hollow cylindrical cavity (see # Figure 3.2.15 B), compared to the non-drilled bone cylinder (Figure 3.2.15 A).

Hence, the development of an extraction protocol allowed obtaining standard size bone cylinders with a defect site to mimic the fracture site and act as a region of interest for biomaterial delivery.

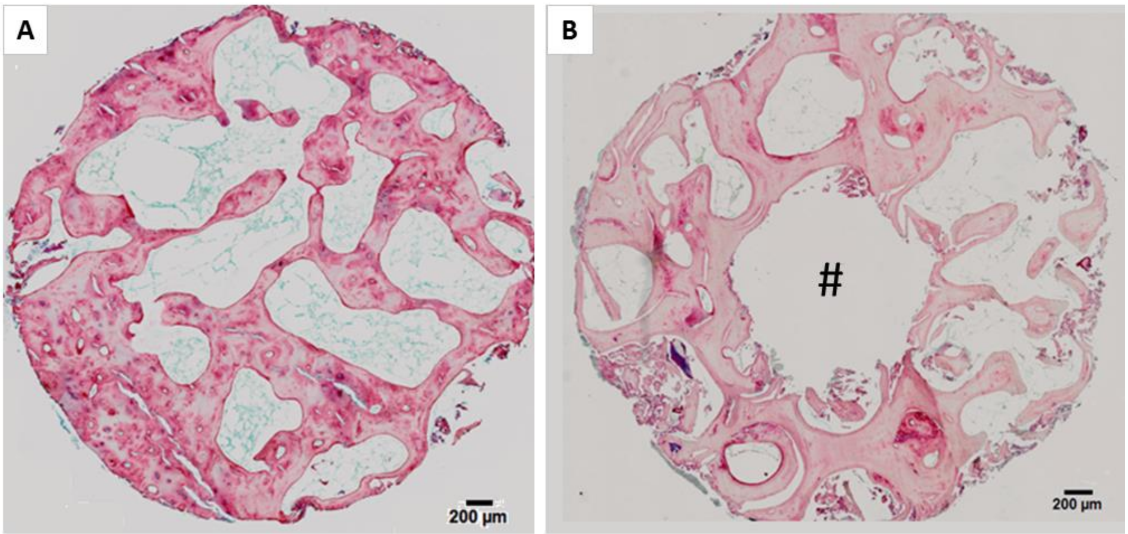

Figure 3.2.15: Drill defect cross-section on human bone cylinders. Human bone grafts were extracted (A) and then perforated following a two-step drilling protocol (B). A 2 mm diameter trephine was used to drill the surface of the femoral head. Then, a hollow saw (6 mm) with a pilot drill (2 mm) attached was used to drill the outer diameter of the graft. Cylinders were then processed for paraffin sectioning and were stained for Alcian Blue and Sirius Red. # indicates drill defect area. See colour legend in Table 2.6.1. Scale bar equivalent to 200 µm.

3.2.3.4 The CAM as a biocompatibility indicator

As previously discussed in section 1.6.3, the CAM has been traditionally used as an *in vivo* toxicology assay due to the sensitivity and early response to external stimuli of the CAM. In a similar manner, the CAM has been used in this study to examine biocompatibility of the implanted bone cylinders by assessing the number of fully developed normal chick embryos at harvest as well as the integration/rejection of the grafts with the membrane.

Seven independent experiments were conducted implanting fresh, viable human bone cylinders extracted from human femoral heads on the CAM over a period of 7-9 days. At harvest, chick embryo development was recorded for each experiment, including 8 to 12 samples per individual experiment (Table 3.2.1).

Table 3.2.1: Chick embryo viability following implantation of live human bone on the CAM in seven independent experiments (Exp 1 to 7). Each experiment conducted using an individual femoral head from a patient undergoing total hip replacement surgery.

	Viable embryos	*Total number of embryos*	*Percentage of viable embryos*
Exp 1	10	10	100.00 %
Exp 2	7	10	70.00 %
Exp 3	4	8	50.00 %
Exp 4	7	10	70.00 %
Exp 5	7	10	70.00 %
Exp 6	10	12	83.30 %
Exp 7	5	8	62.50 %
		Mean	**72.50 %**
		SD	**15.80**

Chick embryo viability was not significantly compromised as the average percentage of viable embryos (Table 3.2.1) compared to the standard rate of 70-75 % survival rate of the standard CAM assay. Chick embryo survival as well as graft integration were key parameters to determine at harvest of the bone cylinders. CAM-integration was assessed at harvest by the enveloping of the bone cylinder within the CAM, surrounded by avian blood vessels (Figure 3.2.16).

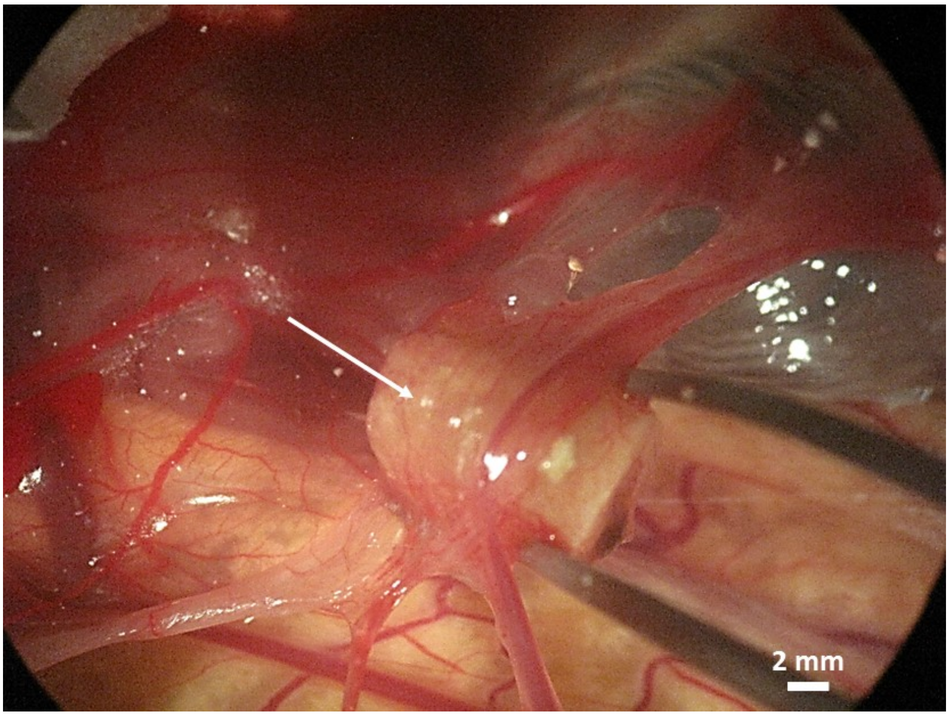

Figure 3.2.16: Integration of bone cylinder with the CAM at harvest. Representative image of the human bone graft collected at the end of the embryo gestational process. Arrow indicate bone cylinder.

The gross morphology of integrated *versus* not-integrated bone cylinders at harvest is shown in Figure 3.2.17. CAM-integrated bone cylinders showed the presence of the membrane around the human graft, rich in avian blood vessels (Figure 3.2.17 A), whereas rejected (non-integrated) bone cylinder showed no apparent evidence contact with the CAM deposition (see white substance in Figure 3.2.17 B).

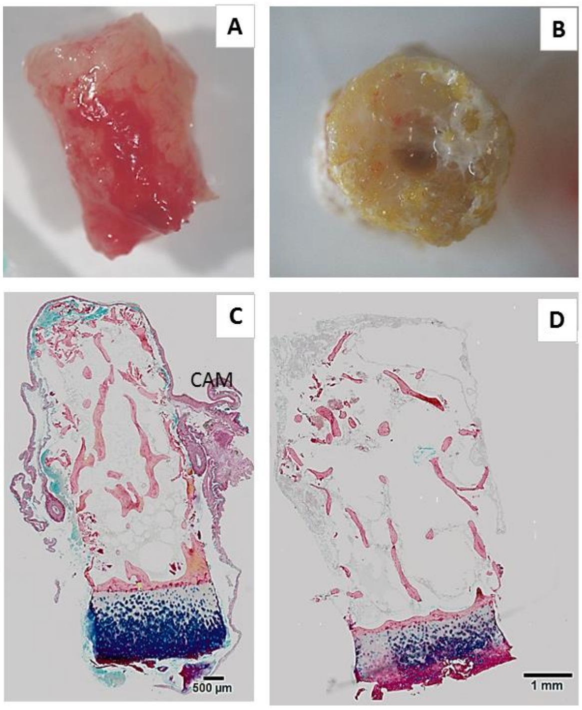

Figure 3.2.17: Differences between an integrated and a non-integrated graft on the CAM. Bone cylinders from the same femoral head were implanted on the CAM and imaged at harvest (A-B), followed by paraffin sectioning and Alcian Blue and Sirius Red staining (C-D). Integrated bone cylinder (A, C) and not integrated bone cylinder (B and D). See colour legend in Table 2.6.1. Chorioallantoic membrane (CAM). Scale bar equivalent to 500 µm (C) and 1 mm (D).

In accordance with the gross morphology examination, histological sections of the integrated cylinder showed the presence of the CAM surrounding and enveloping the entire bone cylinder (Figure 3.2.17 C). In contrast, the rejected bone cylinders showed non-cellular matrix around the graft (Figure 3.2.17 D). Hence, the CAM assay can serve as a biocompatibility assay by examining both the number of viable embryos at the end of the gestational term as well as the integration of the grafts on the membrane.

3.2.3.5 The use of genetically modified chick embryos: GFP CAM

An important consideration in the present thesis was the ability to identify the features attributed to the human autologous cells (bone) and to the extraembryonic avian cells (CAM). To achieve this resolution, the experiments described in the present thesis were conducted using genetically modified chick embryos expressing green fluorescent protein (GFP) for the CAM assay. Hence, it was important to validate the green fluorescence from the GFP CAM as well as assessment of any differences in morphology between wild type (WT) and GFP-CAM.

Cell Tracker Red staining of the GFP and WT day 18 CAM gross tissue indicated the presence of living cells in both groups (Figure 3.2.18 C, D). Green fluorescence was only detected on the GFP-CAM (Figure 3.2.18 B, F); as expected no green fluorescence was observed on the WT CAM (Figure 3.2.18 A, E).

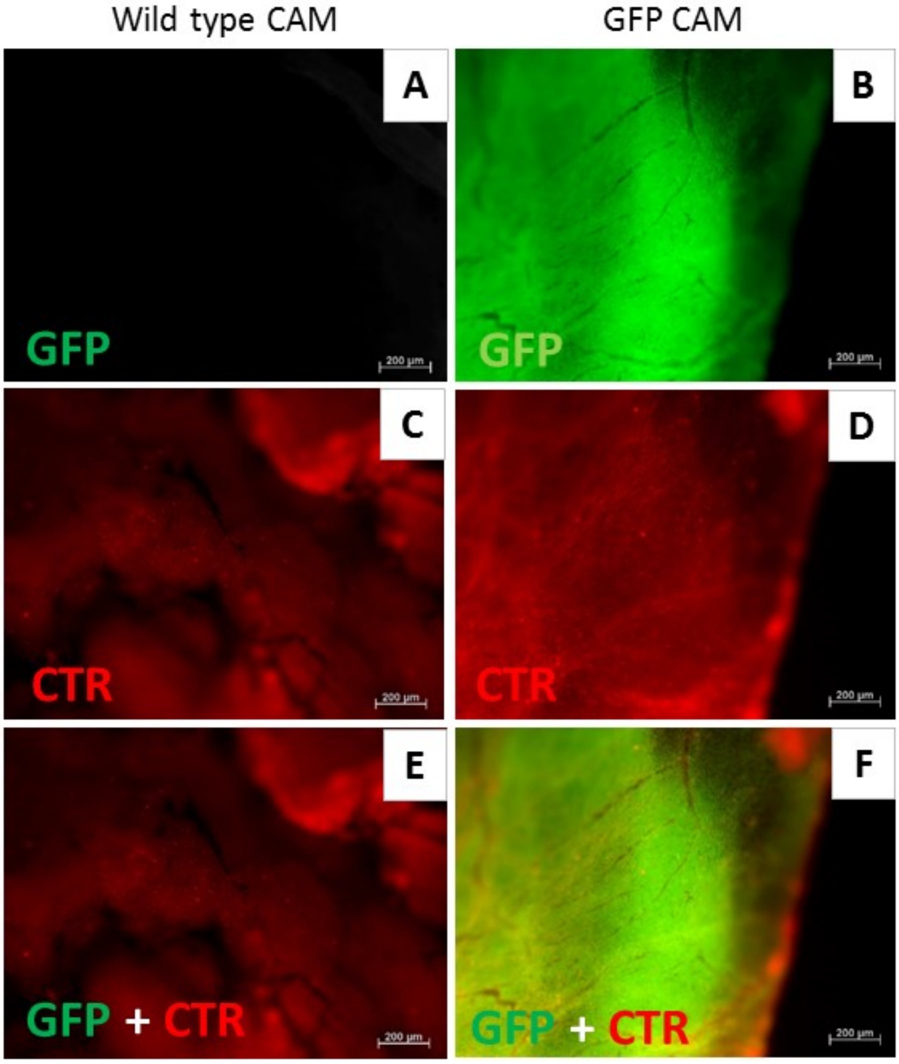

Figure 3.2.18: Green Fluorescence of day 18 CAM from genetically modified chick embryos. CAM tissue was collected at the end of the incubation period (day 18-19) from green fluorescent protein (GFP) transfected chick embryos (B, D and F) and from wild type (A, C, E). Freshly harvested tissue was stained for viability with Cell Tracker Red (CTR) and fixed with paraformaldehyde (PFA). Gross morphology images of the tissue were taken using a fluorescence microscope on the red (C, D) and on the green emission filter (A, B); merged images showed in (E, F). Scale bar equivalent to 200 µm.

Histological examination of the two membranes (thickness, extracellular matrix composition) did not show any significant differences between WT and GFP CAM at day 18-19 of development (Figure 3.2.19). Note the similarities in structure, cellular content (solid arrow Figure 3.2.19 A, B) as well as in blood vessels (see dashed arrow Figure 3.2.19 A, B) between WT and GFP CAM. Given that GFP fluorescence was lost on the paraffin processing procedure, it was necessary to use GFP specific antibodies to detect the avian cells (Figure 3.2.19 C, D).

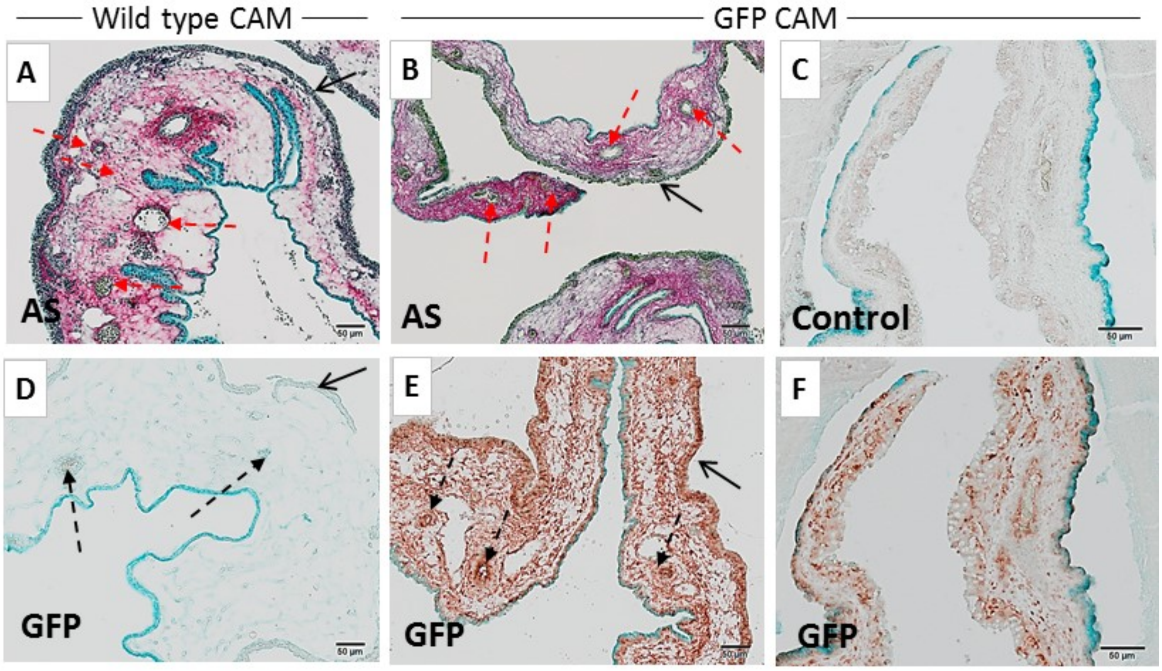

Figure 3.2.19: Histological differences between wild type and GFP CAM day 18 of gestation. CAM tissue was collected from a non-intervened wild type (A, D) and GFP (B, C, E, F) chick embryos at day 18 of gestation, and processed for histology. Representative images from consecutive sections stained for Alcian Blue and Sirius Red (A, B) and immunohistochemistry for GFP (C-F). Positive immunostaining in brown-red colour, counterstained with Alcian Blue to visualize the matrix content. Positive (F) and corresponding Isotype control (C). Solid arrows indicate ectoderm layer of the CAM, dashed arrow indicate CAM blood vessels. Scale bar equivalent to 100 µm.

As expected, immunostaining for GFP showed significant expression in the GFP-CAM (Figure 3.2.19 D), however absence on the wild type CAM (Figure 3.2.19 C). This data indicates that the typical features of the CAM tissue did not vary significantly in the genetically modified animals and that the use of GFP-CAM allowed the identification of avian cells at the histological level.

3.3 Discussion

The ultimate aim of this thesis was to demonstrate the potential of the CAM assay as an *in vivo* model to study human bone regeneration. Hence, the goal of this first chapter was to establish the basis of the model and to resolve the technical constrains to facilitate the subsequent study of the biologically relevant questions. In addition, it was necessary to develop the appropriate methodology to evaluate quantitative and qualitatively the outcome from this human-avian model. In summary, the main findings of the present chapter were:

- Devising of standard sized bone cylinders from human femoral heads including a drill defect to mimic the fracture site and generate a standard region of interest.
- Assessment of tissue viability using Cell Tracker Red as a fluorescence staining.
- High resolution computed tomography (µCT) was validated as a method to examine changes in the mineral content of the bone cylinders.
- CAM-integration of bone cylinders assessed by histological analysis together with chick embryo viability rate at harvest were critical parameters for the evaluation of graft biocompatibility.
- Genetically modified eggs (GFP) were implemented as a way to distinguish avian (GFP+) from human (GFP-) tissue.

In order to establish the platform for the project, a number of technical issues were addressed such as bone cylinder extraction and decalcification. It was concluded that the surgical drill was the most suitable tool to extract the bone cylinders because of the consistency in size and shape of the grafts and the ability to create a standard region of interest (defect site). In addition, the small volume of the extracted bone cylinders (6 mm diameter, 4-6 mm length) allowed provision of a greater number of samples from a single femoral head and reduced the decalcification time; both important limitations for this study. Different rapid demineralization solutions were tested using Faxitron (2D X-ray) and histology, from which Histoline was identified as the most suitable candidate. Histoline reduced the decalcification time from 3-4 weeks of standard protocol (Callis and Sterchi 1998) down to 24 hours, while at the same time preserving the structure integrity of the tissue, as demonstrated by the specific nuclear immunostaining (Figure 3.2.3).

Following the optimization of the bone extraction and decalcification, the next goal was to familiarise with the standard bone and CAM histological features in order to identify the effects of their interactions when cultured together. Bone and avian tissue were clearly distinguishable given their different structure (lamellar bone compared soft membrane) and their different cellular and collagenous content (Figure 3.2.10 and Figure 3.2.12). The established differences from osteoarthritic femoral heads shown in the present chapter (Figure 3.2.13) were in accordance to previous results shown in the literare (Sulzbacher 2013). Both wild type and genetically modified chick embryos displayed the regular features of the CAM (Figure 3.2.19), also similarly as previously reported (Valdes *et al.* 2002). Moreover, the difference between avian and mammalian red blood cells described here (Figure 3.2.10) has been commonly used to distinguish the origin (host *versus* graft) of the blood vessels in the literature (Buschmann *et al.* 2012; Holzmann *et al.* 2010; Roach, Baker, and Clarke 1998). Future experiments could implement the use of a contrast dye to quantify avian blood vessel infiltration on the bone cylinder. However, careful consideration should be given to this approach as it precludes the ability to measure mineral content and tissue regeneration of the bone cylinders.

Despite the use of a xenograft material (human bone) on CAM, embryo viability was reduced by only 27.5% compared to approximately 30% in other CAM studies (Borges *et al.* 2003; Martinez-Madrid *et al.* 2009), supporting the concept that the CAM offers a biocompatible model for explant culture (Borges *et al.* 2003; Valdes *et al.* 2002). Adverse reactions from the CAM to toxins and to artificial materials was described to result in deposition of extensive non-cellular fibres to isolate the graft from the CAM (Valdes *et al.* 2002). Histological assessment allowed validation of CAM-bone integration evaluation, evidenced by the envelopment of the bone tissue within the avian membrane and capillaries (Figure 3.2.17). Complete graft integration by the CAM has also been shown histologically and described as an indicator of the good interaction between grafted tissue and CAM-host in previous studies (Carre *et al.* 2012; Kunzi-Rapp *et al.* 1999). Hence, retention of embryo viability and absence of a sustained fibrotic response support the conclusion that the human bone tissue can integrate with the CAM membrane.

In order to validate µCT analysis as a method to quantify changes on the bone cylinders following CAM-implantation, optimisation of the µCT settings and assessment of reproducibility between scans were required. Choice of scanning resolution and thresholding are two of the key parameters to define in any µCT study (Bouxsein *et al.* 2010). From the available resolutions in the vivo µCT scanner (36, 18 and 9 µm), the middle resolution (18 µm) offered a good compromise between scanning time (exposure time), X-rays dose, dataset size and scan quality (Figure 3.2.7). Three different threshold methodologies were used to quantify bone volume, from which global thresholding assessed by visual inspection appeared to offer the least differences with respect to the lowest resolution (the most accurate measurements of the bone cylinder). In addition, global threshold assessment permitted the application of the same threshold to the pre and post scans within the same experiment, providing enhanced consistency of analysis. For those reasons, global threshold assessment has been used in similar studies quantifying differences between consecutive scans (Birkhold *et al.* 2014; Patel *et al.* 2008; Zhang *et al.* 2010). These two parameters (18 µm resolution and global thresholding) were then used to quantify the bone volume of cylinders subject to changing (demineralisation) and unaltered conditions (PBS storage). Those experiments demonstrated the ability of the µCT analysis to quantify structural changes following demineralisation (Figure 3.2.8), as well as measuring negligible changes for the cylinders which did not experience any biological change (Figure 3.2.9). Thus, the previous experiments demonstrated the potential of µCT as a tool to measure additional changes on the bone cylinders, such as mineral deposition and tissue regeneration following *in vivo* implantation.

Viability assays traditionally used for cell monolayer culture were adapted to inlude bone tissue fragments (Saleh *et al.* 2011; Tomco *et al.* 2016). Cell Tracker Red and Live and Dead staining were tested in bone cylinders, however only the red signal was able to determine changes in bone viability (Figure 3.2.4 and Figure 3.2.6). Previous studies employing Live and Dead staining on bone tissue were unable to distinguish live cells due to bone autofluorescence (Hoke *et al.* 2013), and only dead cells on the red signal were discernable (Stoddart *et al.* 2006). In addition, the same authors reported that live cells fluorescence was quenched after processing, while the current work shows that fluorescence remained after histology processing and sectioning (Figure 3.2.5). However, fluorescence from the GFP-CAM tissue was lost after paraffin tissue processing, as other authors have previously reported (Jiang 2005). To circumvent this issue, GFP immuostaining on paraffin sections was used to identify avian cells (Figure 3.2.19). Future experiments will consider the implementation of cryosectioning or mineralised tissue processing to preserve the endogenous fluorescence of the GFP-CAM.

Overall, the studies reported here provide an initial step in the development of the CAM assay for the *in vivo* culture of human bone and the study of tissue regeneration. Preliminary studies and data generated have allowed optimisation of bone extraction methods as well as decalcification techniques for the bone cylinders, which allowed subsequent histological analysis. Additional parameters for the evaluation of the model were determined such as chick embryo viability, graft integration and µCT analysis to quantify potential changes in the structure of the bone cylinder. Furthermore, challenges with respect the distinction between human and avian cells, or the identification of viable cells within the bone tissue were resolved by implementing genetically modified (GFP) eggs and red fluorescent viability staining for the whole tissue.

In conclusion, this chapter has developed the methods which will be used in the following sections to answer biologically relevant questions, critical to understand and utilise this human-avian model for the study of bone tissue engineering.

Chapter 4: Results Part II. Evaluation of the CAM as an *in vivo* model for bone regeneration

4.1 Introduction

The experiments in the previous Chapter optimised the protocol of the CAM assay for the culture of human living bone by obtaining standard size bone cylinders from a single femoral head, introducing a drill defect to mimic injury environment, as well as implementing the use of GFP-modified chick embryos to distinguish human and avian cells. Moreover, fluorescent viability stains and µCT technology were validated to assess changes on the bone cylinders. Additional findings from the previous chapter established that integration of the bone cylinder on the avian membrane was achieved upon *in vivo* implantation. Hence, an imperative requirement for this project was to establish the effects of the *in vivo* implantation on the CAM in terms of bone cylinder graft viability and tissue regeneration.

As the chick embryo immune system is not fully developed until the last two thirds of the gestation process, the CAM assay has been traditionally used as a model for xenograft culture (Carre *et al.* 2012; Kunzi-Rapp *et al.* 1999; Martinez-Madrid *et al.* 2009). Indeed there are numerous examples demonstrating the potential of xenograft culture such as brain and aorta of rat origin have been implanted successfully on the CAM (Coconi *et al.* 2005; Ribatti *et al.* 2003). Living tissue from human and murine origin have also been implanted on the CAM showing infiltration of avian blood vessels carrying nucleated erythrocytes (Carre *et al.* 2012; Kunzi-Rapp *et al.* 1999; Martinez-Madrid *et al.* 2009). Skin grafts were implanted on the CAM and integration with the chick vasculature was assessed by the appearance of the graft following implantation, displaying pink and healthy aspect for successful transplants compared to the pale and necrotic phenotype of rejected grafts (Carre *et al.* 2012; Kunzi-Rapp *et al.* 1999). Another study implanted cryopreserved human ovarian tissue on the CAM and used Live and Dead fluorescence staining to determine graft viability following implantation (Martinez-Madrid *et al.* 2009). Importantly, these previous studies used the CAM assay as an alternative to the severe combined immunodeficient mouse (SCID) model.

The earliest described use of the CAM to culture bone was described in 1946, when Hancox implanted small chick embryo calvarial fragments – either freshly isolated or after boiling them- on the CAM for a period of 10 days. Blood vessel invasion and new tissue formation on the non-boiled implants was subsequently shown (Hancox 1946). Following the work of Hancox in 1969, Lafferty grafted several avian organs (bones, heart, lymph nodes) from various species (chicken, pigeon and duck embryos) to examine the inflammatory reaction of the CAM-host towards the graft (Lafferty and Jones 1969). Bovine decellularized bone slices have also been implanted to examine the CAM osteoclast activity, showing significant formation of bone resorption pits upon harvest (David M. Webber 1990). Implantation of chick femurs on the CAM has been also used as a model to study cartilage and chondrocytes behaviour (Maeda and Noda 2003; Roach *et al.* 1998). Following a similar approach, bone tissue regeneration was assessed by introducing a defect on chick embryo femurs before CAM-implantation (Takahashi *et al.* 1991). In the previous investigation the authors provided histological data showing complete bridging of the fracture gap after 8 days implantation (Takahashi *et al.* 1991). In 2004, Yang *et al.* took this model further and used the chick femur wedge defect for biomaterials evaluation (Yang *et al.* 2004). The previous study, poly-lactic acid (PLA) containing BMP2 and human bone marrow stromal cells were applied on the wedge after CAM-implantation and demonstrated bone augmentation compared to control (Yang *et al.* 2004).

In the studies detailed above where bone tissue was implanted on CAM, histology was the only tool to assess tissue formation. Since those early reports, a number of techniques have been and are currently employed to assess bone tissue repair in a more precise, quantitative and non-destructive manner. In particular, X-ray imaging technology has proved a gold standard to measure bone formation and as a technique, has evolved to a level in which 3D X-rays scans (µCT) are available minimally invasive *in vivo* at very high resolution. In the present study we hypothesise that the CAM assay can be used for the culture of human living bone, and that this system will allow to examine new tissue regeneration and repair, measured using µCT. Hence the main aim of this chapter was to demonstrate the potential of the CAM as an *in vivo* bioreactor for human bone cylinders, and the individual objectives were:

- To assess whether avian blood vessels can perfuse the human graft tissue
- To examine the viability of the bone graft after CAM-implantation
- To quantify the structural changes after CAM-implantation using µCT
- To validate the observed structural changes by implementing histological analysis.

4.2 Results

4.2.1 Bone cylinders experience CAM surrogate blood supply

The first set of experiments were performed to test if freshly isolated bone cylinders can integrate with the CAM tissue. Bone cylinders from the same femoral head were maintained at the air-liquid interface (organotypic) for *in vitro* culture, or implanted on CAM (*in vivo*) for a period of 7-9 days; chick embryo viability was monitored and graft integration was evaluated at harvest. The gross appearance of the bone cylinders was not altered following culture *in vitro* (Figure 4.2.1 A-C) while the CAM-implanted bone cylinders were widely enclosed by CAM tissue after implantation with presence of chick blood circulation around the bone graft site at the time of harvest (Figure 4.2.1 F-H).

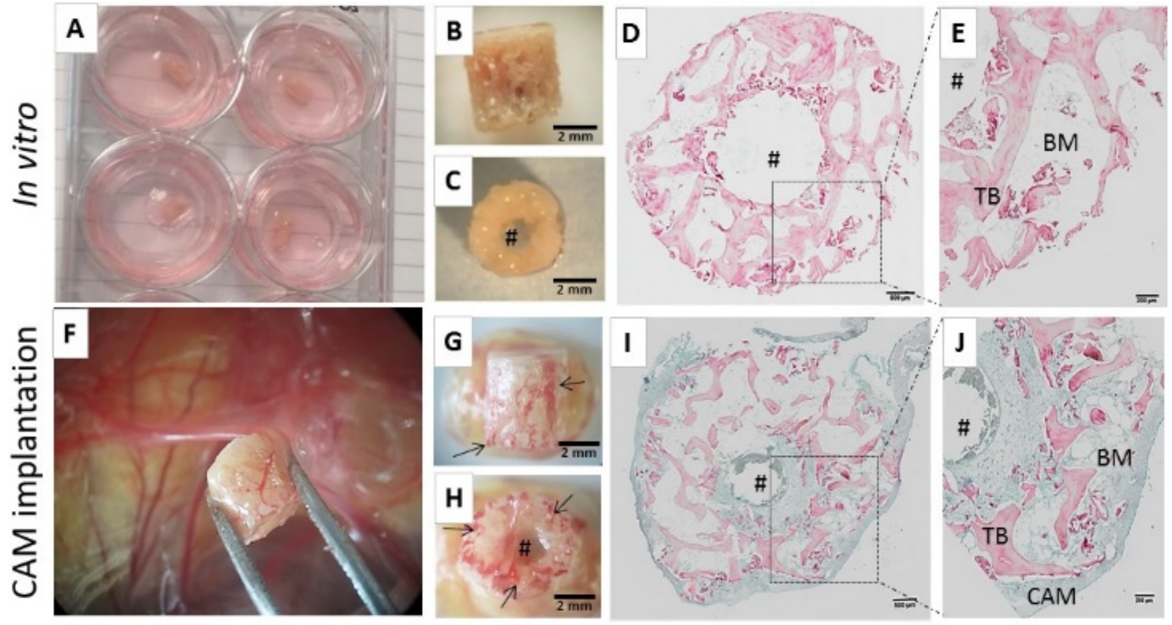

Figure 4.2.1: Avian blood vessels perfuse and infiltrate human bone tissue following CAM-implantation.Bone cylinders were extracted from the same femoral head immediately after surgery and incubated *in vitro* (A-E) or CAM-implanted (F-J) for 7-9 days. Macroscopic evaluation was performed upon harvesting of the bone cylinders (A-C and F-G), followed by histological examination (D-E, I-J). Representative paraffin-embedded cross-sections of the bone cylinders following Alcian Blue (proteoglycans) and Sirius Red staining (collagen) (D-E, I-J). # indicates bone defect area, arrows indicate blood vessels. Alcian Blue and Sirius Red (AS), chorioallantoic membrane (CAM), bone marrow (BM), trabecular bone (TB). Scale bars equivalent to 2 mm (B, C, G and H), 500 µm (D and I) and 20 µm (E and J).

Histological evaluation of the bone cylinders showed the presence of lamellar trabecular bone encapsulating the human bone marrow cells following *in vitro* culture (Figure 4.2.1 D-E). In contrast, CAM-implanted bone cylinders showed extensive integration with the CAM as shown by the increased cellularity and matrix deposition within the bone marrow cavities, reaching the inner core or defect area of the bone cylinders (Figure 4.2.1 I-J).

CAM blood vessels were clearly distinctive macroscopically when harvesting the bone cylinders (Figure 4.2.1), as well as microscopically during histological evaluation (Figure 4.2.2). As described in the previous chapter, the distinction between human and avian blood vessels was determined by the presence of nuclei and the fusiform shape of the avian cells, compared to the enucleated and biconcave mammalian erythrocytes (Figure 3.2.11).

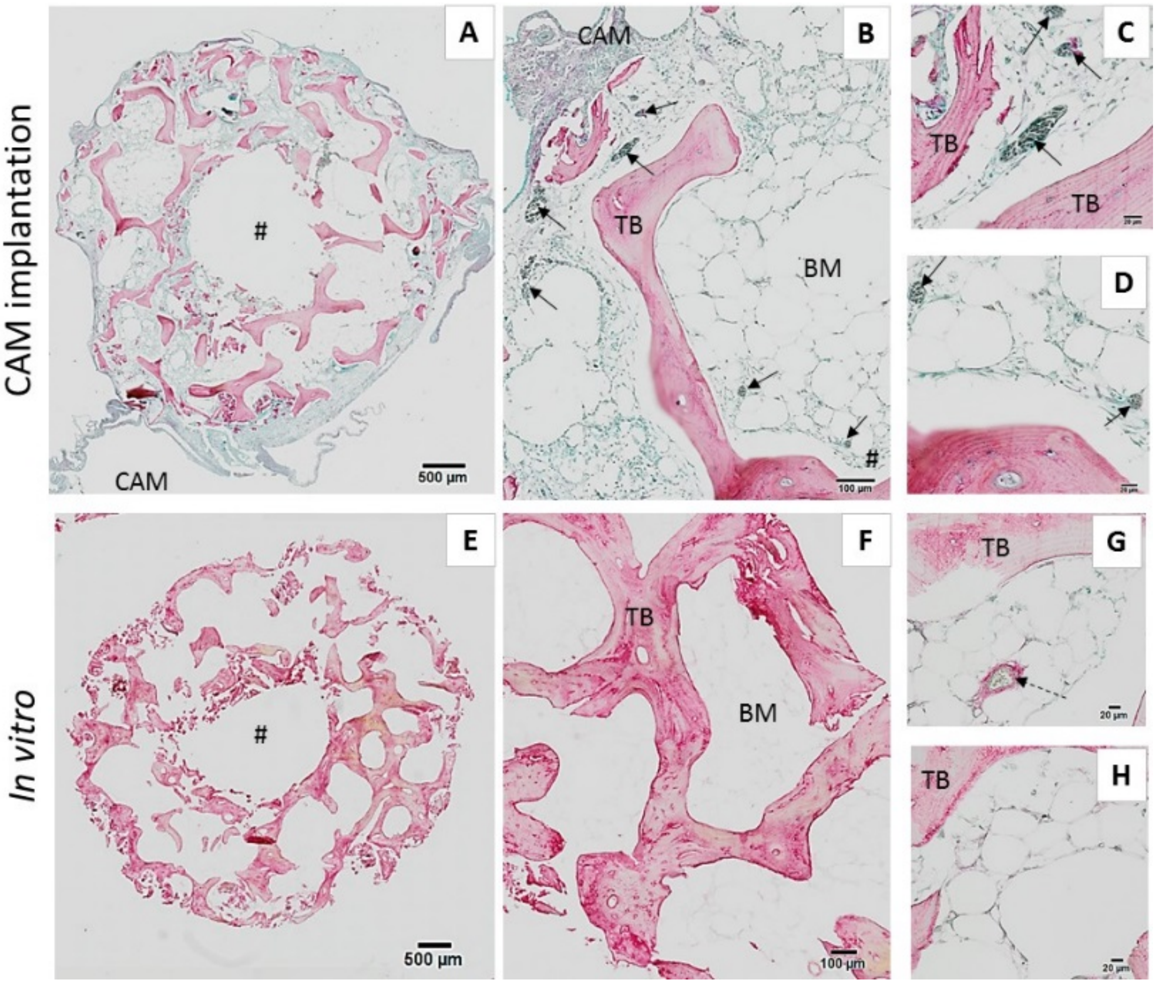

Figure 4.2.2: Avian blood vessels carrying nucleated erythrocytes present within the marrow space of the human bone tissue following CAM-implantation. Bone cylinders were freshly extracted and CAM-implanted (A-D) or cultured *in vitro* (E-H) for the same period. Representative images of paraffin sections stained for Alcian Blue (proteoglycans) and Sirius Red staining (collagen). Solid arrow indicate avian blood vessels, dashed arrows indicate human blood vessels. # indicates bone defect area. Alcian Blue and Sirius Red (AS), chorioallantoic membrane (CAM), bone marrow (BM), trabecular bone (TB). See colour legend in Table 2.6.1. Scale bars equivalent to 500 µm (A, C), 100 µm (B, F) and 20 µm (C, D, G and H).

CAM capillaries were evident at the periphery of the bone cylinder, throughout the trabeculae and in close proximity to the central defect region of the human tissue (see arrows Figure 4.2.2 C-D). Additional examples of the dense capillary network from the avian circulatory system into the human trabecular tissue are shown in Supplementary Figure 7.3.2. As anticipated, *in vitro* cultured bone cylinders only showed human blood vessels containing enucleated erythrocytes (dashed arrow Figure 4.2.2 G-H). Thus, these studies demonstrated extensive CAM integration with the bone cylinders was evident by the infiltration of the surrogate blood supply into the human tissue.

4.2.2 Examination of human cell viability following CAM-implantation

To evaluate the effect of CAM-implantation on the viability of the human bone tissue it was necessary to address whether human autologous cells remained viable in the bone cylinder after 7-9 days following *in vivo* implantation. Cell Tracker Red was used to stain the whole bone cylinders cultured *in vitro* (Figure 4.2.3 A-B), implanted on CAM (Figure 4.2.3 C-D), or maintained at 4 ˚C for the same (control; Figure 4.2.3 E-F), followed by paraffin processing and sectioning. The red signal was detected in both CAM-implanted (Figure 4.2.3 C) and *in vitro* cultured bone cylinders (Figure 4.2.3 A), identifying viale cells; no/negligible staining was observed within the control (Figure 4.2.3 E). Living cells from *in vitro* cylinders were distinguishable at the trabecular bone endosteum (see arrows Figure 4.2.3 A), whereas on the *in vivo* implaned cylinders living cells were present both on bone endosteum and marrow space (see arrows Figure 4.2.3 C).

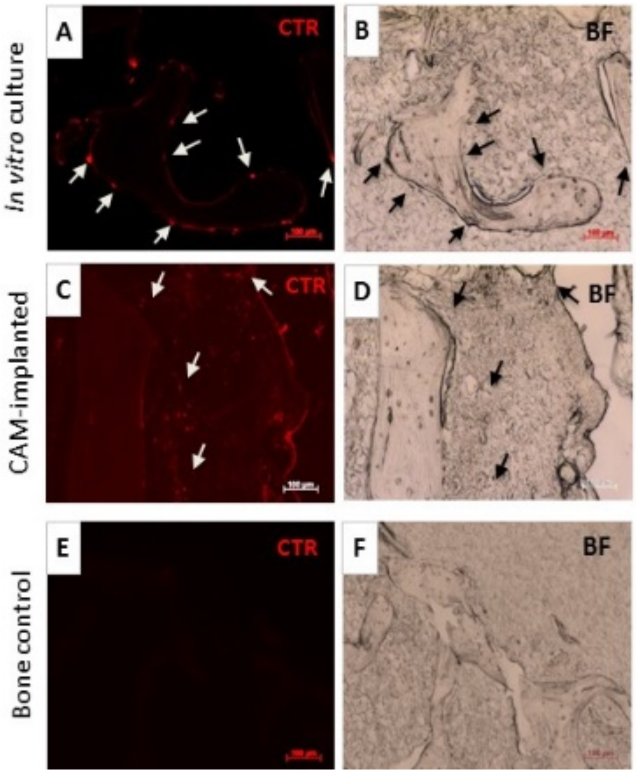

Figure 4.2.3: Cell tracker red-stained cells present at the endosteum surface of the trabecular bone following CAM-implantation. Representative images of paraffin sections from bone cylinders stained for Cell Tracker Red following *in vitro* culture (A-B), CAM-implantation (C-D). Bone cylinders were maintained at 4˚C for the same period were used as control (E-F). Arrows indicate live cells stained for Cell Tracker Red. Scale bar equivalent to 100 µm.

The previous experiment enabled the observation of living cells on bone cylinders following CAM-implantation, however it was not possible to distinguish the human or avian origin of those cells. To achieve this, chick embryos that constitutively expressed green fluorescent protein (GFP) were used to distinguish between host (GFP-CAM) and human cells from bone cylinders. As an alternative method to assess viability, primary cultures of human cells were derived from bone cylinders incubated on the CAM, *in vitro* or maintained at 4 ºC (negative control). Explant culture of freshly isolated bone cylinders (day 0) and GFP-CAM only tissue were examined as well for controls (Figure 4.2.4). See methods section 2.3.3 for more detail

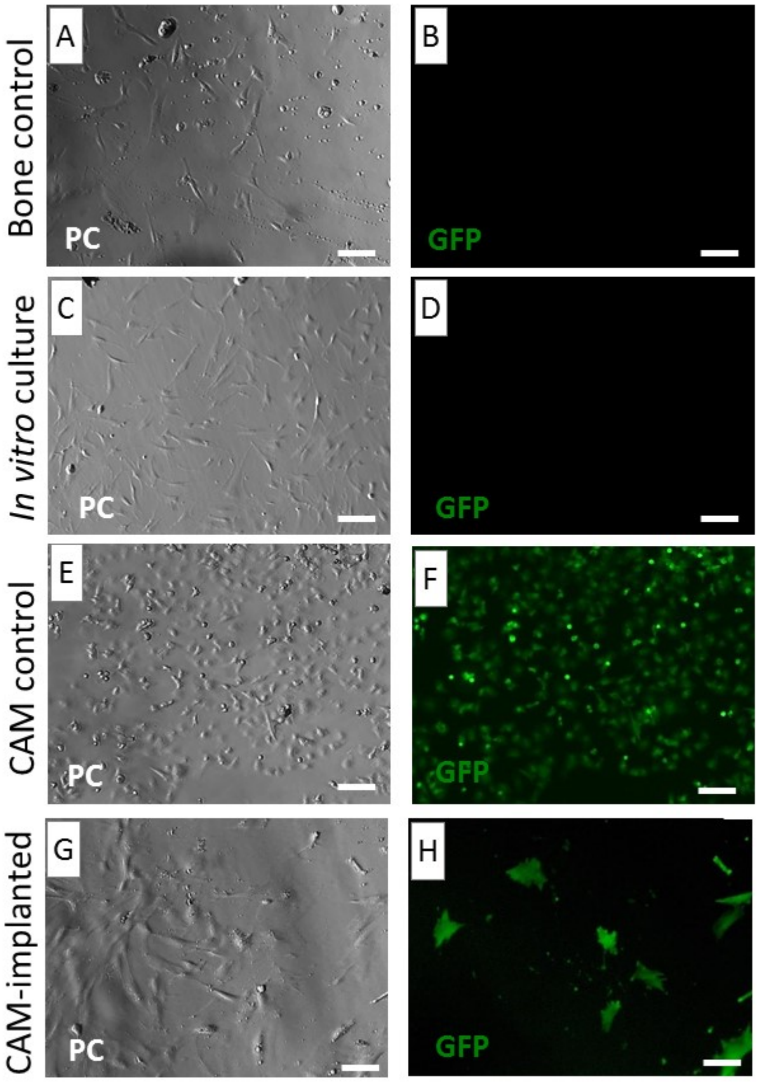

Figure 4.2.4: Cell outgrowth from bone cylinders explanted following CAM-implantation on GFP-chick embryos or *in vitro* culture. Bone cylinders were excised and explanted in tissue culture plastic at day 0 (bone control) (A-B), day 7 of *in vitro* culture (C-D) or day 7 of GFP-CAM implantation (G-H). Images representative from two independent experiments, n=3 cylinders per condition. CAM only tissue was also explanted at harvest as GFP control (E-F). All conditions were imaged following 15 days of explant culture using phase contrast (A, C, E and G) and fluorescence (B, D, F and H) to localize GFP+ cells. Phase contrast (PC), green fluorescent protein (GFP); Scale bars equivalent to 100 µm.

Initial cell outgrowth from explanted bone samples was evident both in the *in vitro* and CAM-implanted group after 9 days and 4 days, respectively. No cells were detected from the bone cylinders maintained at 4 ºC. Furthermore, no green fluorescence was observed in cells derived from the bone cylinders cultured *in vitro* (Figure 4.2.4 C-D) or bone control (Figure 4.2.4 A-B).

Both GFP+ and GFP- cells were present in the CAM-implanted treatment, demonstrating differences in the origin of the cells: avian and human (Figure 4.2.4 G-H). There were morphological dissimilarities in the appearance of GFP+ compared to GFP- cells. The GFP- cells showed a fibroblastic, spindle-like morphology in CAM-implanted and *in vitro* culture groups (Figure 4.2.4 C-D), as well as in the bone control samples explanted at day 0 (Figure 4.2.4 A-B). In contrast, chick GFP+ cells displayed a variable morphology and size (Figure 4.2.4 E-F, I-J). Cell outgrowth from GFP+ cells was evident in the CAM-only tissue (Figure 4.2.4 E-F) and CAM-implanted bone cylinders (Figure 4.2.4 G-H), however the number of cells was observed to start to reduce with a majority of GFP- cells growing in the well following the first week of explant culture. CAM heterogeneity was shown by the presence of (i) giant, round cells with several nuclei (ii) mononucleated large cells with multiple extensions or projections (iii) small and compacted cells (Supplementary Figure 7.3.1); the latter was the most abundant type and similar to Figure 4.2.4 E-F.

To confirm the human origin of the GFP- cells explanted from the CAM-implanted human bone cylinders, flow cytometry was used to examine the cells following immunostaining for Human Leukocyte Antigen (HLA). See methods section 2.3.3.1 for more detail.

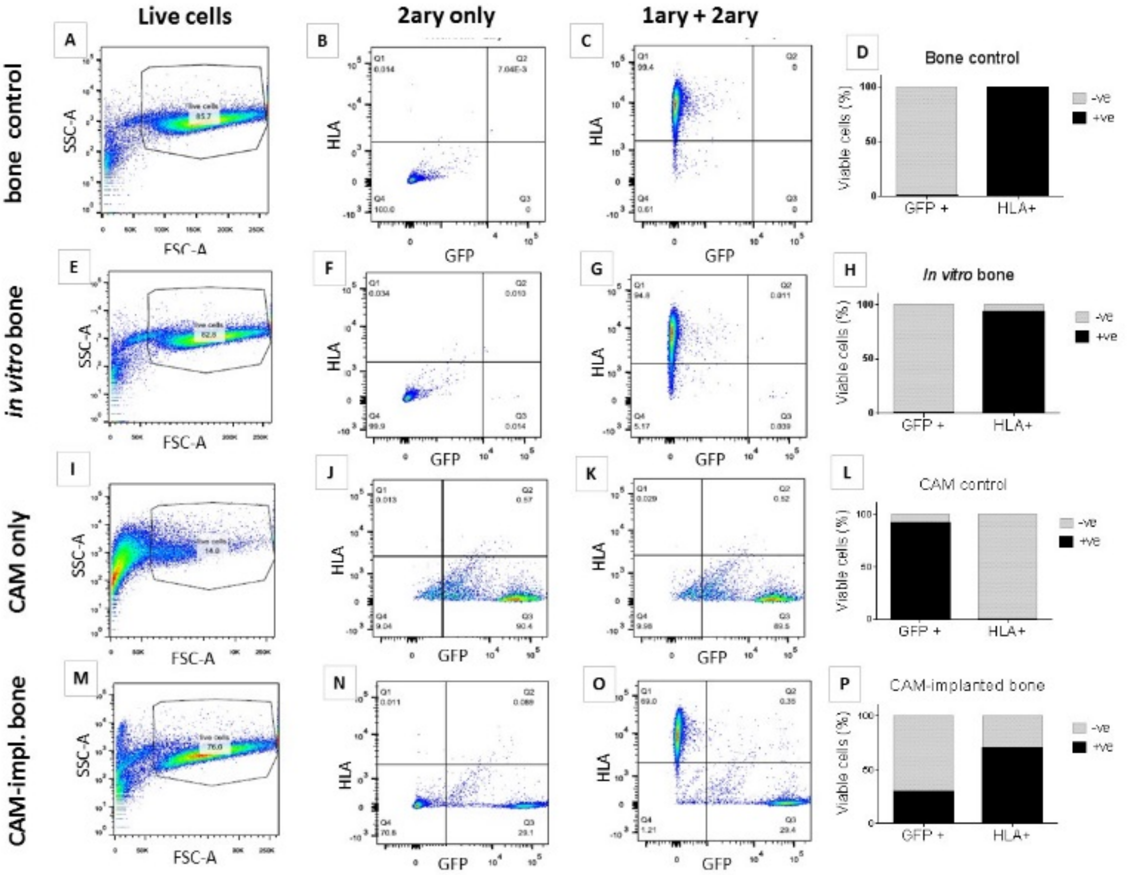

Figure 4.2.5: Human (HLA+) and avian (GFP+) cells present on CAM-implanted bone cylinders following FACS analysis. Bone cylinders were excised and explanted in tissue culture plastic at day 0 (bone control) (A-D), day 7 of *in vitro* culture (E-H) or day 7 of GFP-CAM implantation (M-P). CAM only tissue was also explanted at harvest as GFP control (E-H). Following 15 days of explant culture, cells were stained for a human specific marker (human leukocyte antigen, HLA) and FACS analysis was used to interrogate for HLA+ and GFP+ cell populations (C, F, I and L). The relative number of HLA+ and GFP+ from each treatment was quantified with respect to the number of all viable cells (D, H, L and P). Live cells gating (A, E, I and M) and secondary only control (B, F, J and N).

In agreement with the previous observations on cell outgrowth for CAM-explanted cells after long term culture, flow cytometry analysis showed 14 % of live cells (Figure 4.2.5 I), compared to the

76-86% displayed in the rest of the culture conditions (Figure 4.2.5 A, E and M). FACS analysis indicated the presence of a mixture of GFP+ cells and GFP- cells in the CAM-implanted samples after, with 29.75% GFP+ and 69.35% HLA+ (Figure 4.2.5 G, H). In all cases, GFP- cells stained positively for HLA, confirming their human origin. Bone control and *in vitro* culture groups showed >99.7% of GFP- and > 99% HLA+ cells (Figure 4.2.5 A-D, M-P). No HLA signal was detected on cells where the primary antibody was omitted (Figure 4.2.5 B, F, J and N).

Hence, these results indicate that human cells from human bone tissue remained viable after incubation on the CAM, supporting the concept that CAM incubation supports the sustained survival of explanted cells.

4.2.3 Evaluation of bone formation following CAM-implantation

The previous evaluation of the bone cylinders following CAM-implantation showed the presence of avian cells together with significant infiltration of avian tissue into the human marrow space. Additional investigation of the histological sections showed deposition of new collagen at the interface between the human and the avian tissue (Figure 4.2.6)

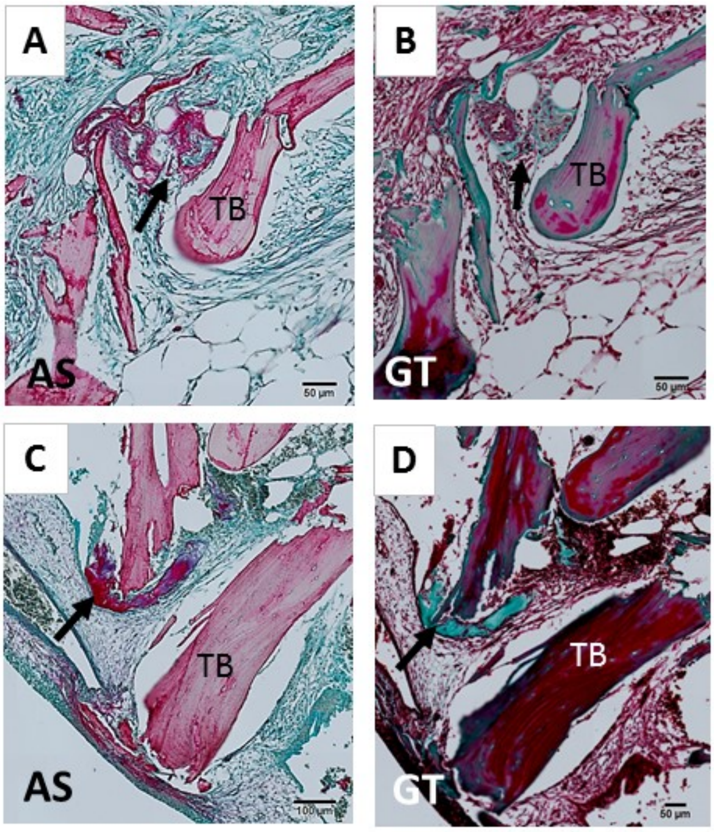

Figure 4.2.6: New collagen disposition on bone cylinders following CAM-implantation. Representative images from bone cylinders implanted on CAM, processed for histology and stained for Alcian Blue and Sirius Red (A and C) and Goldner's Trichrome (B and D). Arrows **indicate matrix deposition. Alcian Blue and Sirius Red (AS), Goldner's Trichrome (GT), trabecular bone (TB). See colour legend in Table 2.6.1. Scale bars equivalent to 100 µm (C-D) and 50 µm (A-B).**

Newly deposited collagen showed an intense pink-purple colour of the disorganised matrix on Alcian Blue and Sirius Red staining, compared to the lamellar pattern of the trabecular bone (see arrows Figure 4.2.6 B, D). The same structure displayed a green pigmentation indicative of collagen on Goldner's Trichrome staining, and again different from the red/purple colour of the mature bone (see arrows Figure 4.2.6 C, E). The organisation of the new collagen was also distinguishable from the CAM tissue given the loose cellularity and fibrous content of the avian membrane (Figure 4.2.6 A-D).

Extracellular matrix deposition on the implanted bone cylinders occurred in the proximity of pre-existing human trabecular bone, avian blood vessels and CAM tissue (Figure 4.2.6). In order to be able to quantify those qualitative changes at the histological level, high resolution computed tomography was used to evaluate the specific changes at the 3D level on the bone cylinders (Figure 4.2.7). See methods section 2.5.1 for more detail.

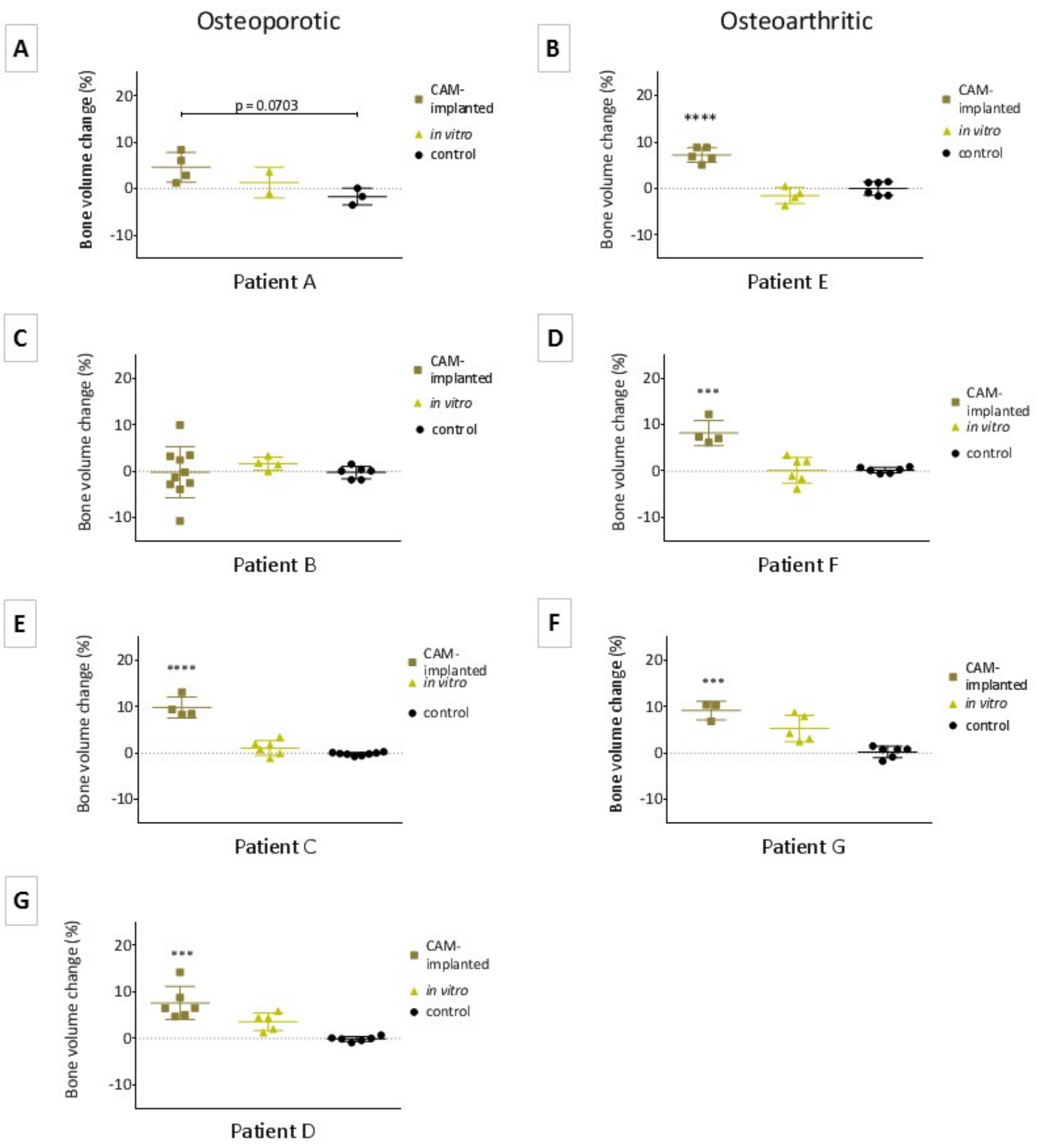

Figure 4.2.7: Bone volume significantly increased following bone cylinders implantation on CAM. Bone cylinders from osteoarthritic (B, D, F) and NOF# osteoporotic (A, C, E and G) patient femoral heads were µCT scanned under same settings before and after implantation on CAM, cultured *in vitro* for 7-9 days, or maintained at 4 °C for the same period as control. Data points indicate the relative bone volume change following incubation of each individual bone cylinder. Error bars indicate mean value ± SD, ***p<0.001, ****p<0.0001.

Seven independent experiments were conducted to evaluate the relative bone volume change in bone cylinders following *in vitro* culture, CAM-implantation, or maintained at 4 °C (control), including both osteoporotic (Figure 4.2.7, D and F) osteoarthritic (Figure 4.2.7A, C, E and G) femoral heads. In 5 out of 7 independent experiments, CAM-implanted bone cylinders showed a significant increase in bone volume (***p<0.001; Figure 4.2.7 B, D-G) compared to *in vitro* cultured and control. Average bone volume change was reduced for *in vitro* cultured bone cylinders (1.64 ± 0.74 SD) and negligible in the control (-0.25 ± 0.54 SD; Supplementary Table 7.3.1). Even if the bone volume increase following CAM-implantation was reproducible across most experiments, one patient was significantly different from the others (Supplementary Figure 7.3.3). F85 NOF# exhibited a decrease in bone volume change (-0.26 % ± 5.5 SD), compared to the average increase (7.77 % ± 1.8 SD) of the six other patients (Supplementary Table 7.3.1; Supplementary Figure 7.3.3), demonstrating patient variability.

Histological examination of CAM-implanted bone cylinders showed deposition of collagen matrix at the interface between human bone and avian tissue (see boxes in Figure 4.2.8 C-E). The new matrix deposition was arranged resembling chondrocyte lacunae with proteoglycan deposition within the cavities as indicated by Alcian Blue staining (see arrows Figure 4.2.8 C-D). Comparison between the histological cross-section and the equivalent µCT 2D slices showed that this new matrix did not attenuate X-rays significantly, indicative of the non-mineralised content (see boxes Figure 4.2.8 B).

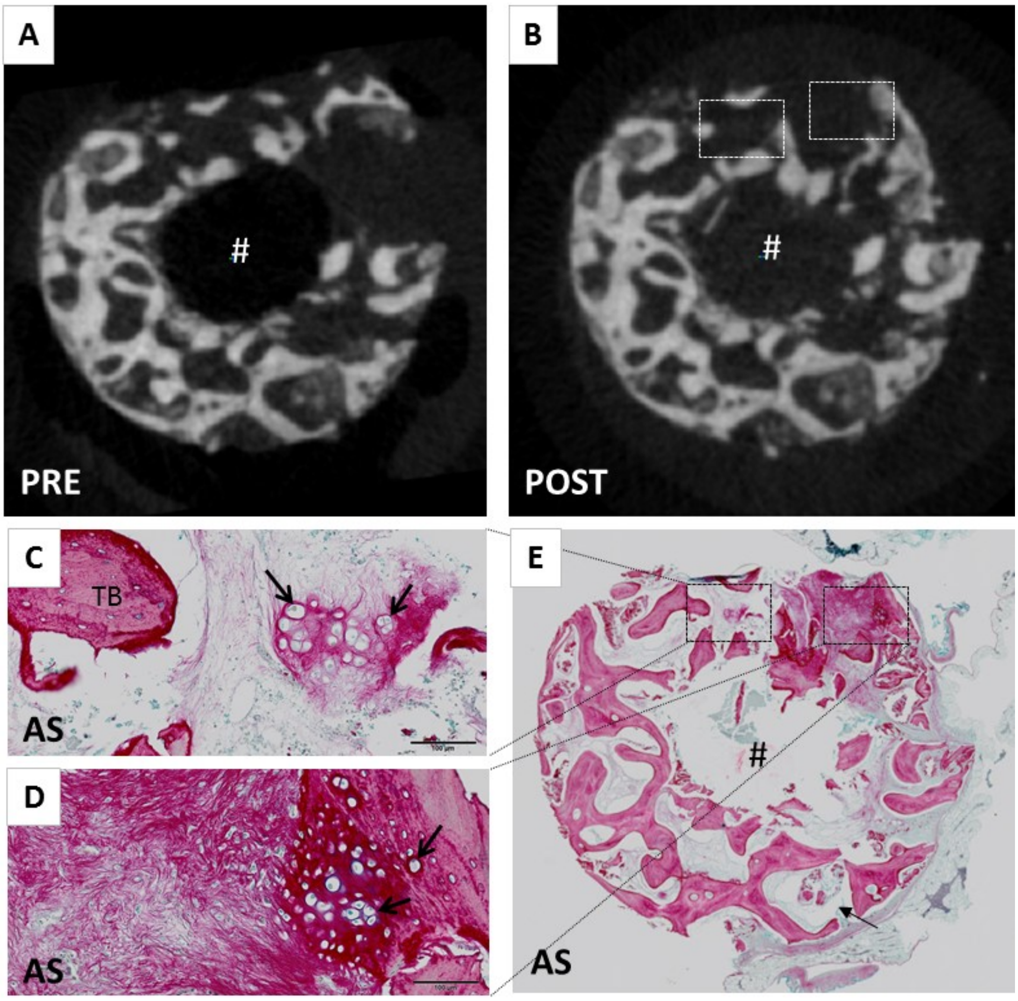

Figure 4.2.8: Endochondral-like matrix deposition following CAM-implantation of human bone cylinders. Bone cylinders were µCT scanned under the same settings (see methods section 2.5.1) before (A) and after (B) implantation on the CAM, followed by decalcification and paraffin processing. Histological sections were stained for Alcian Blue and Sirius Red staining (C-E) of the equivalent µCT cross-sections (A-B). Arrows indicate chondrocyte-like lacunae. Alcian Blue and Sirius Red (AS), trabecular bone (TB) # indicates bone defect region. Scale bars equivalent to 500 µm (A, D) and 50 µm (B, C, E).

To examine whether CAM-implanted bone cylinders were subject to bone resorption in addition to bone deposition, immunohistochemical detection of Cathepsin K, an enzyme secreted by active osteoclasts was conducted. A modified version of Masson's Tetrachrome was also used to observe differences between osteoid (deep blue) and mature bone (pink/orange; Figure 4.2.9).

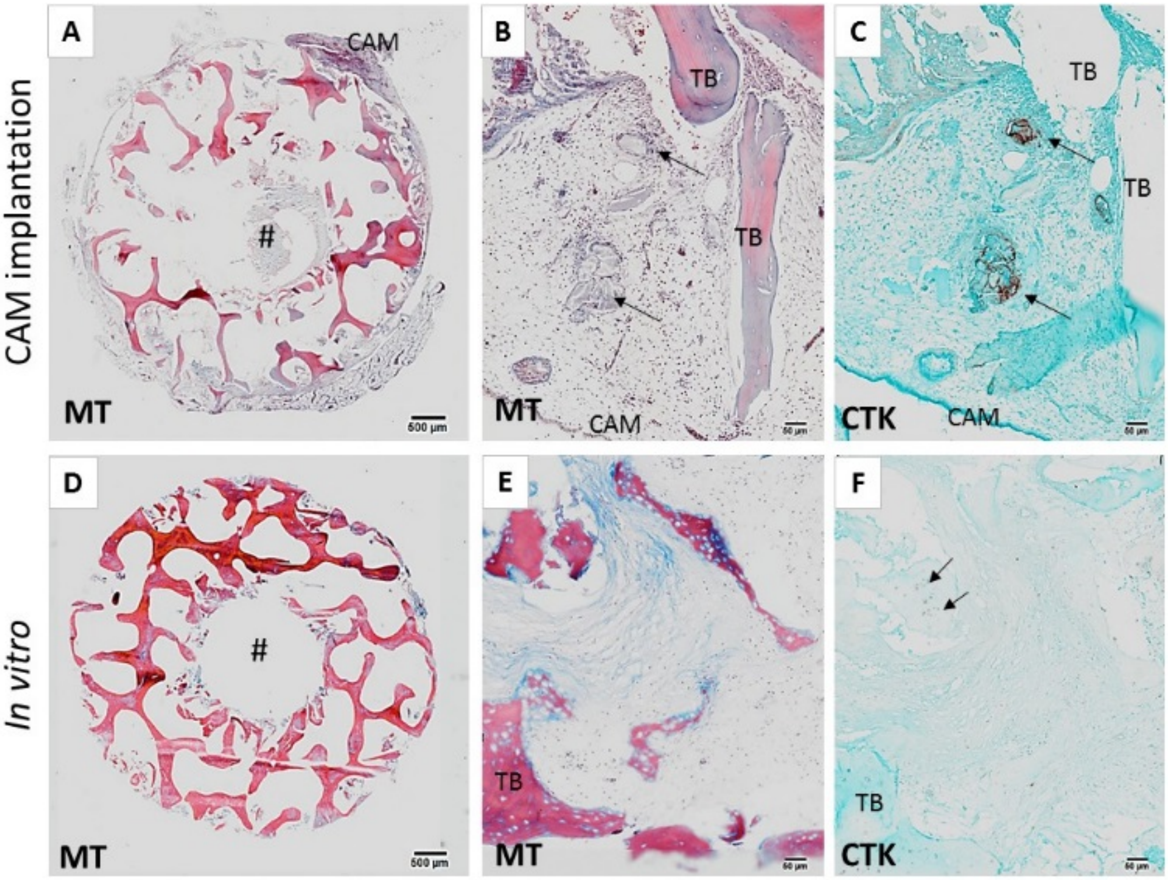

Figure 4.2.9: Osteoclast activity present on CAM-implanted but not in *in vitro* cultured human bone cylinders. Bone cylinders cultured *in vitro* (A-C) or CAM-implantation (D-F), followed by paraffin processing. Representative sequential histological sections were stained for Masson Tetrachrome staining where deep blue stains osteoid and bright red/orange mineralised bone (A, B, D and E) or Cathepsin K (CTK) immunostaining (C, F). Positive immunostaining in brown-red colour, counterstained with Alcian Blue to visualize the matrix content. Solid arrow indicate expression of osteoclast enzyme Cathepsin K. # indicates bone defect region. Masson's Tetrachrome (MT), trabecular bone (TB). Scale bars equivalent to 500 µm (A, D) and 50 µm (B, C, E, F).

Generally, Cathepsin K expression was present on the CAM-implanted bone cylinders (Figure 4.2.9 C), and negligible on the *in vitro* cultured ones (Figure 4.2.9 F). The location of the osteoclast activity in the CAM-implanted bone cylinders corresponded to the trabecular bone debris entrapped within the CAM tissue (see arrows Figure 4.2.9 C), and the same region co-localised with osteoid matrix stained in light blue on Masson's Tetrachrome staining (see arrows Figure 4.2.9 B). Expression of Cathepsin K co-localised with GFP immunostaining on consecutive sections, indicating the avian origin of the bone resorbing cells (Supplementary Figure 7.3.4). These results indicate that culture of human bone using the CAM assay allowed for bone formation as well as bone resorption.

Further histological examination of bone cylinders following CAM-implantation showed extensive deposition of matrix, again located on the interface between human and avian contact (Figure 4.2.10). Alcian Blue and Sirius red staining showed matrix deposition around trabecular bone debris, as shown by the pink colour of the lamellar fragments (Figure 4.2.10 A). Collagen type I immunostaining was identified in the trabecular bone and bone debris (see arrows Figure 4.2.10 C), whereas collagen type II was observed only around bone debris and not in the lamellar bone (see arrows Figure 4.2.10 B). Avian cells from GFP-CAM were identified in the region of matrix deposition, co-localising with the collagen type II staining (see arrows Figure 4.2.10 B, D). Additional examples of co-localisation of matrix deposition and avian cells are shown in Supplementary Figure 7.3.5 A-E. No matrix deposition or GFP expression was found in *in vitro* cultured bone cylinders (Supplementary Figure 7.3.5 F-J)

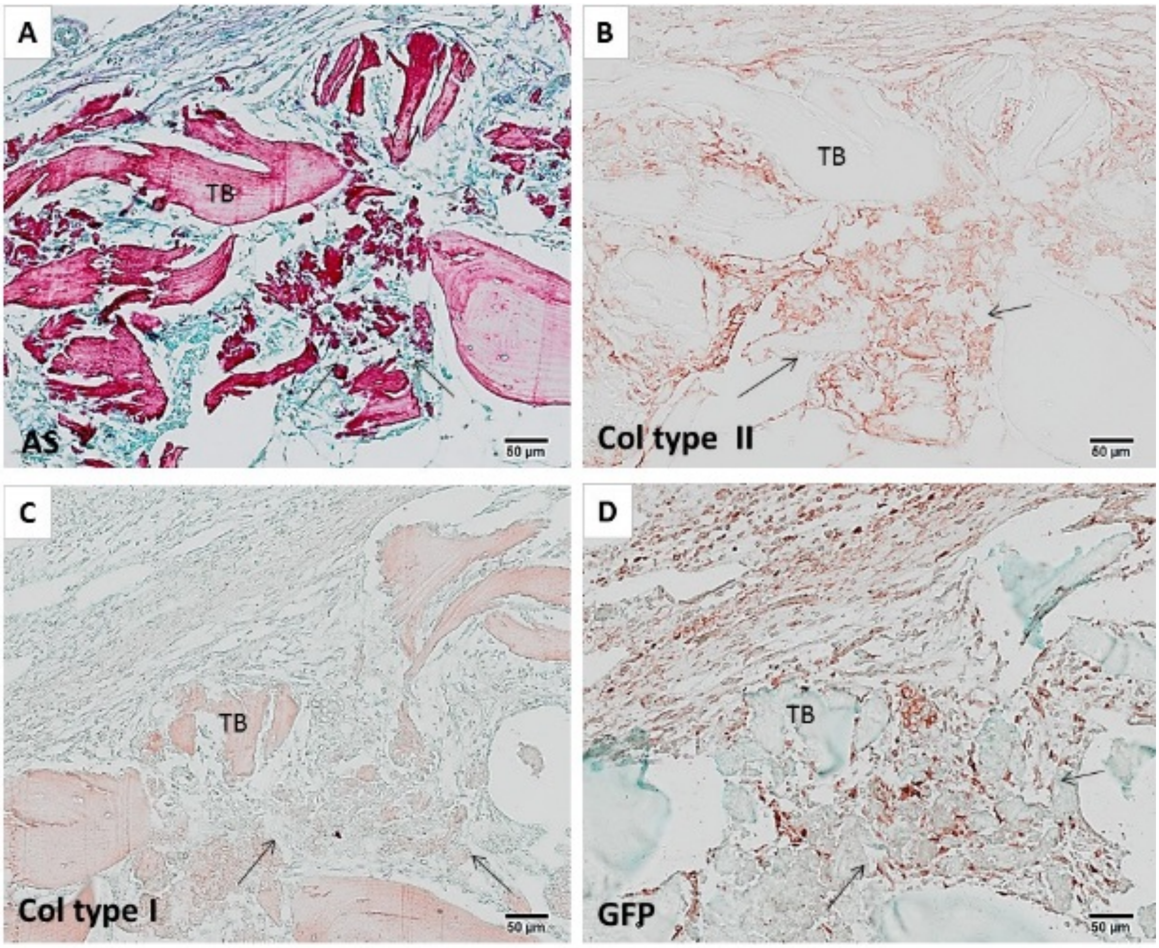

Figure 4.2.10: Extracellular matrix deposition co-localised with avian cells (GFP+) following CAM-implantation of human bone cylinders. Bone cylinders were implanted on CAM and processed for paraffin histology. Representative consecutive sections were stained for Alcian Blue and Sirius Red, and immunostained for collagen type II (B), collagen type I (C) and GFP (D). Positive immunostaining in brown-red colour, counterstained with Alcian Blue to visualize the matrix content. Arrows indicate areas of new matrix deposition. Alcian Blue and Sirius Red (AS), Goldner's Trichrome (GT), chorioallantoic membrane (CAM), trabecular bone (TB). Scale bar equivalent to 50 µm.

In addition to collagen deposition, cellular aggregations were observed only on the CAM-implanted bone cylinders; these condensations were composed of tightly packed cells aligned concentric, forming different shapes or structures within the CAM tissue. Figure 4.2.11 A shows an example of cell condensations formed in the periphery of the bone cylinder, surrounded by type II collagen (Figure 4.2.11 D). Cell condensations expressed high levels of a marker of endochondral formation Sox9 (cartilage) and Runx2 (bone) (Figure 4.2.11 F-G), which co-localised with GFP immunostaining (Figure 4.2.11 C), identifying their avian origin.

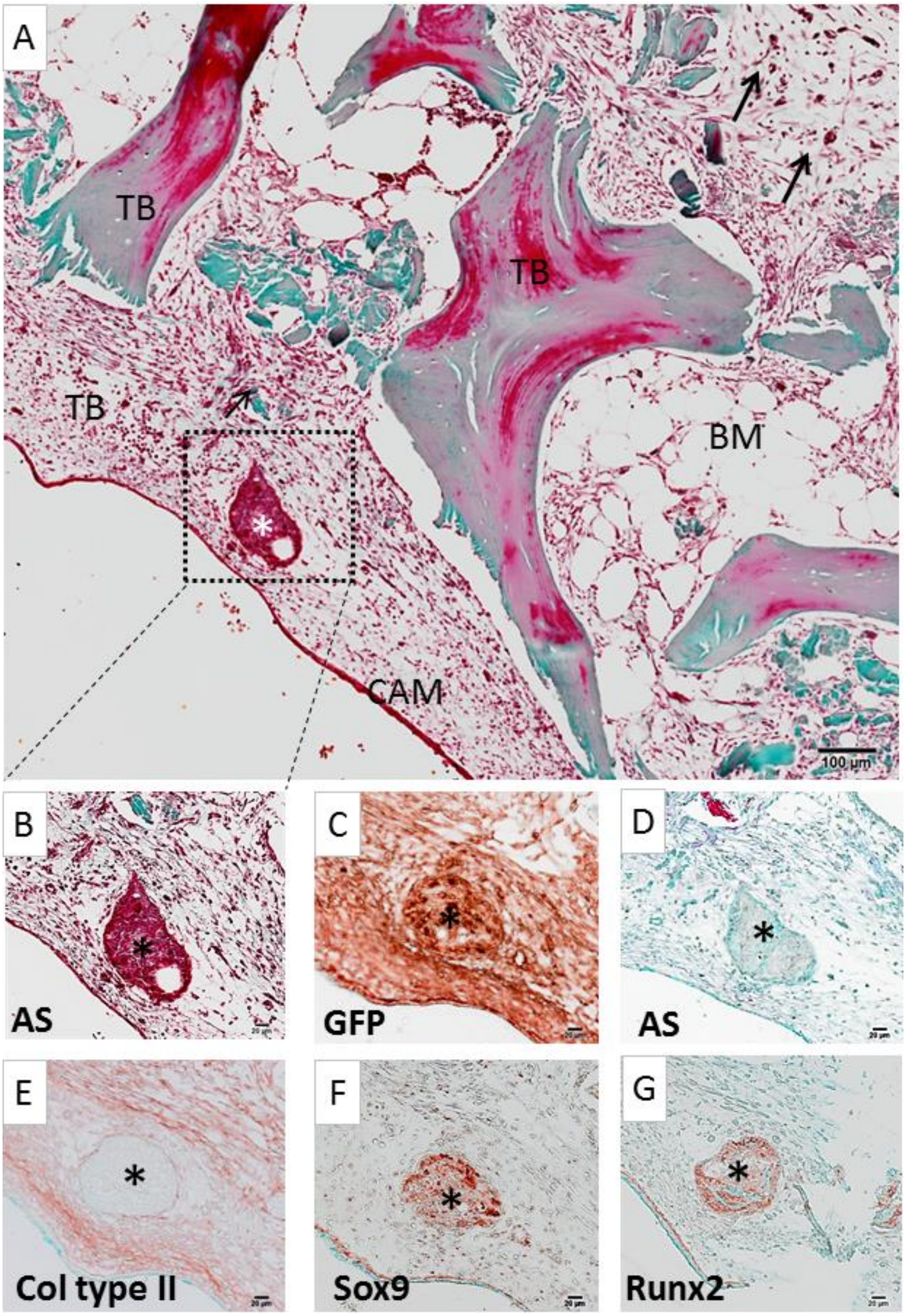

Figure 4.2.11: Endochondral cell condensation formation in the CAM following human bone cylinder implantation. Representative images of bone cylinders implanted on the CAM for one week and then processed for paraffin histology. Low magnification image shows the peripheral location of cell condensation in the CAM stained for GT (A-B). Cell condensation images at higher magnification stained for AS (D) and immunohistochemistry for GFP (C), Collagen type II (E), Sox9 (F) and Runx2 (G). Positive immunostaining in brown-red colour, counterstained with Alcian Blue to visualize the matrix content. Arrows indicate blood vessels in the CAM; *indicates cell condensations. See colour legend in Table 2.6.1. Chorioallantoic membrane (CAM), human bone marrow (BM), human trabecular bone (TB), Alcian Blue and Sirius Red (AS), Goldner's Trichrome (GT). Scale bar equivalent to 100 µm (A) and 20 µm (B-G).

An example of the diversity of cell condensations is shown in Figure 4.2.12, where various structure and shapes are shown in relative proximity. The difference in morphology from cell condensations: oval and small compared to the large and irregular shaped can be clearly observed (see arrow heads and asterisks, respectively Figure 4.2.12). Again, GFP immunostaining indicated the avian origin of the cell condensations (see arrow head and asterisks Figure 4.2.12 B)

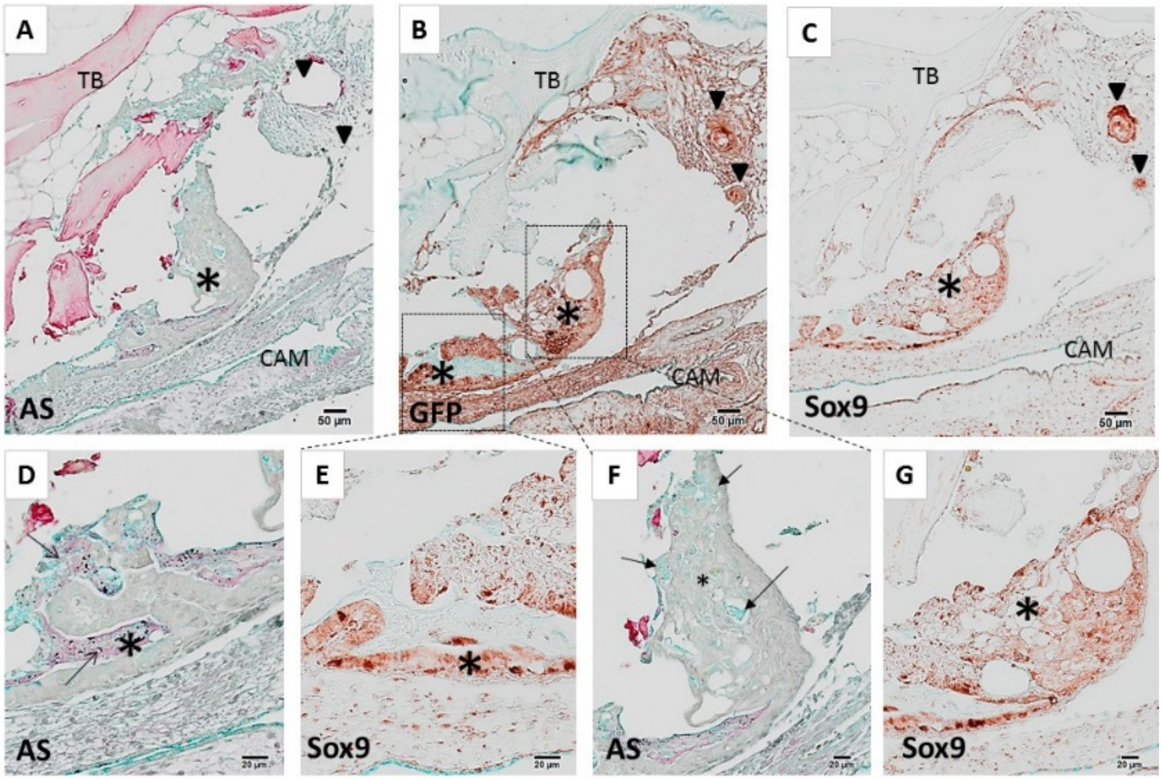

Figure 4.2.12: Collagen and proteoglycan deposition around diversity of cell condensations. Representative images of bone cylinders implanted on the CAM and then processed for paraffin histology and stained for Alcian Blue and Sirius Red staining (A, D and F), and immunohistochemistry for GFP (B) and Sox9 transcription factor (C, E and G). Positive immunostaining in brown-red colour, counterstained with Alcian Blue to visualize the matrix content. Arrows indicate matrix deposition, asterisk and arrow head indicate cell condensations of different morphology. Chorioallantoic membrane (CAM), human trabecular bone (TB), Alcian Blue and Sirius Red (AS), Goldner's Trichrome (GT). Scale bar equivalent to 50 µm (A-C) and 20 µm (D-G).

Cell condensations were identified in Alcian Blue and Sirius Red staining because of their structurally different features from CAM stroma and bone tissue (Figure 4.2.12 A, D, F), as well as by the expression of Sox9/Runx2 in the same location (Figure 4.2.12 C-G). Deposition of cartilaginous-collagen matrix surrounding the condensation was evident, as well as the proteoglycan content within cell condensation cavities (see arrows Figure 4.2.12 D, F). Additional examples demonstrating the diversity of shapes and morphologies of cell condensations formed on CAM-implanted bone cylinders can be seen in Supplementary Figure 7.3.6.

In summary this data showed that CAM-implantation resulted in significant increase in bone volume, accompanied by formation of endochondral cell condensations (Sox9+/Runx2+) and expression of osteoclast markers (Cathepsin K) on the human bone cylinders.

4.2.4 Extension of the CAM model – Strategies for prolonged culture

Bone cylinders were extracted from freshly isolated human femoral heads preserving their structure and cellular content, as detailed in methods section 2.2.1. Previous results showed that the bone marrow of the cylinders became vascularised by the avian blood vessels, as indicated by the presence of fusiform nucleated chick erythrocytes (Figure 3.2.10 and Figure 3.2.11). On one occasion, a blood vessel containing both nucleated (chick) and enucleated (human) erythrocytes was observed (Figure 4.2.13).

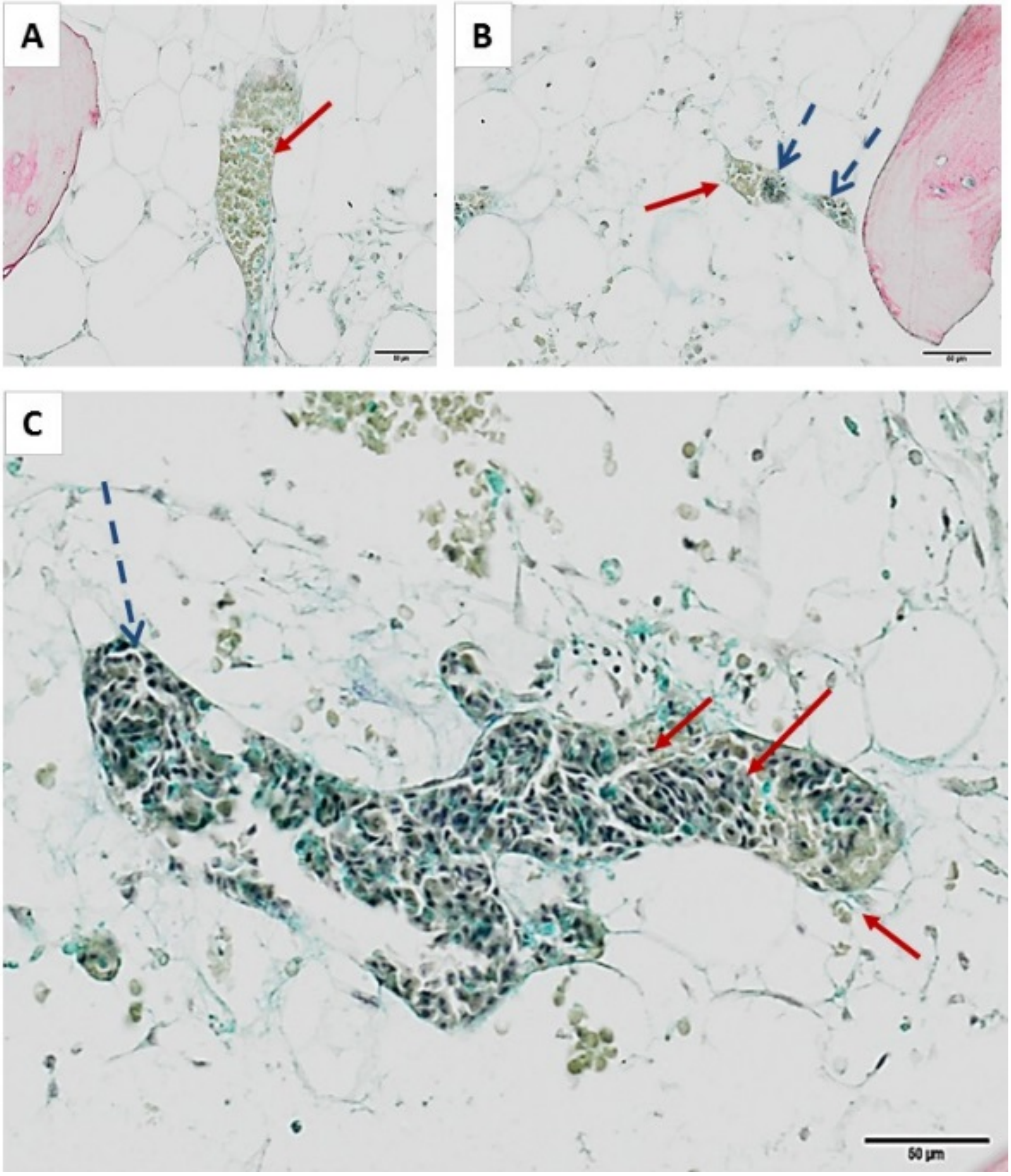

Figure 4.2.13: Anastomosis between human and chick vasculature following CAM-implantation of bone cylinders. Bone cylinders were implanted on CAM, processed for paraffin histology and stained for Alcian Blue and Sirius Red. Dashed arrows indicate avian nucleated erythrocytes, solid arrows indicate enucleated erythrocytes. Scale bar equivalent to 50 µm.

On the same bone cylinder, presence of human (see solid arrow Figure 4.2.13 A, B) and avian (see dashed arrow Figure 4.2.13 B) blood vessels were identified on the CAM-implanted bone cylinders. The proximity of the human and avian capillaries was evident in Figure 4.2.13 B. A possible union of the human and avian circulatory system was observed in Figure 4.2.13 C, showing a vessel carrying both nucleated and enucleated erythrocytes. These results indicate evidence of anastomosis between human and avian blood vessels.

Given that the short CAM implantation period (7-9 days) was a limitation in the study of new bone tissue formation, an attempt was made to extend the incubation time by doing a double CAM experiment. A pilot study was design to evaluate the bone volume changes of bone cylinders implanted in two consecutive CAMs (double CAM). In more detail, freshly isolated bone cylinders were implanted on a GFP-CAM for 9 days, harvested and then implanted on a wild type CAM for an additional 7 days. µCT scans were conducted after each time point and bone volume change was measured with respect day 0 (Figure 4.2.14).

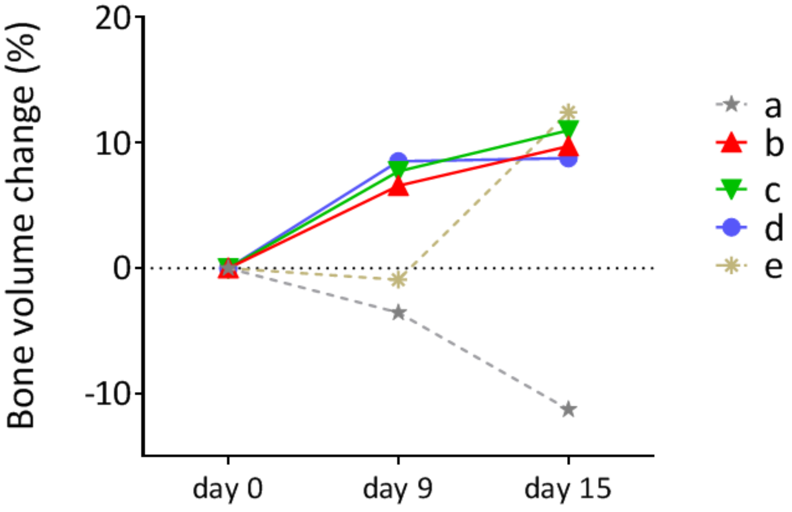

Figure 4.2.14: Bone volume relative change of bone cylinders implanted on a double CAM. Bone cylinders (n=5; a-e) from the same femoral head were implanted for 9 days on GFP-CAM. At harvest, only viable and integrated bone cylinders were cultured *in vitro* overnight to be implanted on a second CAM (wild type) for an additional 7 days incubation. Identical settings for µCT scanning and analysis were used for the three time points. Data points indicate the relative bone volume change with respect day 0 for each individual bone cylinder (a-e). Dashed lines indicate non-integrated or non-viable bone cylinders on the second CAM. Solid lines indicate viable and integrated bone cylinders on the second CAM.

All chick embryos from the first CAM developed, and integrated the graft on CAM, as inspected at harvest. Bone volume change at day 9 showed an increase in samples B-D (7-9 % BV) in a similar fashion as previously reported (Figure 4.2.7), however sample A and E did not show any increase Figure 4.2.14. Harvest of cylinders on the second CAM showed chick viability on samples B-E, whereas chick embryo of sample A did not develop. In accordance, cylinders B-E showed a continued increase in bone volume following second CAM (10-11 % BV), whereas cylinder A showed a decrease (Figure 4.2.14).

Histological examination of the bone cylinders after harvest of the second CAM showed integration between the two membranes (Figure 4.2.15). GFP immunostaining identified the avian cells original from the first membrane (Figure 4.2.15 A), whereas non-GFP cells correspond to the second CAM. Notice the integration of the two sequential membranes, GFP located on the interior and non-GFP located on the exterior.

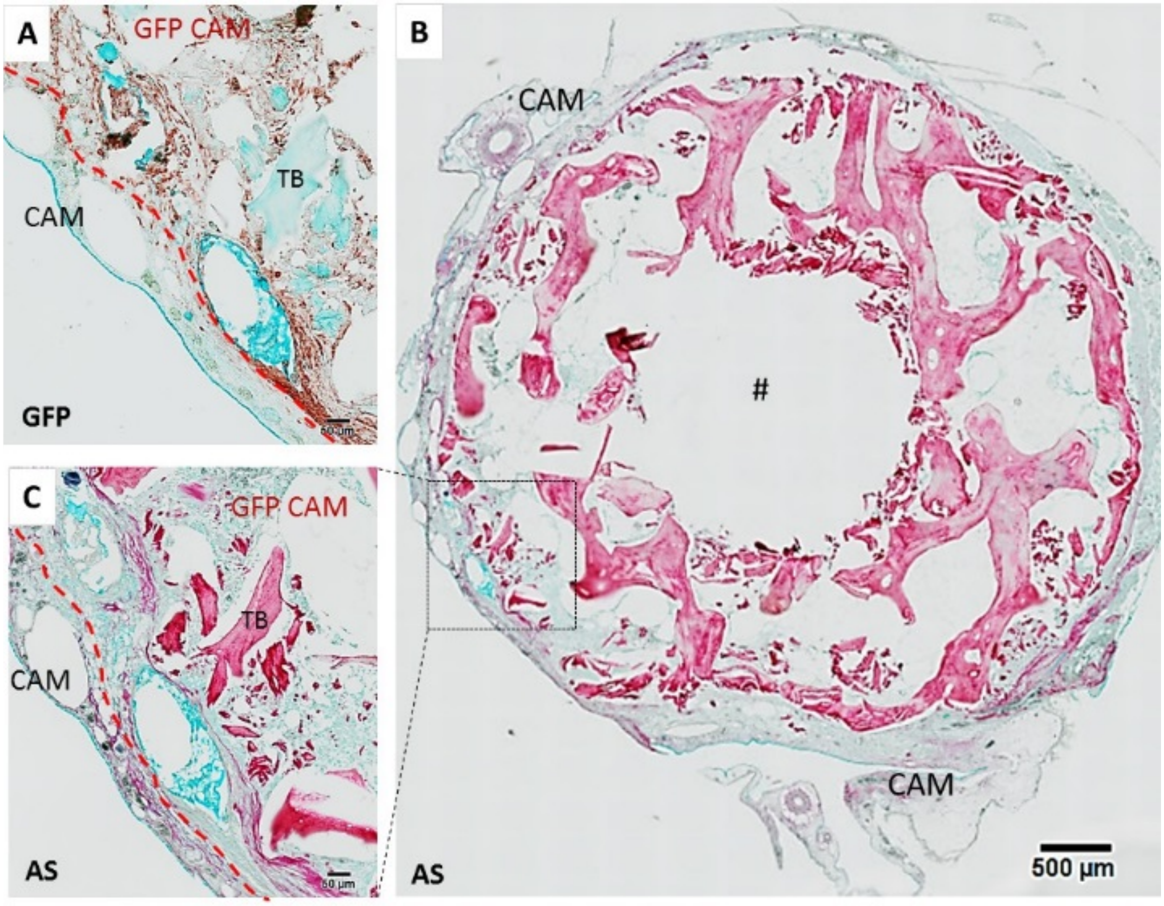

Figure 4.2.15: Distinction between first and second CAM on human bone cylinders following double CAM implantation. Representative images of bone cylinders implanted for 9 days on GFP-CAM, harvested and implanted on a second CAM (wild type) for an additional 7 days incubation. Consecutive paraffin sections were stained for Alcian Blue and Sirius Red (B, C) and immunohistochemistry for GFP (A). Positive immunostaining in brown-red colour, counterstained with Alcian Blue to visualize the matrix content. # indicates bone cylinder defect region. Dashed line indicates separation between first (GFP-CAM) and second (CAM) tissue. chorioallantoic membrane (CAM); green fluorescent protein transfected CAM (GFP-CAM), human trabecular bone (TB), Alcian Blue and Sirius Red (AS). Scale bar equivalent to 50 µm (A, C) and 500 µm (B).

Additional examples of the integration between both CAMs are shown in Figure 4.2.16. The dashed line separates the initial GFP-CAM from the wild type CAM. In addition, GFP expression was observed in regions of the wild type CAM (see arrows Figure 4.2.16 A), indicative of the fusion between both membranes.

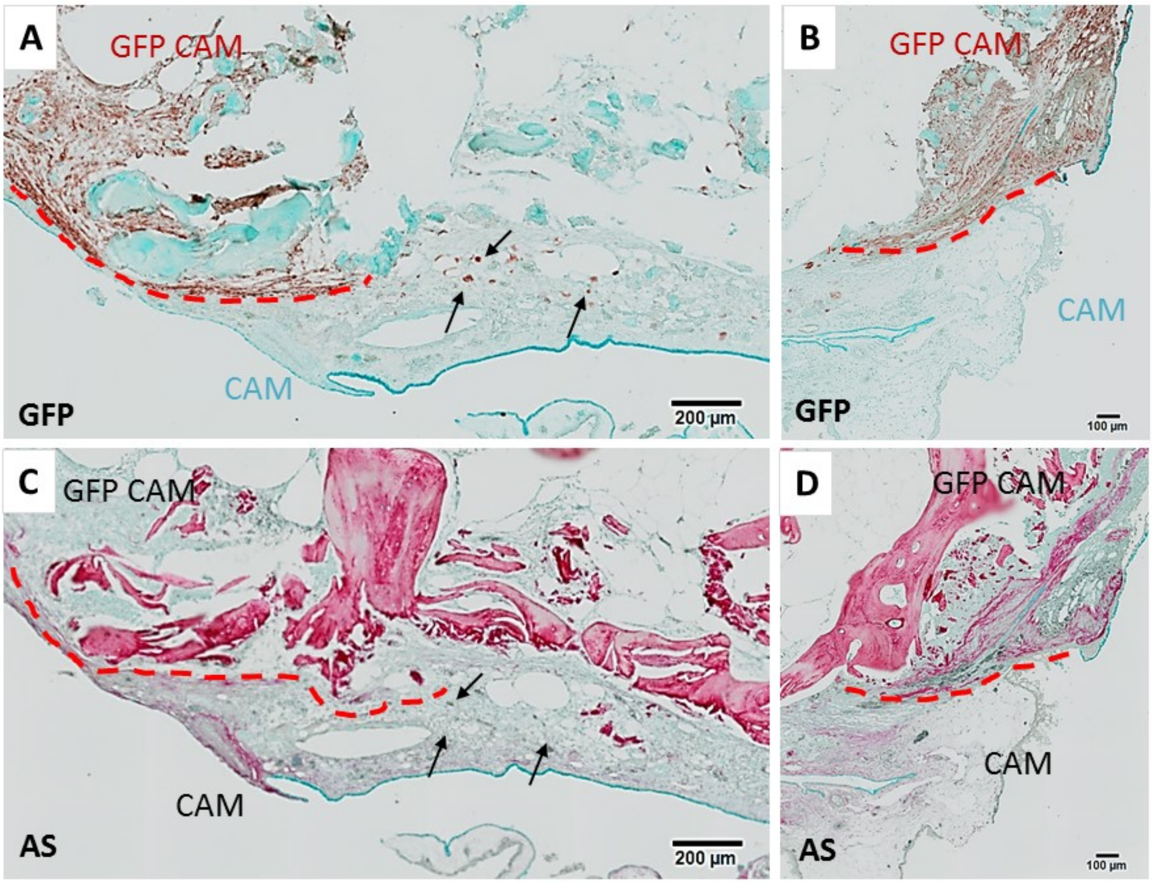

Figure 4.2.16: Integration of sequential CAMs from implanted human bone cylinders. Bone cylinders implanted for 9 days on GFP-CAM, harvested and implanted on a second CAM (wild type) for an additional 7 days incubation. Consecutive paraffin sections were stained for Alcian Blue and Sirius Red (C, D) and immunohistochemistry for GFP (A, B). Positive immunostaining in brown-red colour, counterstained with Alcian Blue to visualize the matrix content. Dashed line indicates separation between first (GFP-CAM) and second (CAM) tissue. Arrows indicate GFP expression within WT membrane. chorioallantoic membrane (CAM); green fluorescent protein transfected CAM (GFP-CAM), human trabecular bone (TB), Alcian Blue and Sirius Red (AS). Scale bar equivalent to 50 µm (A, C) and 500 µm (B).

Thus, these results indicate the potential of performing a double-CAM in the interests of extending the incubation time to allow for tissue regeneration, as noted by the integration occurring between the CAM tissue from different chick embryos.

4.3 Discussion

The aim of this chapter was to evaluate the CAM as an *in vivo* model for the culture of human, living bone tissue. In brief, the current study has demonstrated the potential of the CAM as an *in vivo* bioreactor for the culture of human living bone tissue providing a surrogate blood supply. In summary, the main findings of the present chapter were:

- Perfusion of human tissue by the CAM vasculature was evident by macroscopic and microscopic evaluation, with extensive penetration of avian capillaries into the human bone tissue.
- Human tissue was observed to remain viable after cultivation on the CAM membrane, similar to human bone cultured *in vitro* for the same period.
- CAM-implantation of bone cylinders elicited new extracellular matrix deposition, resorption and formation of endochondral cell condensations in the human tissue.
- The previous histological observations were further validated using µCT, which showed a significant increase in the bone volume ($p<0.001$) after 7-9 days incubation on the CAM.

To our understanding, this is the first report of the culture of viable human bone tissue on the CAM and implements µCT analysis to examine tissue regeneration. A previous study has implanted fresh human bone on the CAM and examined the angiogenic response of the bone chips after each stage of the allograft banking procedure (Holzmann *et al.* 2010). The authors did not report invasion of avian blood vessels in the graft and showed minimal CAM-integration of isolated bone debris (Holzmann *et al.* 2010). In contrast, here we have shown the infiltration of CAM blood vessels through the human bone tissue with extensive integration of the entire bone cylinder. These striking differences compared to the present study could be explained by i) the length of the CAM-implantation period (2 days by Holzmann *et al.* (Holzmann *et al.* 2010) compared to 7-9 days in this investigation) and, ii) dissimilarities in the methodology (*i.e.* bone extraction, CAM assay). Another study used the CAM assay to evaluate the invasive potential of musculoskeletal sarcomas (Sys *et al.* 2012). In the previous publication, the connection between the graft and the host vasculature (anastomosis) was described (though not shown) by the presence of both nucleated and enucleated erythrocytes on the same capillary (Sys *et al.* 2012). In agreement with the work of Sys *et al.* the present study found evidence to support the vascular connection between the human and the avian blood vessels present in the marrow space of the bone tissue (Figure 4.2.13), however not in a reproducible manner.

The potential of this human-avian system to study bone regeneration was evidenced by the viability of human cells following GFP-CAM implantation. Human (GFP-/HLA+) cell outgrowths displayed a spindle-like and elongated shape morphology, typical of skeletal cells (Kern *et al.* 2006). *In vitro* treated bone cylinders demonstrated similar cell morphology after explant culture. Interestingly, cell outgrowth from the bone tissue was observed to be slower (4 days) compared to cell outgrowth from CAM-implanted cylinders (9 days). The previous dates refer to the first observation of cells sprouting out from explanted bone cylinders. A potential explanation would be that CAM growth impacted on the autologous human tissue, resulting in i) greater cell survival as a consequence of increased nutrient supply and ii) enhanced cell outgrowth as a result of matrix remodelling, which was not seen *in vitro*. Thus, the cell response from the human bone grafts was enhanced following CAM-implantation in comparison to *in vitro* culture. Future experiments following this research will consider examining expression of cell markers, proliferation and differentiation potential of those cells to further understand the effect of CAM-implantation on the autologous cell from the bone cylinder.

Remarkably, formation of cell condensations strongly expressing Sox9 and Runx2 protein, essential transcription factors for endochondral bone formation (Akiyama *et al.* 2002), were observed in the CAM tissue in proximity to the human bone cylinder and new matrix deposition (Figure 4.2.11). Moreover, these cells also co-stained with GFP, confirming their avian origin. Similar cell condensations have been reported in studies which implanted living bone tissue from various origins or delivered BMP into the CAM (Hancox 1946; Ramoshebi and Ripamonti 2000). In addition, new matrix deposition was observed in the CAM-implanted bone cylinders, however this newly formed collagen appeared faintly under the X-rays, probably due to its early stage, osteoid-like composition (Figure 4.2.8). All those observation at the histological level (formation of endochondral cell condensations and new matrix deposition) were absent in the *in vitro* cultured cylinders, demonstrating again their CAM origin. In agreement with those findings, μCT analysis showed a significant increase ($p<0.001$) in bone volume on the CAM-implanted cylinders compared to the *in vitro* culture group (Figure 4.2.7), supporting the observation of new bone or cartilage formation occurring on the CAM.

The results of the current study set out the hypothesis that the changes in bone volume were driven by: i) the deposition of new low density matrix, possibly through CAM-derived ectopic bone formation, as evidenced by the histology (Sox9 and Runx2 cell condensations); and ii) mineralisation of the pre-existing trabecular bone. It is important to consider that less than 24 hours before *in vivo* implantation, those bone cylinders were involved in a certain stage of a bone remodelling cycle within the human organism. Hence, it is likely that this already on-going process could have been maintained and/or boosted upon implantation on the CAM; indeed it is well known that the CAM performs the calcium transport from the egg-shell to the chick embryo to allow for skeleton mineralisation. Not only new matrix/mineral deposition but also bone resorption, Cathepsin K expression, was observed on the CAM-implanted bone cylinders (Figure 4.2.9). This was not unexpected given that the osteoclastic potential of the CAM has been previously established in the literature (David M. Webber 1990). These results support the conclusion that the CAM assay provides a unique vascular component in which bone tissue formation and resorption (hence bone remodelling) can be evaluated *in vivo*. Future experiments will consider the implementation of mineralised tissue processing to test those options, limited in the current study by decalcification required on the paraffin processing.

Curiously, few experiments showed patient-dependent variable response compared to the standard increase in bone volume for CAM-implanted bone cylinders (Supplementary Figure 7.3.3). There was no pattern or observed effect associated with patient gender, age or phenotype (osteoarthritic or osteoporotic). Indeed, it is well-known that patient derived cells exhibit variable gene expression and proliferation potential (Georgi *et al.* 2015). In contrast, a study evaluating gene expression from patient-derived osteoblast cells showed that osteoarthritic phenotype expressed higher levels of VEGF compared to osteoporotic and healthy derived osteoblast (Neve *et al.* 2013). It might be likely that the CAM-bone tissue response is affected by the particular medical conditions (metabolic disease, smoker, drug treatment, etc.) of each patient. Hence, access to the full medical records of the donors (considering ethical approval and informed patient consent) would have provided further crucial insights on establishing the cause of the patient-specific observed effects.

As opposed to the significant increase in bone formation observed on the CAM-implanted bone cylinders, minimal changes were observed on the *in vitro* culture group (Figure 4.2.7). This was despite the observation of a similar level of cell outgrowth and cell viability after the incubation period (Figure 4.2.4). In contrast, Kanczler *et al.* reported substantial mineralisation of early stage chick femurs following 10 days organotypic culture (Kanczler *et al.* 2012). This mineralisation process occurred in the absence of blood vessel supply; however the incubated tissue was a healthy and rapidly growing embryo organ. The present study evaluated bone from elderly patients with either osteoarthritis or osteoporosis, which is likely to grow significantly more slowly than embryonic bone and probably present altered metabolic (catabolic) profile.

Given that most *in vivo* studies start to observe mineral deposition 14 days post-fracture (Shah *et al.* 2014; Yuasa *et al.* 2014), extended incubation periods were required to shed more light on this CAM-human model. To do so, a pilot double CAM study was conducted, showing a continued increase in bone volume following 15 days of *in vivo* implantation (Figure 4.2.14). Histological analysis showed the good interaction between first and second CAM, as shown by the GFP+ cells within the wild type CAM (Figure 4.2.15 and Figure 4.2.16). In support of those findings, Ausprunk *et al.* described complete integration and revascularisation of CAM tissue implanted onto a host CAM (Ausprunk *et al.* 1975). More experiments including greater sample size as well as an *in vitro* culture group as a control for the second CAM would be required to draw definite conclusions. However, the integration of the two CAM at the histological level (Figure 4.2.16) holds great promises on the potential of this novel approach, not used before for tissue engineering in the literature.

In conclusion, this chapter has demonstrated the ability of the CAM to maintain the viability of the human bone cylinders and provide them with a surrogate blood supply. Moreover the effects of the CAM-implantation were noticeable at the histological and at the µCT level, indicating the prospective of using this human-avian model to test biomaterials.

Chapter 5: Results Part III. Evaluation of biomaterials using the CAM

5.1 Introduction

5.1.1 Three-dimensional (3D) registration for µCT analysis

In the previous Chapter it has been shown that CAM-implantation of human bone cylinders results in a significant bone volume increase determined by µCT and histological analyses. However, given the dynamic nature of bone in which changes can include both bone deposition and bone resorption, there is a need to find new approaches focused on uncoupling both processes from a single output (*i.e.* measurement on the X-ray scan). Superposition of two or more sequential scans (named 3D registration) to identify separately the areas of bone formation and resorption, has been described in several studies (Birkhold *et al.* 2014; Schulte *et al.* 2011; J. H. Waarsing *et al.* 2004). 3D registration would be particularly relevant in this project as a mean to visualise the positive changes in the bone volume of the cylinders following CAM-implantation, described in the previous chapter. Importantly, this approach would bypass one of the limitations of this study: the inability to differentiate pre-existing bone from newly formed mineralised tissue. In order to understand the advantages and limitations of 3D registration, the next section will discuss this method in more detail.

In the medical field, there has been a need for registering consecutive CT, PET or MRI scans from the same patient for disease diagnosis and prognosis (Jaffray and Siewerdsen 2000; Kitamura *et al.* 2002; Smitsmans *et al.* 2005). In both medical scans and in bench-top *in vivo* scanners, registration of sequential animal scans has also been explored (Birkhold *et al.* 2014; Lambers *et al.* 2015; J. H. Waarsing *et al.* 2004). 3D registration comprises the rotation and translation of one of the two scans so it overlaps the other, matching their geometry and structure with minimal error. The registration of two scans consists of an iterative process to find the best matching/fit between two scans and, irrespective of the precision achieved, it is invariably not perfect and hence includes a certain degree of error. Various registration approaches based on different computational algorithms have been designed in order to improve the outcome of the matching process (Boyd *et al.* 2006; P. Thévenaz, U.E. Ruttimann 1998; J. H. Waarsing *et al.* 2004). Those studies tested the reproducibility and accuracy of their registration method by scanning unchanged bone tissue multiple times (Boyd *et al.* 2006; P. Thévenaz, U.E. Ruttimann 1998; J. H. Waarsing *et al.* 2004).

In 2004, Waarsing *et al.* were the first to describe a 3D registration method to identify the mismatched pixels between two consecutive scans, with pixels only present on initial scan identified as resorbed bone and pixels only present on the post scan identified as new bone (J. H. Waarsing *et* *al.* 2004). The authors used this method to visualise the differences between ovariectomised (OVX) rats and sham controls, including as well control scans to show the relative error of the method as a reference/comparator to the actual biological changes (*i.e* reproducibility study in Figure 5.1.1).

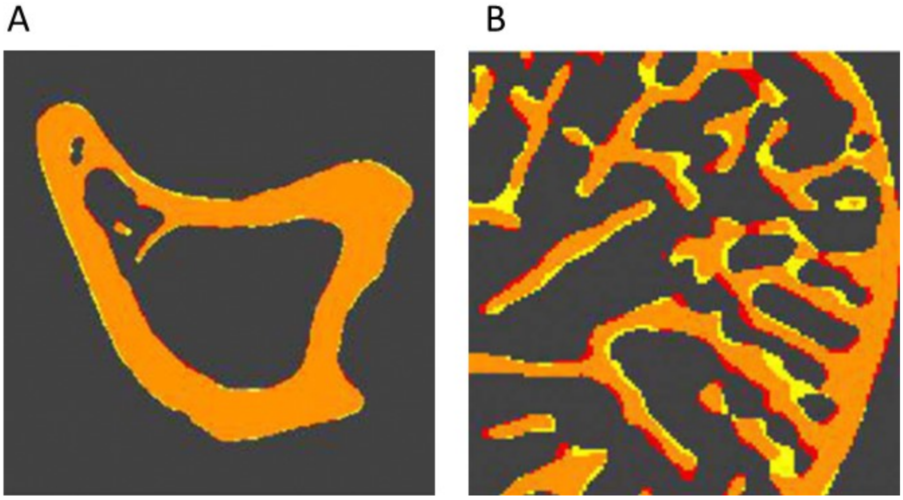

Figure 5.1.1. Example of the registration method developed by Waarsing *et al.* in control samples. The authors showed registered/superposed cross-sections from a rat femur scanned twice in the same day for a reproducibility (control) study to observe the output in the absence of negligible biological changes. Orange indicates where the scans overlap, red (only present on post-scan) and yellow (only present on pre-scan) show the mismatch or difference between images. (A) Diaphyseal cross-section with mainly cortical bone. (B) Detail of epiphyseal trabecular bone. Reprinted with permission from Elsevier from (J. H. Waarsing *et al.* 2004), Copyright.

To validate the newly formed bone, the red-marked difference on the registered image was compared with *in vivo* fluorescent calcein deposition histologically (J. H. Waarsing *et al.* 2004). 3D registration allowed observing significant differences when comparing four-week apart scans on the healthy and OVX phenotype (Figure 5.1.2); showing a majority of red-marked difference (newly deposited bone) on the sham control (Figure 5.1.2 A) compared to OVX treatment with mostly yellow-marked difference (resorbed bone) (Figure 5.1.2 B; (J. H. Waarsing *et al.* 2004)).

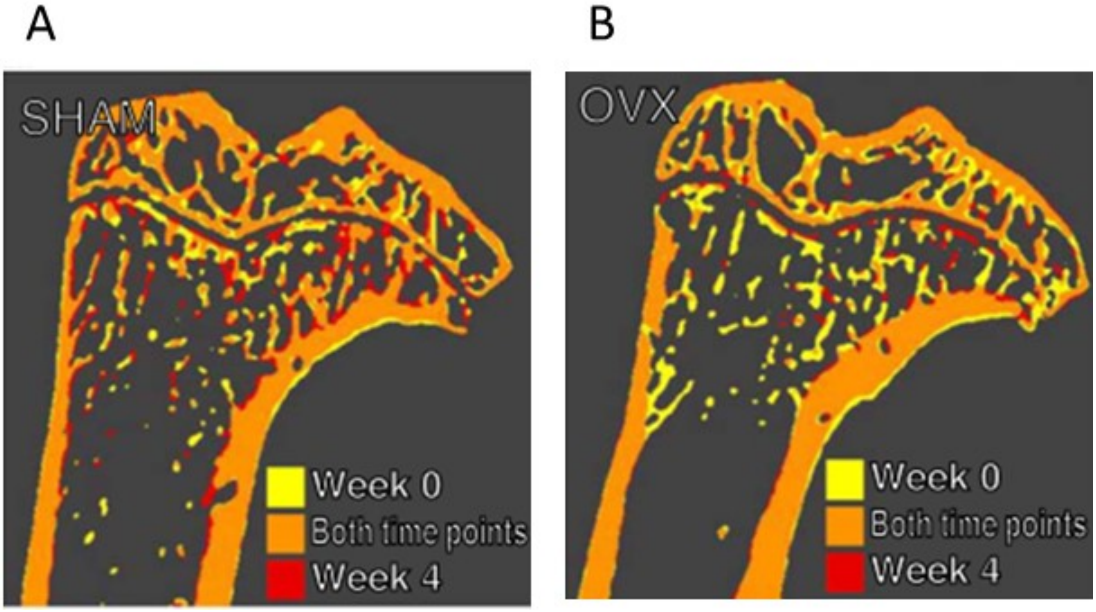

Figure 5.1.2: Registered datasets of (A) sham and (B) ovariectomised (OVX) rats at week 0 and week 4 post-surgery. Orange indicates where the scans overlap, red (only present on post-scan) and yellow (only present on pre-scan) show the mismatch or difference between images. Reprinted with permission from Elsevier from (J. H. Waarsing *et al.* 2004), Copyright.

Following the previous study, one other investigation has been published using similar approaches to evaluate bone deposition and bone resorption. Schulte *et al.* described a sophisticated registration method that allowed them to not only visualise the new or resorbed bone, but also to quantify the resorption and apposition rates by applying an algorithm to the registered image (Schulte *et al.* 2011). This quantification approach allowed them to obtain dynamic morphometric parameters such as mineralised surface and mineral apposition rate comparable to the ones obtained in standard histomorphometry (R=0.78; R=0.68 respectively); unfortunately histological validation of the mineral resorption rate was not available (Schulte *et al.* 2011).

Using the previously described registration methods by Waarsing *et al.* and Shulte *et al.,* a few studies have quantified the changes following consecutive scans to study the biological interventions: effect of vertebra mechanical loading by cyclic compression on the mouse tail (Lambers *et al.* 2011), effect of mechanical loading on bone deposition/formation rates for young, adult and elderly mice (Birkhold *et al.* 2014), and mechanical stimuli assessed by finite element analysis (Lambers *et al.* 2015). Hence, as indicated by these few studies, there is an emerging interest to try to apply 3D registration for the uncoupling of bone formation from bone resorption in *in vivo* μCT analysis.

5.1.2 BMP2 as a potent osteoinductive growth factor

In parallel to the use of 3D registration for the visualisation of the newly formed bone, the experiments of this chapter aimed to test the effect of an established, widely accepted factor to induce bone formation and validate µCT as a tool to quantify those changes. As previously discussed in 1.3.2, fracture healing involves an orchestrated cascade of events (*i.e.* inflammation, angiogenesis, matrix deposition, mineralisation) to achieve successful bone formation. There are several cytokines which play a key role during the healing process, including BMP2, which is a well-known potent osteoinductive factor (Rosen 2009).

BMP2 was approved in 2002 by the Food and Drug Administration as a replacement to the gold standard (bone autograft) in spinal fusion surgery (McKay, Peckham, and Badura 2007), and from that date it has been extensively used for clinical applications. Typically, BMP2 is used as human recombinant BMP2 protein soaked into an acellular collagen sponge vehicle (Geiger, Li, and Friess 2003), resulting in the formation of bone both ectopically and orthotopically (for more details see section 1.4.2.2). Commercial BMP2 for clinical applications, named InductOs™ (EU) or InFUSE® (USA), are available in the same format at a recommended dose of 1.5 mg / ml for application in spinal fusion and open tibia fracture surgeries (Medtronic SofamorDanek, Memphis, USA).

While there is no doubt that BMP2 has great potential in the induction of bone formation, it has also been associated with adverse reactions both in preclinical and clinical studies (heterotopic ossification, inflammation and excessive osteoclastogenesis) (Carragee *et al.* 2011; Kaplan *et al.* 2008; Poynton and Lane 2002; Shore *et al.* 2006). In fact, 10 years after the use of the commercial BMP2 in the clinic (InductOs™), the negative effects associated with the bulk, single-burst release of BMP2 are well-known to the scientific community (Simmonds *et al.* 2013; Synthesis and Sharing 2013). Considering the side effects associated with this potent osteogenic factor, current research is focusing on achieving controlled and local release of this osteoinductive factor to prevent undesired side effects while effectively promoting bone repair. Section 01.4.3 reviewed the potential of hydrogels as delivery vehicles for bone tissue engineering, and in particular a clay-based hydrogel (Laponite) as a promising candidate because of its high adsorption capacity.

There have been a few studies which have introduced biomaterials containing various concentrations of BMP and implanted the growth factor-scaffold construct on the CAM model, however those studies aimed to evaluate an angiogenic response from the avian membrane and not the induction of bone formation (Bai *et al.* 2014; Ramoshebi and Ripamonti 2000; Smith *et al.* 2007).

In the present Chapter I aim to test the effects of an FDA-approved, widely clinically used commercial product, BMP2 (InductOs™), as well as newly developed hydrogel (Laponite) to deliver BMP2 to induce bone formation on the CAM-human model. Moreover, Laponite will be examined as well in the context of delivery of angiogenic growth factor (VEGF) and primary cells to promote bone formation. Hence, the hypothesis of this investigation was that BMP2 delivery on the CAM can induce the formation of new bone and μCT can be used as a sensitive tool to measure those changes.

Thereby, the general aim of this chapter was to i) visualise the change in bone volume following CAM-implantation and ii) examine the potential of BMP2 to induce bone formation on the CAM ectopically and on the human bone cylinders. Hence, the individual objectives of this chapter were:

- To visualise the structural changes following incubation by implementing the 3D registration plug-in from DataViewer to superpose consecutive scans from the same bone.
- To identify the bone mineral density of the newly formed bone following CAM-implantation.
- To assess the role of the human autologous cells on the process of bone formation.
- To examine whether the CAM can be utilised as a model of ectopic bone formation.
- To evaluate the osteogenic potential of BMP2 on the human bone cylinders by using two delivery methods: single burst release (collagen sponge) and controlled release (Laponite hydrogel).
- To examine the effects of a clay-based hydrogel-vehicle of growth factors (*i.e.* BMP2, VEGF) and primary cells on bone formation.

5.2 Results

5.2.1 Insights from the µCT analysis on the visualisation of newly formed bone

The initial aim of this chapter was to identify the location of newly deposited bone and, following that, to measure its bone mineral density (BMD). To address this question, 3D registration of consecutive scans was implemented in order to i) visualise the changes between pre- and post-scans and ii) create a region of interest (ROI) to specifically select the newly formed bone and assess its BMD and location.

To visually identify the changes between consecutive scans, 3D registration tool in the DataViewer software was used to superpose consecutive scans of human bone cylinders that had been CAM-implanted, cultured *in vitro* or maintained at 4°C (internal control) for 7-9 days. In brief, pre- and post-scans in greyscale were both loaded and the software inverted the greyscale of the post-scan; hence the bone tissue in was displayed as white for the pre scan, and black for the post scan just before registration (Figure 5.2.1 A-C). Successful superposition of pre (white) and post (black) dataset was displayed in the sum of both colours (grey), while the unmatched structures remained in the colours displayed upon loading; white and black respectively (Figure 5.2.1 D-F).

For more details and explanation on this method see section 2.5.3.

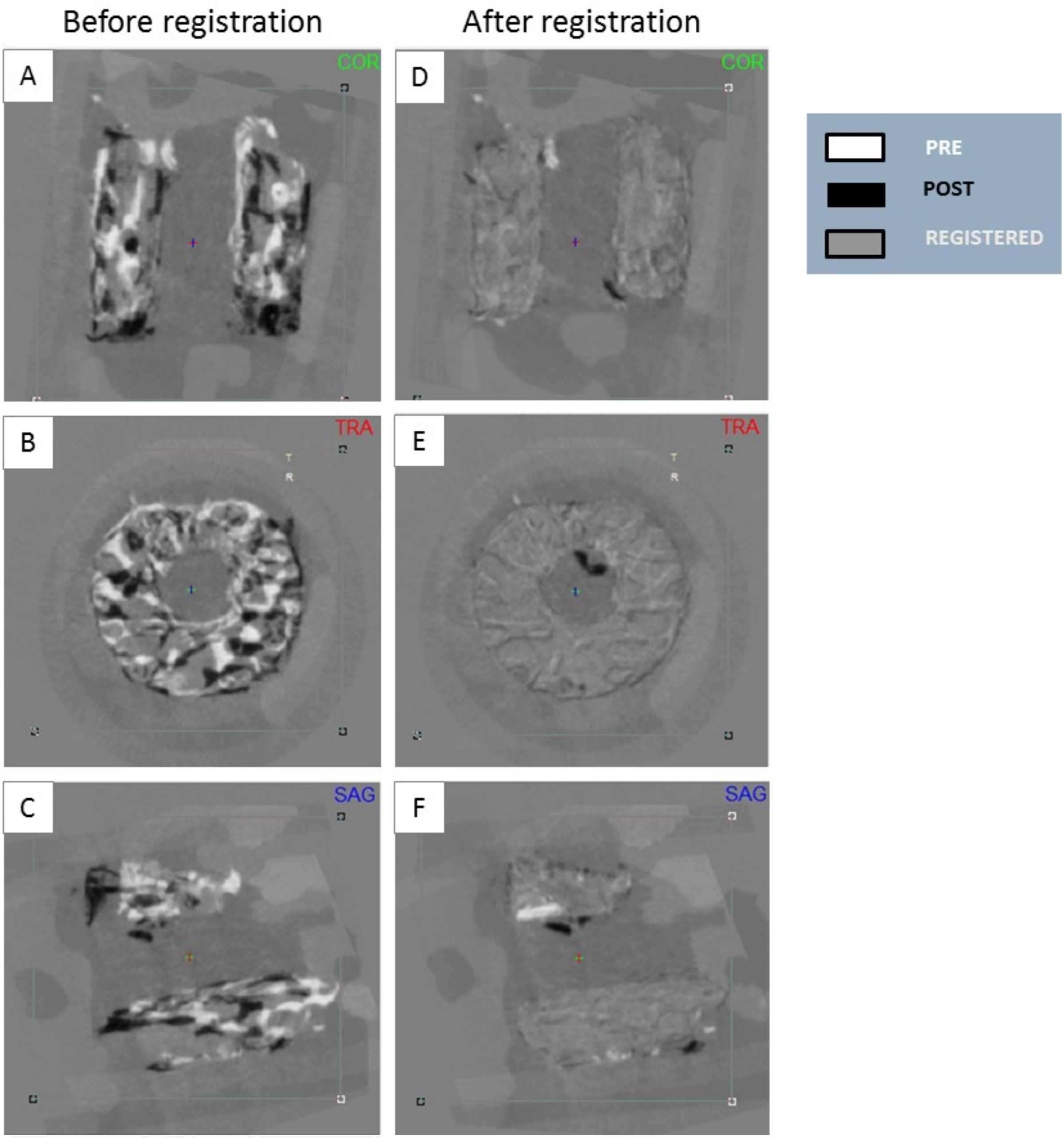

Figure 5.2.1: Three-dimension registration of two sequential scans of the same human bone cylinder under the same X-ray settings and reconstruction parameters. Bone cylinder was scanned under the same X-ray settings with a week interval, obtaining day 0 scan (pre) and day 7 scan (post). (A-C) Before registration, DataViewer software loads pre and post dataset, however after inverting the greyscale of the post dataset (black). Following registration (D-F) successful superposition of pre and post dataset results in grey colour, while the unmatched structures remain in the colours displayed upon loading. Sagittal (SAG), transaxial (TRA) and coronal (COR) cross-sections.

In order to visualise the location of the newly formed bone, the registered dataset was saved and image-processed as explained in Methods section 2.5.3. In short, following 3D superposition the mismatched structures corresponding to the pre-scan were displayed in green (labelled as “pre-diff” in Figure 5.2.2 A, E, I), and corresponding to the post-scan displayed in purple (labelled as “post-diff” in Figure 5.2.2 B, F, J). These images were then combined to show the location of the mismatched (pre-diff and post-diff) structures (Figure 5.2.2 C, G, K). The original sample, pre-scan in regular greyscale, was included as a reference for the original structure of the bone cylinder (Figure 5.2.2 D, H and L). Images representative of 4 independent experiments (Supplementary Figure 7.4.1; Supplementary Figure 7.4.2).

In a simpler explantation, structures displayed in green identify potential resorbed bone (named 'pre-diff') while structures displayed in purple identify potential formed bone (bone (named 'post-diff'). Moreover, while grey colour displayed the constant or unchanged bone structure for the same sample (Figure 5.2.2). For more details and explanation see section 2.5.3.

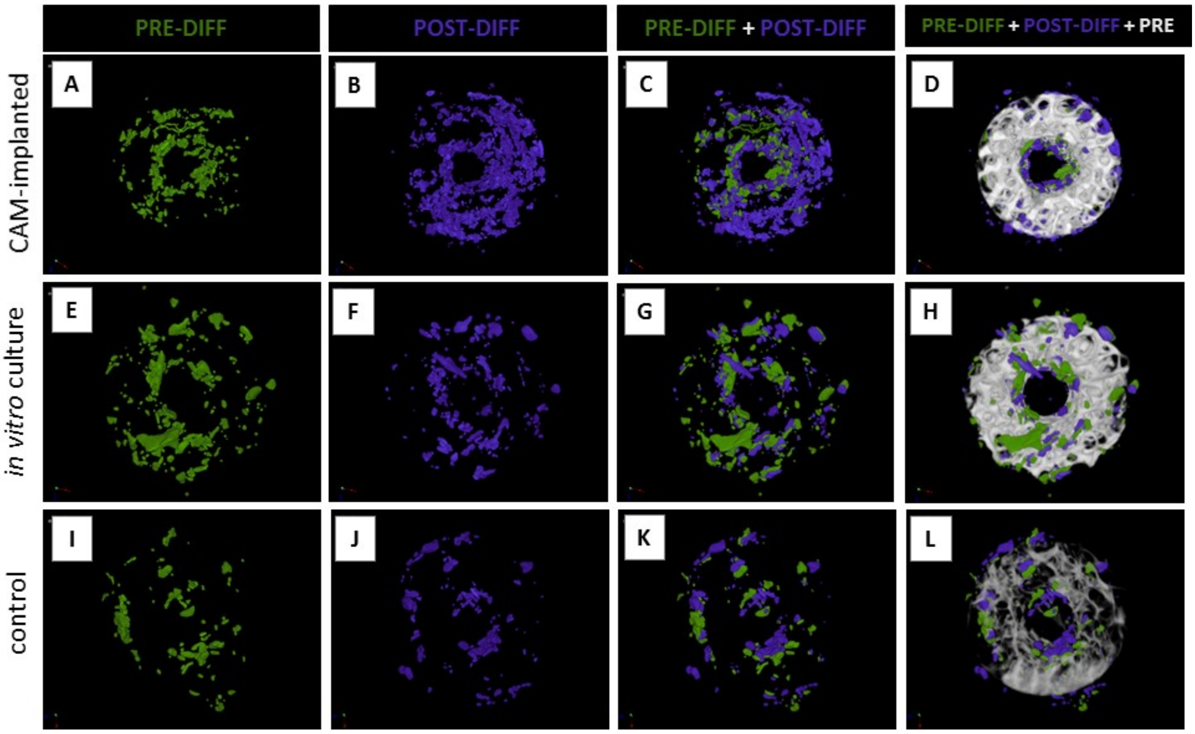

Figure 5.2.2: Visualisation of pre-diff and post-diff of human bone cylinders following image 3D registration processing. Pre and post scans of bone cylinders under different culture conditions (CAM-implantation A-D, *in vitro* E-H and control I-L) were superposed by 3D registration and the difference image was digitally processed to display pre-dif in green (potentially resorbed bone), post-diff in purple (potentially newly formed bone). Control bone cylinders were maintained at four degrees for the same incubation period. The original pre scan was shown as well in ivory colour as a reference. Images representative of 4 independent experiments.

The registration of the control bone cylinder showed there were a large number of bone structures identified as mismatched (Figure 5.2.2 I-L); however, there was a negligible change in bone volume in the same cylinder (-0.26 % BV). Similarly, *in vitro* treatment showed very little difference of the pre-diff with respect to post-diff ratio (Figure 5.2.2 E-H), again in agreement with almost a negative change in bone volume for the same sample (-0.11 % BV). Yet, even if the three conditions showed the presence of mismatched structures, CAM-implanted bone cylinders showed a greater proportion of post-diff over pre-diff as evidenced by comparison of Figure 5.2.2 B (CAM) to Figure 5.2.2 J and F (control and *in vitro*). These results were in accordance to the previous quantification for that particular sample (+8.13 % BV), which together with the rest of the cylinders of that treatment (CAM-implantation) showed a significant increases compared to *in vitro* cultured bone cylinders from the same donor (M79 NOF; p<0.001; Figure 4.2.7).

In addition, the presence of post-diff structures was not homogeneous through the whole object but localised in the periphery and more prominently in one of the sides from the bone cylinder (Figure 5.2.2 C), probably corresponding to the integration site of the bone cylinder on the CAM. This graphic method allowed the observation that, despite the relative degree of misaligned error introduced by the 3D registration on unchanged samples, CAM-implanted bone cylinders showed higher deposition of X-ray attenuating material, likely mineralised tissue.

Since it was not possible to use the 3D registration to identify neatly the bone mineral density of the newly formed tissue, an alternative image analysis approach was designed. Similarly as explained before (see section 2.5.3), 3D registration was used to create a difference image dataset, which was then thresholded to select conservatively the mismatched structures corresponding to pre and post scan, respectively (see methods Figure 2.5.1. E). These two pre and post differences masks were loaded as a ROI on the original scans (pre and post datasets respectively), to obtain the image in greyscale within the ROI. These two new datasets (named pre-diff and post-diff; Figure 2.5.1 J, K) contained the structures identified during registration as “pre” (resorbed) and “post” (deposited) in original greyscale. This previous approach allowed obtaining a histogram of the voxels contained just within mismatched regions contained within the original scans (pre and post respectively), hence containing the original density in greyscale values, which allowed estimating their corresponding bone mineral density. For a more detailed description of the image processing, see Methods section 2.5.3.

The previous image processing analysis was applied to obtain the histograms from control, *in vitro*, and CAM-implanted bone cylinders of the pre-diff and post-diff (Figure 5.2.3); representative of the same analysis conducted on three additional donor samples, each representing an independent experiment (Supplementary Figure 7.4.3).

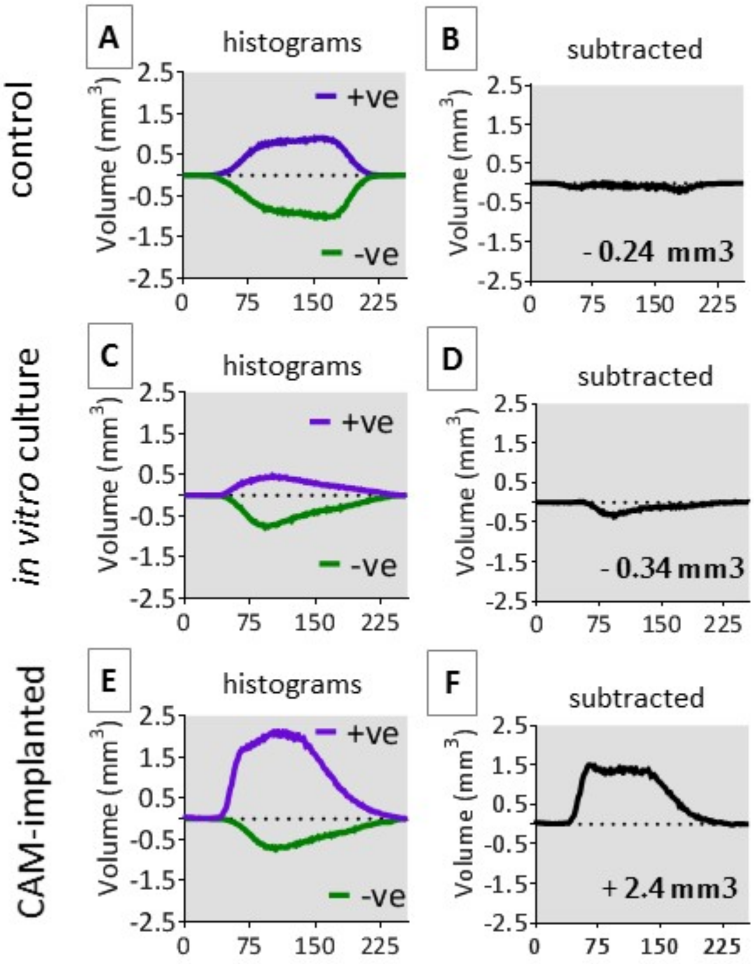

Figure 5.2.3: Histogram distribution of pre-diff and post-diff scans following the application of a 3D-registration-based ROI. Bone cylinders from donor sample M79 NOF# were maintained at 4°C (A-B), *in vitro* cultured (C-D) or CAM-implanted (E-F) for 9 days. Pre and post incubation µCT scans were registered to obtain the difference image, which was then used as a ROI on top of the original scans to obtain the pixel distribution in original greyscale (0 white, 255 black) from the pre-diff (green line) and the post-diff (purple) dataset on the same histogram (A, C and D), or subtracted (B, D, F). Neck of femur fracture (NOF#)

The area under the curve of the histogram of the pre-diff and post-diff dataset indicated the volume of pixels of a certain density (0-255) from the mismatched structures. The histogram distribution from pre-diff dataset (green line) and post-diff (purple line) dataset were shown separately (Figure 5.2.3 A, C and E) or one subtracted from another to observe the net change (Figure 5.2.3 B, D, F).

The baseline relative error of the registration method was evidenced on the histograms of the control sample, where there was a similar distribution in terms of volume and density between pre-diff and post-diff (Figure 5.2.3 A), however negligible following subtraction (Figure 5.2.3 B). Histogram from *in vitro* sample showed a modest increase in the volume of pre-diff with respect to post-diff, which again corresponded with an almost negligible net change (Figure 5.2.3 D). In contrast to the small changes described above, the histogram from CAM-implanted sample showed an increase in the area under the curve (volume) of the post scan, as well as shift on the greyscale distribution (Figure 5.2.3 F). In addition to the pixels contained within a similar range as the pre-diff (90-150 greyscale), additional pixels appeared within the 45 to 75 greyscale range on the post-diff, indicative of low density material (Figure 5.2.3 E). These changes in the histograms also corresponded to the previous bone volume changes in the same samples: control (+0.26 %), *in vitro* (+0.11 %) and CAM-implanted (+8.13 %). Hence, plotting the pixel distribution of these specific regions of interest from the original datasets allowed observing quantitatively the changes observed on the 3D rendering images of the same samples (Figure 5.2.3).

With the aim of selecting a potential cut-off value from which new matrix deposition started to appear on the CAM-implanted samples, a greyscale value in which pre-diff and post-diff distribution of pixels on the histogram began to differ was chosen arbitrarily. Continuing from the histograms shown previously, the shift from pre-diff to post-diff histogram was noticeable from greyscale value of 45 (Figure 5.2.3). The attenuation coefficient of the phantom (µCT internal standard control) allowed estimating the corresponding value in bone mineral density, which was calculated to be 0.1492 g HA/cm^3. The same analysis was conducted for three other independent experiments (Supplementary Figure 7.4.3), resulting in similar BMD values (Table 5.2.1), however lower compared to standard trabecular bone density 0.25 g HA/cm^3.

Table 5.2.1: Estimated cut-off value in greyscale and in bone mineral density (BMD) to detect potentially newly formed bone Four independent experiments (M80 NOF#, F81 NOF#, M79 NOF#, M57 OA). Choice of arbitrary based on the inspection of histograms.

Experiment	Greyscale	BMD (g HA/cm^3)
M80 NOF#	45	0.1470
F81 NOF#	45	0.1492
M79 NOF#	45	0.1404
M57 OA	47	0.1867

In summary, the previous set of results investigated 3D registration on the CAM-implanted samples, which allowed visualising the newly formed bone as well as the implementation of a region of interest to identify the corresponding bone mineral density.

5.2.2 Role of the autologous cells from bone cylinders

Previous experiments had shown that bone cylinders implanted on CAM experienced a significant increase in bone volume compared to bone cylinders cultured *in vitro* (Figure 4.2.7). To test whether the deposition of mineral following CAM-implantation was due to the osteogenic effect of the human cells within the tissue, bone cylinders were treated with paraformaldehyde (PFA), or high temperature (heat), before CAM-implantation. Bone cylinders were cellular-inactivated ('dead') or maintained in standard culture conditions ('live') prior to CAM-implantation, and chick embryo viability was evaluated at harvest.

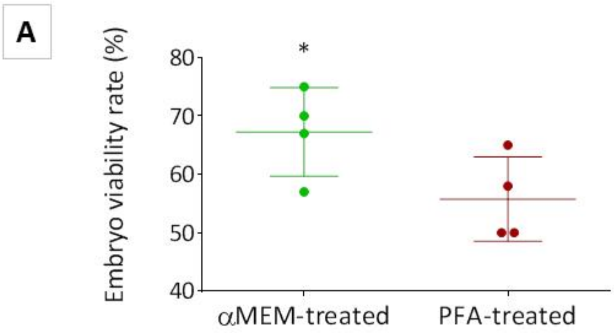

B

	αMEM-treated	PFA-treated	Heat-Treated
M70 OA	4/7	5/10	-
F86 OP	7/10	7/12	-
F85 OA	10/12	6/12	-
F81 OA	5/8	2/3	1/6

Figure 5.2.4: Significant reduction of chick embryo viability following CAM-implantation of non-viable bone cylinders. (A) Bone cylinders were fixed in paraformaldehyde (PFA), heat-treated at 121 ˚C followed by thorough PBS washes or maintained through-out in standard culture conditions (basal media at 37 ˚C) before CAM-implantation. Data points represent chick embryo viability following 4 independent experiments with 4 donor samples: M70, F86, F85 and F81. Statistical analysis conducted using a t-test (comparison between 2 groups). Error bars indicate mean ± SD, *p<0.05. (B) Raw data: Fraction indicating the number of viable embryos from the total number of CAMs with M70, F86, F85 and F81 femoral heads donors.

PFA treatment prior to CAM implantation resulted in significant decrease in subsequent embryo viability (Figure 5.2.4 A-B), and this effect was reproducible across 4 different donor samples, regardless of OA or OP phenotype (p=0.0120; Figure 5.2.4 A-B). An attempt was made to use high temperature to induce cell death on the bone cylinders, resulting in very low chick embryo survival rate (1/6) compared to standard cultured bone cylinders (5/8), as well as to PFA-treated bone cylinders (2/3) (Figure 5.2.4 B). Histological examination of the heat-treated cylinders showed no signs of cells present within the bone marrow (Supplementary Figure 7.4.4 A-B), compared to the normally cultured bone cylinders following CAM-implantation (see arrows Supplementary Figure 7.4.4 C-D).

The detrimental effect on chick embryo viability of both PFA and heat-treated bone cylinders did not allow an assessment of the effect of bone volume change following CAM-implantation due to the low number of samples at harvest. Hence, it was necessary to explore alternative options to induce bone cylinder cell death without compromising the CAM assay biocompatibility. Hydrogen peroxide (H_2O_2), commonly used to produce allograft bone during surgery, was used to decellularise the bone cylinders before CAM-implantation. H_2O_2-treated bone cylinders did not show a significant negative impact on chick embryo viability (65.13 % ± 20 SD; two independent experiments), compared to the standard harvest viability rate (70 % ± 17 SD, 6 independent experiments) depending on graft properties. µCT analysis was conducted to examine the effect of cellular component in bone volume formation (% BV) of the bone cylinders following CAM-implantation.

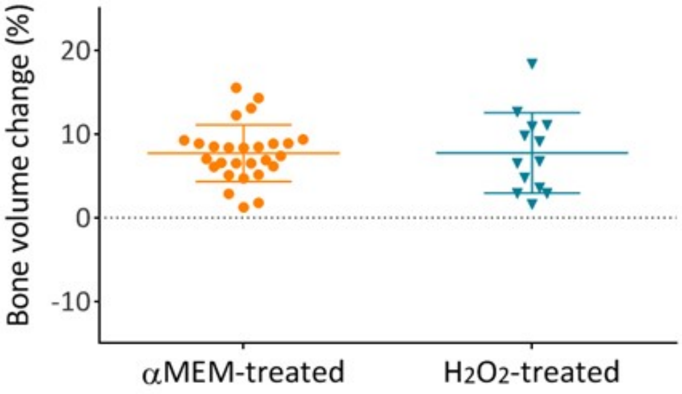

Figure 5.2.5: 'Dead' (H_2O_2 treated) bone cylinders presented similar increase in bone volume following CAM-implantation compared to 'Live' cylinders (standard culture). Bone cylinders were treated with hydrogen peroxide to remove the cellular content (two independent experiments) or maintained in standard culture conditions prior to CAM-implantation (6 independent experiments). Data points indicate relative bone volume change of individual bone cylinders before and after CAM-implantation. Error bars indicate mean ± SD.

There was no apparent differences in bone volume change of the H_2O_2-treated bone cylinders (7.68 ± 3.38 SD) compared to standard culture conditions (7.72 ± 4.8 SD; Figure 5.2.5). However, histological examination of the decellularised bone cylinders showed some different features compared to the 'live' tissue (Figure 5.2.6).

In general, both 'live' and 'dead' bone cylinders were CAM-integrated and showed CAM growth from the outer periphery to the inner defect core of the bone cylinders (Figure 5.2.6 B-C and E-F). Avian blood vessels were found in the marrow space of both 'live' and 'dead' bone cylinders, indicative of biocompatibility between graft and host tissue (see arrows Figure 5.2.6 B-C and E-F). However, the marrow space of the H_2O_2–treated cylinders (Figure 5.2.6 A) showed lesser extracellular matrix deposition and cellular density compared to standard culture conditions (Figure 5.2.6 D).

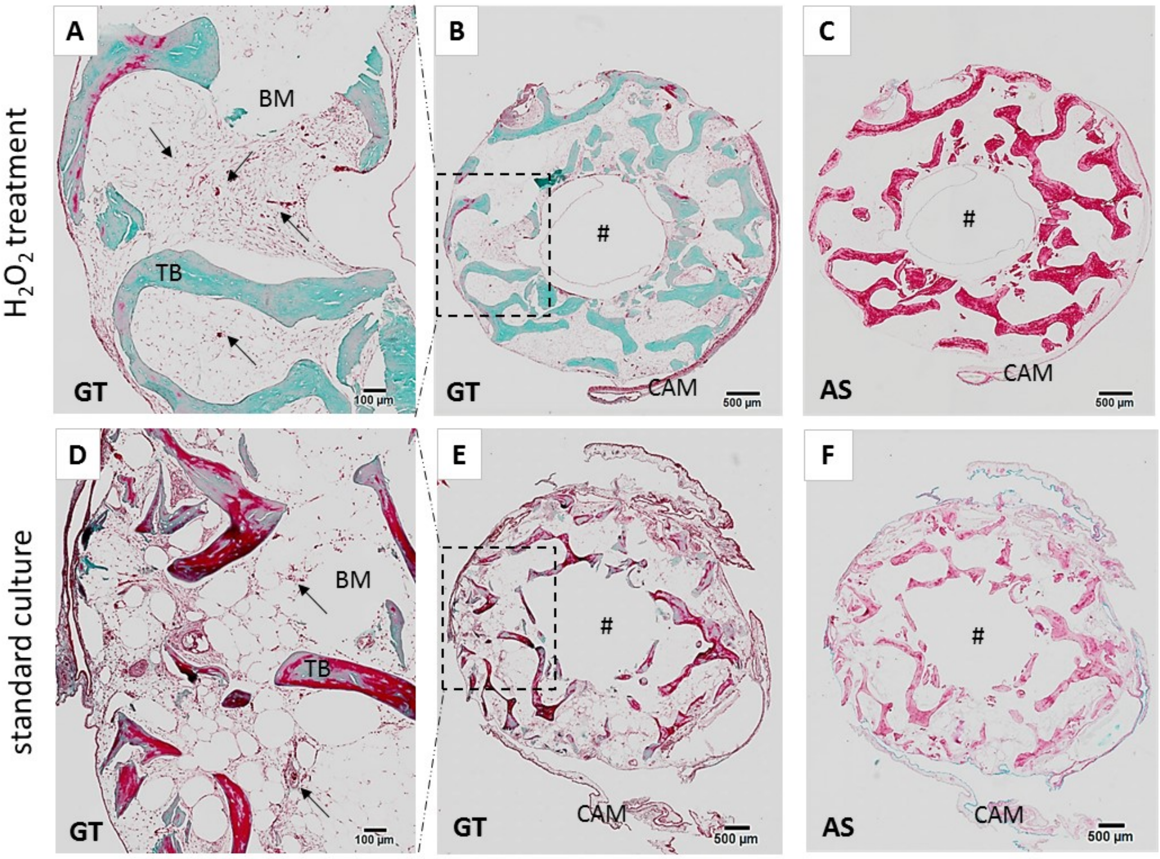

Figure 5.2.6: CAM integrates and perfuses with blood vessels the bone tissue from 'live' and 'dead' bone smples, but induces greater interaction on 'live' cylinders. Bone cylinders were harvested from CAM-implantation of decellularised bone tissue: 'dead' cylinders (A-C) or bone tissue cultured in media; 'live' cylinders (D-F). Paraffin sections stained for GT (A, B, D and E) and AS (C and F). Arrows indicate avian blood vessels. Images representative of two independent experiments of each treatment. (CAM) chorioallantoic membrane, Goldner's Trichrome (GT), Alcian Blue and Sirius Red (AS), # bone cylinder defect region. See colour legend in Table 2.6.1. Scale bars equivalent to 500 µm (B, C. E and F) and 100 µm (A and D).

Regardless of this qualitative distinction of the histological CAM-bone interaction on the 'live' bone cylinders compared to the 'dead' ones, the bone volume change following CAM-implantation did not reflect any obvious difference between standard or decellularised cylinders (Figure 5.2.5).

5.2.3 Mechanisms of bone formation: role of BMP2

The fact that the increase in bone volume did not appear to be dependent on the cellular component of the bone cylinders lead to the hypothesis that the intrinsic osteoinductive properties of the bone exctracellular matrix was sufficient to ellicit an osteogenic response from the CAM.

To test this hypothesis, a potent osteinductive factor commonly used in the clinic (InductOs^{TM}, hrBMP2) was delivered to the CAM using a decellularised bovine collagen sponge as a vehicle. Three different doses of BMP2-InductOs™ (0 µg/mL, 7.85 µg/mL and 150 µg/mL) were applied to the standard size collagen sponges just before CAM-implantation or *in vitro* culture for 9 days, followed by µCT analysis (see section 2.5.2 for more details). Hence, the final BMP2 dose delivered to the collagen sponges was 0 µg, 0.125 µg and 2.4 µg of BMP2 (total volume of 16 µl collagen sponge), respectively. See section 2.4.1.2 for more details.

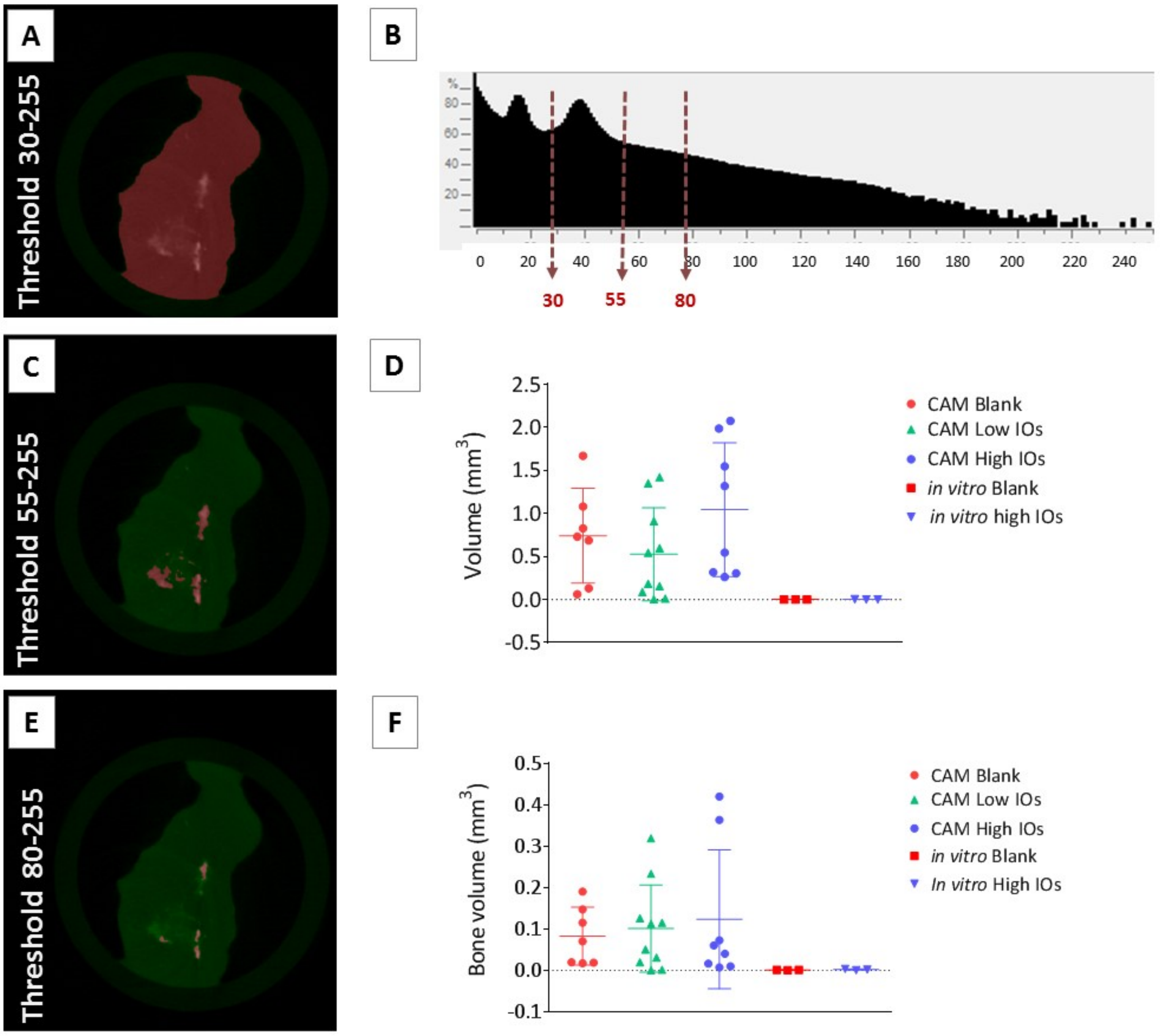

Figure 5.2.7: Deposition of X-ray dense material on collagen sponges containing BMP2 cultured on CAM or *in vitro*. Standard size collagen sponges of were applied with vehicle control buffer (Blank; 0 µg/mL), 0.125 µg BMP2 InductOs™(Low IOs; 7.85 µg/mL) and 2.4 µg BMP2 InductOs™(High IOs; 150 µg/mL) before CAM-implantation or *in vitro* culture for 9 days. Collagen sponges were µCT-scanned at harvest and different thresholds were applied to visualise the selection (pink) over the background (green) on the same µCT slice. (A) Threshold 30-255 to include the collagen sponge, (C-D) Threshold to exclude the collagen sponge and include tissue volume and (D-E) Threshold 80-255 to quantify material of bone mineral density equivalent to previous experiments with bone cylinders (Table 5.2.1). Volume quantified for each threshold (D and F). Data collected from 3 independent experiments. Error bars indicate mean ± SD.

As shown in the histogram from the sponge dataset, a threshold value of 30 would include the volume of the collagen sponge as well as the newly deposited tissue (Figure 5.2.7 A-B). In order to select the newly deposited material (Figure 5.2.7 C), a cut-off value of 55 was used for the tissue volume quantification (Figure 5.2.7 C). This global threshold of 55 was selected on the basis of separating the collagen sponge matrix from the denser material contained within (Figure 5.2.7 C). In general, CAM-implantation induced significant increase in tissue volume (0.5483 ± 0.50SD mm^3) compared to *in vitro* culture (0.0068 ± 0.006 SD mm^3). Despite the large variability between conditions, the high BMP2 dose showed more tissue deposition (0.67 ± 0.56 SD mm^3) compared to low BMP2 dose (0.526 ± 0.53 SD mm^3) and blank (0.437 ± 0.431 SD mm^3) on CAM, though the change was not significant (p=0.69; Figure 5.2.7 D). As expected, no tissue formation was observed on *in vitro* cultured bone cylinders (0.0068 ± 0.006 SD mm^3; Figure 5.2.7 D).

In order to allow for comparison between scans conducted under different X-ray settings, a phantom was used to calculate the reference cut-off value previously used for the analysis of bone cylinders' bone volume (0.14 g HA / cm^3; Table 5.2.1). This BMD was equivalent to the value of 80 on the greyscale of the histogram previously shown, and hence the quantification of bone volume was conducted using this threshold (Figure 5.2.7 F). The difference between tissue volume (55-255) to bone volume selection (80-255) was noticeable when comparing foreground (pink) from background (green) for the same μCT slice, being more conservative on the 80 threshold (Figure 5.2.7 C and E). Again, the increase in bone volume was higher on the CAM implanted samples (0.118 ± 0.11 SD mm^3) compared to the negligible effect on the *in vitro* cultured sponges (0. 0012 ± 0.001 SD mm^3). The bone volume quantification did not allow to observe categorical differences between treatments due to the wide spread of the samples (Figure 5.2.7 F).

Collagen sponges were processed for histology omitting the decalcification step. Histological examination showed complete integration and encapsulation of CAM-implanted sponges (Figure 5.2.8 A), whereas the *in vitro* cultured ones remained unchanged (Figure 5.2.8 D). CAM-implanted sponges showed significant extracellular matrix deposition and cell invasion (Figure 5.2.8 B) as well as mineral deposition, indicated by black pigmentation (Figure 5.2.8 C), absent on *in vitro* culture (Figure 5.2.8 F). Compare the differences between collagen from unchanged sponge (Figure 5.2.8 E) to the disorganised newly deposited collagen and proteoglycan matrix and mineral deposition following CAM-implantation (Figure 5.2.8 B, C).

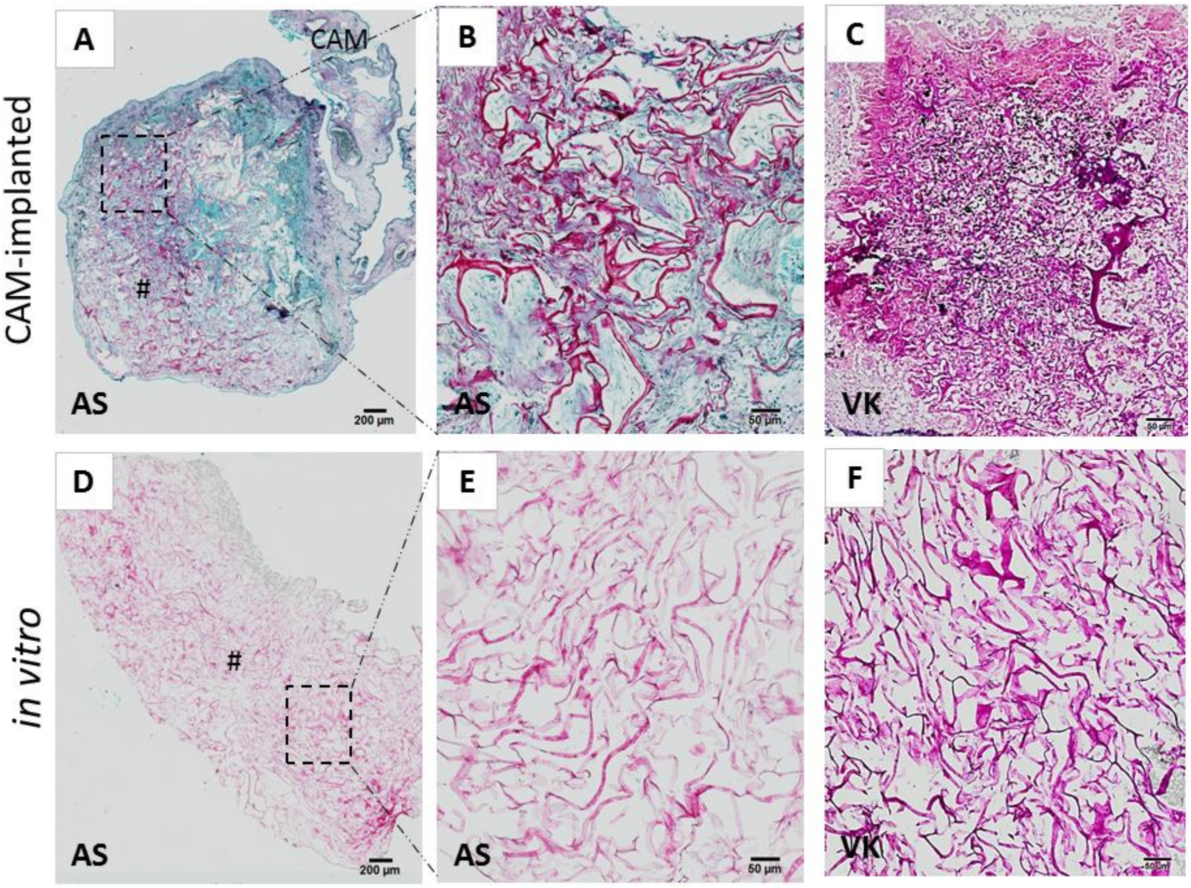

Figure 5.2.8: Observation of extracellular matrix deposition and cell infiltration on collagen sponge implanted on CAM, but not *in vitro*. Collagen sponges of standard size were CAM-implanted (A, C) or cultured *in vitro* for 9 days (B, D). At harvest, samples were fixed, processed for paraffin section. Representative images from consecutive sections stained for Alcian Blue and Sirius Red (A, B, D, E) and von Kossa (C and F). (CAM) chorioallantoic membrane (CAM), for Alcian Blue and Sirius Red (AS, von Kossa (VK). See colour legend in Table 2.6.1. # collagen sponge. Scale bars equivalent to 200 µm (A, D) and 50 µm (B, C, E and F).

Invasion of blood vessels was evident in the *in vivo* implanted collagen sponges (see arrows Figure 5.2.9 B and E), as well as formation of cell condensations; see examples in Figure 5.2.9 C and F).

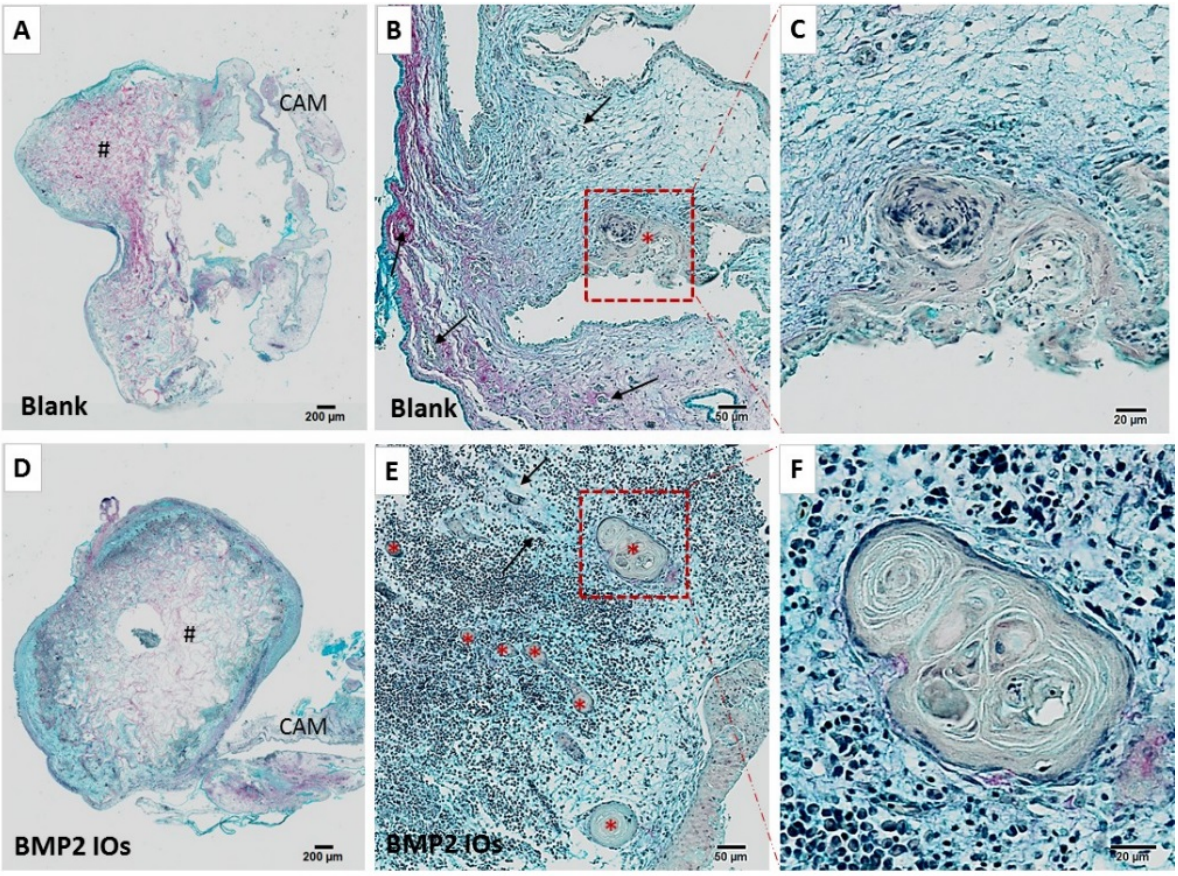

Figure 5.2.9: Increased formation of cell condensations following BMP2 InductOs™ delivery on CAM-implanted collagen sponges. Collagen sponges of standard size were administered at 0 ug/mL BMP2– blank (A-C) and 150 µg/mL BMP2 (D-F) before CAM-implantation for 9 days. At harvest, samples were fixed, processed for paraffin section and stained for Alcian Blue and Sirius red. Arrows indicate blood vessels, *indicate cell condensations. See colour legend in Table 2.6.1. Scale bars equivalent to 200 µm (A, D), 50 µm (B, E) and 20 µm (C, F).

The morphology and shape of these cell condensations, shown as well in Chapter 4 (Figure 4.2.11, Figure 4.2.12), was variable (compare Figure 5.2.9 C and D). However, cell condensations were clearly distinguishable from the surrounding matrix by their tight conformation of concentric layers of densly packed cells (see asterisks in Figure 5.2.9). In addition, cell condensations expressed both Sox9 and Runx2 transcription markers (Supplementary Figure 7.4.5). A blinded observer counted number of cell condensations from two stained tomographic sections per sample (n=4 per treatment). Cell condensations were more numerous in the high BMP2 treatment yet not significantly compared to blank (2.3 ± 2.4 SD vs. 0.5 ± 0.5 SD; p=0.08), and absent in *in vitro* cultured collagen sponges (Figure 5.2.8 D).

As a validation of the µCT data (Figure 5.2.7 F), the implanted collagen sponges showed mineral deposition upon von Kossa staining (see arrows Figure 5.2.10). New mineral deposition was associated with the collagen sponge region (see arrows Figure 5.2.10 B-C), and present within cell condensations in the CAM tissue (see asterisks Figure 5.2.10 A and D).

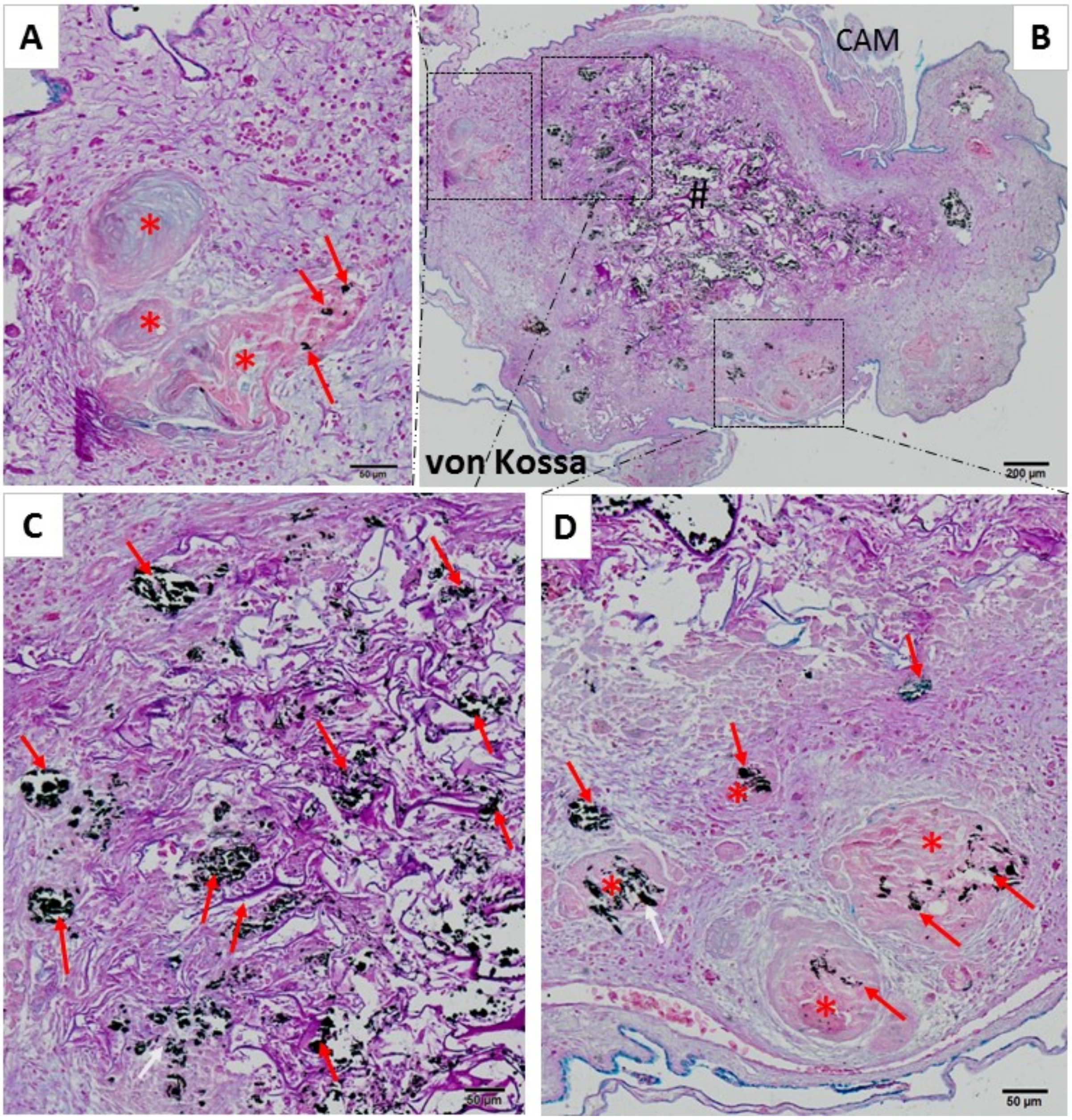

Figure 5.2.10: Validation of mineral deposition following BMP2 delivery on collagen sponges implanted on CAM. Collagen sponges of standard size were administered 150 µg/mL BMP2 before CAM-implantation for 9 days. At harvest, samples were fixed, processed for paraffin sectioning and stained for von Kossa (VK); mineral stained in black, proteoglycans in blue and cell cytoplasm in pink. Scale bars equivalent to 200 µm (B) and 50 µm (A, C, D).

Together, this data demonstrates that implantation of acellular collagen sponges containing BMP2 can induce the deposition of mineral in association with cell condensations formed by the CAM.

5.2.4 BMP2 delivery in human bone cylinders

In order to observe whether the endogenous osteoinductive properties of the bone cylinders could be further modulated by adding exogenous BMP2, the same InductOs™ treatment (acelluar collagen sponge containing BMP2) was applied to the defect region of the bone cylinders before CAM-implantation or *in vitro* culture for 9 days. See section 2.4.1.1 for more details.

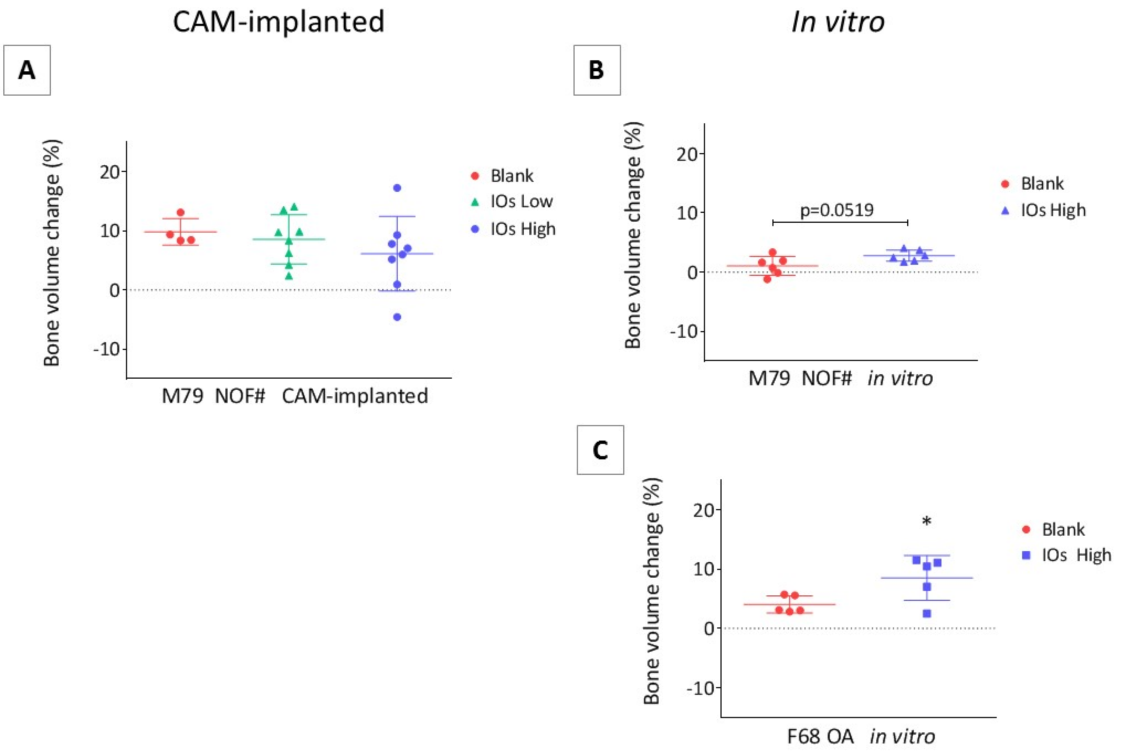

Figure 5.2.11: Significant increase of bone volume in InductOs™ BMP2 treated bone cylinders cultured *in vitro*, but not *in vivo*. Bone cylinders were treated with collagen sponge containing 0 µg/mL, 7.85 µg/mL and 150 µg/mL BMP2 InductOs™ and cultured *in vitro* (B, C) or CAM-implanted (A) for 9 days. Data points indicate net bone volume of the implanted collagen sponges (A); or relative bone volume change of individual bone cylinders (B-C) before and after 9 days culture. Error bars indicate mean ± SD, *p<0.05.

The effect of the high dose of BMP2 on *in vitro* cultured bone cylinders was positive, as shown by the significant increase in bone volume ($p<0.05$; Figure 5.2.11 B, C). This data indicates that the autologous cells of the human bone cylinder were responding to the BMP2, as the collagen sponge alone (biomaterial control) in the same culture conditions did not show any changes (Figure 5.2.7 F). While the BMP2 effect was positive *in vitro*, the CAM-implanted cylinders showed almost negative or no change or effect (Figure 5.2.11 A). As previously described, osteoclastic activity was present on the CAM-implanted samples, however, appeared to be negligible in those cultured *in vitro* (Supplementary Figure 7.4.7). No differences in Cathepsin K expression were found between BMP2 doses on CAM-implanted bone cylinders.

Histological analysis showed that BMP2 delivery on CAM-implanted bone cylinders induced the formation of cell condensations (see asterisks Figure 5.2.12 D-E), however vehicle control (Blank) cylinders showed proteoglycan matrix deposition (see arrows Figure 5.2.12 A-C).

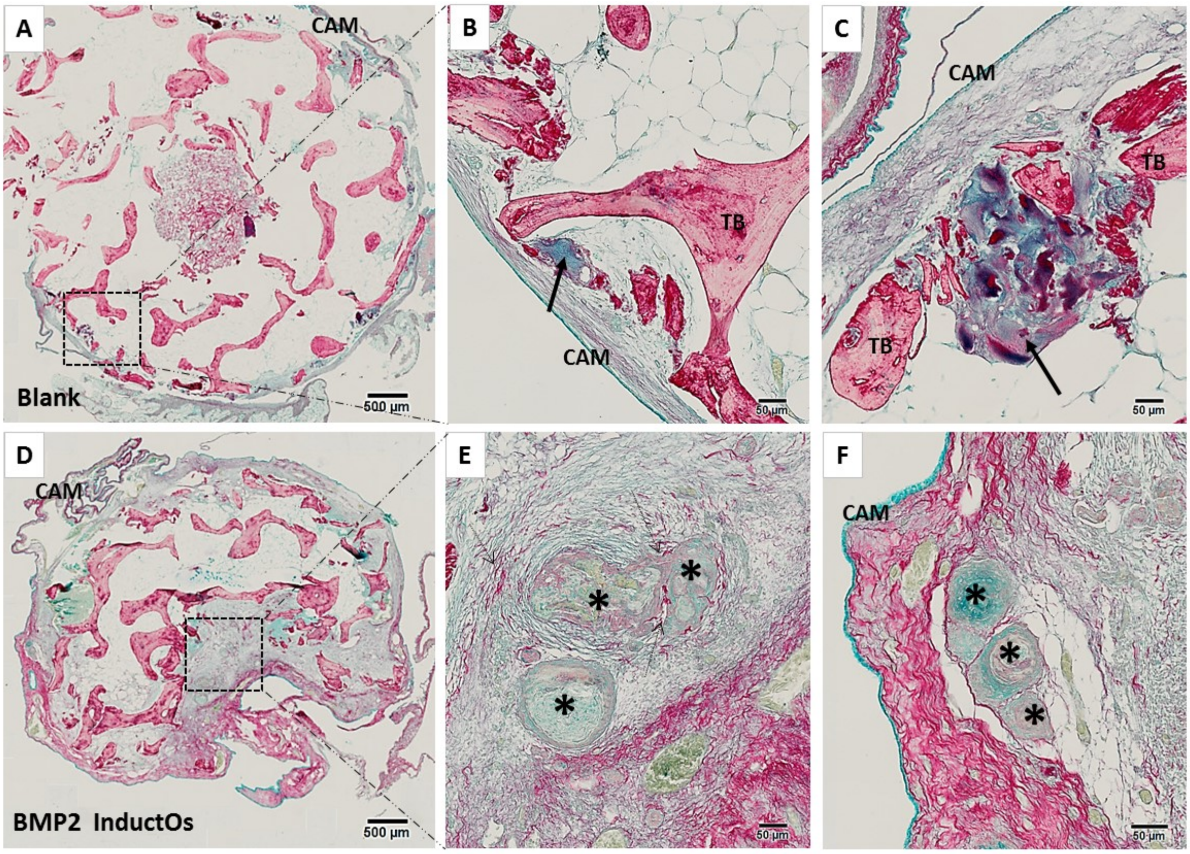

Figure 5.2.12: BMP2 delivery induces the formation of cell condensations, while Blank cylinders show proteoglycan deposition on CAM-implanted bone cylinders. Collagen sponge containing 150 µg/mL BMP2 (D-F) or vehicle control, blank (A-C) was applied on the defect region of the bone cylinders before CAM-implantation for 9 days. Consecutive representative paraffin sections were stained for Alcian Blue and Sirius Red staining. (TB) trabecular bone, (CAM) chorioallantoic membrane, * indicates cell condensation, arrows indicate proteoglycan deposition, dashed arrows indicate collagen deposition. See colour legend in Table 2.6.1. Scale bars equivalent to 500 µm (A) and 50 µm (B-E).

Cell condensations and proteoglycan deposition were found on the interface between human and avian tissue (see arrows and asterisk Figure 5.2.12 C and F). The same condensations appeared to have proteoglycan content on the interior (round cell cavities stained in blue) and collagenous component in the exterior (Figure 5.2.12 E-F). The extracellular matrix on the periphery of the condensations appeared stained in blue for the Masson's Tetrachrome staining, indicative of osteoid (Supplementary Figure 7.4.6 A-C). Quantification of cell condensations as described before was higher for the BMP2 treatment (5.25 ± 8.6 SD) compared to Blank (2.25 ± 2.27 SD), however this difference was not significant.

In summary, delivery of BMP2 appeared to induce deposition of mineral tissue on *in vitro* cultured bone cylinders, however the same effects were not reproduced on CAM-implanted cylinders, which in turn showed formation of numerous cell condensations.

5.2.4.1 Effect of a bone resorption inhibitor (Alendronate) on BMP2 treatment

Considering the osteoclastic potential of the CAM demonstrated in Chapter 4 (Figure 4.2.9), we hypothesised that BMP2 could affect the deposition/resorption balance of the bone cylinders. To investigate whether the nature of the different effect of BMP2 *in vitro* compared to *in vivo* (CAM assay) was due to osteoclast-induced activity via osteoblast-osteoclast cross-talk, an anti-resorptive drug was used. A pilot study to assess whether alendronate (ALD), an FDA-approved bisphosphonate, could elicit any toxic effects on the CAM assay was conducted; bone cylinders were incubated overnight in basal media containing 0 µM, 10 µM and 100 µM ALD followed by repeated PBS washes before CAM-implantation. Chick embryo survival rate was not compromised (3/3, 4/5 and 4/5, respectively) indicative of good biocompatibility with the human-avian system.

To test the whether the potential activation of osteoclast activity following BMP2 InductOs™ delivery could be inhibited using ALD, bone cylinders were pre-incubated with media containing 0 µM (Blank) or 100 µM (ALD) overnight (for more details see section 2.4.2). After repeated washes, a collagen sponge containing 0 µg/ml (Blank) or 150 µg/ml BMP2 (IOs) was placed on the defect region of the bone cylinders prior to a 9 day incubation *in vitro* or *in vivo* (CAM). µCT analysis showed an increase in bone volume following BMP2 InductOs™ application on the *in vitro* culture of +ALD-cylinders, and variable results for the –ALD treatment (Figure 5.2.13 B). CAM-implantation of +ALD/+IOs bone cylinders appeared to have an effect, however this was not conclusive due to the spread data and reduced numbers per treatment due to limited number of collected cylinders (Figure 5.2.13 A).

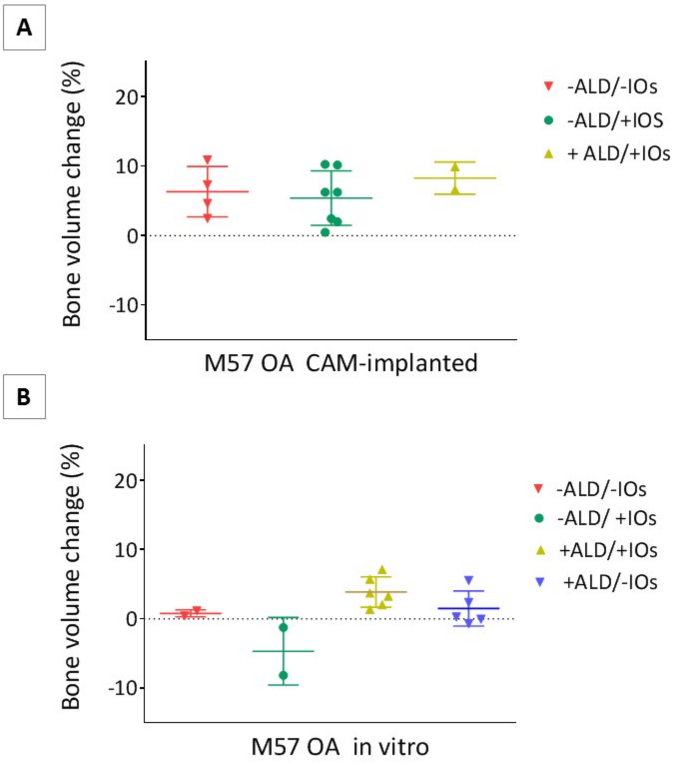

Figure 5.2.13: The effect of Alendronate in combination with BMP2 InductOs™ in bone human bone cylinders. Bone cylinders were pre-incubated in serum-free media supplemented with 100 µM alendronate (+ALD) or 0 µM alendronate (-ALD) overnight. Following incubation, a collagen sponge containing 0 µg/mL (-IOs; vehicle control) and 150 µg/mL InductOs™(+IOs) was placed on the defect region of bone cylinders before culture *in vitro* (B) or implantation on CAM (A) for 9 days. Data points indicate relative bone volume change of individual bone cylinders before and after 9 days of culture. Error bars indicate mean ± SD.

Immunostaining for Cathepsin K, a marker of osteoclast activity, showed that this enzyme was expressed in all treatments following CAM-implantation, including the bone cylinders pre-treated with ALD (Figure 5.2.14 A-E), indicating that ALD did not efficiently prevent osteoclast bone resorption in this experiment.

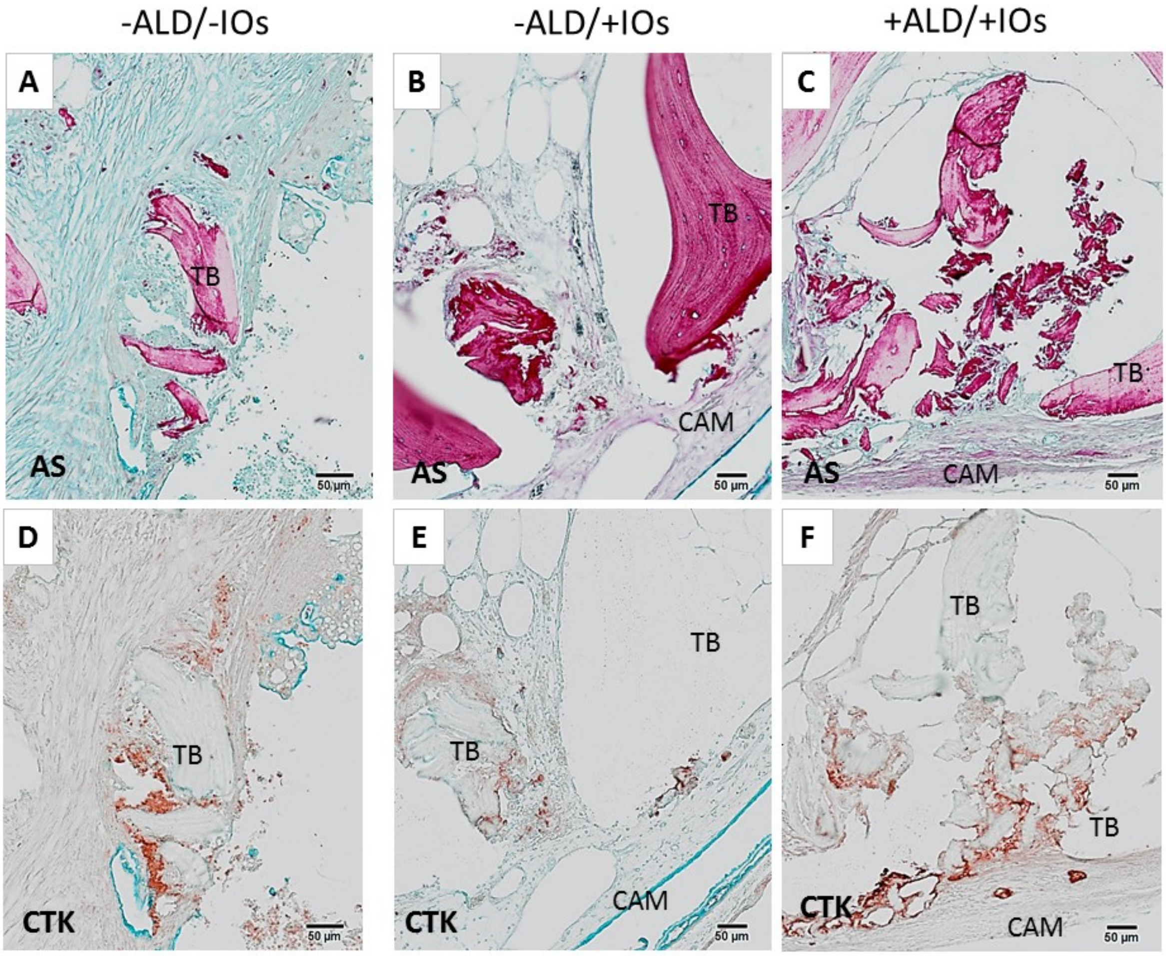

Figure 5.2.14: Cathepsin K expression on Alendronate treated bone cylinders following CAM-implantation. Bone cylinders extracted from M57 OA were pre-incubated in serum-free media supplemented with (C, F) or without alendronate (A, B, D, E) overnight. Following incubation, a collagen sponge containing 150 µg/mL BMP2 InductOs™(+IOs) or 0 µg/mL BMP2 (-IOs) was placed on the defect region of bone cylinders before culture implantation on CAM for 9 days. Representative images of paraffin sections stained for Alcian Blue and Sirius Red (A-C), and Cathepsin K immunostaining (D-E). Positive immunostaining in brown-red colour, counterstained with Alcian Blue to visualize the matrix content. (TB) trabecular bone, (CAM) chorioallantoic membrane. (ALD) alendronate. Scale bars equivalent to 50 µm.

In this chapter, a commercially available treatment in orthopaedics (hrBMP2; InductOs^{TM}) was used to induce bone formation. InductOs™ increased significantly bone volume measurements of the bone cylinders culture *in vitro*; however InductOs™ had the opposite effect *in vivo* when bone cylinders were implanted on CAM. Given that the InductOs™ delivery method (mechanical retention by an acellular collagen sponge) results in a single burst release of BMP2, alternative delivery methods based on a more controlled approach could be explored to see if this would improve the osteoinductive properties of BMP2.

5.2.5 Evaluation of Laponite as a hydrogel for tissue engineering

The ultimate aim of the CAM assay for the culture of human bone was to establish a method to test biomaterials for tissue engineering. In order to examine the effect of a controlled and sustained delivery of BMP2 on this human-avian model, a clay-based hydrogel, Laponite, was examined. In order to compare the results of Laponite to InductOs, a concentration of 7.85 µg/mL BMP2, the same as in previous InductOs™ study, was used. In addition, the potential of Laponite to promote bone formation by encapsulating and delivering angiogenic growth factors (VEGF) and cells (endothelial and mesenchymal cells) was examined as well using the CAM-human model.

Initial experiments were designed to evaluate the biocompatibility of Laponite in the human bone cylinders using the CAM assay. A pilot study was conducted to examine any potential negative effects on CAM following the direct contact of Laponite on the bone cylinders. A standard volume of Laponite was applied to the exterior of the bone cylinder to maximise Laponite exposure to CAM, or left as Blank. The hydrogel biocompatibility was assessed by the normal development of the chick embryo following implantation for 7 days, as well as the interaction with the avian membrane histologically. Chick embryo survival rate at harvest was similar between the Laponite (6/8) and Blank (5/8), indicating no negative effects of Laponite on chick development compared to the bone cylinder alone. In addition, Laponite-treated samples exhibited significant integration with the CAM (Figure 5.2.15 A-B), compared to Blank cylinders (Figure 5.2.15 C-D).

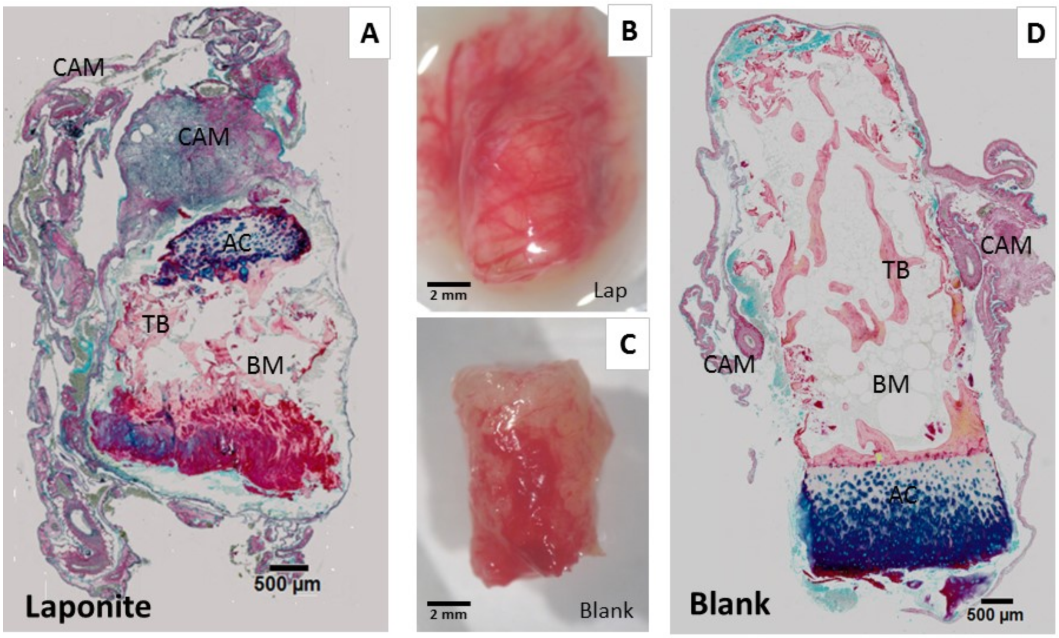

Figure 5.2.15: Bone cylinders with Laponite applied peripherally integrate with the CAM following implantation. A standard volume of Laponite was applied on the periphery of the bone cylinder (A-B) or left as Blank (C-D) before CAM-implantation for 7 days. At harvest, cylinders were imaged (B-C) processed for paraffin section and stained for Alcian blue and Sirius red (A and D). (BM) bone marrow, (TB) trabecular bone, (CAM) chorioallantoic membrane, (AC) articular cartilage. Scale bars equivalent to 500 µm.

The invasion of numerous capillaries and blood vessels from the CAM caused Laponite hydrogel breakdown (Figure 5.2.16 A-C). Laponite fragmentation was evident in the proximity of high cellular density (Figure 5.2.16 B and C). Trabecular bone fragments and avian erythrocytes were entrapped within the broken matrix of Laponite, as indicated by the arrows in Figure 5.2.16 C. Alcian blue and Sirius red staining dyed Laponite in a pinkish colour (Figure 5.2.16 C) and Goldner's Trichrome in green (Figure 5.2.16 B), both pigmentations indicative of collagen tissue, however exhibiting different morphology compared to bone or CAM tissue. Polarised light filter was used to further distinguish between bone collagen matrix and Laponite hydrogel (Supplementary Figure 7.4.8).

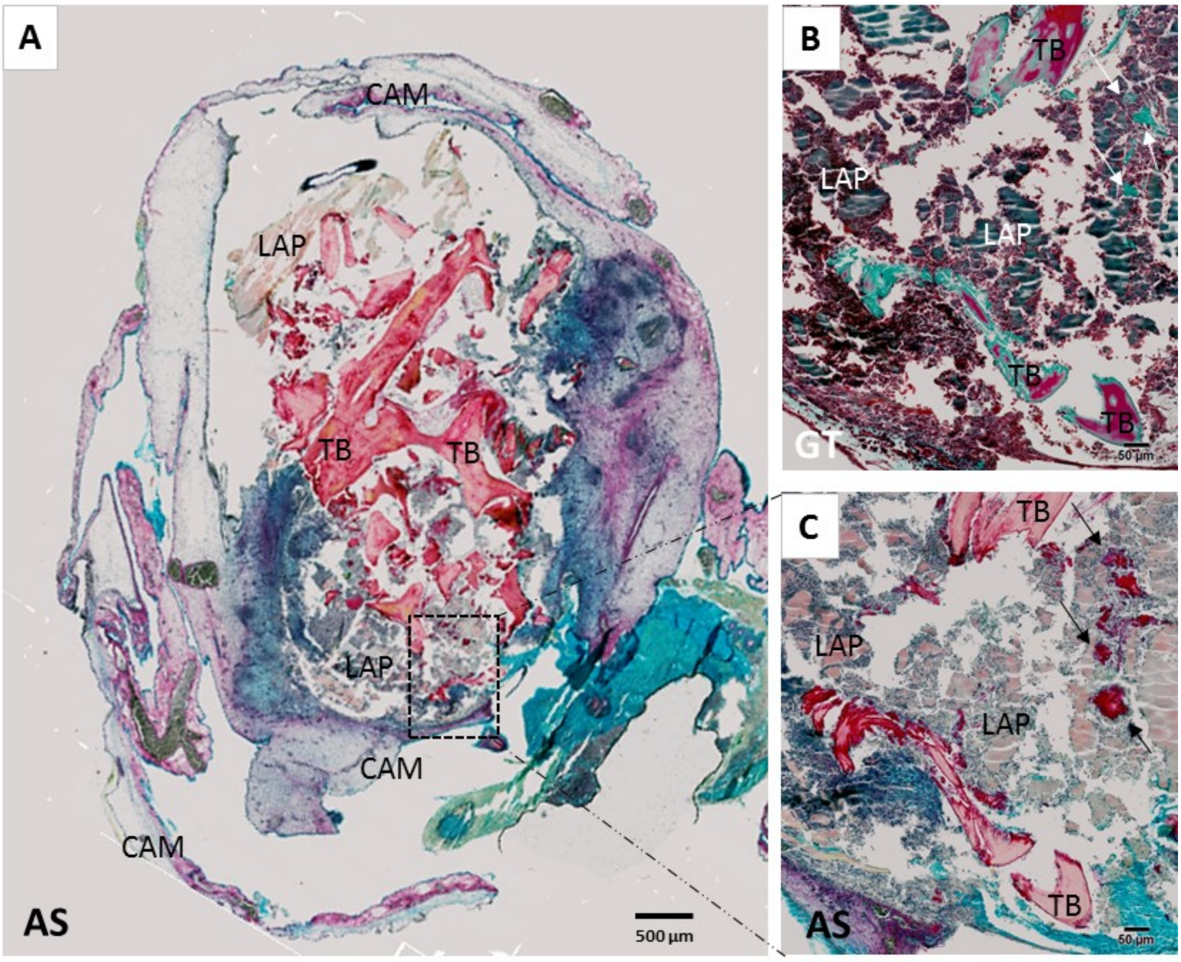

Figure 5.2.16: Laponite delivered to bone cylinders breaks down following CAM-implantation for 7 days. Laponite was applied on the periphery of the bone cylinder before CAM-implantation for 7 days. Consecutive paraffin sections were stained for Alcian blue and Sirius red (A and C) or Goldner's Trichrome (B). Arrows indicate bone debris entrapped within Laponite and avian erythrocytes. LAP (Laponite), (TB) trabecular 150oné, (CAM) chorioallantoic membrane, (AC) articular cartilage. See colour legend in Table 2.6.1. Scale bars equivalent to 500 µm (A) and 50 µm (B-C).

5.2.5.1 Effect of Laponite-BMP2 delivery on human bone cylinders

These initial results showed that peripheral application of Laponite, with immediate contact with the CAM, had no apparent negative effect on biocompatibility as shown by macroscopic and histological evaluation (Figure 5.2.15 and Figure 5.2.16). However, external application of Laponite to the cylinder did not allow for a defined, constrained 'defect' space for the hydrogel, and hence the effect of the treatment would not be localised to any specific region of the bone cylinder. In order to have a standard region of interest, an empty cylinder core ('defect area') was used to perfuse the hydrogel Laponite material; as described in section 2.4.3.1 for more experimental detail.

The delivery of BMP2 InductOs™ via collagen sponge offered a mechanical retention of the growth factor, and hence a single burst release on the bone cylinder. In contrast to that, Laponite encapsulated the protein within the hydrogel matrix, provided a physical retention. To test whether Laponite-BMP2 could elicit an osteoinductive response in the human-avian model, this treatment was tested in bone cylinders from 4 independent experiments were examined in CAM and *in vitro* (see section 2.4.3.1 for more detail). Due to the limited amount of bone cylinders from the same femoral head (donor head size variability), *in vitro* group setup was not always included.

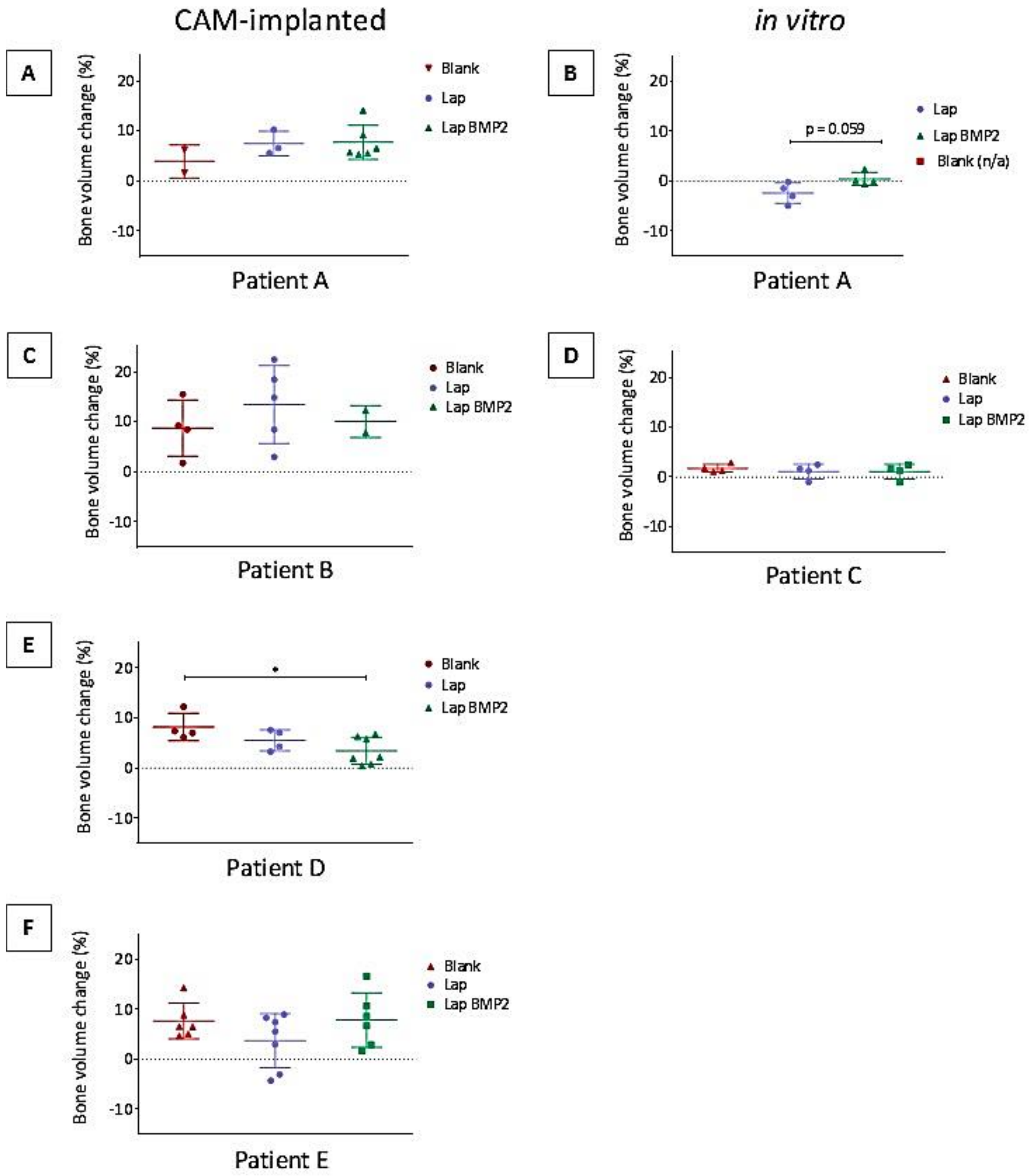

Figure 5.2.17: Laponite- BMP2 delivery in CAM-implanted bone cylinders presented variable response in 5 donor samples. Bone cylinders were treated with Laponite, Laponite-BMP2 (7.85 µg/mL) or Blank followed by *in vitro* culture (B and D) or CAM implantation (A, C, E-F). Data collected from 5 independent experiments: M80 NOF# (A-B), F69 OA (C), M64 OA (D), F67 OA (E) and F81 NOF# (F). Data points indicate relative bone volume change of individual bone cylinders before and after 7-9 days of culture. Error bars indicate mean ± SD, *p<0.05.

In a similar manner to BMP2 InductOs™, *in vitro* cultured cylinders from fractured femoral heads were trending towards significance in bone volume following Laponite BMP2 delivery compared to vehicle control (p=0.059; Figure 5.2.17 B); however this effect was not reproduced in patient donor C (Figure 5.2.17 D). CAM-implantation resulted in a significant increase in bone volume for the blank group with respect to Laponite-BMP2 in an osteoarthritic donor's sample D (p=0.0313; Figure 5.2.17

E). Nevertheless, the three other patients examined exhibited the opposite effect as the trend in increase in bone volume of Laponite BMP2 was similar or greater compared to Blank group (Figure 5.2.17 A, C and F). Hence, the effect of BMP2 delivery on CAM-implantation was variable between donor samples, with no clear pattern between osteoarthritic and osteoporotic phenotype bone cylinders (Figure 5.2.17 A, C, E and F).

Histological examination of donor samples with opposite response pattern to Laponite BMP2 (Figure 5.2.17 A-B: Patient A and Figure 5.2.17 E: Patient D) showed different morphological features for the treatments with higher bone volume change. Bone cylinders from patient D exhibited a significant increase in bone volume when implanted as Blank; histological examination showed the presence of a mixture of proteoglycan-rich matrix, sprouting from pre-existing trabecular located on the CAM-bone interface (see arrows Figure 5.2.18 A, B).

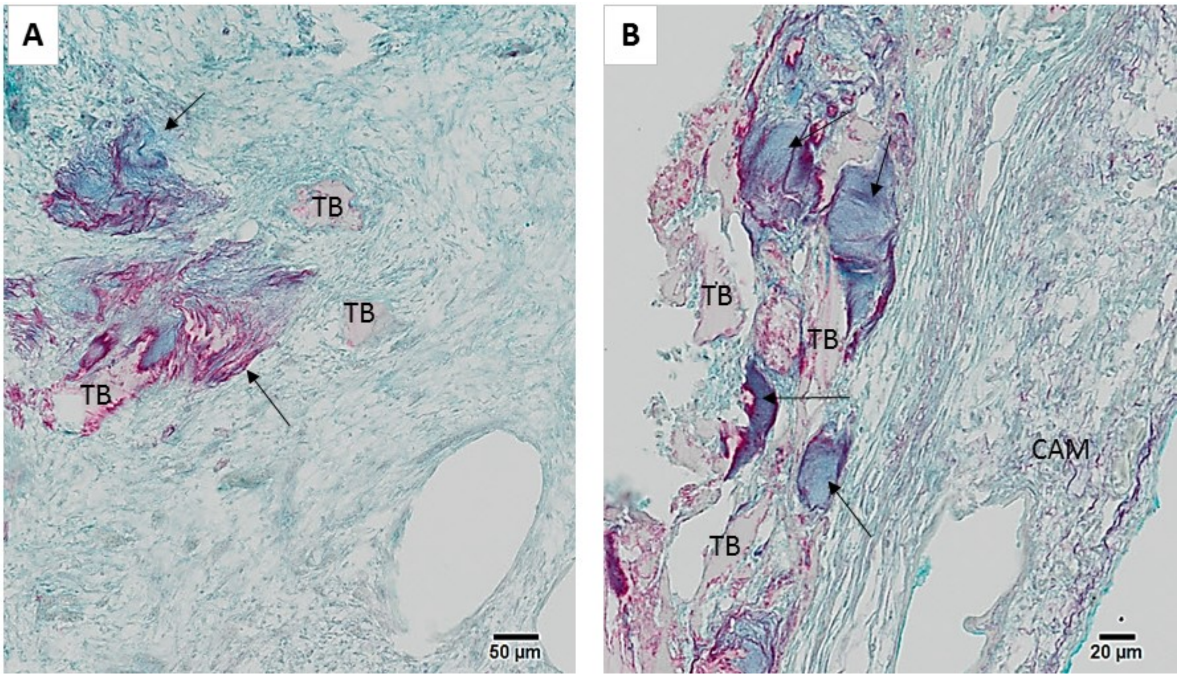

Figure 5.2.18: Deposition of new tissue on the Blank group of bone cylinders from Donor D (F67 OA). Freshly isolated bone cylinders from F67 OA were CAM-implanted. Paraffin sections were stained with Alcian Blue (proteoglycan) and Sirius Red (collagen). (TB) trabecular bone, (CAM) chorioallantoic membrane. Arrows indicate newly formed tissue. See colour legend in Table 2.6.1. Scale bars equivalent to 50 µm (A) and 20 µm (B).

In contrast, Donor A showed the highest increase in bone volume following Laponite-BMP2 treatment (Figure 5.2.17 A); which histologically showed formation of endochondral cell condensations and no proteoglycan-like matrix deposition (Figure 5.2.19 A-E).

Cell condensations from Donor A were predominant in the bone marrow of the bone cylinder, which was invaded intensively by the CAM tissue. Cell condensations were found in clusters (see asterisks in Figure 5.2.19 B-E) and had collagenous fibres deposited around them as shown by the pink colour of the Sirius red staining (Figure 5.2.19 A). The number of condensations was higher in Laponite BMP2 treatment (10.25 ± 9.01 SD) compared to Blank (2.67 ± 1.67 SD), however not significant. In addition, cell condensations showed expression of Sox9 (Figure 5.2.19 B), and co-localised with immune detection for GFP confirming their avian origin (Figure 5.2.19 D). Collagen type II was laid down in the CAM matrix, whereas collagen type X was intensively expressed around the cell condensations and trabecular bone spicules (Figure 5.2.19 E).

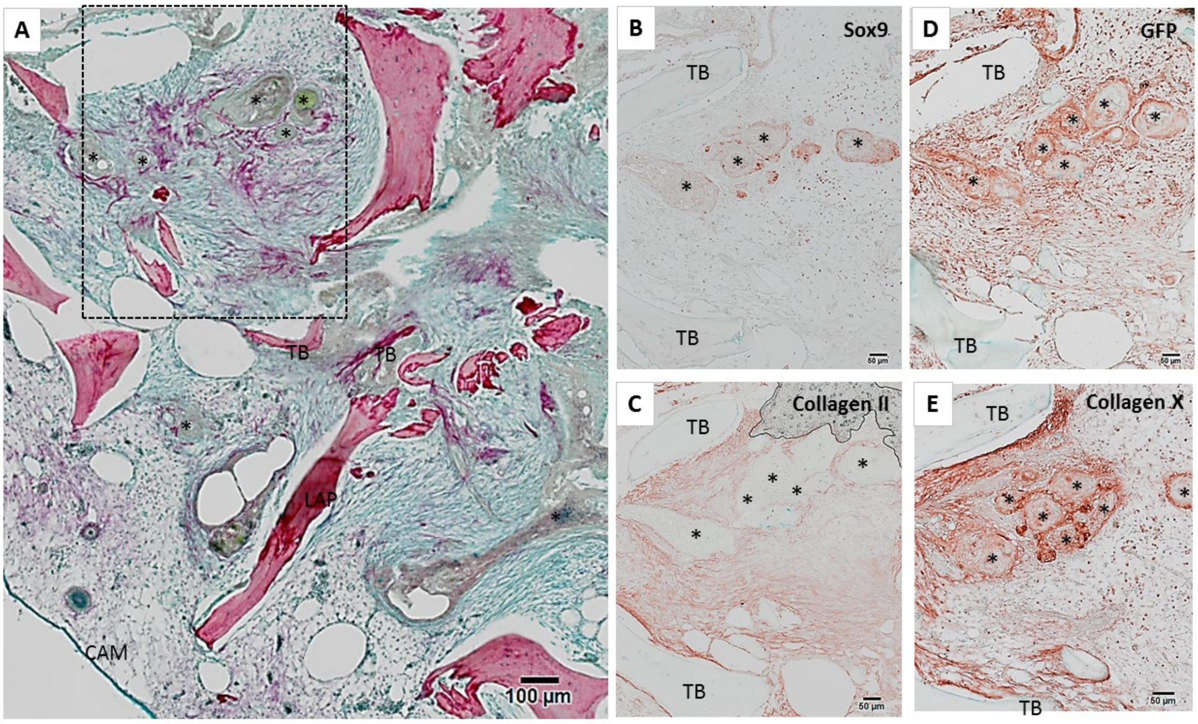

Figure 5.2.19 Formation of endochondral cell condensations following Laponite BMP2 delivery on bone cylinders from M80 NOF#. Freshly isolated bone cylinders from M80 NOF were perfused with Laponite containing 7.85 ug/ml before CAM-implantation. Consecutive paraffin sections were stained with Alcian blue and Sirius red staining (A) and immunohistochemistry for Sox9 (B), GFP (D), Collagen type II (D) and Collagen type X (E). Positive immunostaining in brown-red colour, counterstained with Alcian blue to visualize the matrix content. *Indicates cell condensations. (TB) trabecular bone, (CAM) chorioallantoic membrane, (LAP) Laponite. Scale bars equivalent to 100 µm (A) and 50 µm (B-E).

Additional images of the cell condensations following BMP2 delivery are provided in Supplementary Figure 7.4.9. The expression of Sox9 was variable among cell condensations: high expression of Sox9 could be throughout or just on the outer periphery of the concentric structure (Supplementary Figure 7.4.9 B). Again, these cells originated from avian tissue as those cells co-localised with GFP immunodetection (Supplementary Figure 7.4.9)

To test whether the above response(s) to Laponite and BMP2 delivery were dependent on the presence of human bone cells in the implanted bone cylinders, grafts were first decellularised prior to implantation. In short, bone cylinders were treated with H_2O_2 for three days, thoroughly washed, and then perfused with Laponite, Laponite BMP2 or Blank before CAM-implantation.

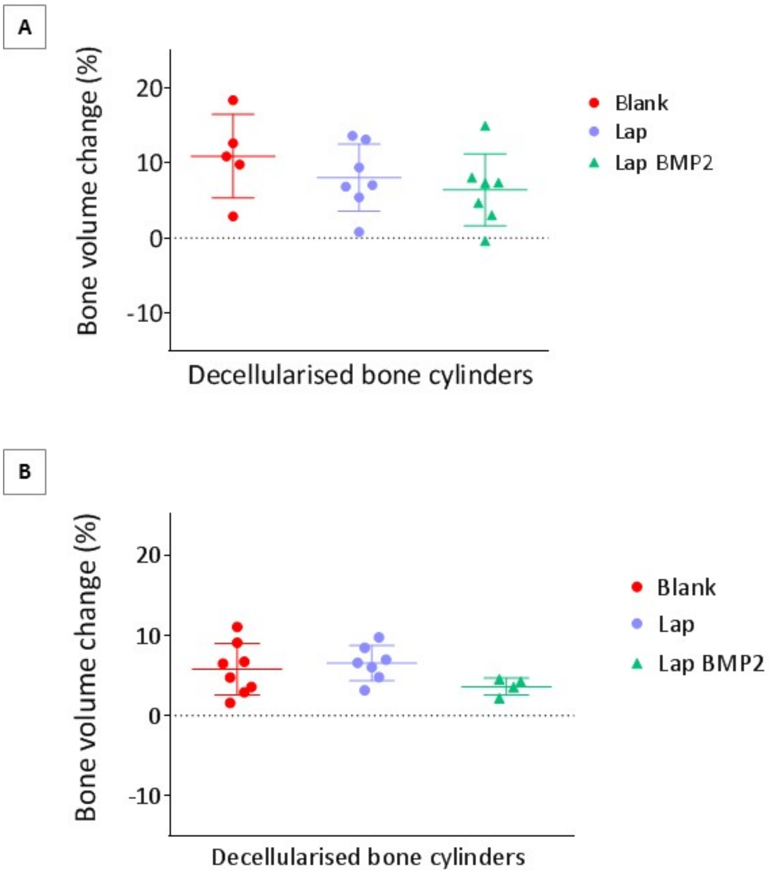

Figure 5.2.20: Variable response of acellular bone cylinder to Laponite containing BMP2. Bone cylinders were decellularized with H_2O_2 before Laponite, Laponite and BMP2 or left as Blank perfusion on the defect region, followed by CAM implantation. Two independent experiments conducted with M59 (A) and F82 (B). Data points indicate relative bone volume change of individual bone cylinders before and after 7-9 days culture. Error bars indicate mean ± SD, $^*p<0.05$.

No significant differences were observed in either of the two experimental repeats, though there was an underlying reduction in bone volume for the Laponite BMP2 treatment (Figure 5.2.20 A-B). This similar trend was previously shown when using viable human bone cylinders (Figure 5.2.17 E). However, in the decellularised experiment the Blank and Laponite groups showed a similar bone volume change (Figure 5.2.20 B), instead of a reduction in Laponite group compared to Blank, as shown in the ‘live’ cylinders (Figure 5.2.17 E). However none of the previous results were significant.

The decellularised bone cylinders shown in Figure 5.2.20 C were further analysed histologically and showed similar CAM-integration as standard cultured ones (Figure 5.2.21 A). The marrow space was invaded by the CAM tissue, confirmed by the extensive invasion of cells and matrix from the avian membrane, as shown in the GFP immunostaining (Figure 5.2.21 D). However, even if there was a minimum presence of Sox9 positive cells (Figure 5.2.21 E), the number of cell condensation clusters was negligible.

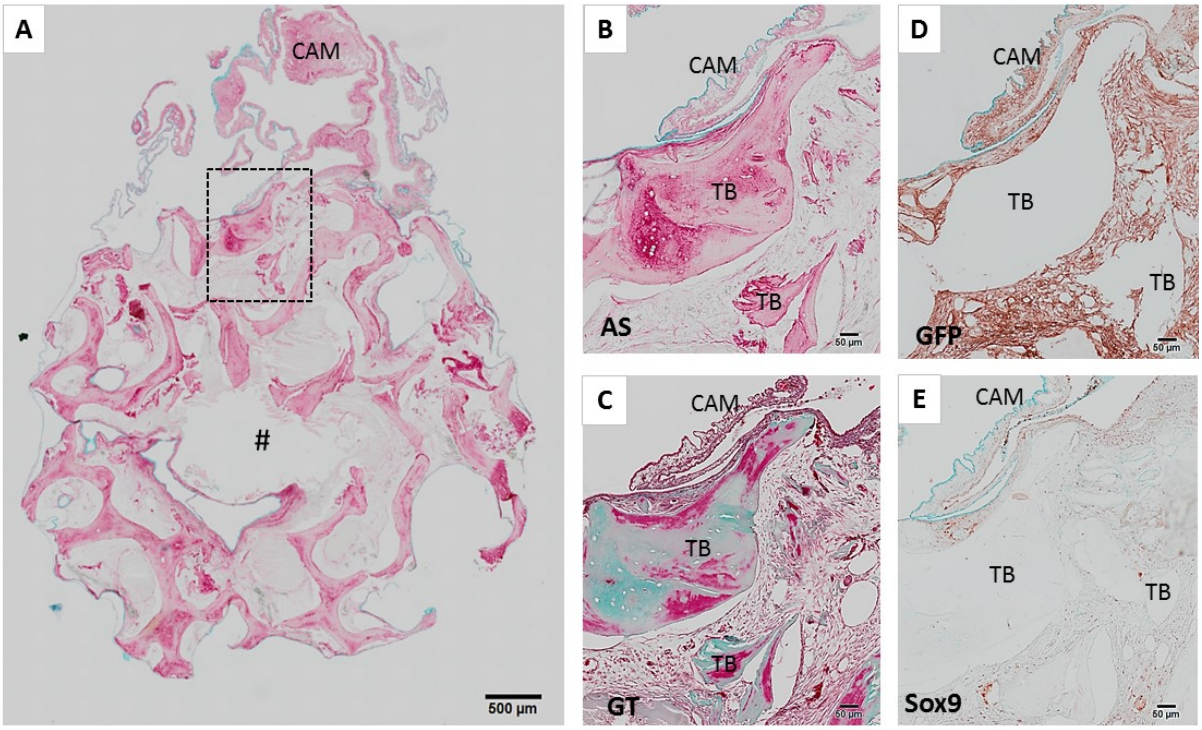

Figure 5.2.21: H_2O_2-treated bone cylinders experience CAM interaction and integration, although with minimal expression of Sox9 in cells. Freshly isolated bone cylinders were decellularised with H_2O_2 for 3 days followed by thorough washes. Plain Laponite was perfused in the defect region of the bone cylinders before CAM-implantation. Consecutive paraffin sections were stained for Alcian blue and Sirius red staining (A-B), Goldner's Trichrome (C) and immunohistochemistry for GFP (D) and Sox9 (E). Positive immunostaining in brown-red colour, counterstained with Alcian blue to visualize the matrix content. # Indicates the location of Laponite on the bone cylinder defect region. (TB) trabecular bone, (CAM) chorioallantoic membrane. Scale bars equivalent to 100 µm (A) and 50 µm (B-E).

Cellularised matrix was found in the junction between the CAM blood vessels and Laponite tissue (see arrows Figure 5.2.22 A-D), with also neighbouring deposition of collagen fibres, as shown by the pink colour on the Sirius red staining and in green for the Goldner's Trichrome (see dashed arrows Figure 5.2.22 A-D).

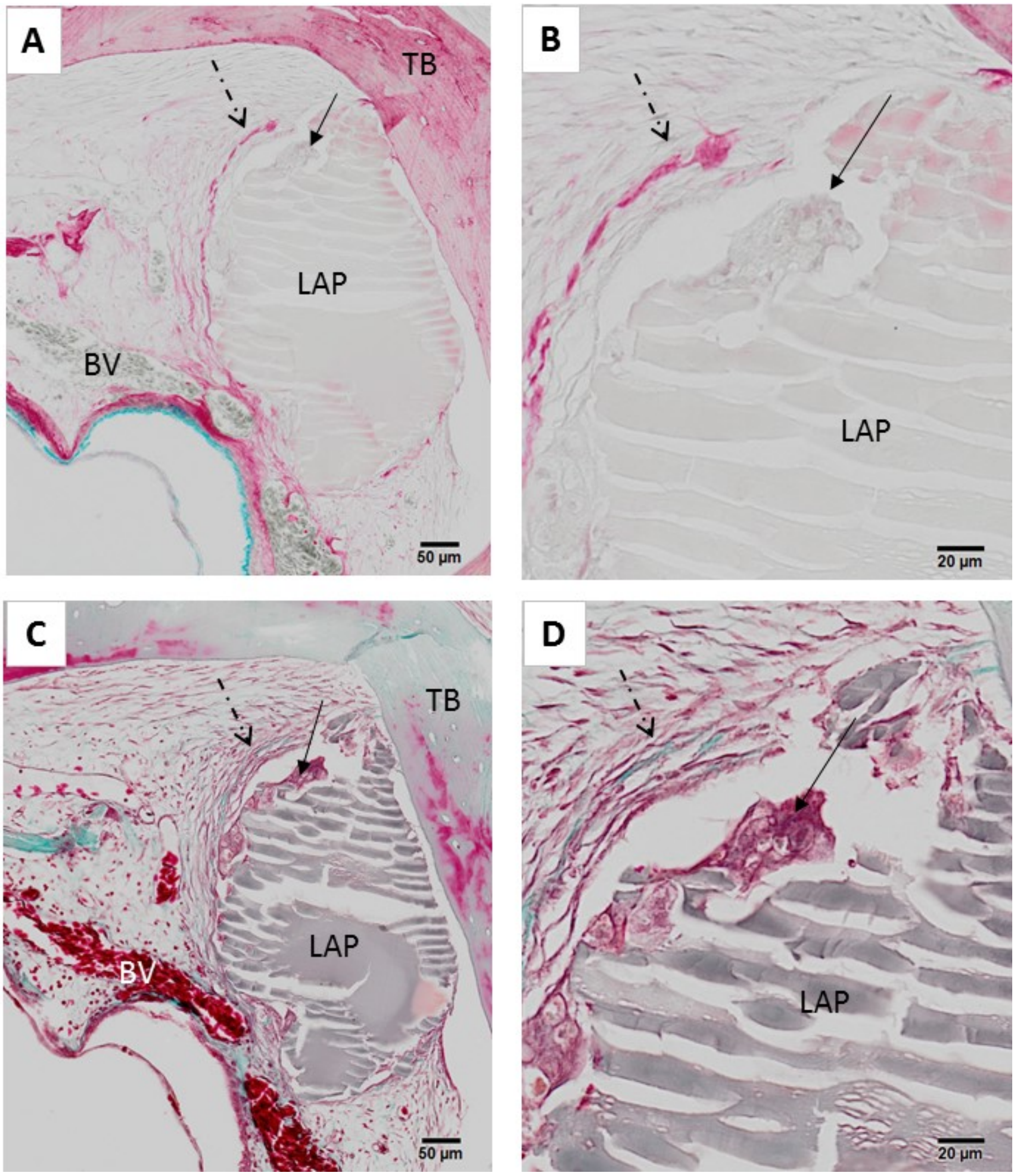

Figure 5.2.22: Cellular and collagen deposition on the CAM-Laponite interface on bone cylinders H_2O_2-treated. Freshly isolated bone cylinders were decellularised with H_2O_2 for 3 days followed by thorough PBS washes. Plain Laponite was perfused in the defect region of the bone cylinders before CAM-implantation. Consecutive paraffin sections were stained for Alcian blue and Sirius red staining (A-B) and Goldner's Trichrome (C-D). Dashed arrows indicate location of collagen deposition; solid arrow indicates cellular aggregations around Laponite. (TB) trabecular bone, (CAM) chorioallantoic membrane, (LAP) laponite, (BV) avian blood vessel. See colour legend in Table 2.6.1. Scale bars equivalent to 50 µm (A, C) and 20 µm (B, D).

In summary, delivery of Laponite-BMP2 to appeared to significantly reduce bone volume formation compared to the other treatments consistently in one out of four independent experiments, accompanied by formation of endochondral cell condensations. The same treatment applied to decellularised bone cylinders did not appear to elicit any changes in X-ray dense material deposition or formation of cell condensations.

5.2.5.2 Effect of Laponite-VEGF delivery on human bone cylinders

Having tested the ability of the CAM-human model to observe differences following the addition of an osteoinductive protein (BMP2), the next question to address was if the addition of an angiogenic growth factor, a potent stimulator of the CAM, would have an effect on the formation of bone. As described in Methods section 0, empty core of bone cylinders from the same donor was perfused with Laponite, Laponite VEGF or left as Blank before CAM-implantation or *in vitro* culture for 7-9 days.

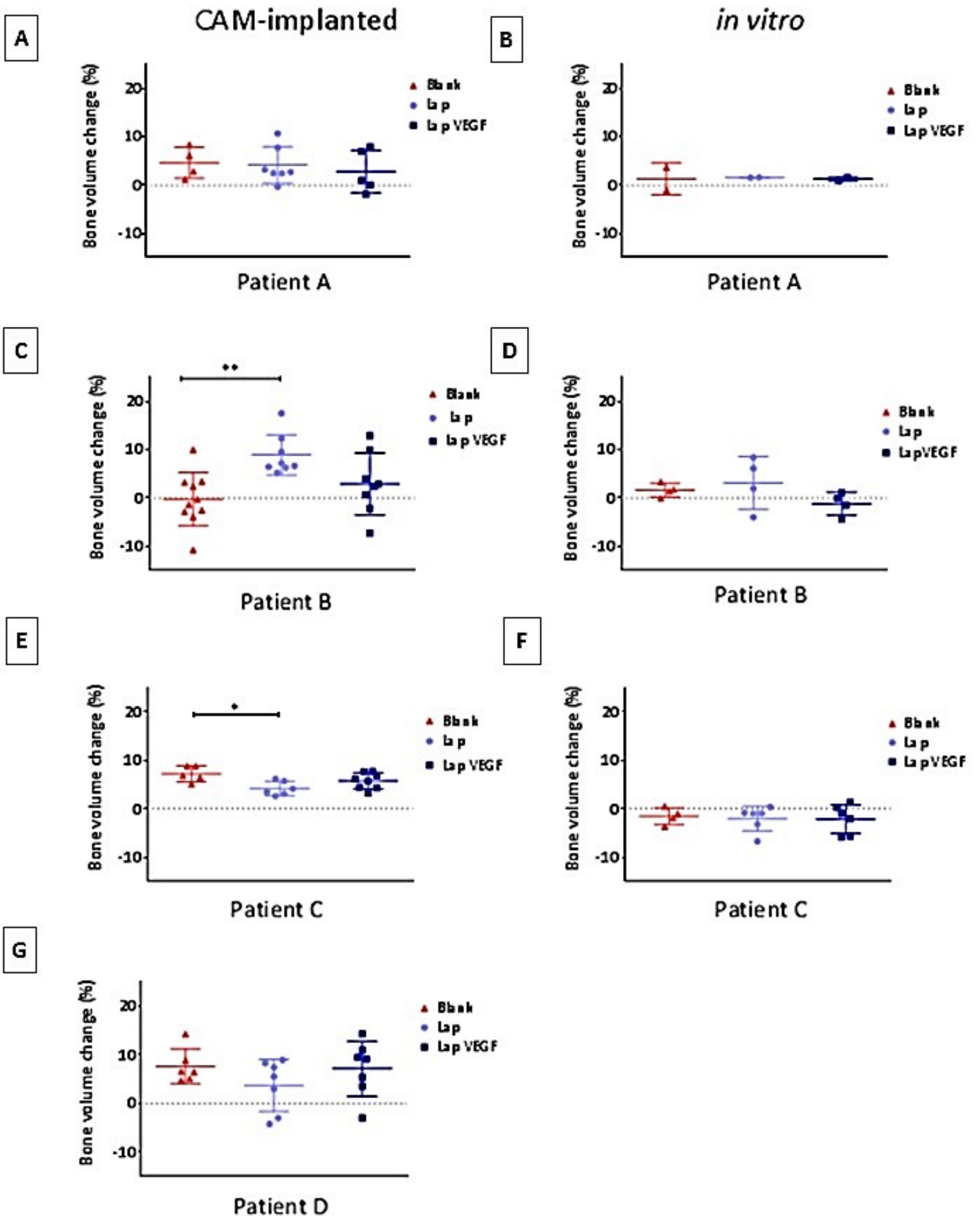

Figure 5.2.23: Laponite-VEGF delivery in CAM-implanted bone cylinders variable response in 5 patient donor samples. Bone cylinders were treated with Laponite, Laponite and VEGF or left as Blank and cultured *in vitro* (B, D and F) or CAM implanted (A, C, E and G). Data collected from 4 independent experiments; donors A-D, respectively: M49, F85 NOF#, M68 OA and F81 NOF#. Data points indicate relative bone volume change of individual bone cylinders before and after 7-9 days culture. Error bars indicate mean ± SD, *p<0.05.

In general, *in vitro* incubation of bone cylinders did not show any differences between treatments (Figure 5.2.23 B, D and F); due to limited amount of bone cylinders from the same femoral head, *in vitro* groups were not always available. CAM-implantation did show significant changes, however varied between donors (Figure 5.2.23 A, C, E and G). Patient donors C and D showed lower bone volume change for Laponite treatment ($p<0.05$; Figure 5.2.23 E, G); whereas Donor B for the same treatment showed the highest increase in bone volume ($p<0.01$; Figure 5.2.23 C). Notice that Donor B showed a negative baseline response in the Blank group (-0.26 % ± 5.5 SD), significantly different ($p<0.01$) to the standard baseline response in bone volume change (7.7 ± 1.75 SD; data obtained from 6 independent experiments Supplementary Table 7.3.1; Supplementary Figure 7.3.3).

Histological analysis of Patient B showed deposition of cartilaginous matrix on the outer periphery of the Laponite-treated bone cylinders (Figure 5.2.24 A-E), indicating positive collagen type II staining (Figure 5.2.24 D). New matrix deposition was found sprouting from pre-existing trabeculae (Supplementary Figure 7.4.10 A-C) as shown by specific type II staining on the emerging matrix (Supplementary Figure 7.4.10 D) and the disorganised fibre arrangement under the polarised filter (Supplementary Figure 7.4.10 E).

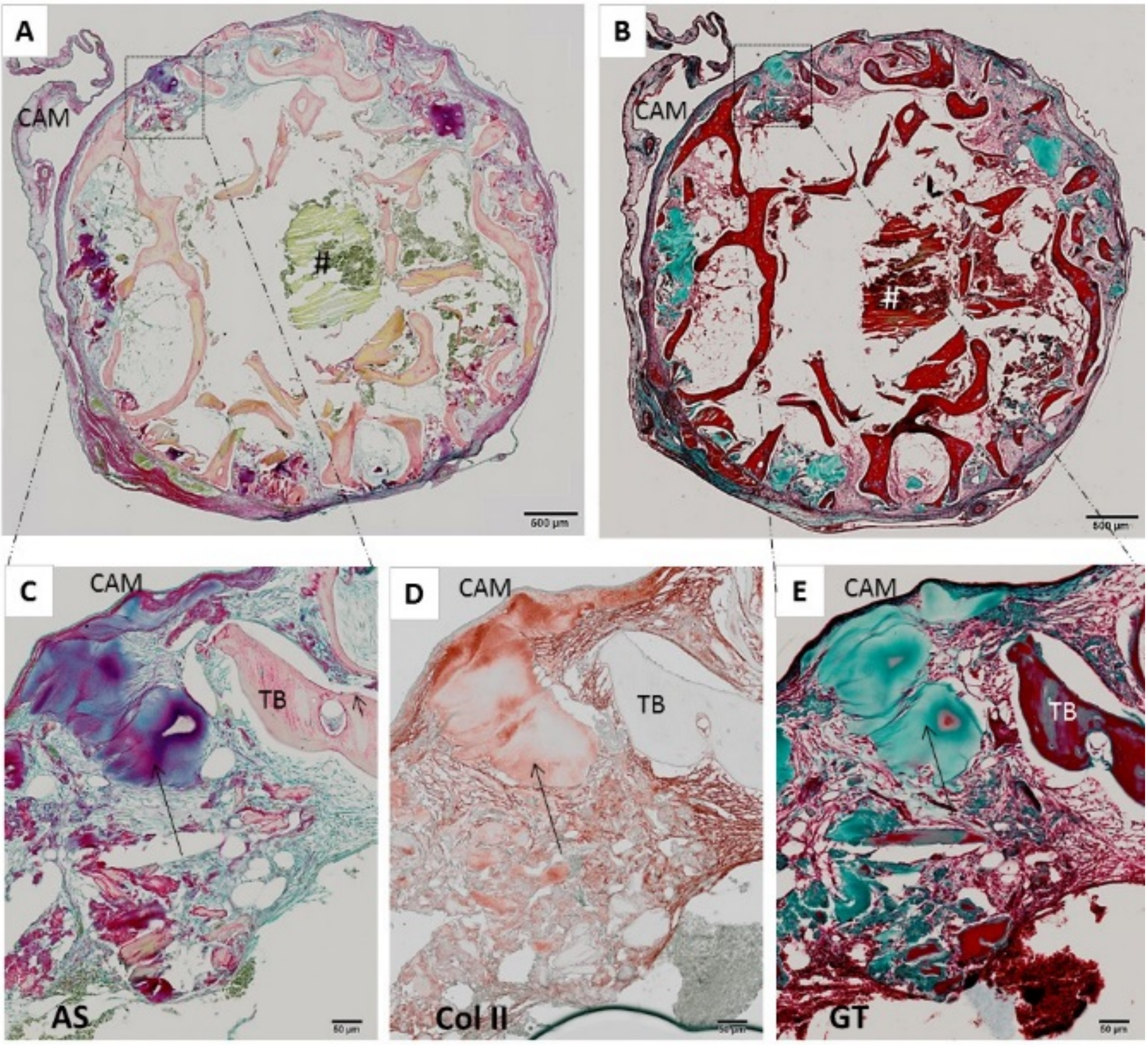

Figure 5.2.24: Matrix deposition on bone-CAM periphery of Laponite treated bone cylinders from F85 NOF#. Plain Laponite was perfused in the defect region of the bone cylinders from F85 NOF# before CAM-implantation. Consecutive paraffin sections were stained with Alcian blue and Sirius red (A, C) and Goldner's Trichrome (B, E) and immunohistochemistry for Collagen type II (D). Positive immunostaining in brown-red colour, counterstained with Alcian blue to visualize the matrix content. Arrows indicate location of matrix deposition. (TB) trabecular bone, (CAM) chorioallantoic membrane, (LAP) Laponite, # indicates Laponite location on the bone cylinder defect region. See colour legend in Table 2.6.1. Scale bars equivalent to 100 µm (A) and 50 µm (B-E).

Bone volume change from Donor C (M68 OA) showed a the lowest increase in bone volume for the Laponite VEGF group ($p<0.05$; Figure 5.2.23); however histological examination of the same samples showed deposition of collagen type II (see arrows Figure 5.2.25 A, D, G) in the vicinity of Sox9 + cell condensations and avian blood vessels from the CAM (see asterisk Figure 5.2.25 B). In addition, the core of the bone cylinder where the hydrogel was perfused was extensively invaded by CAM tissue (see # in Figure 5.2.25 F).

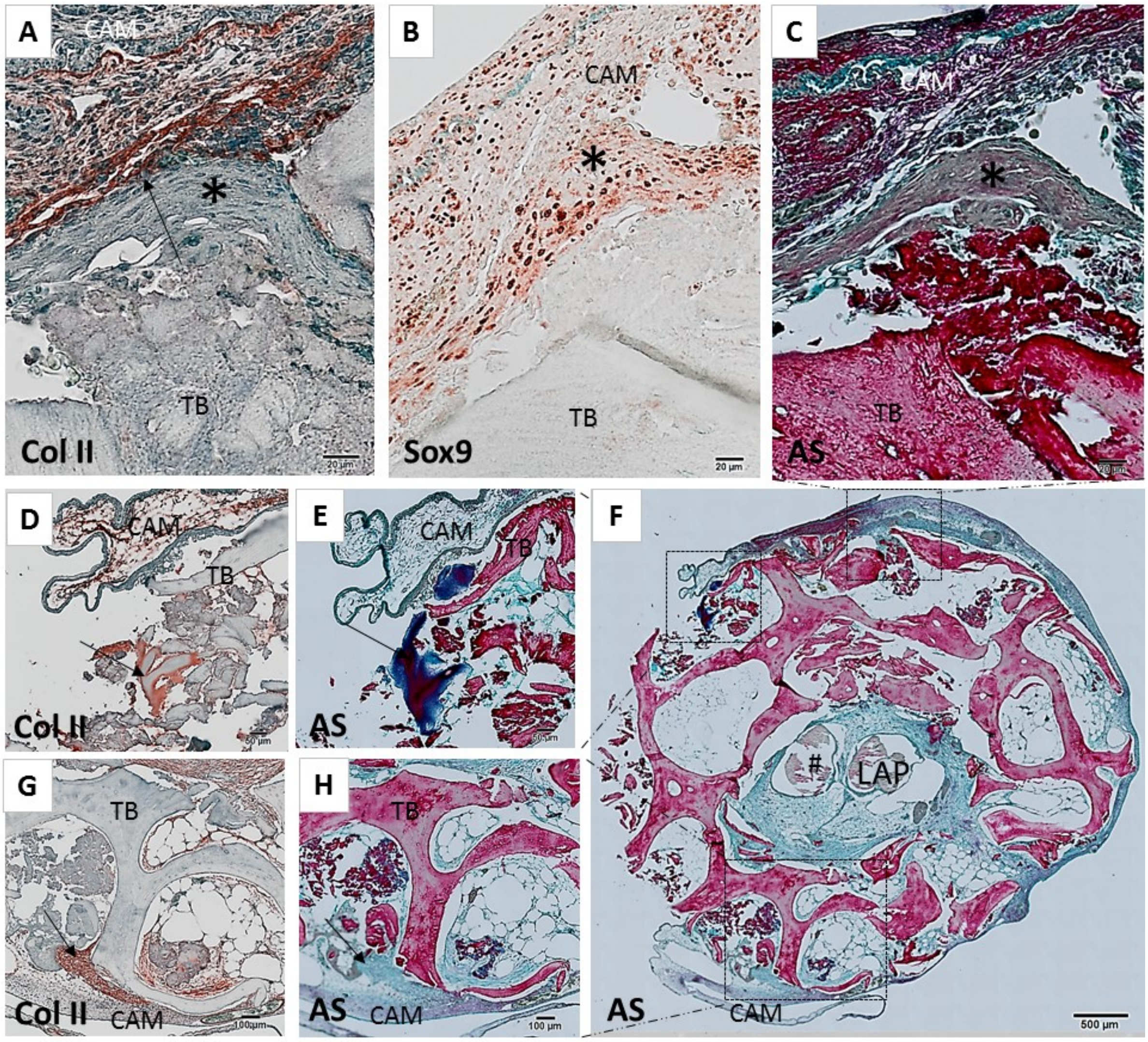

Figure 5.2.25: Cell condensations and collagen deposition on the CAM-bone interface on bone cylinders from Donor C (M68 OA) following the application of Laponite-VEGF. Laponite containing 150 µg/ml hr-VEGF$_{165}$ was perfused in the defect region of the bone cylinders from M68 OA before CAM-implantation. Consecutive paraffin sections were prepared for immunohistochemistry of Collagen type II (A, D, G), Sox9 (B) and Alcian blue and Sirius red staining (C, E, H and F). Positive immunostaining in brown-red colour, counterstained with Alcian blue to visualize the matrix content. Arrows indicate matrix deposition. (TB) trabecular bone, (CAM) chorioallantoic membrane. Scale bars equivalent to 20 µm (A-C), 50 µm (D, E), 100 µm (G, H) and 500 µm (F).

In summary, two out of four independent experiments showed lesser bone formation for the Laponite group in comparison to Laponite VEGF and blank, and this effect was also associated with formation of Sox9+ cell condensations and extracellular matrix deposition. Hence, delivery of Laponite-VEGF on the CAM-implanted bone cylinders appeared to elicit apparent changes between treatments, however not consistently between independent experiments.

5.2.5.3 Effect of Laponite-primary cells delivery on human bone cylinders

In order to observe whether the delivery of cells would have a modulatory effect on bone deposition, two different primary cell types were isolated from human tissue: human umbilical vein endothelial cells (ECs) and human bone marrow stromal cells (SSCs). See section 2.3.42.3.5and 2.3.5 for more detail. These cells types were pre-mixed individually or together with Laponite to be applied in bone cylinder defect (see section 2.4.3.3 for more detail). Plain Laponite and Blank bone cylinders were included as well as controls for CAM-implantation.

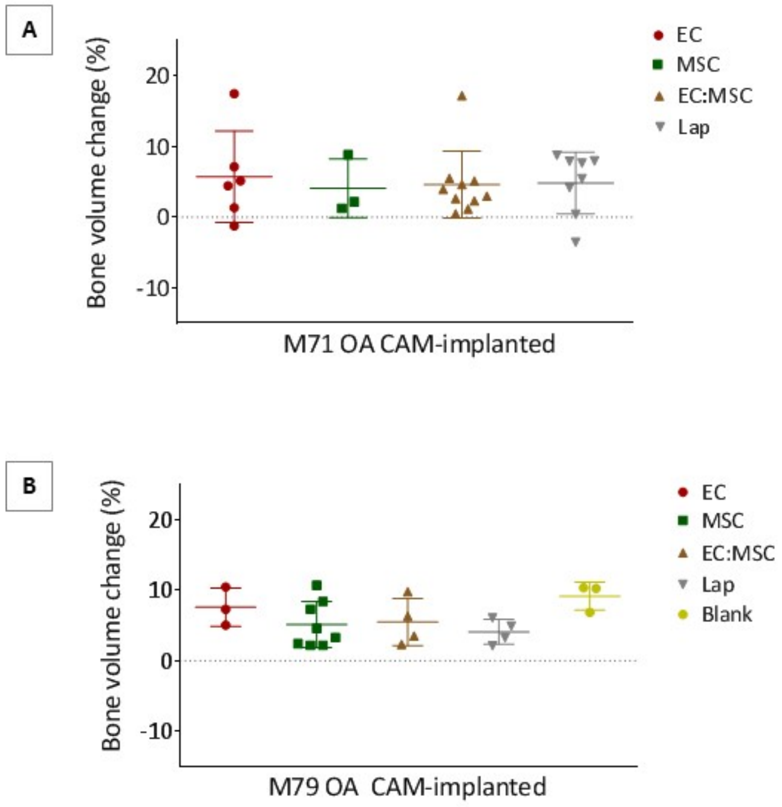

Figure 5.2.26: Primary cell delivery using Laponite as a hydrogel vehicle does not elicit changes in bone volume. Bone cylinders were perfused with Laponite-EC, Laponite-SSC, Laponite EC:SSC, Laponite vehicle control or left as Blank followed by CAM implantation. Two independent experiments M71 OA (A) and M79 OA (B). Data points indicate relative bone volume change of individual bone cylinders before and after 7-9 days culture. Human umbilical vein endothelial cells (EC); human bone marrow stromal cells (SSC), Laponite (Lap). Error bars indicate mean ± SD.

No obvious differences were shown between mono or co-delivery of cells, however the delivery of endothelial cells (ECs) appeared to cause a similar increase in bone volume compared to Blank group (Figure 5.2.26 A-B). In accordance to the previous results shown in this section, Laponite vehicle group had the lesser increase in bone volume (Figure 5.2.26 A-B), however not statistically significant. Formation of multiple cell condensations were found throughout the bone cylinder following SSC and EC delivery (see asterisk on Figure 5.2.27 A, C and D) as well as deposition of collagenous matrix (Figure 5.2.27 E). Notice as well the empty cavities left by the human on the Laponite hydrogel located at the defect region of the bone cylinder (Figure 5.2.27 B).

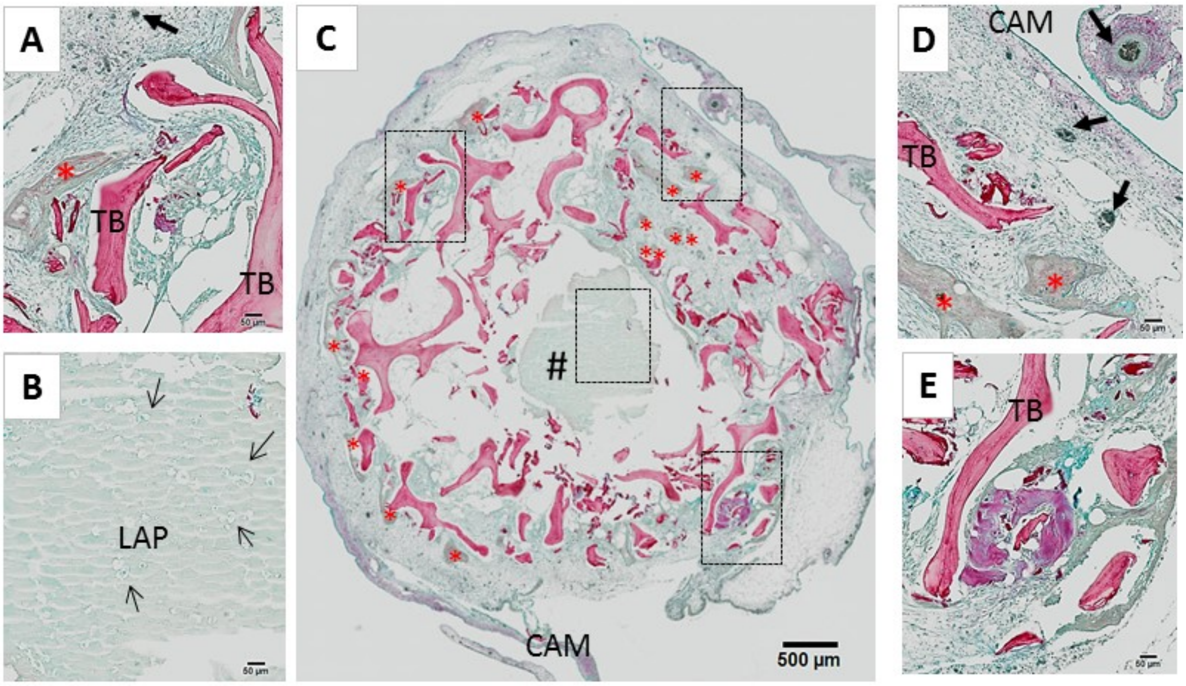

Figure 5.2.27: Formation of numerous cell condensations following delivery of primary cells encapsulated in Laponite on bone cylinders from M79 OA. Laponite containing both ECs and SSC was perfused in the defect region of the bone cylinders from M79 OA before CAM-implantation. Paraffin sections stained with Alcian blue and Sirius red, low magnification (C) and high magnification (A, B, D, and E). Arrows indicate empty cell cavities on Laponite hydrogel. *indicate cell condensations. (TB) trabecular bone, (CAM) chorioallantoic membrane. Scale bars equivalent to 50 µm (A, B, D, E) and 500 µm (C).

In the junction between the CAM, bone and biomaterial, matrix deposition surrounded by cells was observed in Laponite-EC group (Figure 5.2.28). Those tightly packed cobblestone cells and the matrix around them stained in a similar pattern to osteoid on Masson Tetrachrome, as shown by the blue coloured matrix surrounding the cells (Figure 5.2.28 D). In addition, these cells were positive for Sox9 and GFP (Figure 5.2.28 C and D), demonstrating the chondroprogenitor nature of the avian cells.

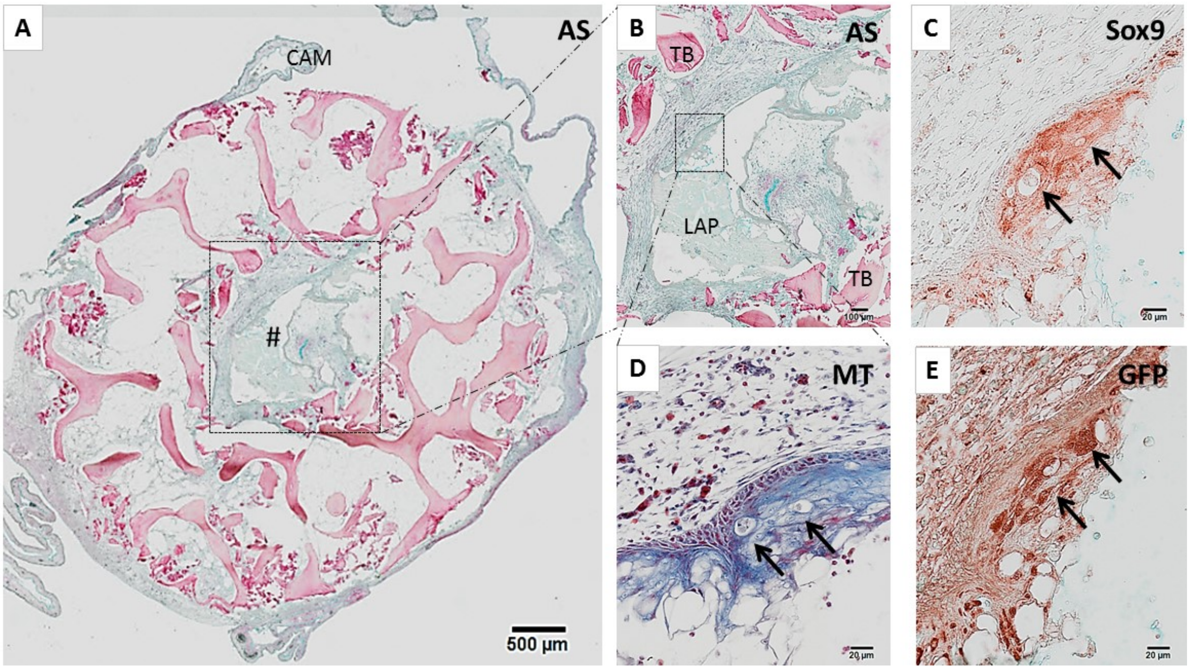

Figure 5.2.28: Osteoid deposition in the vicinity to Laponite containing endothelial primary cells from bone cylinders. Laponite containing ECs was perfused in the defect region of the bone cylinders from M79 OA before CAM-implantation. Consecutive paraffin sections were stained with Alcian blue and Sirius red (A-B), Masson's Tetrachrome: osteoid in blue; mature bone in orange-red (D) and immunohistochemistry for Sox9 (C) and GFP (E). Positive immunostaining in brown-red colour, counterstained with Alcian blue to visualize the matrix content. Arrows indicate cell within osteoid matrix. (TB) trabecular bone, (CAM) chorioallantoic membrane. See colour legend in Table 2.6.1. Scale bars equivalent to 500 µm (A) and 20 µm (B-E).

High magnification images of the defect region from the same sample show the presence cells to be confined within the Laponite hydrogel (see arrows Figure 5.2.29 A-B). GFP immunostaining identified their avian origin, and these cells formed a tightly aligned cell condensation with matrix deposition around the biomaterial, as indicated by the osteoid colour upon Masson Tetrachrome staining (see asterisk Figure 5.2.29 B-C). Besides displaying different shapes, cell condensations exhibited variable levels of GFP expression on the CAM-implanted bone cylinders.

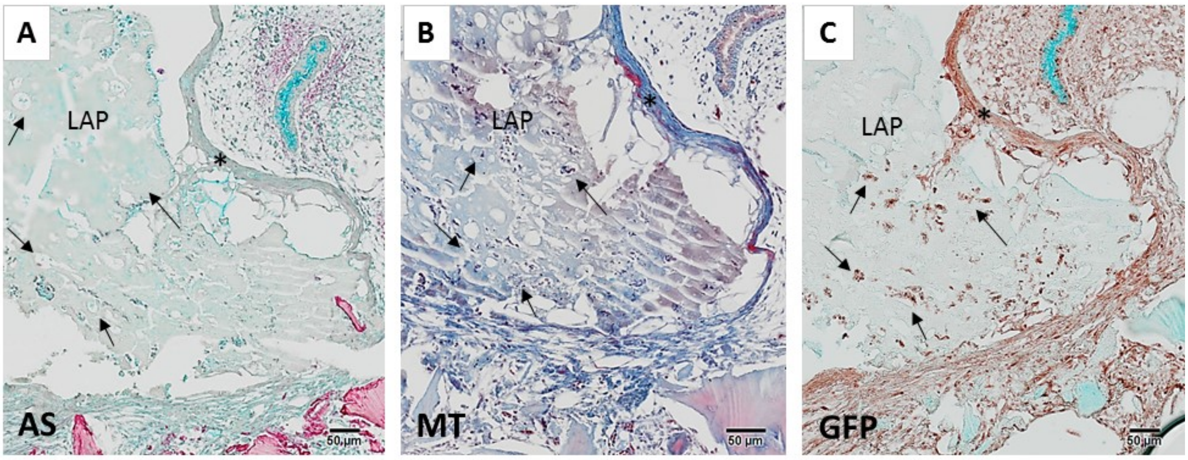

Figure 5.2.29: Avian cells within hydrogel of bone cylinders treated with Laponite containing human primary cells. Laponite containing ECs was perfused in the defect region of the bone cylinders from M79 OA before CAM-implantation. Consecutive paraffin sections were stained with Alcian blue and Sirius red (A), Masson's Tetrachrome: osteoid in blue; mature bone in orange-red (B) and immunohistochemistry for GFP (C). Arrows indicate avian cells within Laponite matrix. *indicate cell condensations structures. (TB) trabecular bone, (CAM) chorioallantoic membrane. See colour legend in Table 2.6.1. Scale bars equivalent to 50 µm.

In summary, even if histological examination appeared to show osteoblast-like cells in the vicinity of newly deposited matrix, µCT analysis did not show any difference following the delivery of Laponite in combination with ECs and SSCs primary human cells.

5.3 Discussion

The experiments described in this chapter addressed two different aims: first the visualisation and analysis of the newly formed bone following CAM-implantation, and second the evaluation of the human-avian model to respond to biomaterial treatments (*i.e.* BMP2, VEGF delivery). In summary, the current studies have shown that:

- 3D registration can be applied to the human bone cylinders and the ability of this image processing method to allow identifying the bone mineral density of the newly formed bone.

- Deposition of new tissue on the CAM-implanted bone cylinders was driven by the native osteoinductive properties of the bone matrix, and was not critically dependent on the presence of the autologous cells in the bone tissue.

- Addition of exogenous BMP2 alone (collagen sponge) on the CAM resulted in formation of endochondral cell condensations (Sox9+/Runx2+), matrix and mineral deposition, however BMP2 delivery on human bone cylinders appeared to induce bone formation *in vitro*, but not *in vivo*.

- Cathepsin K immunostaining suggest that CAM-implantation over a short time might have resulted in an imbalance towards bone resorption, compared to bone deposition.

To visualise the formation and resorption changes in the bone cylinders, 3D registration was performed. The degree of error of 3D registration software was demonstrated in the control samples, which showed presence of mismatched structures while there was no change in bone volume measurements (Figure 5.2.2-3). In a similar manner, Waarsing *et al.* described that a single pixel shift on their registration image resulted in a 15 % mismatch on the total 3D structure, however the same scans did not show any changes for other architectural parameters such as bone volume (J. H. Waarsing *et al.* 2004). This type of error upon 3D registration has been previously examined in the literature when scanning end-point subjects multiple times, for which various studies tried applying different algorithms to improve the outcome of the registered image (Boyd *et al.* 2006; P. Thévenaz, U.E. Ruttimann 1998; J. H. Waarsing *et al.* 2004). Hence, any registration output was the sum of two variables; namely registration error and actual biological change, which at the same time were dependent on the magnitude of the biological change and the scanning resolution.

This limitation was addressed in the present chapter by implementing additional image processing focused specifically on selecting the greyscale image contained in the regions of mismatch (*i.e.* potential newly deposited or resorbed bone; Methods section 2.5.3). This method allowed observation of significant differences on the CAM-implanted cylinders compared to negligible changes on the internal controls, validating the reproducibility of those measurements in four independent experiments (Supplementary Figure 7.4.1-2). Importantly, the difference between the potential newly formed bone (post-diff) and the resorbed tissue (pre-diff) was estimated to have a minimum bone mineral density of 0.14 ± 0.02 g HA/cm^3 at a resolution of 18 µm (Table 5.2.1). This value was relatively lower than the bone mineral density of the *in vivo* scanner phantoms corresponding to trabecular bone (0.25 g HA/cm^3) and cortical bone (0.75 g HA/cm^3). Previous studies scanning at a resolution of 10.5 µm cortical bone of the mouse tibia following mechanical loading established a threshold of 0.813 g HA/cm^3 to quantify bone volume (Birkhold *et al.* 2014). Another study measuring volume of calcified callus in a mouse femur critical size defect used a threshold of 0.55 g HA/cm^3, scanning at a resolution of 12.5 µm (Mehta *et al.* 2010). More recently Kamiya *et al.* scanned the mouse distal femur and the lumbar vertebra using a lower resolution 26.6 µm, reporting an average BMD of 0.12 ± 0.03 g HA/cm^3 and 0.28 g HA/cm^3, respectively, on the control subjects (Kamiya *et al.* 2016). Those previous studies illustrate an important consideration: estimation of bone mineral density depends on the scanning resolution, becoming more conservative with higher resolution and hence compromising the accurate comparison across studies (Bouxsein *et al.* 2010; Christiansen 2016; Jan H Waarsing *et al.* 2004). In any case, it would not be unreasonable to assume that tissue with a much lower, yet positive density, measured in the present study (0.14 g HA/cm^3; Table 5.2.1) might correspond to the early stage mineralisation of newly deposited tissue.

Implantation of decellularised bone cylinders showed a similar increase in bone volume compared to freshly isolated, living bone cylinders following CAM-implantation (Figure 5.2.5). However, BMP2 delivery on *in vitro* cultured bone cylinders resulted in a significant increase in bone formation in a reproducible manner (Figure 5.2.11 and Figure 5.2.17), which could likely be explained by an active process of mineralization by the human osteoblasts. From these results, it was concluded that the increase in bone volume of the CAM-implanted cylinders was mainly attributed to the avian cells, with a minor contribution from the human cells. In agreement with these results, it has been shown that the implantation of extracellular matrix components to the CAM (collagen type I, hyaluronic acid and fibronectin) triggered greater vascular response compared to growth factor delivery (FGF, BMP2, PDGF-BB) (Smith *et al.* 2007). Hence, it was possible that the implantation of bone tissue was a sufficient stimulus for the CAM to induce a reaction, regardless if those contained human living cells or not.

To examine whether the CAM was able to reproduce a model of ectopic bone formation, collagen sponges alone containing 0, 0.125 and 2.4 µg BMP2 were implanted *in vivo* for 9 days followed by X-rays scanning to quantify the bone volume. In general, the high BMP2 dose showed more bone formation according to the µCT (Figure 5.2.7) and increased formation of cell condensations compared to blank collagen sponges (Figure 5.2.9); however the difference was not significant. Remarkably, the histological processing of the mineralised collagen sponges allowed observing calcium deposition within the cell condensations (Figure 5.2.10), something not available when processing bone cylinders due to decalcification. Previous studies evaluating the effect of growth factors (BMP2, FGF, VEGF) compared to extracellular matrix components (collagen) on the CAM showed that the latter presented with significantly improved response from the avian membrane (Smith *et al.* 2007), which could explain that the vehicle control of BMP2 (acelluar collagen sponge) elicited bone formation by itself.

Another investigation examined the ability of BMP2-collagen sponges to elicit bone formation in a subcutaneous rat model with a range of BMP2 doses (0.46 – 115.3 µg) over a period of 21 days (Wang *et al.* 1990). The authors reported bone formation as early as 5 days post implantation in the rodent model at the highest BMP2 dose (115.3 µg) (Wang *et al.* 1990). In comparison to the present study, the dose of BMP2 was approximately 100 times higher and, even with that dose, bone and cartilage formation were only apparent in half of the implants after 7 days (Wang *et al.* 1990). Similar doses to the ones used in the present study (0.125 and 2.4 µg BMP2) only showed bone formation after 14 and 10 days respectively in the investigation by Wang *et al.* (Wang *et al.* 1990). In addition, those early studies evaluated the collagen sponge in a confined environment (subcutaneous pocket). In contrast, the CAM experiences the movements of the developing chick embryo and, given the low retention of the collagen sponge to the growth factor, it might be possible that the BMP2 effects were not local to the collagen sponge itself or the neighbouring implantation area. Moreover, the sensitivity of the evaluation techniques (2D histomorphometry) proposed by Wang *et al.* might not have provided as much precision compared to the 3D µCT analysis conducted in the present study, which could further explain the differences between the two investigations.

In contrast to the significant increase following BMP2 delivery when cultured *in vitro,* bone cylinders implanted on CAM showed opposite trend (Figure 5.2.11). This effect was proportional to the dose of BMP2, both in the InductOs^{TM} (collagen sponge burst release; Figure 5.2.11) and Laponite materials (controlled release; Figure 5.2.20). Given that CAM-implantation showed active sites of bone remodelling (Cathepsin K+) in the bone tissue, it was hypothesised that BMP2 was promoting osteoclast activity via osteoblast cross-talk. An attempt was made to evaluate the effects of an anti-resorptive drug (alendronate) together with BMP2 delivery; however, results were inconclusive probably due to the use of non-optimal drug concentration (Figure 5.2.13 and Figure 5.2.14). Future experiments could implement additional doses which do not compromise chick embryo viability while having a significant effect on bone resorption.

Histological examination of the CAM-implanted bone cylinders showed formation of Sox9+ and Runx2+ cell condensations following BMP2 delivery (Figure 5.2.12, Figure 5.2.19 and Supplementary Figure 7.4.5). It was unsurprising that those histological features were absent in the *in vitro* culture, since Sox9+ and Runx2+ cells co-localised with cells expressing GFP, only present in the avian cells. In contrast, previous studies exploring live imaging of *in vitro* cell cultures showed that chondroprogenitor cells (Sox9+) could form compacted clusters or condensations in under 3 hours, followed by collagen type II expression (Barna and Niswander 2007). Moreover, expression of collagen type X by avian chondroprogenitors has been previously described as a response of chick embryo derived chondrocytes to hrBMP2; also demonstrating the conserved effect of BMP2 across species (Enomoto-Iwamoto *et al.* 1998).

In the present chapter, two different carrier biomaterials were examined for the delivery of BMP2: a FDA-approved acellular collagen sponge (InductOs^{TM}) and a novel clay-based hydrogel (Laponite). In the first case, the delivery of high BMP2 doses resulted in a decrease in bone volume, however increased formation of cell condensations was observed (Figure 5.2.11). In the case of Laponite, the results appeared more variable among patients (Figure 5.2.17). It was interesting to observe that, when bone volume increase was seen on the absence of growth factors (blank or laponite groups), the histological features of the samples showed deposition of cartilaginous matrix (Figure 5.2.18 and Figure 5.2.24). However, on the instance that Laponite-BMP2 caused a significant reduction on bone volume increase, formation of endochondral-like cell condensations expressing Sox9 and Runx2 were observed (Figure 5.2.19, Figure 5.2.25, Supplementary Figure 7.4.5). These previous observations, together with the fact that it was not possible to assess the actual amount of growth factor delivered from the hydrogel *in vivo*, lead to the speculation that the administration of growth factor may have elicited two different effects: cartilage formation or endochondral bone formation. In support to the previous suggestion, Wang *et al.* described two different patterns of tissue deposition (bone or cartilage) in a model of ectopic bone formation depending on i) the administered dose of BMP2 and ii) the implantation time (Wang *et al.* 1990). The authors reported cartilage deposition for earlier time points and lower BMP2 doses, and bone formation associated with the opposite effect. Hence, it may be possible that the incubation time of the present study (7-9 days) limited the observation of the early stage effects of growth factor delivery, which might have been sufficient to allow for the peak of cartilage or bone formation, in a donor-dependent way.

In the experiments where Laponite-VEGF was examined, a bone volume increase on Blank compared to Laponite group was observed; reproducible in two independent experiments ($p<0.05$; Figure 5.2.23, However, Laponite-VEGF did not appear to elicit any differences with respect the other treatments (Figure 5.2.23). This was an unexpected finding since the rationale behind the delivery of VEGF was to enhance bone formation by attracting blood vessels into the bone cylinder (Kanczler and Oreffo 2008). Numerous studies have reported the osteogenic effect of VEGF delivery on its own and in combination with other growth factors (Kanczler *et al.* 2008; De la Riva *et al.* 2010; Ramazanoglu *et al.* 2013; Zhang *et al.* 2014). An investigation delivering 25 ng/ml of VEGF to the CAM showed significant increase in blood vessel formation (Bai *et al.* 2014). Other studies have implanted VEGF-encapsulated PLGA or PLA hydrogels or scaffolds, inducing the formation of blood vessels from the CAM at a doses approximately around 10 ng/ml (Kanczler *et al.* 2007; Lee *et al.* 2015). In contrast, all of the above VEGF doses were lower compared to the ones used in the present investigation (150 ng/ml) and the assessed outcome was blood vessel formation and not tissue formation. Hence, the results of VEGF delivery using Laponite appeared to be inconclusive, probably due to the short incubation period and the inability to assess growth factor release profile from Laponite hydrogel.

Two independent experiments were conducted to evaluate the effect of primary cell delivery using Laponite, however there were no clear differences between groups (Figure 5.2.26). Due to cell number limitation, the ratio of ECs:SSCs cells was 6:1, thus the cell number for the SSCs monoculture was significantly reduced (approximately 28000 cells/sample) compared to the EC monoculture (approximately 167150 cells/sample). Previous studies conducted on murine models reported increased ectopic bone formation in EC:SSC compared to monoculture (Usami *et al.* 2009), though the number of cells delivered was around 10^7 compared to the 200,000 described here. In addition to higher cell number, future experiments will also include a 1:1 co-culture ratio, since it has been described to have both osteogenic and angiogenic potential in multiple studies (see systematic review by (Hadjizadeh and Doillon 2010).

In conclusion, the results in this chapter have demonstrated the ability of µCT analysis to visualise the location and the bone mineral density of the newly deposited tissue, as well as the capability of the human-avian system to detect changes upon different treatments or interventions (*i.e.* BMP2 delivery).

Chapter 6: Discussion, conclusions and final remarks

6.1 Research summary

As outlined in section 1.7, the main hypothesis under test was that the CAM assay can be used as a surrogate blood supply 'bioreactor' for human living bone grafts, and that tissue repair could be measured using µCT and histology analysis. Hence, the aim of the present thesis was to develop a less-sentient *in vivo* model to study and examine bone tissue regeneration using the chorioallantoic membrane (CAM) of the developing chick embryo. The thesis achieved these aims by showing that:

- Human bone cylinders can be used to mimic a bone defect injury model and their implantation on the CAM resulted in biocompatible integration, as shown by the retained viability of the chick embryos and the integration between the human and avian tissue.

- Avian blood vessels infiltrated the human bone cylinders after CAM-implantation, and viable human cells were recovered from the same cylinders, demonstrating graft viability after *in vivo* implantation.

- µCT analysis of the bone cylinders showed a significant increase in bone volume following CAM-implantation ($p<0.001$), validated on histology by extensive deposition of collagenous matrix and formation of endochondral cell condensations (Runx2+ / Sox9+ / von Kossa).

- CAM-implantation of the bone cylinders showed expression of Cathepsin K, showing the resorption capacity of the CAM and hence demonstrating the bone remodelling capacity of the model.

- Growth factor (BMP2) delivery using two different biomaterials elicited significant differences (even if different to the anticipated effect), validating the use of this human-avian model to assess constructs for bone tissue engineering.

The feasibility of the CAM assay for the culture of human living bone was assessed using two different approaches, as detailed in Chapter 4: Firstly, the viability of the autologous human cells was assessed by explant culture of the bone cylinders following CAM-implantation, demonstrating the capability of the human cells to grow following *in vivo* grafting. Moreover the non-GFP (non-avian) cells were further examined for the expression a specific human marker (HLA) to confirm their human origin (Figure 4.2.5). Secondly, the interaction between the human and avian tissue was assessed macroscopically at harvest, showing complete encapsulation in the membrane with extensive vascularisation around the graft (Figure 4.2.1). These findings were further assessed histologically as shown by the presence of blood vessels carrying nucleated avian erythrocytes, located in the bone marrow of the human bone cylinder (Figure 4.2.2). In addition, the biocompatibility of the human-avian *in vivo* model was demonstrated by the retention of chick embryo viability at harvest, and the absence of a fibrotic (rejection) response to the human graft (Figure 4.2.2).

Bone cylinders were µCT-scanned individually before and after incubation, showing a significant increase ($p<0.001$) in relative bone volume change following CAM-implantation. This finding was corroborated at the histological level as shown by the deposition of collagen and the formation of cell condensations expressing Sox9 and Runx2, both markers of endochondral bone formation (Figure 4.2.11). Not only bone formation but also bone resorption was observed on the CAM-implanted bone cylinders, evidenced by the expression of Cathepsin K, a marker of osteoclast activity (Figure 4.2.9). Likewise, 3D registration of the bone cylinders allowed visualisation of the location of the new mineralised tissue, comparably greater to the *in vitro* and control treatments (Figure 5.2.2). Superposition of the two sequential scans was used to detect the regions of the tissue apposition and identification of corresponding bone mineral density (Figure 5.2.3). Taken together, these findings demonstrated the bone remodelling potential of the human-avian system to test biomaterials.

Bone cylinders were devised to have a concentric defect area to facilitate a region of interest for biomaterial delivery (Figure 3.2.14 and Figure 3.2.15).This bone defect region was perfused with a collagen sponge containing BMP2 to test whether this growth factor could induce bone formation. In marked contrast, BMP2 did not increase bone formation *in vivo,* however, it did have a positive effect *in vitro* (Figure 5.2.11). In the same experiment, BMP2 delivery induced the formation of endochondral cell condensations in the CAM-implanted bone cylinders (Figure 5.2.12). Another biomaterial, a clay-based hydrogel, was used to deliver BMP2 at the defect site, however the results were more challenging to interpret due to different patterns of patient response. Nevertheless, these experiments demonstrated the ability of this human-avian model to show differences between treatment groups, addressing a central aim of the proposed studies.

6.2 Considerations of *in vivo* culture of human, living bone tissue

A critical requirement for the success of the CAM assay for the culture of human living bone was the integration and vascularisation of the CAM in the human tissue. The viability of the human tissue and the complete development of the chick embryo demonstrated good biocompatibility of the model. Other studies implanting xenograft tissue on the CAM reported similar results; human living skin showed complete integration within the CAM mesoderm on approximately 75 % of eggs and also preserved HLA expression in the grafted tissue (Kunzi-Rapp *et al.* 1999). Another study implanting fetal mouse skin described complete integration after 24 hours implantation (Carre *et al.* 2012). The same authors induced a laser wound to the skin graft 48-hours after CAM-implantation, showing scar-less healing after a further 6 days (Carre *et al.* 2012). In contrast to the injury model used in this thesis, the injury was made post-implantation, the graft was healthy fetal tissue and the tissue size was significantly smaller and lighter, hence facilitating CAM-incorporation.

These previous studies demonstrated the biocompatibility between CAM and xenograft implant (Carre *et al.* 2012; Kunzi-Rapp *et al.* 1999). However, there are a number of publications demonstrating a primitive immune response from the developing chick embryo (Bellairs and Osmond 2014; Friend *et al.* 1990; Lafferty and Jones 1969). Valdes *et al.* reported the presence of heterophils, leukocytes and giant cells as well as compact fibre deposition after 1, 7 and 11 days of implantation of cotton threads and bacterial endotoxin, which the authors described as acute (1 day) and chronic fibrotic (7-11 days) responses (Valdes *et al.* 2002). Friend *et al.* described granulation on the site of implantation after stimulation with surfactant and alcohols when testing the acute inflammatory response of the CAM (Friend *et al.* 1990). Another study implanted multiple species grafts (spleen tissue from duck, pigeon, sheep) and detailed rejection as a consequence of the heavy infiltration of mononuclear cells and granulocytes (Lafferty and Jones 1969). In contrast, the same investigation implanted chick embryo femurs on the CAM and the response was described by the author as “synergic”, showing infiltration of CAM blood vessels into the bone tissue. In accordance to that, our study showed loose matrix deposition, rich in proteoglycan and collagenous content, strongly associated with the presence of the avian cells (GFP+) and blood vessels. Given that fibrotic responses are typically associated with disease (Meneghin and Hogaboam 2007), the reported findings further highlight the potential of the CAM assay as a tool to evaluate graft biocompatibility, able to elicit a primary immune response and, in particular for the present investigation, the good interaction between the human living bone and the CAM tissue.

6.3 Challenges and significance of µCT analysis

In the current research bone formation was assessed by measuring changes in the bone cylinder structure before and after incubation. The ability of this method to quantify changes was tested in Chapter 3:, (see section 3.2.2), as shown by the significant loss of bone volume when bone cylinders were exposed to decalcifying solution, compared to the negligible changes in mineral content when the cylinders were not exposed to altered conditions (Figure 3.2.8 and Figure 3.2.9). From those pilot studies it was concluded that internal controls should be scanned in parallel with the treatment samples to ensure the precision of the measurements in the absence of biological changes as well as reproducibility between independent experiments. Employing a medium resolution (18 µm), the µCT scans allowed detecting an average increase of 7.77 % ± 1.8 in bone volume for the CAM-implanted bone cylinders, hence being able to measure the early stages of bone tissue regeneration. In comparison, it is worth noticing that the chick embryo skeleton becomes mineralised over a 8-9-day (EED 11 until EDD 18) period (Kanczler *et al.* 2012; Thompson, Owens, and Wilson 1989), hence, it was unsurprising that the current investigation observed an increase in mineralisation over a 7-9 day period of CAM-implantation. The fast and rapid growth of the CAM has been previously established by Steffens *et al.* who compared the vasoproliferative response of the CAM model with the subcutaneous mouse implant (Steffens *et al.* 2009). Remarkably, the previous study showed greater micro-vessel density in the 7 day CAM assay (50.4 ± 17.3 SD), compared to the 21 days implantation (43.5 ± 16.3 SD) in the rodent model (Steffens *et al.* 2009). Thus, even a short-term CAM assay, limited to 7-10 days incubation, offers a robust angiogenic response from a rapidly developing embryo.

Typically, tissue regeneration following an *in vivo* bone defect is examined by measuring bone volume within a region of interest, and results are expressed as net bone volume (Kempen *et al.* 2009; Lienemann *et al.* 2015; Patel *et al.* 2008). In comparison, the present study measured the whole cylinder including the region of interest (bone volume measured in mm^3), before and after incubation to provide the relative change in bone volume as an output for each individual cylinder. The rationale behind that was that i) neglect variances length and different locations of femoral head between cylinders, ii) inability to differentiate between net bone formation and pre-existing bone and iii) inability to predict location of bone cylinder CAM-integration due embryo movement over developing period. As an alternative to the approach employed in the present thesis, two different regions of interest could have been applied to the cylinders: one including one millimetre of the cylinder outer periphery and another one measuring the defect site (2 mm empty core). However this would have resulted in additional variability given that the new bone formation might have occurred at different locations for each cylinder, depending on integration site.

Histological analysis demonstrated that both bone formation (Runx2+, Sox9+) and bone resorption (Cathepsin K+) occurred in parallel in the bone cylinders (Figure 4.2.9 and Figure 4.2.11), however µCT analysis included both processes in a single measurement (bone volume measured in mm^3). The fact that bone resorption occurs at a faster rate than bone deposition (Birkhold *et al.* 2014; Clarke, 2008), together with the short length of the incubation period available on the CAM (7-9 days) could explain the relatively small magnitude of the bone volume change following implantation. In addition, the nature of µCT was to quantify mineralised tissue, hence when applied to this particular human-avian scenario, µCT analysis might be more sensitive to bone resorption than to bone formation, considering that newly formed matrix and osteoid fall below the threshold used for quantification. Therefore the inability to uncouple bone formation from bone resorption was considered a significant limitation on this study, masking the anabolic potential of the human-avian model to examine bone regeneration.

The osteoclastic/bone resorptive ability of the CAM was documented as early as 1990 when Webber *et al.* implanted decellularised bovine bone fragments on the CAM and showed significant resorption pits on the bone chips following implantation (David M. Webber 1990). Hence it was not surprising to observe osteoclast activity on the CAM-implanted bone cylinders, in particular when considering that some regions of the bone cylinders might be necrotic due to lack of oxygen and nutrient supply, hence requiring osteoclast-mediated removal. Moreover it might be possible that bone cylinders integrate with the CAM in the same way that bone implants integrate with the host tissue: with an initial resorption phase. In this process, named creeping substitution, cortical bone grafts become vascularised through an initial phase of osteoclastic resorption which precedes bone formation (Apelt *et al.* 2004; Kalfas 2001; Oryan *et al.* 2014). Creeping substitution also occurs when the integration of the graft requires resorption of the old necrotic bone at the fracture site (Kalfas 2001). In fact, osteoclast activity has been shown to be crucial to allow for successful bone healing in a mouse tibia defect model, showing impaired bone formation as a result of lack of osteoclast precursors (Alexander *et al.* 2011). The same authors showed osteoclast activity at the fracture site as early as four days after injury, and remarkable TRAP activity at day 9 post fracture (Alexander *et al.* 2011). Hence it might be possible that the process of tissue regeneration on the CAM occurred with an initial phase of resorption due to the nature of the implanted tissue (bone from elderly, diseased patients) to allow for subsequent bone formation, yet limited by the short incubation period (7-9 days).

Finally it is important to consider that due to the paraffin processing of the samples, bone cylinders were decalcified after the µCT analysis to enable examination of tissue morphology, which in turn precluded mineral visualisation histologically. However, paraffin processing of mineralised collagen sponges following CAM-implantation showed mineral deposition and matrix deposition, demonstrating that cell-driven mineralisation occurred and it was associated with endochondral cell condensations. Thus it is highly likely that, given that the same cell condensations were located on CAM-implanted bone cylinders, those cellular structures might have been driving the mineralisation process. To validate that, future experiments including fluorescent labelling of calcium deposition of the bone cylinders and mineralised tissue processing should be performed.

6.4 Xenograft culture: Human *versus* Avian cells

CAM-implantation of human living tissue maintained the viability of the autologous (HLA+) cells together with a significant increase in bone formation ($p<0.001$) (Figure 4.2.5 and Figure 4.2.7); hence raising an important question with regards the origin of the cells responsible for this regenerative effect. Experiments conducted to evaluate that revealed that CAM-implantation of decellularised bone cylinders resulted in a similar increase in bone volume, however lesser matrix deposition and cell aggregation formation (Figure 5.2.5 and Figure 5.2.6). However, *in vitro* incubation of living bone cylinders following BMP2 delivery resulted in a significant increase, indicative of the endogenous human cells responding to the osteoinductive factor (Figure 5.2.11). One possible interpretation of the previous results would be that avian cells were the main responsible for the increase in mineral deposition; yet the extent of the contribution from the human cells, however small, should not be ignored.

In agreement with the previous interpretation, GFP immunostaining demonstrated the avian origin of the endochondral cell condensations, responsible for the expression of Sox9 and Runx2 (Figure 4.2.11). While Sox9 identifies both skeletal stem cells committed to the chondrocyte and osteoblast lineage, Runx2 expression occurs subsequent to Sox9 osteoprogenitors, both in endochondral and intramembranous bone formation (Long 2011). During embryonic development of vertebrates most bones develop from mesoderm-derived osteoblast, however the cranio-facial skeleton develops from neural ectoderm-derived osteoblast from the neural crest (Bronner and LeDouarin 2012; Sommerfeldt and Rubin 2001). In fact, Sox9 is expressed in progenitor cells of spinal cord and intestine epithelium during mouse embryogenesis, both ectoderm-derived tissues (Akiyama *et al.* 2005).

The previous facts relate to the findings noted in the present thesis, as Sox9 and Runx2 expressing cells observed to be derived from the ectoderm layer of the CAM (Supplementary Figure 7.4.5). In accordance with that, a study showed the formation of similar cell condensations following delivery of angiogenic and osteogenic growth factors encapsulated in agarose/gelatine beads on the CAM (Ramoshebi and Ripamonti 2000). Literally described by the authors as “formation of clusters of cells with a similar appearance to the stratified ectoderm were embedded within the mesoderm” (Ramoshebi and Ripamonti 2000), those cellular structures shared appearance with the cell condensations described here (Figure 5.2.9). Moreover, previous studies on placenta derived multipotent stem cells differentiated towards osteogenic, chondrogenic and adipogenic lineage *in vitro*, demonstrating the plasticity of cells from the mammalian extraembryonic membrane (Miki *et al.* 2005; Ulrich *et al.* 2013). Another study showed formation of cell condensations following the implantation of chick embryo calvarial fragments on CAM for 10 days (Hancox 1946). In a similar manner as described here, cell condensations, named by the author “ectodermal pearls”, were positioned in vicinity to the bone tissue (Hancox 1946). Taken together, these findings were not unexpected given the clinical gold standard biomaterial is bone autograft (Oryan *et al.* 2014), which provides a unique osteogenic microenvironment as a consequence of the plethora of growth factors within the bone matrix (*i.e.* BMP, IGF, TGF-B) as well as the presence of viable osteogenic cells (Centrella *et al.* 1991; Hayden *et al.* 1995; Oryan *et al.* 2014). Therefore, it is likely that the implantation of such an osteoinductive material (*i.e.* living human bone cylinder) on the CAM can result in ectopic bone formation; certainly, Hopkins *et al.* established that BMP proteins have significant structural similarity and function across species (Hopkins, Keles, and Greenspan 2007). In fact, human recombinant BMP has been shown to induce differentiation of chicken embryo-derived chondrocytes (Enomoto-Iwamoto *et al.* 1998).

A common limitation in using the CAM assay, in this thesis and generally in the literature, is the inability to distinguish between host and graft tissue due to antibody cross-reactivity between species (Balke *et al.* 2011; Coconi *et al.* 2005; Kunzi-Rapp *et al.* 1999). This issue was circumvented by implementing genetically modified chick embryos which ubiquitously express green fluorescent protein (GFP)(Chapman *et al.* 2005). The use of GFP-CAM allowed identifying the avian origin of Sox9, Runx2 and Cathepsin K expressing cells by evaluating GFP expression on consecutive sections (Figure 4.2.11). Importantly, this method allowed determining the species responsible for the anabolic/catabolic processes, which was a key consideration in this study. Future experiments could include double immunostaining on the same sections, or mineralised tissue processing to preserve the GFP fluorescence. Moreover, the use of the GFP-labelled CAM served in to differentiate the two CAMs used on the double CAM experiment; bone cylinders implanted on a GFP-CAM were harvested and implanted onto a second wild type CAM (double CAM), resulting in a continuous increase in bone volume (Figure 4.2.14). In that way the double CAM might offer the possibility to bypass the short incubation time-frame of the CAM and observe the following stages in bone formation on the cylinders. Future experiments should explore the potential of this model by examining graft viability following incubation as well as comparison with the relevant controls (*in vitro* culture).

6.5 Evaluation of biomaterials and BMP2 delivery

The ultimate aim in developing the CAM assay for the culture of human bone was to use this system as a screening platform for osteogenic biomaterials. Hence, this study focused on the optimisation of the culture conditions for the human tissue as well as developing the appropriate methodology to measure the subsequent changes (output) and evaluate the effect of the interventions. In the present thesis two different materials (an FDA-approved acellular collagen sponge and a novel clay-based hydrogel, Laponite) were used to evaluate the effect of BMP2 delivery on the human bone cylinders following CAM-implantation. CAM-implantation of human bone cylinders allowed observing significant differences between different biomaterial treatments, even if sometimes unexpected (Figure 5.2.11 and Figure 5.2.17).

BMP2 delivery resulted in a significant increase of bone volume when cultured *in vitro* and had the opposite response when implanted on CAM (Figure 5.2.11), also inducing the formation of endochondral cell condensations upon *in vivo* culture (Figure 5.2.12). When considering that i) osteoclast resorption was present on CAM-implanted bone cylinders (David M. Webber 1990) and ii) the potential of BMP to induce osteoclast activity *in vivo* (Okamoto *et al.* 2006), it might be possible that BMP2 stimulation of osteoblast indirectly resulted in osteoclast activation via a osteoblast-osteoclast crosstalk. In evidence of that, one study examined TRAP activity on bone marrow derived COX2 $^{+/+}$ and COX2 $^{-/-}$ cells following BMP2 delivery and showed a significant increase in osteoclast activity dependent on the presence of COX2, primarily derived from osteoblast cells in culture (Chikazu *et al.* 2002). Hence, the previous facts (probability of enhanced bone resorption upon BMP2 delivery) together with the short incubation period on CAM (7-9 days), support the conclusion that an imbalance towards bone resorption than formation might have occurred upon BMP2 delivery. In agreement with the previous suggestion, animal studies examining BMP2 effect on fracture healing at different time points have also reported increased resorption at the early stage, however followed by bone deposition at a later time point (Seeherman 2010; Yu *et al.* 2010). Indeed, excessive bone resorption was a well-documented side effect of BMP2 in clinical trials (Aro 2011; Poynton and Lane 2002). Future experiments including fluorescent or radio labelling of BMP2 to examine their release profile *in vivo* (CAM assay) would provide essential information to understand the nature of the effects observed here, both in terms of the quantity of growth factor as well as the precise time-point of delivery.

To test whether the CAM could serve as a model of ectopic bone formation, collagen sponges impregnated with BMP2 were implanted on CAM for 9 days, resulting in increased formation of endochondral cell condensations. Importantly, bone formation was validated by histological analysis as shown by mineral deposition within cellularised matrix and endochondral cell condensations (Figure 5.2.9 and Figure 5.2.10) Although µCT analysis failed to record significant differences between treatments, the fact that three treatments (collagen sponge blank, low BMP2 and high BMP2 dose) had sufficient mineral deposition to be captured with X-rays was an interesting finding by itself, as it demonstrated the differentiation potential of the membrane. Other studies have reported that ECM proteins are able to elicit greater angiogenic response from the CAM compared to BMP2 delivery (Smith *et al.* 2007), however the delivered dose was comparably lower (1 ng) than the one used in this study (125 ng and 2400 ng BMP2). Another study showed that 1 µg BMP7 delivery resulted in formation of cell clusters within the CAM mesoderm, however mineralisation was not evaluated (Ramoshebi and Ripamonti 2000).

In comparison with other animal models of ectopic bone formation, the dose applied in the CAM assay was significantly lower (2.4 µg) relative to larger animals such as the rat (115.3 - 150 µg), and the implantation period was shorter (9 days) compared to a minimum of three weeks in those rat studies (Cai *et al.* 2014; Luca *et al.* 2011; Wang *et al.* 1990). Wang *et al.* scored bone formation based on histology and described bone formation as early as day 5 post-implantation over 21 days follow up (Wang *et al.* 1990); More recently Luca *et al.* examined bone formation using µCT and reported bone formation 3 weeks after injection (Luca *et al.* 2011). BMP2 loaded nanoparticles were injected into the back of a mouse and 8 weeks after resulted in tissue mineralisation (Seo *et al.* 2015). Thus differences with previous literature in terms of dose and implantation period might explain the inability of the current experimental setup to allow the observation of differences in bone formation. Future experiments will consider explore the therapeutic window of the BMP2 dose (without compromising chick embryo viability) to confirm the CAM as a model of ectopic bone formation.

6.6 Limitations and future indications

A limitation of this thesis was the inability to monitor the graft during incubation to examine the interaction between the graft and the CAM tissue. Moreover, additional X-rays scans over the incubation period could have provided further insights into the bone remodelling process of the bone cylinders. One previous study attempted to follow the development of the implant over a period of time using MRI to scan multiple times the whole egg; however this also involved technical difficulty to differentiate the graft from the embryo on the scans (Zuo *et al.* 2015). Another solution for the present investigation might have been to include an *ex ovo* (shell-less) approach, although this method implies a viability drop down to 20-30% by the end of the gestational process (Klueh *et al.* 2003; Lokman *et al.* 2012). Moreover it is worth noting that in the absence of the eggshell, the CAM can uptake the mineral content from other sources (*i.e.* biomaterial) to restore calcium levels for skeletal development (Vargas *et al.* 2009), and hence the use of an *ex ovo* approach might have compromised the deposition of new mineral.

Given the relatively small magnitude of the change (approximately 8 % BV) and the resolution settings (18 µm), significant changes in bone volume (global measurement) would not have necessarily be reflected in other parameters such as trabecular number (local measurements). In agreement with the previous speculation, other studies measuring tissue regeneration observed much greater changes in bone volume compared to other structural parameters (Smith *et al.* 2014a, 2014b). The use of higher resolution settings could be explored as a means to increase the precision of the measurement, however radiation dose and scanning time would need to be considered not to affect graft viability. Additional limitations of this investigation related to the µCT analysis were the inability to uncouple bone formation and bone resorption from the µCT output measurements and the inability to distinguish precisely between pre-existing and newly formed bone for quantification. These constrains together with the short incubation period of the CAM (limited to 7-9 days) might have prevented the quantification of the actual changes occurring in the bone cylinders.

Future investigations could contemplate development of a 3D registration method and subsequent application for the quantification of bone resorption and bone formation, similar as previous studies have recently reported (Birkhold *et al.* 2014; Lambers *et al.* 2015). A different approach based on µCT analysis could consider creating alternative regions of interest on the scanned datasets to measure more localised changes, for example the outer periphery of the bone cylinders. Additional recommendations for future research would include the use of mineralised tissue processing to enable detecting fluorescent mineral deposition as well as further histochemical stains to distinguish osteoid *versus* mature bone (i.e Masson Trichrome, Goldner's Trichrome, etc.) on the bone cylinders for histomorphometry. However, these techniques involve sample destruction, require special equipment for mineralised bone processing and fluorescent labels can disappear in the case of excessive bone turnover. Moreover, quantitative analysis based on histology is limited at the 2D scale and it does not allow quantifying bone resorption but only deposition.

Finally, the use of fluorescent or radio labelling of the growth factors (i.e BMP2, VEGF) prior to CAM-implantation or *in vitro* culture would allow gaining critical insights about the actual delivered dose in a spatio-temporal monitored manner. This type of experiment would characterise better the release pattern of the biomaterials as well as provide understanding of the biological effect observed on this human-avian model.

6.7 Final remarks and conclusion

In summary, the development of this project has provided a novel, simple, and less sentient *in vivo* model to examine regeneration of human bone tissue. The significance of this research lies in the usage of human living bone, as it provides a clinically relevant scenario to evaluate tissue regeneration while minimising the use of additional animal models in research. The use this CAM-avian system as a screening platform for biomaterials has the potential of improving the accuracy while reducing the length of the process to bring new therapies into the clinic. In an indirect manner, patients could benefit from the implementation of this *in vivo* model by improving the efficacy of preclinical testing in tissue engineering, and more globally, in the field of biomedicine. Importantly, this research provides a framework for the exploration of the response of the autologous graft cells to personalised, anti-cancer therapies. Indeed, it has been reported that patient tumours preserve their characteristics even after subcutaneous implantation in mice (DeRose *et al.* 2011) and in the CAM (Sys *et al.* 2012). This novel approach could serve to avoid the side-effects of experimental therapies while tailoring the treatment opportunities for individual patients in the clinic.

Investigating novel ideas and strategies for regenerative medicine is equally important as developing robust, efficient and reproducible methods for improved research quality. This project has attempted to do both by i) demonstrating the feasibility of the CAM assay as an *in vivo* system to culture human bone and ii) testing this model in the context of potential treatments for bone tissue engineering. Importantly, this study has demonstrated the ability to examine bone regeneration in the context of human physiology, while at the same time exploring alternative approach to traditional *in vivo* models (*i.e.* murine subcutaneous implants).

Thus, the CAM model serves as a link between the *in vitro* and the *in vivo* models, optimising and reducing the number of animals required in later stages of preclinical research. Careful consideration is taken when considering any *in vivo* study, as animal studies involve great responsibility and hold significant implications with respect to cost, time, resources and infrastructure. However, even greater efforts are needed to ensure the obligations to reduce, refine and replace (3Rs) in animal research are met. Hence, it is a long-term aim of this project to make this refinement model accessible for the widest research community, both in the private and public sector. Ideally, future scientists will adopt this model not only for biomaterial testing but also to address research questions which require the short-term culture of human bone (or any other tissue) as a context for the *in vivo* scenario. The fact that the CAM is able to provide both a rapidly growing vascular bed and a pseudo-immune response (further developed upon gestational stage) offer great advantages over *in vitro* models, incapable of provide such physiological response. Moreover, the CAM assay becomes an attractive alternative to murine subcutaneous implants given the simplicity and short-term duration of the CAM compared to current, more invasive animal models. Thus the CAM assay holds great promise as it has the plasticity and the capacity to be tailored into multiple applications, as demonstrated by the diverse uses of the CAM assay over the years.

In conclusion, the present study describes a novel method to study human bone regeneration *in vivo* using the CAM assay as a short-term animal model. The significance of this research lies in the use of human bone tissue, freshly derived from patients and hence a more clinically relevant situation to study bone healing. In addition to examining the response from the human tissue, the design of a concentric defect on the bone grafts allow to mimicry of an injury model in an osteogenic environment and hence a region of interest for new treatments. This investigation has demonstrated the ability of the human-avian system to assess significant changes *in vivo* over a 7-9 days incubation period with a developed method of µCT analysis. Moreover this method allowed observing the effects of different treatments/interventions on the CAM-implanted bone cylinders, establishing the capability of this model to assess biomaterial performance in BTE applications. This cost-effective, rapid and simple method will have a critical impact on the reduction and replacement of the number of animals used in classical *in vivo* bioengineering models.

Chapter 7: Appendices

7.1 Appendix A - Introduction

Supplementary Table 7.1.1: Summary table of the studies implanting biomaterials in combination with growth factors and/or cells on the CAM to evaluate their performance *in vivo*.

Title	Biomaterial	Growth factor	Cells	Evaluation	CAM assay	Reference
Improved growth factor directed vascularization into fibrin constructs through inclusion of additional extracellular molecules	Collagen type I, hyaluronic acid and fibronectin	FGF-, VEGF$_{165}$, PDGF-BB and BMP2 (10ng/ml)	--	QD to quantify angiogenesis	*Ex ovo* day 3 to day 6	(Smith *et al.* 2007)
Cell mediated delivery of FGF2 and VEGF on the CAM	Gelatin sponge	FGF2 and VEGF (1ug total dose) *not same isoforms as delivered by the cell lines.	Tumour cell lines expressing FGF or VEGF. 20.000	Macroscopic quantification of angiogenic response with stereomicroscope	*In ovo* day 8 to day 12	(Ribatti *et al.* 2001)
Ex ova chick chorioallantoic membrane as a novel model for evaluation of tissue responses to biomaterials and implants	Nylon mesh and siliastic tubing	--	---	Macroscopic evaluation of material integration. Histology *Comparison to mammalian immune response.	*Ex ovo* day 7 to day 15 *50% embryo dead *ex ovo* during first 3 days.	(Klueh *et al.* 2003)
Supercritical carbon dioxide generated vascular endothelial growth factor encapsulated poly(DL-lactic acid) scaffolds induce angiogenesis in vitro	PLGA mixed with growth factors using CO2 supercritical fluid mixing.	hrVEGF$_{165}$	--	Macroscopic quantification of angiogenic response with stereomicroscope Histology	*In ovo* day 10 to day 14	(Kanczler *et al.* 2007)
Biocompatibility and bone mineralization potential of 45S5 Bioglass -derived glass–ceramic scaffolds in chick embryos	Effect of Bioglass ceramic on chick skeleton in the absence of natural source of Ca++ (eggshell)	----	----	Chick embryo viability and skeleton mineralization.	*Ex ovo* day 10 to day 15	(Vargas *et al.* 2009)
Preparation and characterization of Antheraea assama silk fibroin based novel non-woven scaffold for tissue engineering applications	Silk fibroin	--	--	Macroscopic quantification of angiogenic response with stereomicroscope *No real angio-quantification.	*Ex ovo* day 4 to 6	(Hadjizadeh and Doillon 2010)
Microporous collagen spheres produced via thermally induced phase separation for tissue regeneration	Microporous PCL and collagen spheres	---	----	Macroscopic quantification of angiogenic response with stereomicroscope	*Ex ovo* Day 10 to 14	(Keshaw *et al.* 2010)
Scaffolds with covalently immobilized VEGF and Angiopoietin-1 for vascularization of engineered tissues	Porous collagen sponge	Mouse recombinant VEGF 165 and human recombinant Ang1 immobilized in scaffolds (50ng/ml)	---	Biochemical assay to quantify angiogenesis (haemoglobin) Histology	*In ovo* Day 4 to day 7.	(Chiu and Radisic 2010)
The effect of vascular endothelial growth factor (VEGF) presentation within fibrin matrices on endothelial cell branching	Low and High dense bounding polyestirene particles in fibrin gels	VEGF (2 ng/ml)	---	Macroscopic quantification of angiogenic response with stereomicroscope Perfusion with FITC-dextran	*Ex ovo* day 7 to day 9.	(Anderson *et al.* 2011)
Delivery of VEGF using Collagen-coated Polycaprolactone Scaffolds Stimulate Angiogenesis	Collagen- PCL scaffold 1ug vegf	hrVEGF$_{165}$ (1 ug)		Macroscopic quantification of blood vessels.	*Ex ovo* day 8 to day 10. *Same construct on mice subcut, no direct comparison.	(Shivani. 2013)
Biodegradable electrospun nanofibers coated	Poly capolactone electrospun nanofibers	Platelet rich plasma (GF cocktail) PDGF-BB, VEGF,	----	Macroscopic quantification of angiogenic response	*In ovo* day 10 to 12	(Diaz-Gomez *et al.* 2014)

with platelet-rich plasma for cell adhesion and proliferation		TGFB1		with stereomicroscope		
A bio-inspired, microchanneled hydrogel with controlled spacing of cell adhesion ligands regulates 3D spatial organization of cells and tissue	Alginate bimodal gel modified with RGD peptides.	VEGF encapsulated in PLGA capsules	----	Histology processing for aSMA immunostaining and image processing for quantification.	No information available e*x ovo / in ovo.* Incubation day 7 to day 14	(Lee *et al.* 2015)
Osteogenic Protein-1, a Bone Morphogenetic Protein, Induces Angiogenesis in the Chick Chorioallantoic Membrane and Synergizes With Basic Fibroblast Growth Factor and Transforming Growth Factor-beta	Agarose beads	BMP (100 ng or 1,000 ng), bFGF (500 ng), pTGF-b1 (20 ng), BMP /bFGF (100/100 ng), BMP /pTGF-B1 (100/5 ng or 100/20 ng)	----	Macroscopic quantification of angiogenic response with stereomicroscope Histology: Thickness ratio central to peripheral CAM	*In ovo* day 10 to day 15. *Cell Condensations	(Ramoshebi and Ripamonti 2000)
Endothelin-1, a regulator of angiogenesis in the chick chorioallantoic membrane	Gelatin sponges	bFGF-2 (1 ug scaffold)	Cell line (CHO) transfected with endothelin-1. $5x10^6$ /scaffold	Macroscopic quantification of angiogenic response with stereomicroscope Histology and in situ hybridization	*Ex ovo* day 8 to day 12	(Cruz *et al.* 2001)
Thrombin peptide, TP508, stimulates angiogenic responses in animal models of dermal wound healing, in chick chorioallantoic membranes, and in cultured human aortic and microvascular endothelial cells.	Agar	Thrombin peptide (TP508) 1 ug	-----	Macroscopic quantification of angiogenic response with stereomicroscope	*In ovo* day 9 to day 13	(Norfleet *et al.* 2000)
Osteocalcin is angiogenic in vivo	Gelatin sponges	Osteocalcin (50 ng), FGF-2 (500 ng)		Macroscopic quantification of angiogenic response with stereomicroscope Histology	*Ex ovo* Day 8 to day 12	(Cantatore *et al.* 2005)
Adipose precursor cells (preadipocytes) induce formation of new vessels in fibrin glue on the newly developed cylinder chorioallantoic membrane model (CAM)	Fibrin glue	hr VEGF (40 ng) and hr bFGF (50 ng)	Primary human adipocytes	Histomorphometric analysis to quantify angiogenic response	*In ovo* day 8 to day 16	(Borges *et al.* 2006)
Effects of combinations of BMP-2 with FGF-2 and/or VEGF on HUVECs angiogenesis *in vitro* and CAM angiogenesis in vivo	---	FGF-2 (0.1 ng/mL), BMP-2 (1 ng/mL); VEGF (25 ng/mL, and co-delivery	----	Macroscopic quantification of angiogenic response with stereomicroscope Histology to evaluate mesoderm thickness	*In ovo*, day 7 to day 10, day 10 to day 12 and day 7 to day 12.	(Bai *et al.* 2014)
Tissue engineered bone grafts based on biomimetic nanocomposite PLGA/amorphous calcium phosphate scaffold and human adipose-derived stem cells	Nanocomposite PLGA/amorphous calcium phosphate	----	Primary human adipose cells	Macroscopic quantification of angiogenic response with stereomicroscope Histology (HE, GT, Alizarin Red) to perform histomorphometry analysis	*Ex ovo* day 8 to day 15	(Buschmann *et al.* 2012)
Microfabrication of proangiogenic cell-Laden alginate-g-Pyrrole hydrogels	Alginate-g-Pyrrole hydrogel	---	----	Macroscopic quantification of angiogenic response with stereomicroscope	*In ovo* day 7 to day 14	(DeVolder *et al.* 2012)

				Histological analysis based on aSMA immunostaining and histomorphometry		
Differentiation of lung stem/progenitor cells into alveolar pneumocytes and induction of angiogenesis within a 3D gelatin e Microbubble scaffold	Gelatin/microbubble-scaffolds	----	Mouse primary pulmonary progenitor cells	Histology Hemoglobin concentration to quantify angiogenesis	*In ovo* day 7 to day 15 *same biomaterial on SCID mice	(Ling *et al.* 2014)
***In vivo* studies on angiogenic activity of two designer self-assembling peptide scaffold hydrogels in the chicken embryo chorioallantoic membrane**	Functionalized peptide hydrogels	----	----	Macroscopic quantification of angiogenic response with stereomicroscope Histology	*In ovo* day 8 to day 12	(Liu *et al.* 2012)
Human Osteoprogenitor Bone Formation Using Encapsulated Bone Morphogenetic Protein 2 in Porous Polymer Scaffolds	PLA on segmental chick femur defect	hrBMP2 (100 ng/mg PLA)		Histological analysis for bone formation	*In ovo* day 10 to day 17	(Yang *et al.* 2004)
***In vivo* engineering of a human vasculature for bone tissue engineering applications**	Processed bovine cancellous bone	Endothelial and human osteoblast spheroids coculture (200.000 cells/spheroid)	hrVEGF-A and bFGF (500 ng)	Histomorphometric analysis based on immunostaining for angiogenic markers	*In ovo* day 7 to day 15 *Same material implanted and evaluated in SCID mouse	(Steffens *et al.* 2009)
Chorioallantoic membrane angiogenesis model for tissue engineering: a new twist on a classic model	Fibrinogen and thrombin gel	Adipocytes		Macroscopic quantification of angiogenic response with stereomicroscope Histology	*In ovo* day 8 to day 16 *Cylinder implantation technique	(Borges *et al.* 2003)

7.2 Appendix B – Materials and Methods

7.2.1 List of media and reagents:

Unless otherwise stated, all reagents were purchased from Sigma-Aldrich, USA.

Composition of the tissue culture media employed:

- Plain media: αMEM media supplemented with 100 U/ml of Penicillin G and 100 µg/ml of Streptomycin.
- Complete media: αMEM media supplemented with 100 U/ml and 100 µg/ml of Penicillin G and Streptomycin, respectively, and 10% foetal bovine serum (FBS).
- EC media: M199 media supplemented with with 100 U/ml and 100 µg/ml of Penicillin G and Streptomycin, respectively, 10% FBS and 10 µg/ml of endothelial cell growth supplement and heparin (ECGS, Lonza).

7.2.2 Histochemistry additional information

Supplementary Table 7.2.1: List of steps for sample paraffin processing:

Step	Reagent	Time	Temperature
1	4% PFA in PBS	16h	4 ˚C
2	PBS wash	16h	4 ˚C
3	Histoline	24h	4 ˚C
4	PBS wash	16h	4 ˚C
5	50% EtOH	2h	20 ˚C
6	90% EtOH	2h	20 ˚C
7	100% EtOH	2h	20 ˚C
8	100% EtOH	2h	20 ˚C
9	Histoclear	2h	20 ˚C
10	Histoclear	2h	20 ˚C
11	Paraffin	2h	70 ˚C
12	Paraffin	2h	70 ˚C

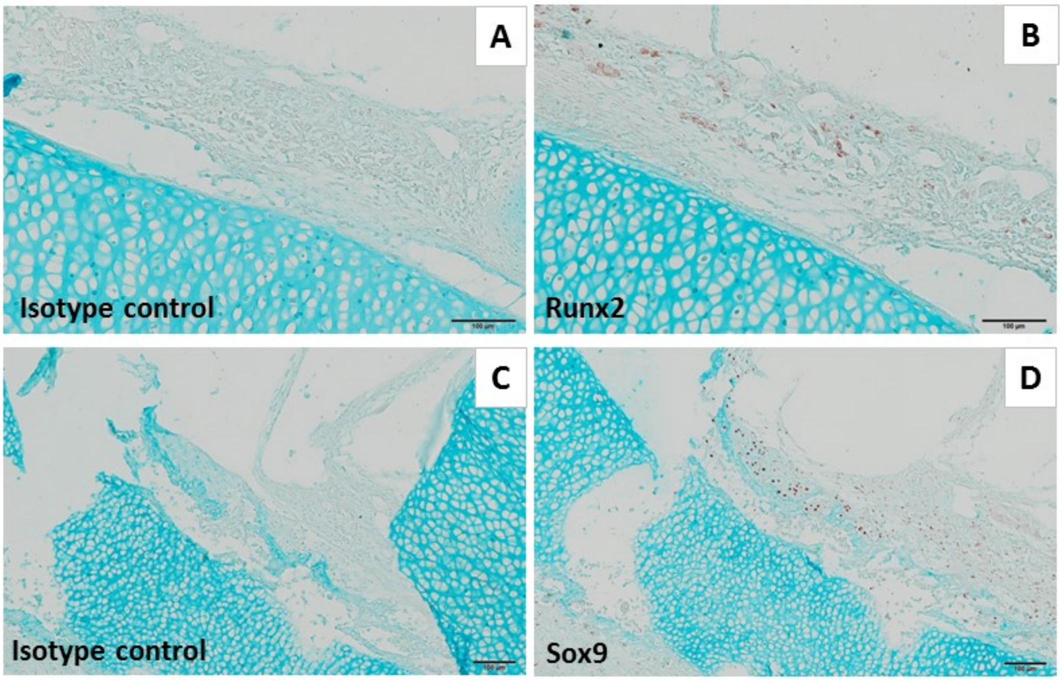

Supplementary Figure 7.2.1: Chick femur positive control stained for Sox9 (C-D) and Runx2 (A-B). Consecutive sections were stained with isotype control (A, C). Positive immunostaining in brown-red colour, counterstained with Alcian Blue to visualize the matrix content. Scale bar detailed in the image

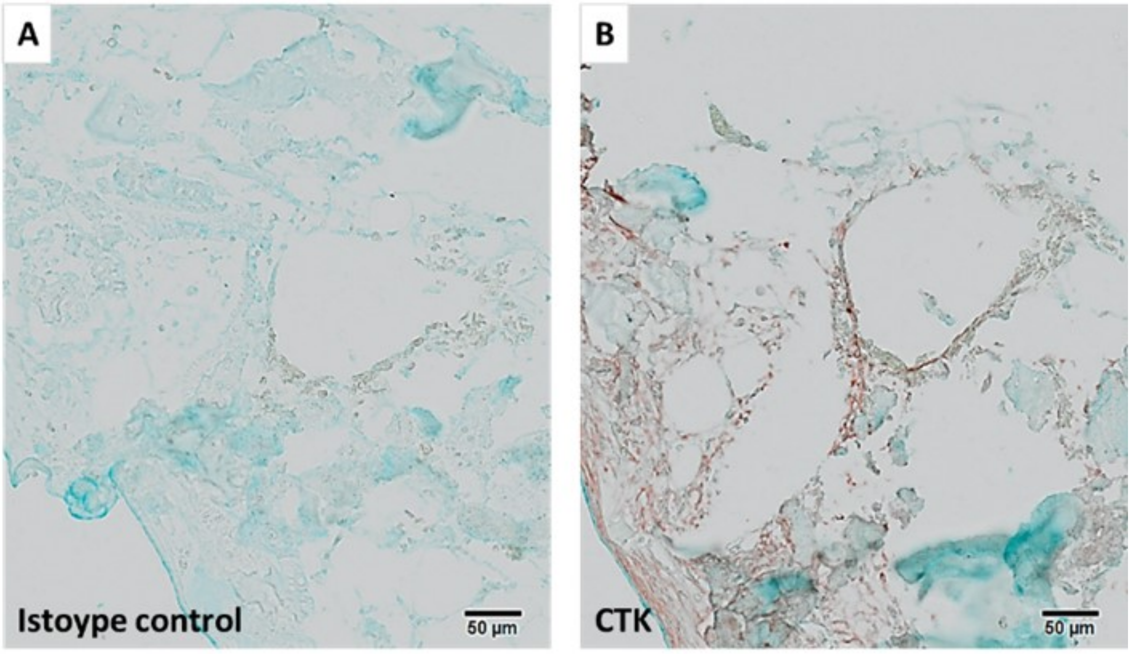

Supplementary Figure 7.2.2: Immunohistochemistry control for Cathepsin K. Human bone tissue stained for Cathepsin K. Consecutive section was stained with isotype control (A).). Positive immunostaining in brown-red colour, counterstained with Alcian Blue to visualize the matrix content. Scale bar detailed in the image.

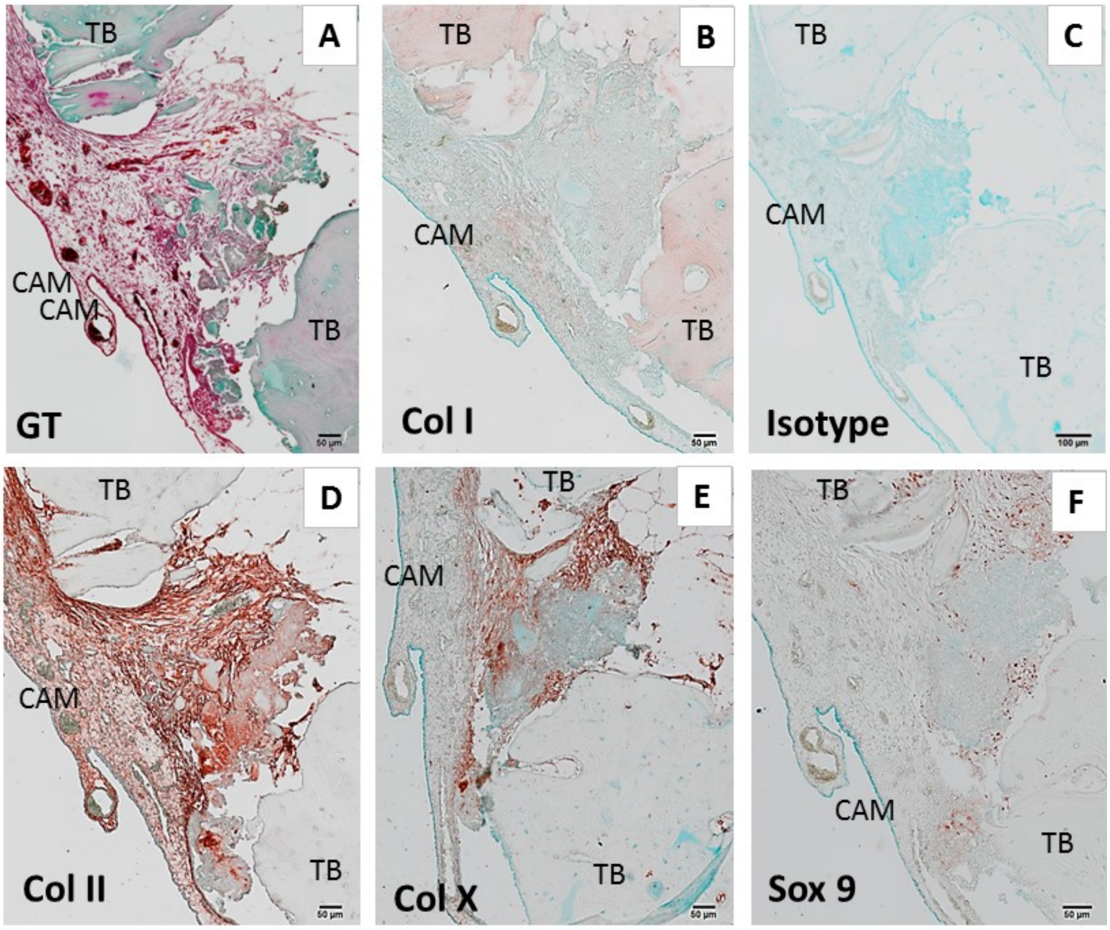

Supplementary Figure 7.2.3: Immunohistochemistry control for Collagen type I, type II and type X. Consecutive sections from CAM-implanted human bone tissue stained for Goldner's Trichrome (GT), Collagen type I (B), type II (D), type X (E) and Sox9 (F) and isotype control (C).). Positive immunostaining in brown-red colour, counterstained with Alcian Blue to visualize the matrix content. Scale bar detailed in each picture.

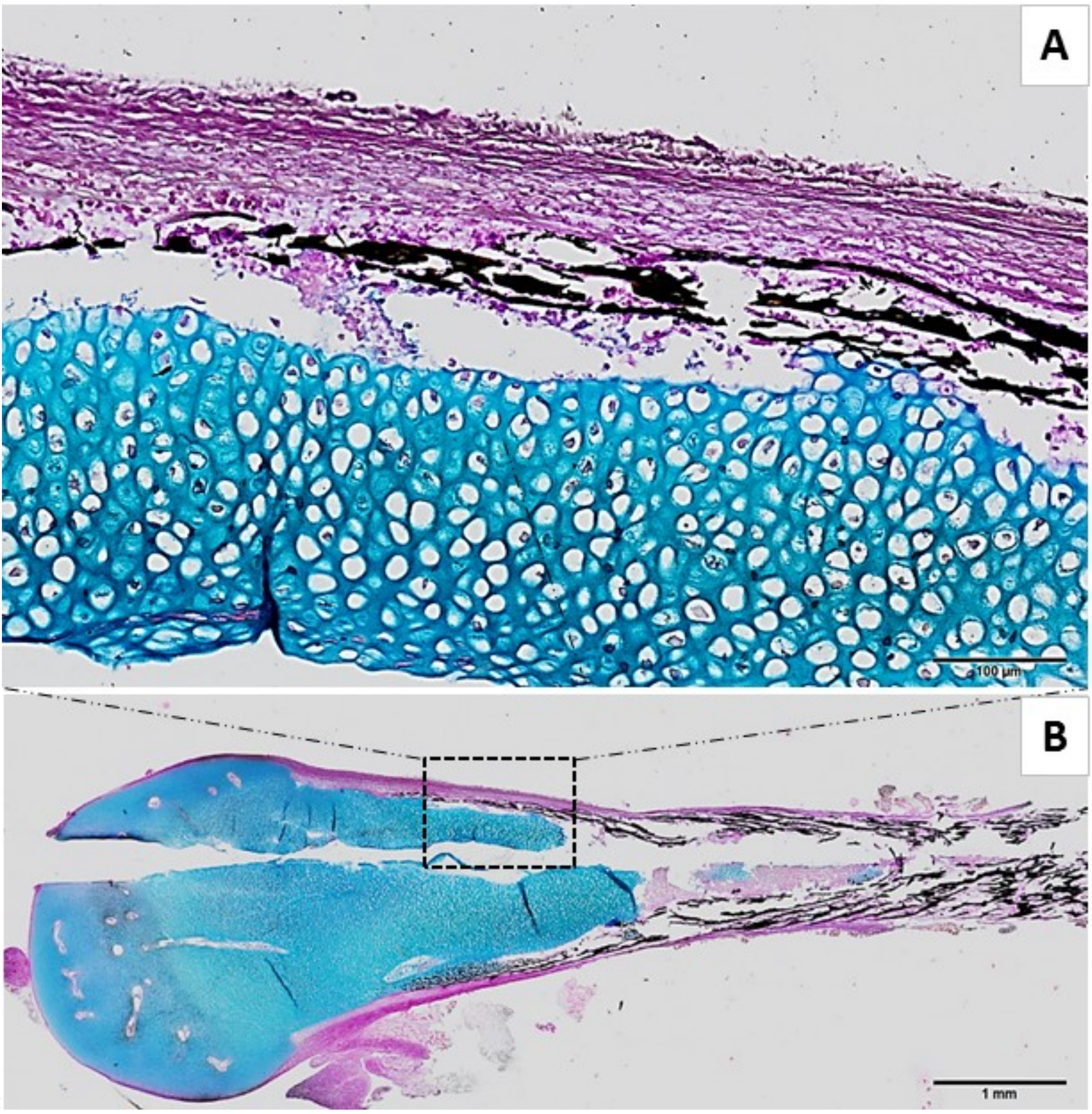

;

Supplementary Figure 7.2.4: Positive control for von Kossa staining of day 18 chick femurs as a positive control (A-B). Mineral content indicated in black, proteoglycan in blue colour. Scale bar detailed in each picture.

7.3 Appendix C – Results Part II

Supplementary Table 7.3.1: Bone volume change (%) from bone cylinders following culture. Bone cylinders were µCT scanned before and after implantation on CAM, cultured *in vitro* or maintained at four degrees as control. Data collected from seven independent experiments.

	Patient details	**A**	**B**	**C**	**D**	**E**	**F**	**G**
		M 49 OA	M68 OA	F85 NOF#	F67 OA	M79 NOF#	M79 OA	F81 NOF#
CAM-impl.	Mean	4.62	7.23	-0.26	8.18	9.79	9.14	7.65
	SD	3.2	1.6	5.5	2.74	2.24	1.99	3.55
In vitro	Mean	1.32	-1.5	1.59	0.16	1.06	5.26	3.6
	SD	3.32	1.74	1.38	2.76	1.60	2.85	1.9
control	Mean	-1.67	0.04	-0.27	0.19	-0.19	0.2	-0.08
	SD	1.8	1.47	1.33	0.62	0.33	1.23	0.54

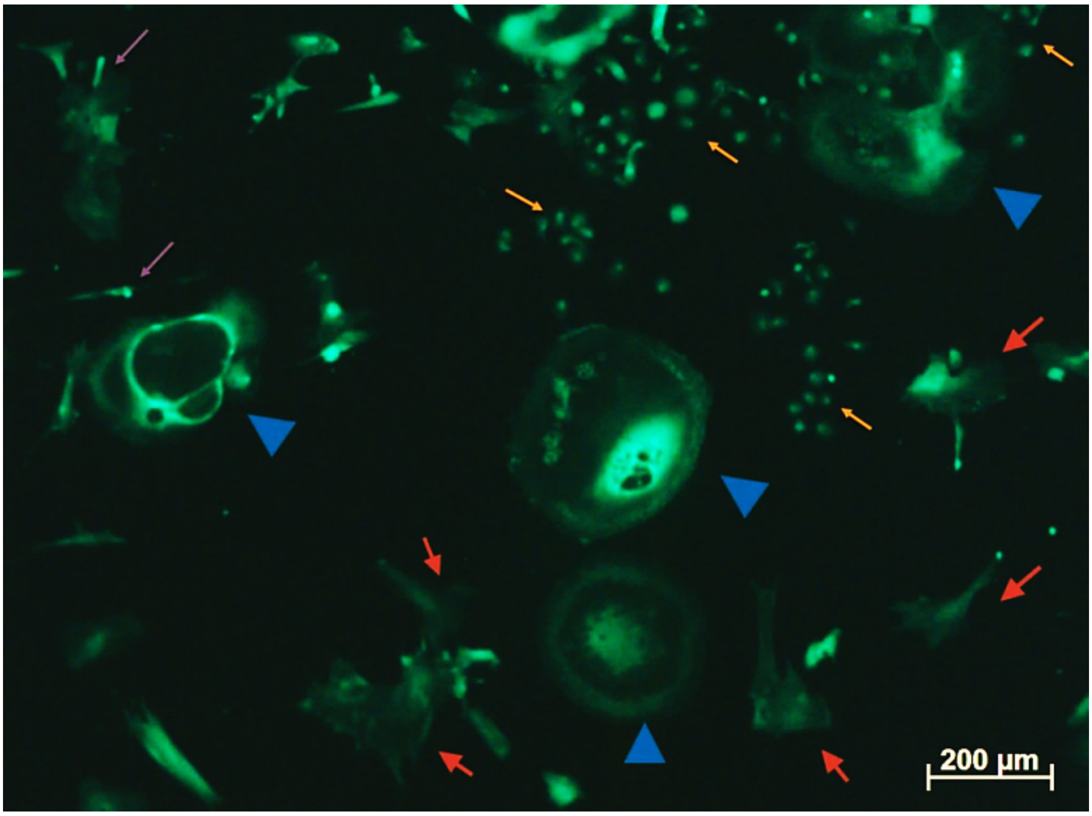

Supplementary Figure 7.3.1: Heterogeneous population of avian cells obtained from GFP-CAM-implanted bone cylinders. Bone cylinders were implanted on a GFP-CAM, harvested, excised into fragments and maintained in standard culture conditions. Cell outgrowth from the bone fragments were imaged using a fluorescence scope. Arrows indicate the different cell morphologies: multinucleated giant cells (blue arrow), large cells with filopodia extensions (red arrows) and small and compact (orange arrows). Scale bar equivalent to 200 µm.

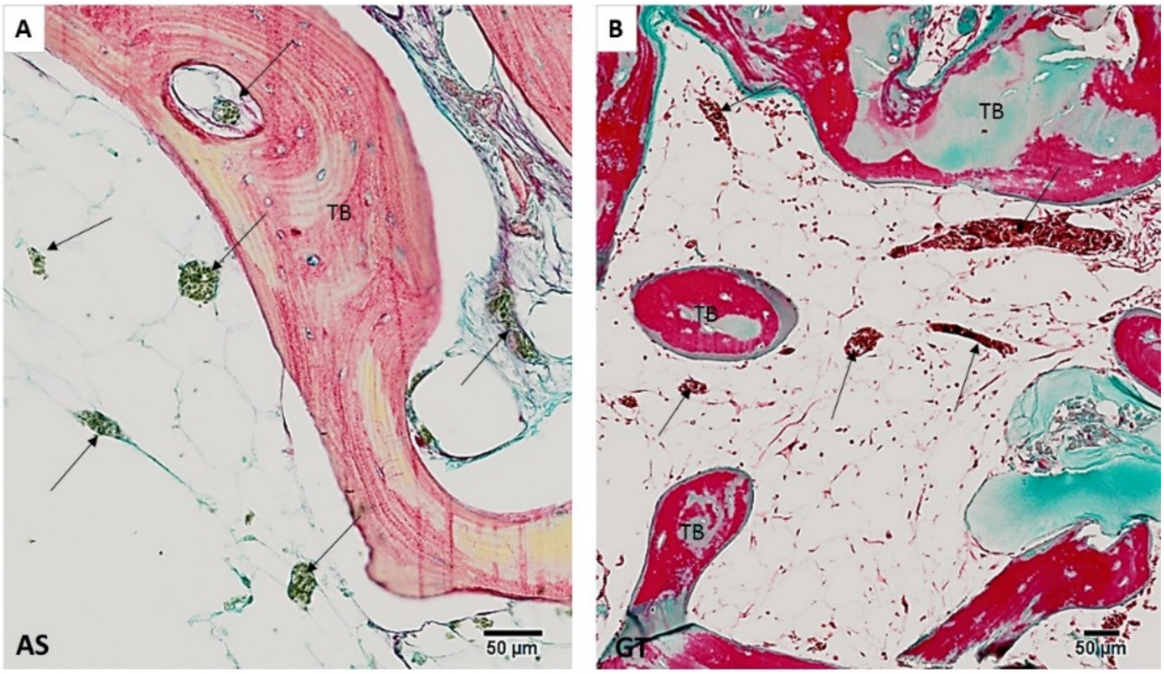

Supplementary Figure 7.3.2: Avian blood vessels carrying nucleated erythrocytes present within the marrow space of the human bone tissue following CAM-implantation. Bone cylinders were freshly extracted and CAM-implanted, processed for paraffin section and stained for Alcian blue and Sirius Red (A) and Goldner's Trichrome (B). Solid arrow indicate avian blood vessels. Alcian Blue and Sirius Red (AS), Goldner's Trichrome (GT), trabecular bone (TB). Scale bars detailed in each picture.

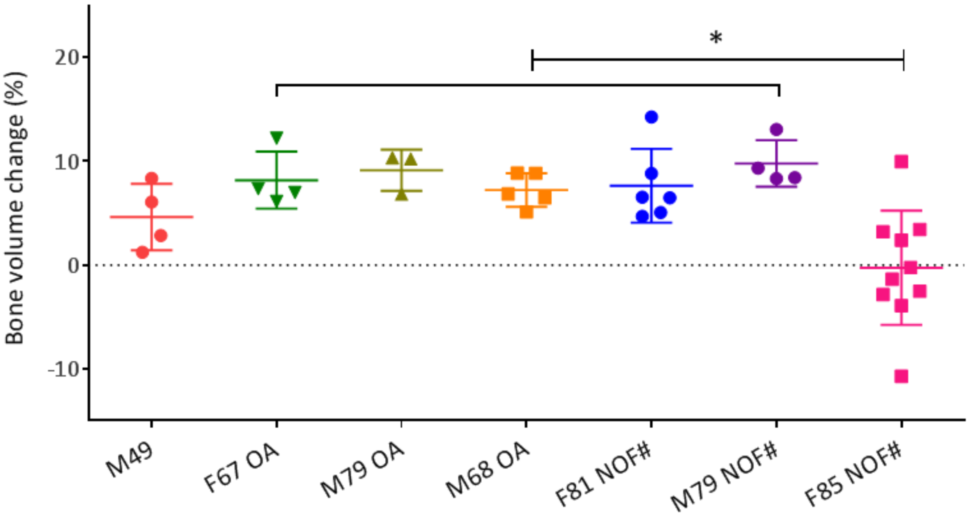

Supplementary Figure 7.3.3: Patient specific variability in bone volume relative change following CAM-implantation. Bone cylinders from osteoarthritic (B, D, F) and NOF# osteoporotic (A, C, E and G) patient femoral heads were µCT scanned under same settings before and after implantation on CAM. Data points indicate the relative bone volume change following incubation of each individual bone cylinder. Error bars indicate mean value ± SD, *p<0.05.

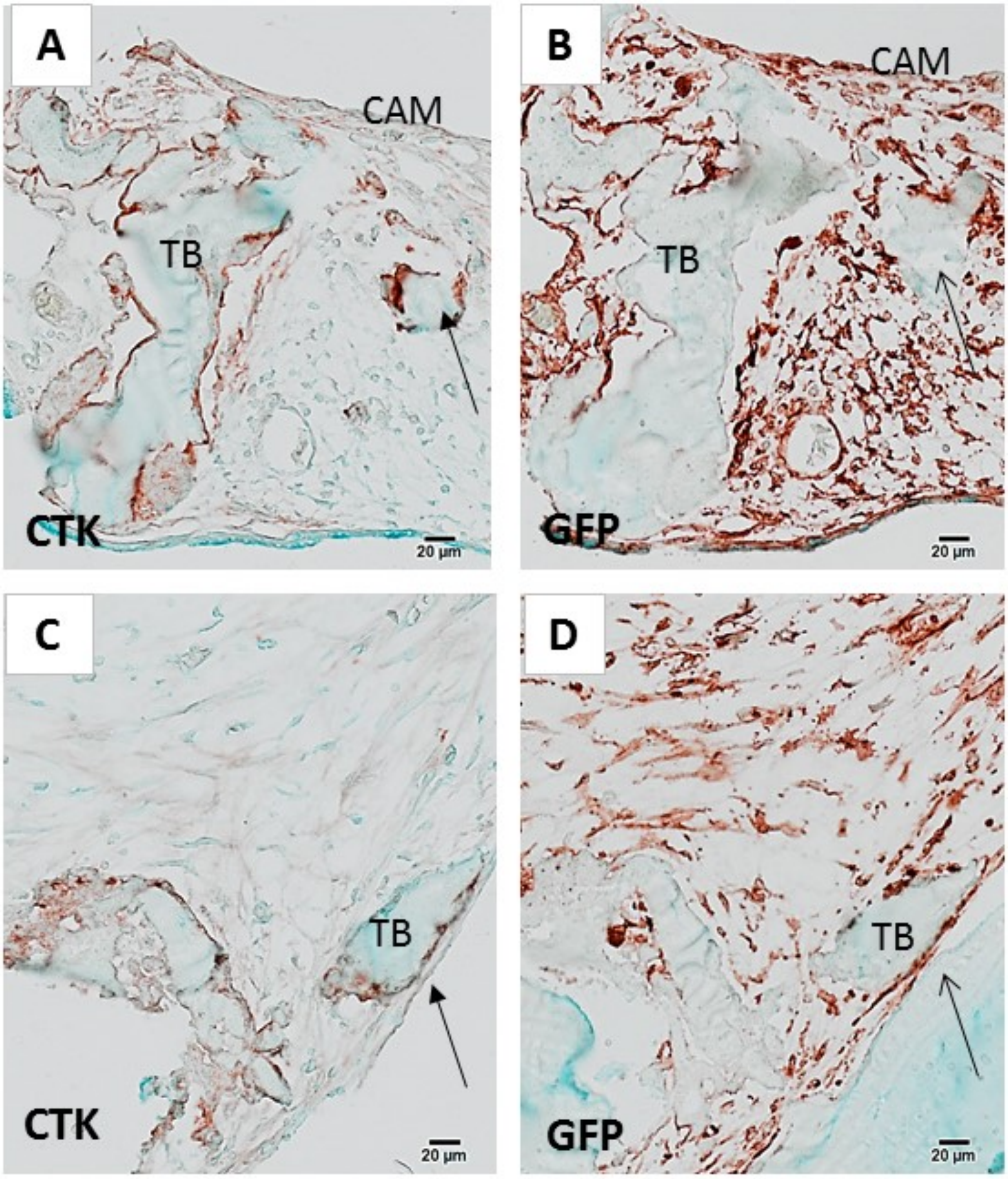

Supplementary Figure 7.3.4: Cathepsin K and GFP expression co-localise following CAM-implantation of human bone cylinders. Bone cylinders were CAM-implantated, processed for paraffin sectioning and immunostained for Cathepsin K (A,C) and GFP (B,D). Positive immunostaining in brown-red colour, counterstained with Alcian Blue to visualize the matrix content (C, F). Solid arrow indicate expression of osteoclast enzyme Cathepsin K (CTK) and GFP. trabecular bone (TB) chorioallantoic membrane (CAM). Scale bars equivalent to 20 µm.

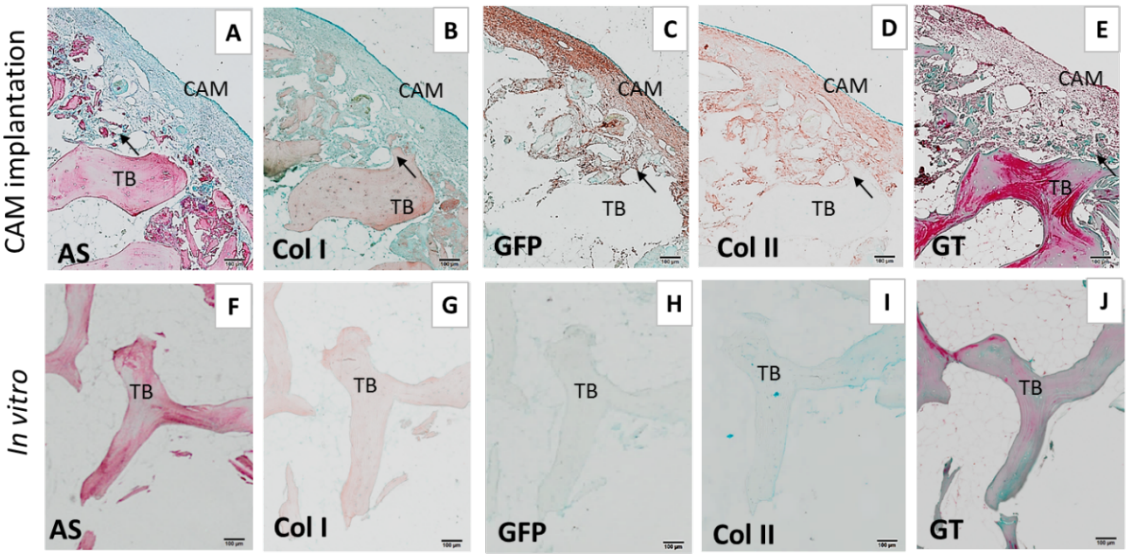

Supplementary Figure 7.3.5: Extracellular matrix deposition localises with avian cells (GFP+) following CAM-implantation of human bone cylinders, and it is absent in *in vitro* cultured group. Bone cylinders were implanted on CAM and processed for paraffin histology. Consecutive sections were stained for Alcian Blue and Sirius Red, and immunostained for collagen type II (B), collagen type I (C) and GFP (D). Positive immunostaining in brown-red colour, counterstained with Alcian Blue to visualize the matrix content. Arrows indicate areas of new matrix deposition. Alcian Blue and Sirius Red (AS), Goldner's Trichrome (GT), chorioallantoic membrane (CAM), trabecular bone (TB). Scale bar equivalent to 50 µm.

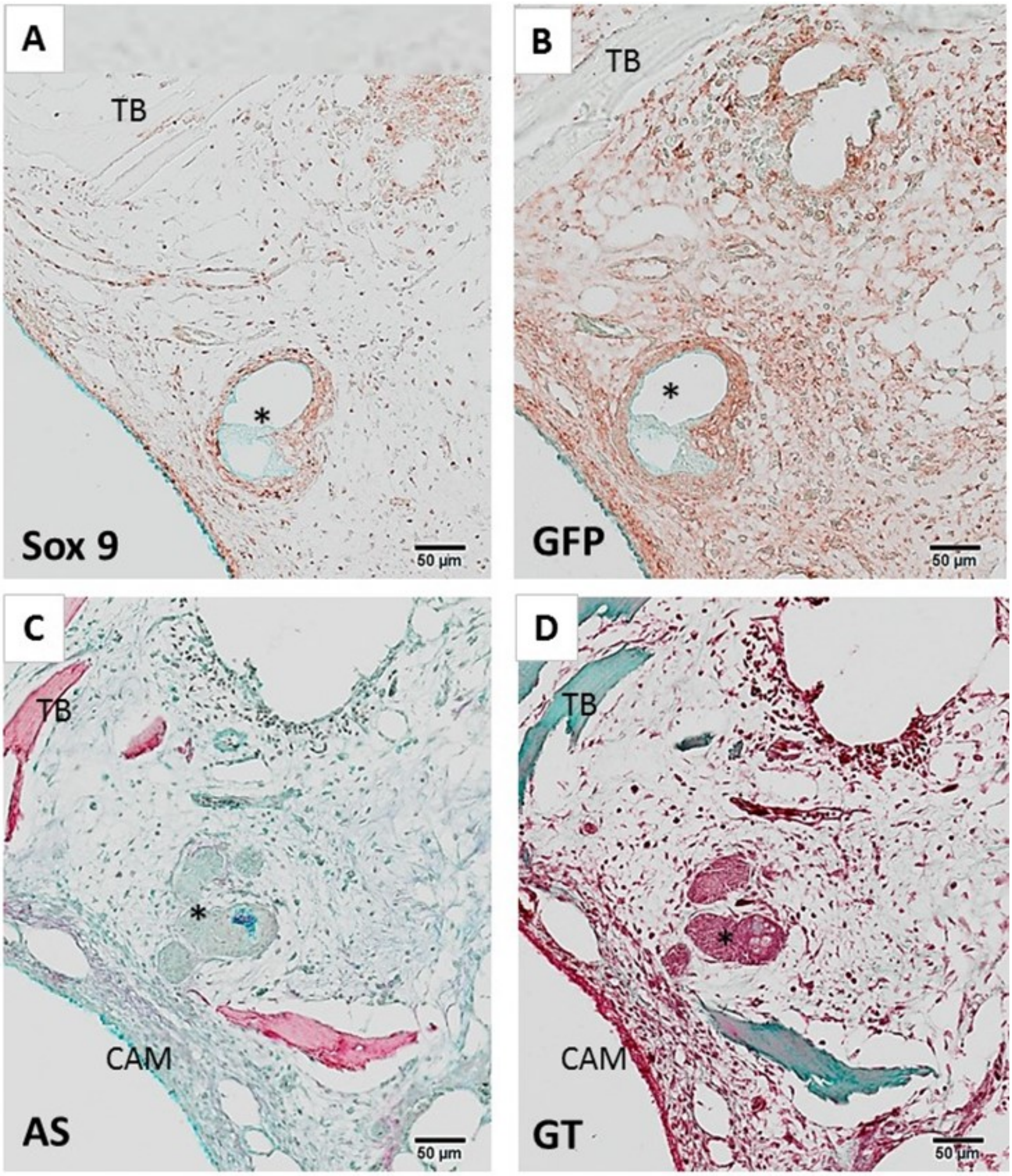

Supplementary Figure 7.3.6: Avian endochondral cell condensations following CAM-implantation of human bone cylinders. Representative images of bone cylinders implanted on the CAM for one week and then processed for paraffin histology and stained for Alcian Blue and Sirius Red staining (C), Goldner's Trichrome (D), and immunohistochemistry for GFP (B) and Sox9 transcription factor (A). Arrows indicate matrix deposition, *indicate cell condensations of different morphology. chorioallantoic membrane (CA), Alcian Blue and Sirius Red (AS), Goldner's Trichrome (GT). Scale bar equivalent to 50 µm.

7.4 Appendix D – Results part III

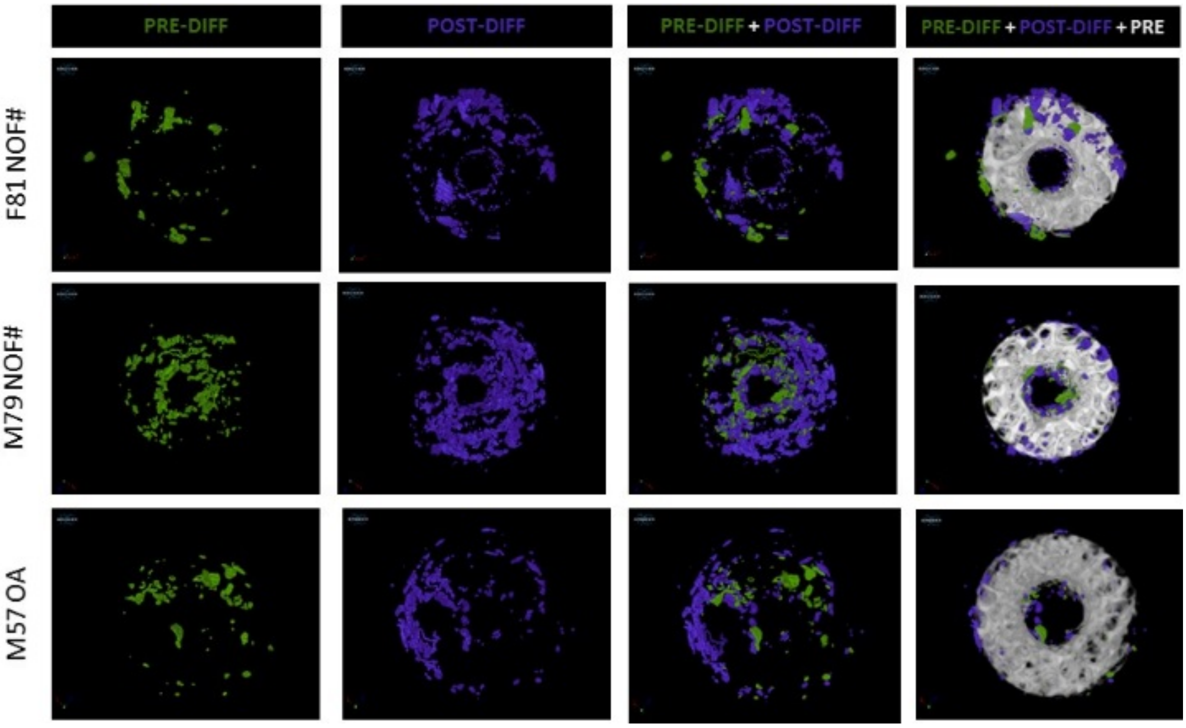

Supplementary Figure 7.4.1: Visualisation of pre and post differences of CAM-implanted human bone cylinders following image 3D registration processing. Pre and post scans of bone cylinders cultured *in vitro* were 3D registered and the difference image was digitally processed to display pre-difference in green, post-difference in purple, loaded on top of the original (pre) dataset in ivory colour. Representative images from three independent experiments conducted with F81 NOF#, M79 NOF# and M57 OA femoral heads.

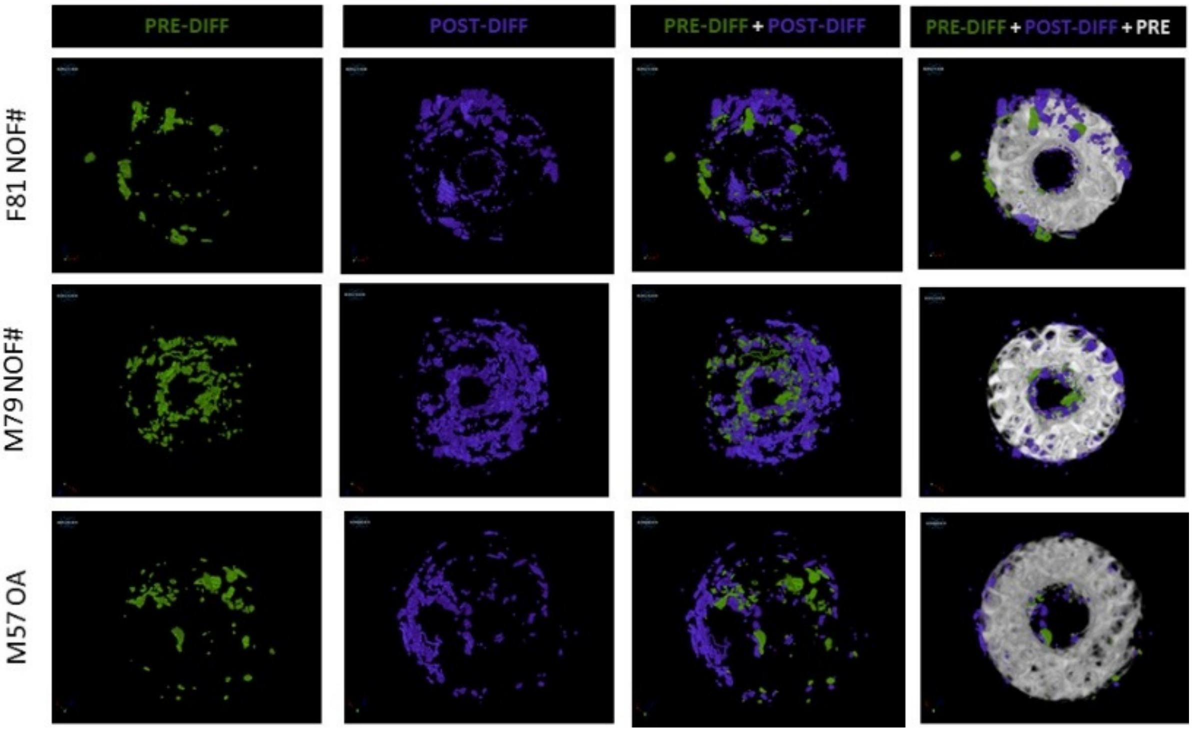

Supplementary Figure 7.4.2: Visualisation of pre and post differences of *in vitro* -cultured human bone cylinders following image 3D registration processing. Pre and post scans of bone cylinders cultured *in vitro* were 3D registered and the difference image was digitally processed to display pre-difference in green, post-difference in purple, loaded on top of the original (pre) dataset in ivory colour. Representative images from three independent experiments conducted with F81 NOF#, M79 NOF# and M57 OA femoral heads.

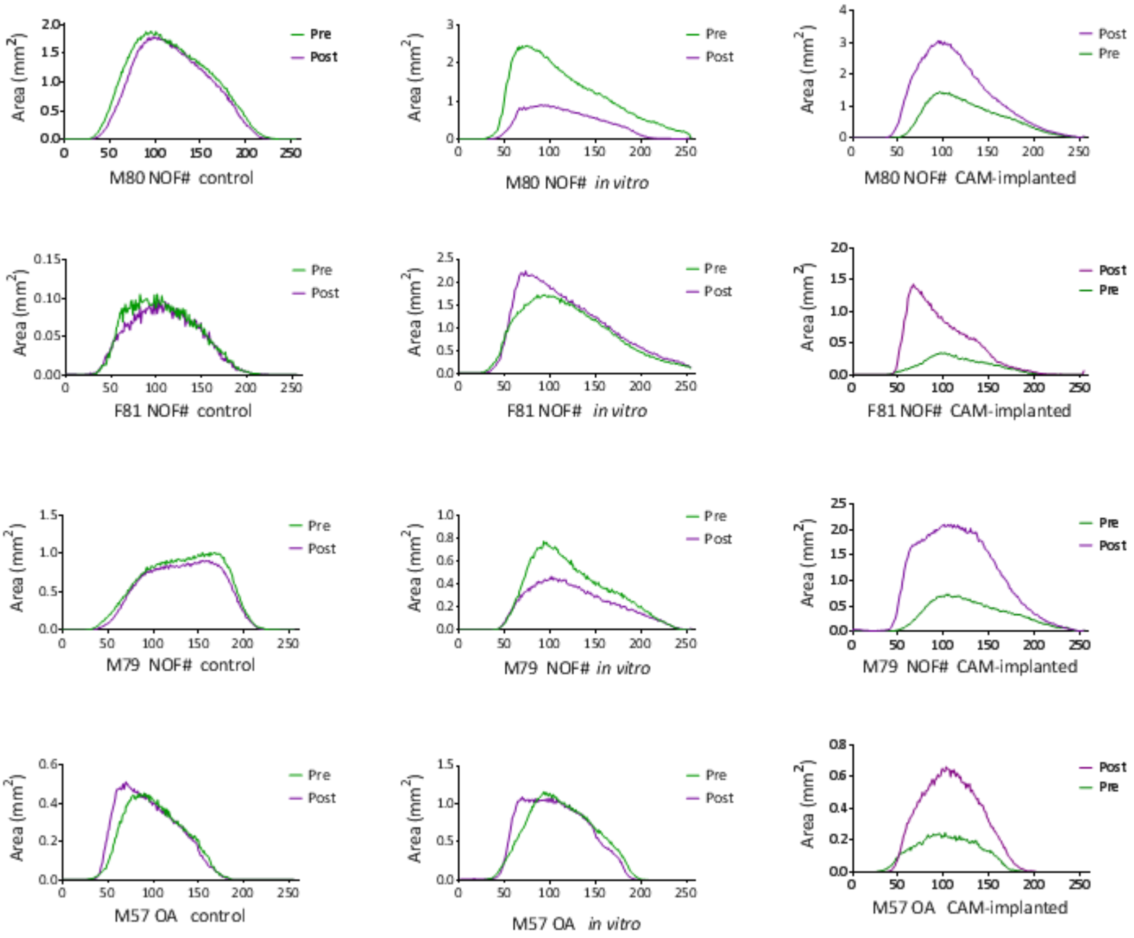

Supplementary Figure 7.4.3 Histogram distribution of pre and post scans following the application of a 3D-registration-based ROI. Bone cylinders from M80 NOF#, F81 NOF#, M79 NOF# and M57 OA patients were CAM-implanted, *in vitro* cultured or maintained at four degrees (C) for 7 days. Pre and post incubation µCT scans were registered to obtain the difference image, which was then used as an ROI on top of the original scans to obtain their pixel distribution on from the pre (green line) and the post (purple) on the same histogram. Representative scans were used for the image processing pipeline from each experimental repeat and patient.

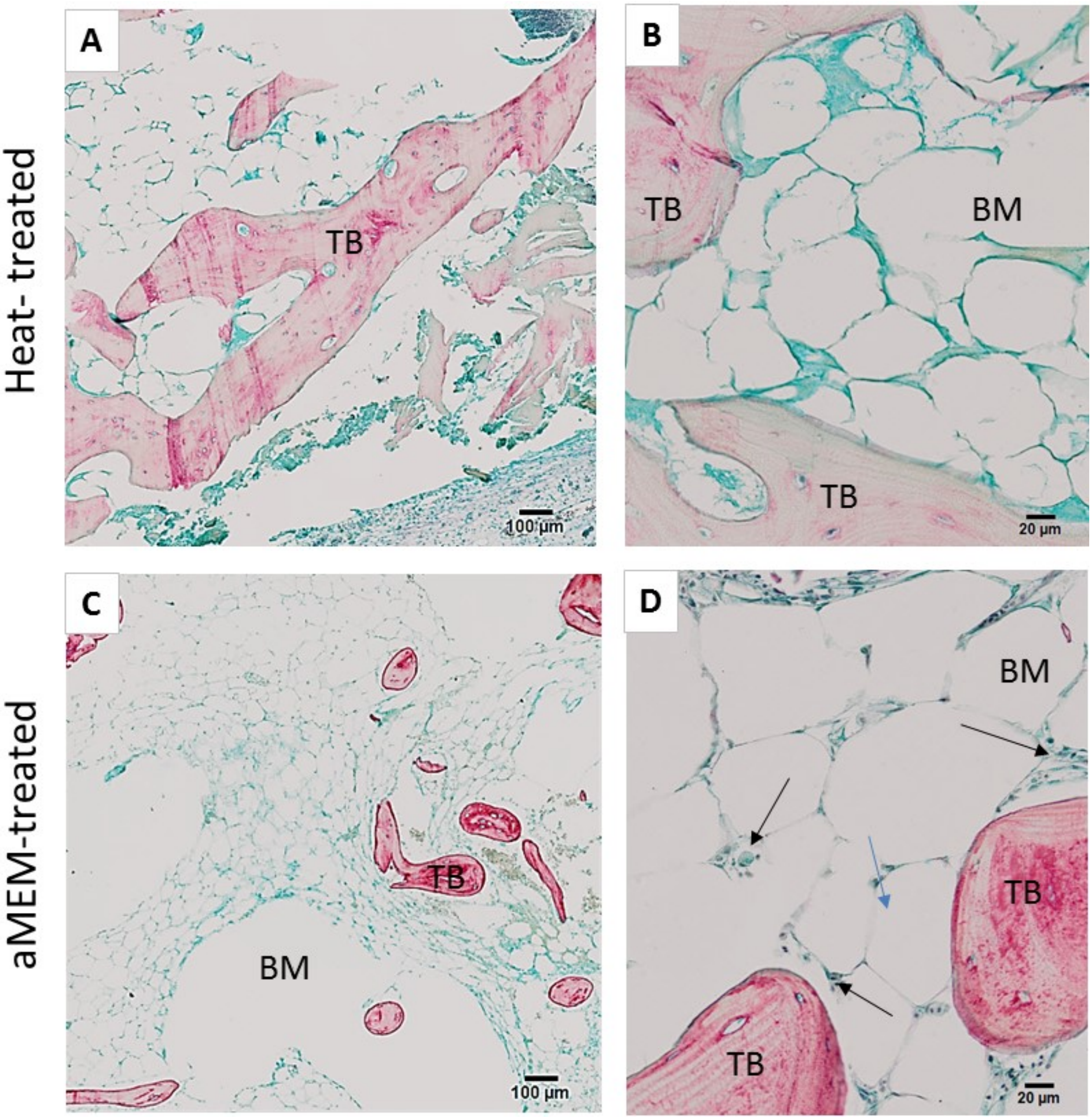

Supplementary Figure 7.4.4: Absence of cellular component on the marrow cavity following cell death by heat - treatment. Bone cylinders were high (121 °C) temperature treated (A-B) or maintained in standard culture conditions (C-D) prior CAM-implantation for 7 days, chick embryo viability was assessed at harvest and samples were processed for histology. Paraffin sections were stained for AS. Arrows indicate presence of nucleated cells. (BM) bone marrow, (TB) trabecular bone. Scale bars equivalent to 100 µm (A, C) and 20 µm (B, D).

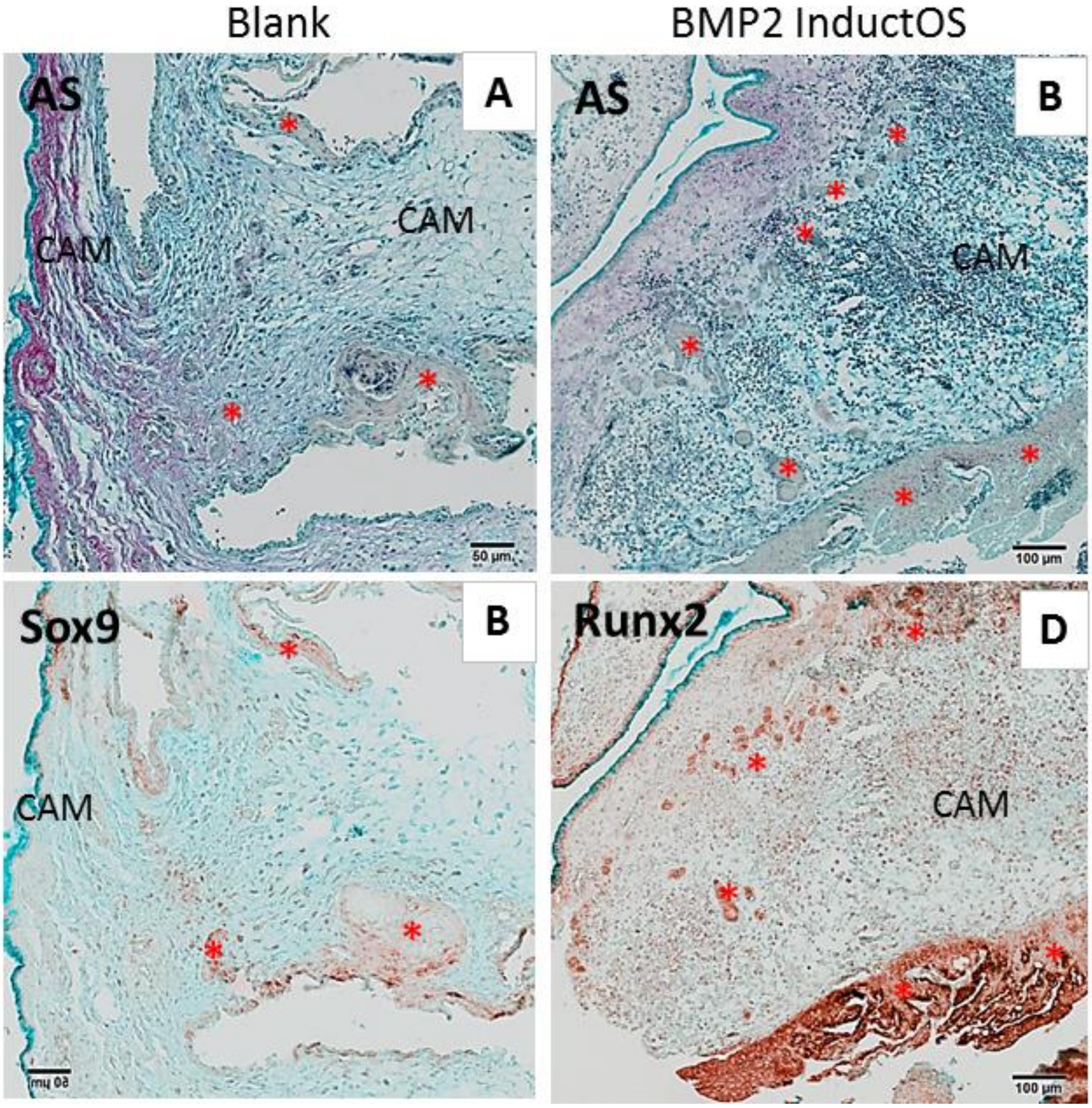

Supplementary Figure 7.4.5: Endochondral cell condensations on CAM-implanted collagen sponges following BMP2 delivery. Collagen sponges of standard size were administered 0 ug/mL BMP2– blank (A, B) and 150 µg/mL BMP2 (C,D) before CAM-implantation for 9 days. At harvest, samples were fixed, processed for paraffin section. Consecutive sections were stained for Alcian Blue and Sirius Red (A, C) and immunohistochemistry for Sox9 (B) and Runx2 (D). Positive immunostaining in brown-red colour, counterstained with Alcian Blue to visualize the matrix content. *indicate cell condensations. chorioallantoic membrane (CAM), Alcian Blue and Sirius Red (AS). Scale bars equivalent to 50 µm (A, B) and 100 µm (C, D)

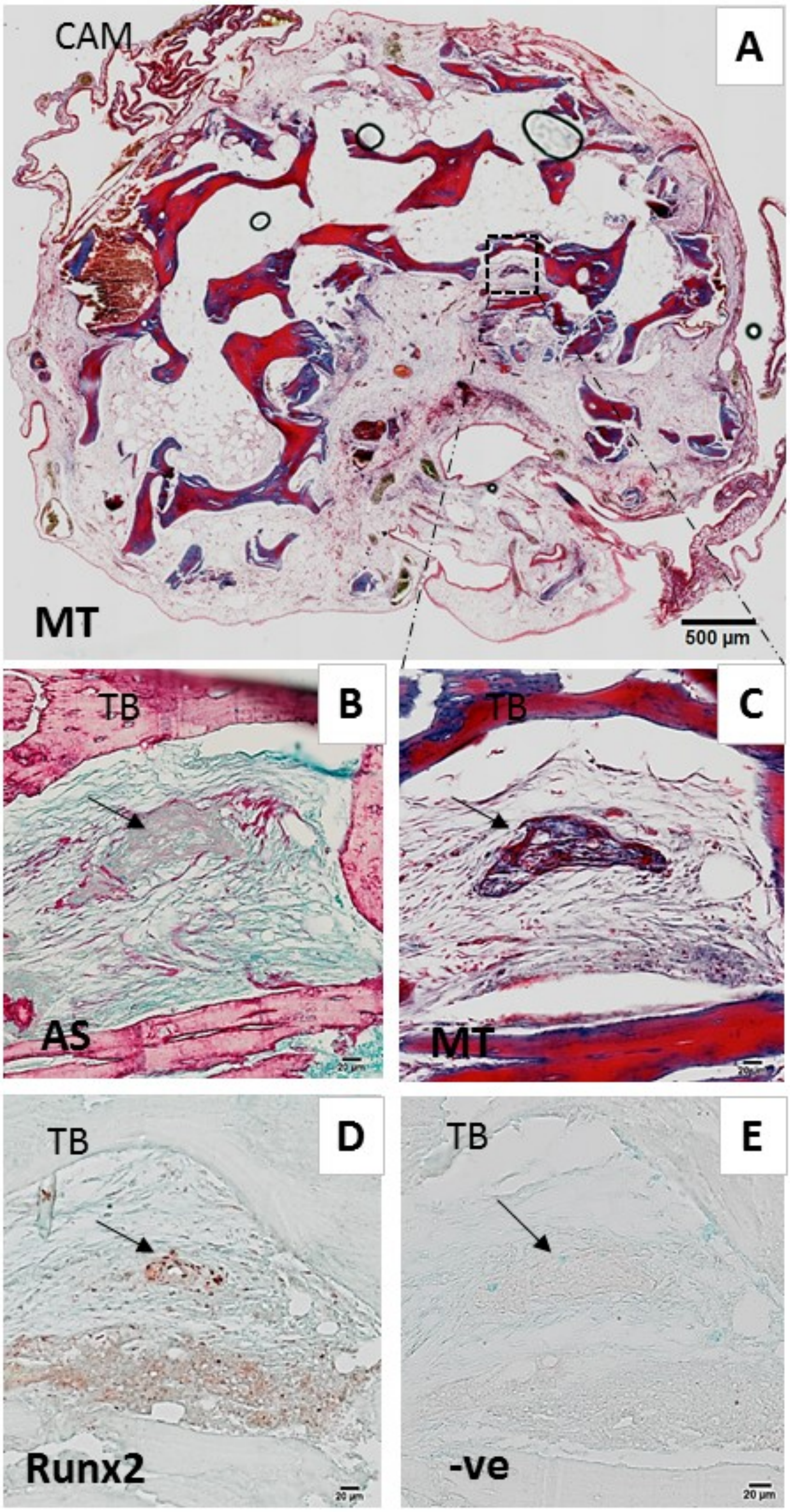

Supplementary Figure 7.4.6: Matrix deposition and cell condensations following the addition of high dose of BMP2 InductOs™on CAM-implanted bone cylinders. Collagen sponge containing 150 µg/mL BMP2 (InductOs) was applied on the defect region of the bone cylinders before CAM-implantation for 9 days. Consecutive representative paraffin sections were stained for Modified Masson's Tetrachrome staining osteoid in deep blue, lamellar bone in bright red, red blood cells in yellow and cartilage in light blue (A, C) and Alcian Blue and Sirius Red (B) and immunohistochemistry for Runx2 (D) . Positive immunostaining in brown-red colour, counterstained with Alcian Blue to visualize the matrix content. (TB) trabecular bone, (CAM) chorioallantoic membrane, arrows indicate cell condensation. Scale bars equivalent to 500 µm (A) and 20 µm (B-E).

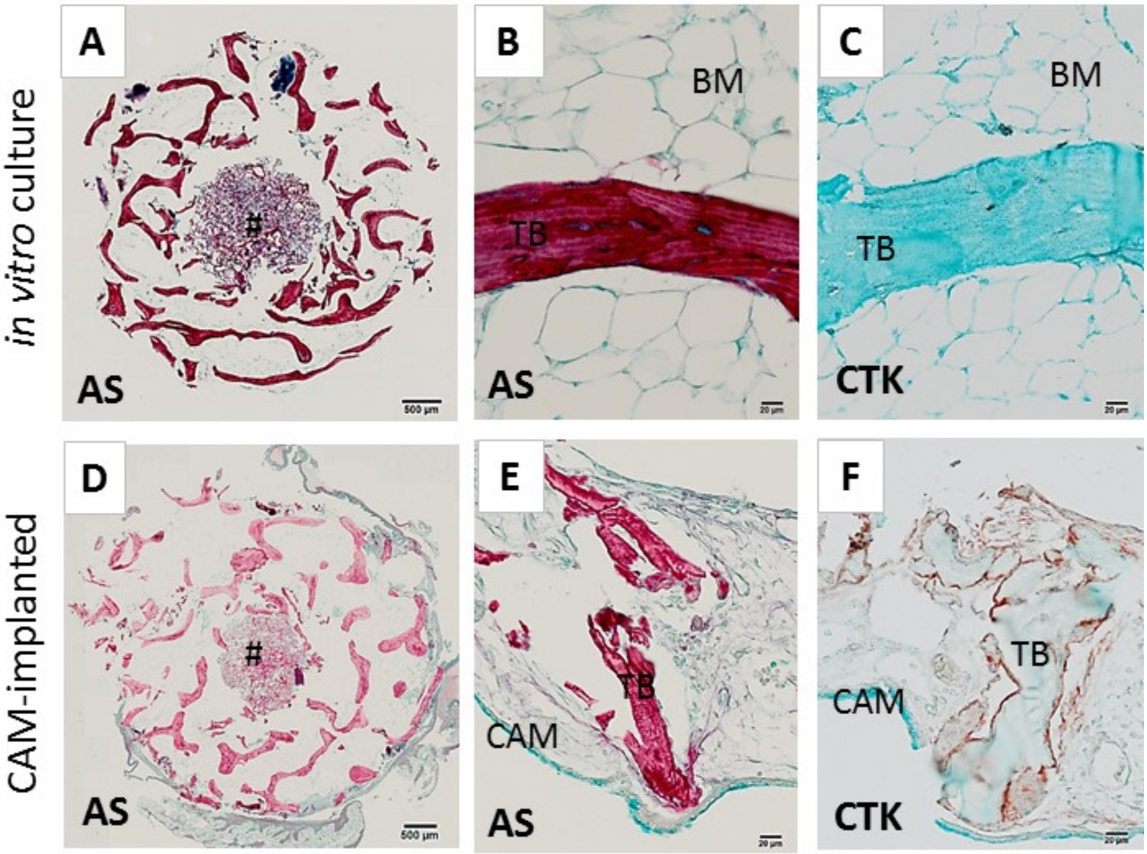

Supplementary Figure 7.4.7: Osteoclast activity on CAM-implanted bone cylinders following delivery of BMP2-InductOs. A collagen sponge containing 150 µg/ml BMP2 was applied on the defect region of the bone cylinders extracted from the same femoral head before CAM-implantation or *in vitro* culture for 9 days. Consecutive paraffin sections stained for Alcian blue and Sirius red (A-B and D-E) and immunohistochemistry for Cathepsin K (C and F). Positive immunostaining in brown-red colour, counterstained with Alcian Blue to visualize the matrix content. (TB) trabecular bone; (BM) bone marrow; (CAM) chorioallantoic membrane, # indicate location of collagen sponge in the bone defect area. Scale bars equivalent to 500 µm (A, B) and 20 µm (B-F).

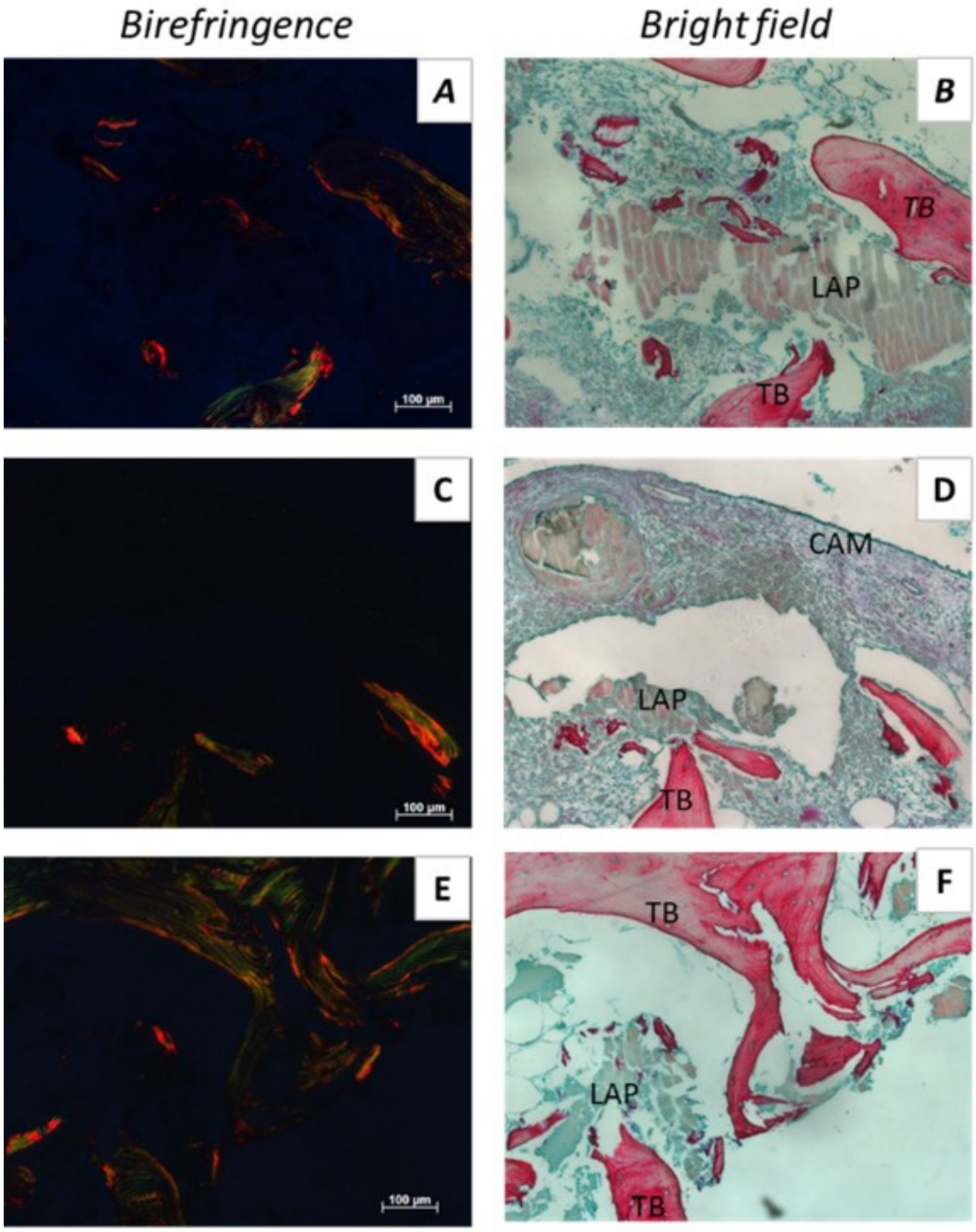

Supplementary Figure 7.4.8: Laponite does not appear under the polarized filter, but collagen does. Laponite was applied on the bone cylinders before CAM-implantation for 7 days. Consecutive paraffin sections were stained for Alcian blue and Sirius red (B, D and F) and then imaged under polarized filter (A, C and D). LAP (Laponite) (TB) trabecular bone, (CAM) chorioallantoic membrane. Scale bars equivalent to 100 µm (A) and 50 µm (B-E).

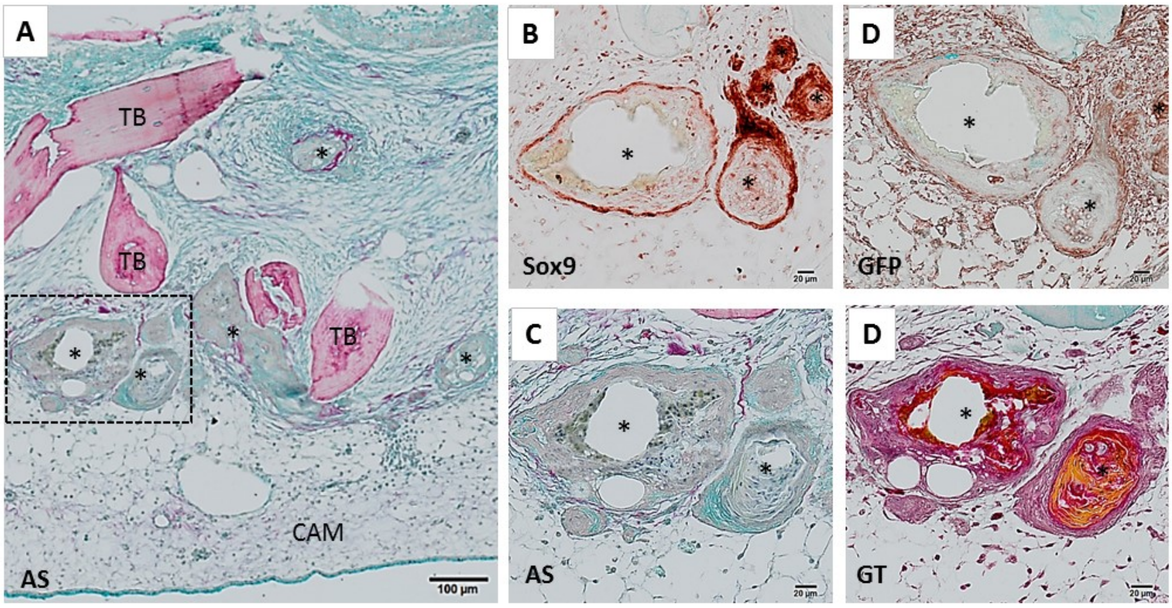

Supplementary Figure 7.4.9: Additional example of endochondral cell condensations following Laponite BMP2 delivery on bone cylinders from M80 NOF#. Freshly isolated bone cylinders from M80 NOF were perfused with Laponite containing 7.85 µg/ml before CAM-implantation. Consecutive paraffin sections were stained for Alcian Blue and Sirius red staining (A, C), Goldner's Trichrome (D) and immunohistochemistry for Sox9 (B), GFP (D). * Indicate endochondral cell condensations. (TB) trabecular bone, (CAM) chorioallantoic membrane. Scale bars equivalent to 100 µm (A) and 50 µm (B-E).

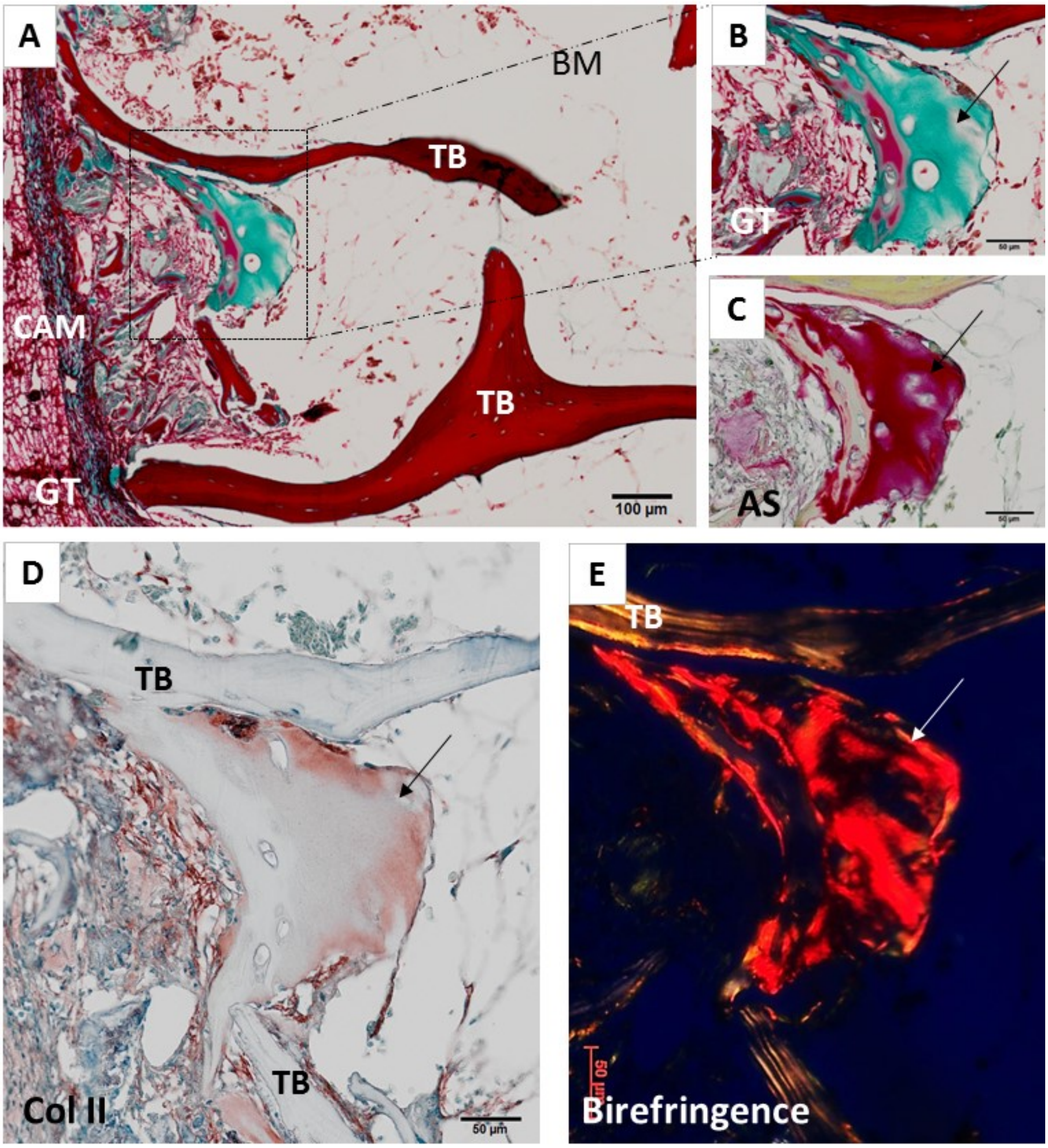

Supplementary Figure 7.4.10: New collagen deposition sprouting from pre-existing bone on Laponite treated bone cylinders from F85 NOF#. Plain Laponite was perfused in the defect region of the bone cylinders from F85 NOF# before CAM-implantation. Consecutive paraffin sections were stained for Alcian Blue and Sirius red staining (A, C) and Goldner's Trichrome (B) and immunohistochemistry for Collagen type II (D). Positive immunostaining in brown-red colour, counterstained with Alcian Blue to visualize the matrix content. Birefringence images (E) were capture using polarized filter following picro-red staining (C). Arrows indicate location of matrix deposition. (TB) trabecular bone, (CAM) chorioallantoic membrane, (LAP) Laponite, # indicates Laponite location on the bone cylinder defect region. Scale bars equivalent to 100 µm (A) and 50 µm (B-E).

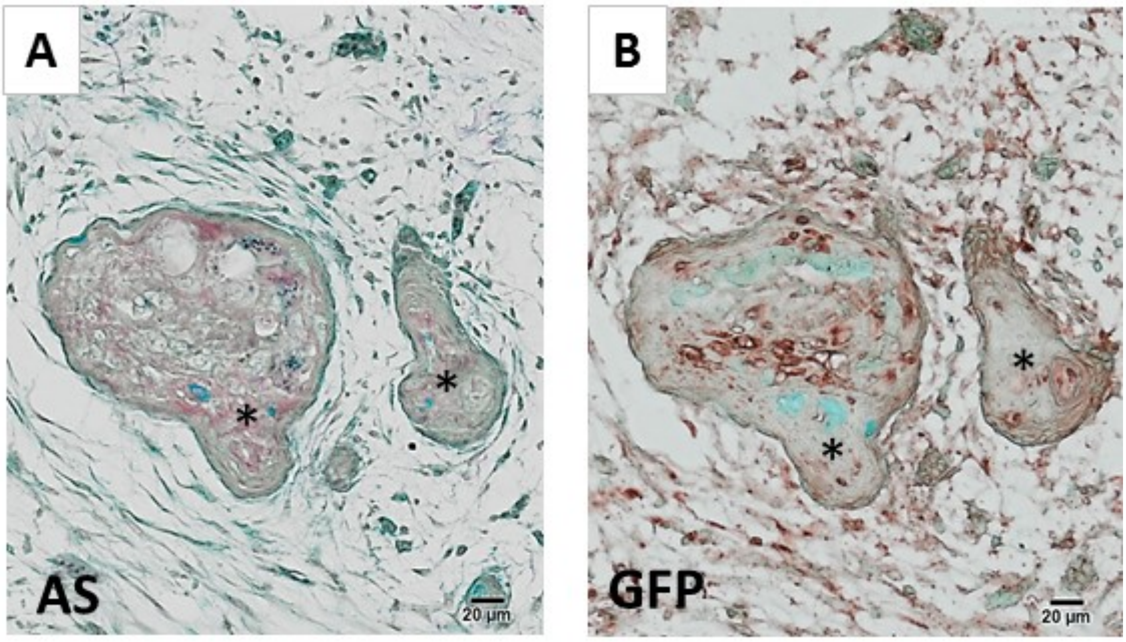

Supplementary Figure 7.4.11: Cell condensations express variable levels of the reporter GFP gene. Laponite containing EC was perfused in the defect region of the bone cylinders from M79 OA before CAM-implantation. Consecutive paraffin sections were stained for Alcian Blue and Sirius red (A) or and immunohistochemistry for GFP (B). Positive immunostaining in brown-red colour, counterstained with Alcian Blue to visualize the matrix content. *indicate cell condensations structures. Scale bars equivalent to 20 µm.

References

Ai-Aql, Z. S., a S. Alagl, D. T. Graves, L. C. Gerstenfeld, and T. a Einhorn. 2008. “Molecular Mechanisms Controlling Bone Formation during Fracture Healing and Distraction Osteogenesis.” *Journal of dental research* 87(2):107–18.

Akiyama, Haruhiko et al. 2005. “Osteo-Chondroprogenitor Cells Are Derived from Sox9 Expressing Precursors.” *Proceedings of the National Academy of Sciences of the United States of America* 102(41):14665–70.

Akiyama, Haruhiko, Marie Christine Chaboissier, James F. Martin, Andreas Schedl, and Benoit De Crombrugghe. 2002. “The Transcription Factor Sox9 Has Essential Roles in Successive Steps of the Chondrocyte Differentiation Pathway and Is Required for Expression of Sox5 and Sox6.” *Genes & Development* 16:2813–28.

Alexander, Kylie A. et al. 2011. “Osteal Macrophages Promote in Vivo Intramembranous Bone Healing in a Mouse Tibial Injury Model.” *Journal of Bone and Mineral Research* 26(7):1517–32.

Andersen, Thomas Levin et al. 2009. “A Physical Mechanism for Coupling Bone Resorption and Formation in Adult Human Bone.” *The American journal of pathology* 174(1):239–47.

Anderson, Sean M., Shayne N. Siegman, and Tatiana Segura. 2011. “The Effect of Vascular Endothelial Growth Factor (VEGF) Presentation within Fibrin Matrices on Endothelial Cell Branching.” *Biomaterials* 32(30):7432–43.

Apelt, D. et al. 2004. “In Vivo Behavior of Three Different Injectable Hydraulic Calcium Phosphate Cements.” *Biomaterials* 25(7-8):1439–51.

Aro, Hannu T. 2011. “Recombinant Human Bone Morphogenetic Protein-2: A Randomized Trial in Open Tibial Fractures Treated with Reamed Nail Fixation.” *The Journal of Bone and Joint Surgery (American)* 93(9):801.

Ausprunk, D. H., D. R. Knighton, and J. Folkman. 1975. “Vascularization of Normal and Neoplastic Tissues Grafted to the Chick Chorioallantois. Role of Host and Preexisting Graft Blood Vessels.” *The American journal of pathology* 79(3):597–618.

Azzarello, Joseph, Michael a Ihnat, Bradley P. Kropp, Linda a Warnke, and Hsueh-Kung Lin. 2007. “Assessment of Angiogenic Properties of Biomaterials Using the Chicken Embryo Chorioallantoic Membrane Assay.” *Biomedical materials (Bristol, England)* 2(2):55–61.

Baek, Miri, and Soo Jin Choi. 2012. “Effect of Orally Administered Glutathione-Montmorillonite Hybrid Systems on Tissue Distribution.” *Journal of Nanomaterials* 2012:1–7.

Bai, Yan et al. 2013. “Localized Delivery of Growth Factors for Angiogenesis and Bone Formation in Tissue Engineering.” *International Immunopharmacology* 16(2):214–23.

Bai, Yan et al. 2014. “Effects of Combinations of BMP-2 with FGF-2 And/or VEGF on HUVECs Angiogenesis in Vitro and CAM Angiogenesis in Vivo.” *Cell and Tissue Research* 356(1):109–21.

Baiguera, Silvia et al. 2010. “Tissue Engineered Human Tracheas for in Vivo Implantation.” *Biomaterials* 31(34):8931–38.

Baiguera, Silvia, Paolo Macchiarini, and Domenico Ribatti. 2012. “Chorioallantoic Membrane for in Vivo Investigation of Tissue-Engineered Construct Biocompatibility.” *Journal of Biomedical Materials Research - Part B Applied Biomaterials* 100 B(5):1425–34.

Balke, Maurice et al. 2011. “A Short-Term in Vivo Model for Giant Cell Tumor of Bone.” *BMC cancer* 11(1):241.

Bandyopadhyay, Amitabha et al. 2006. “Genetic Analysis of the Roles of BMP2, BMP4, and BMP7 in Limb Patterning and Skeletogenesis.” *PLoS Genetics* 2(12):2116–30.

Barna, Maria, and Lee Niswander. 2007. “Visualization of Cartilage Formation: Insight into Cellular Properties of Skeletal Progenitors and Chondrodysplasia Syndromes.” *Developmental Cell* 12(6):931–41.

Bellairs, Ruth, and Mark Osmond. 2014. *Atlas of Chick Development*.

Birkhold, Annette I. et al. 2014. “Mineralizing Surface Is the Main Target of Mechanical Stimulation Independent of Age: 3D Dynamic in Vivo Morphometry.” *Bone* 66:15–25.

Bohner, Marc. 2010. “Design of Ceramic-Based Cements and Putties for Bone Graft Substitution.” *European Cells and Materials* 20(1-2):1–12.

Bolland, B. J. R. F., J. M. Kanczler, D. G. Dunlop, and R. O. C. Oreffo. 2008. “Development of in Vivo uCT Evaluation of Neovascularisation in Tissue Engineered Bone Constructs.” *Bone* 43(1):195–202.

Bonn, Daniel, Hamid Kellay, Hajime Tanaka, Gerard Wegdam, and Jacques Meunier. 1999. “Laponite:What Is the Difference between a Gel and a Glass?” *Langmuir* 15(14):7534–36.

Borges, Joerg et al. 2003. “Chorioallantoic Membrane Angiogenesis Model for Tissue Engineering: A New Twist on a Classic Model.” *Tissue engineering* 9(3):441–50.

Borges, Joerg et al. 2006. “Adipose Precursor Cells (Preadipocytes) Induce Formation of New Vessels in Fibrin Glue on the Newly Developed Cylinder Chorioallantoic Membrane Model (CAM).” *Minimally invasive therapy & allied technologies : MITAT : official journal of the Society for Minimally Invasive Therapy* 15(4):246–52.

Bouxsein, Mary L. et al. 2010. “Guidelines for Assessment of Bone Microstructure in Rodents Using Micro-Computed Tomography.” *Journal of Bone and Mineral Research* 25(7):1468–86.

Boyce, W. J., and M. P. Vessey. 1985. “Rising Incidence of Fracture of the Proximal Femur.” *The Lancet* 150–51.

Boyd, Steven K. et al. 2006. “Evaluation of Three-Dimensional Image Registration Methodologies for in Vivo Micro-Computed Tomography.” *Annals of Biomedical Engineering* 34(10):1587–99.

Bronner, Marianne E., and Nicole M. LeDouarin. 2012. “Development and Evolution of the Neural Crest: An Overview.” *Developmental Biology* 366(1):2–9.

Burge, Rt, D. Worley, A. Johansen, and U. Bose. 2008. “The Cost of Osteoporotic Fractures in the United Kingdom.” *Value in Health* 4(2):66–67.

Buschmann, Johanna et al. 2012. “Tissue Engineered Bone Grafts Based on Biomimetic Nanocomposite PLGA/amorphous Calcium Phosphate Scaffold and Human Adipose-Derived Stem Cells.” *Injury* 43(10):1689–97.

Cai, Wei Xin et al. 2014. “Effect of Different rhBMP-2 and TG-VEGF Ratios on the Formation of Heterotopic Bone and Neovessels.” *BioMed Research International* 2014:1–7.

Callis, Gayle, and Diane Sterchi. 1998. “Decalcification of Bone: Literature Review and Practical Study of Various Decalcifying Agents. Methods, and Their Effects on Bone Histology.” *Journal of Histotechnology* 21(1):49–58.

Calori, G. M., W. Albisetti, A. Agus, S. Iori, and L. Tagliabue. 2007. “Risk Factors Contributing to Fracture Non-Unions.” *Injury* 38(SUPPL. 2):s11–18.

Calori, G. M., E. Mazza, M. Colombo, and C. Ripamonti. 2011. “The Use of Bone-Graft Substitutes in Large Bone Defects: Any Specific Needs?” *Injury* 42(SUPPL. 2):S56–63.

Cantatore, Francesco Paolo, Enrico Crivellato, Beatrice Nico, and Domenico Ribatti. 2005. “Osteocalcin Is Angiogenic in Vivo.” *Cell Biology International* 29(7):583–85.

Carmeliet, P. et al. 1996. “Abnormal Blood Vessel Development and Lethality in Embryos Lacking a Single VEGF Allele.” *Nature* 380(6573):435–39.

Carragee, Eugene J., Eric L. Hurwitz, and Bradley K. Weiner. 2011. “A Critical Review of Recombinant Human Bone Morphogenetic Protein-2 Trials in Spinal Surgery: Emerging Safety Concerns and Lessons Learned.” *Spine Journal* 11(6):471–91.

Carre, Antoine L. et al. 2012. “Fetal Mouse Skin Heals Scarlessly in a Chick Chorioallantoic Membrane Model System.” *Annals of Plastic Surgery* 69(1):85–90.

Centrella, M., T. L. McCarthy, and E. Canalis. 1991. “Current Concepts Review. Transforming Growth Factor-Beta and Remodeling of Bone.” *J Bone Joint Surg* 73-A:1418–28.

Chapman, Susan C. et al. 2005. “Ubiquitous GFP Expression in Transgenic Chickens Using a Lentiviral Vector.” *Development (Cambridge, England)* 132(5):935–40.

Chappuis, Vivianne et al. 2012. “Periosteal BMP2 Activity Drives Bone Graft Healing.” *Bone* 51(4):800–809.

Chen, Z. et al. 1997. “Noninvasive Imaging of in Vivo Blood Flow Velocity Using Optical Doppler Tomography.” *Optics letters* 22(14):1119–21.

Chikazu, Daichi et al. 2002. “Bone Morphogenetic Protein 2 Induces Cyclo-Oxygenase 2 in Osteoblasts via a Cbfa1 Binding Site: Role in Effects of Bone Morphogenetic Protein 2 in Vitro and in Vivo. 2002.” *Journal of bone and* *mineral research the official journal of the American Society for Bone and Mineral Research* 20(10):1888–98.

Chiu, Loraine L. Y., and Milica Radisic. 2010. “Scaffolds with Covalently Immobilized VEGF and Angiopoietin-1 for Vascularization of Engineered Tissues.” *Biomaterials* 31(2):226–41.

Cho, Andrew. 2010. “A Method for Rapid Demineralization of Teeth and Bones.” *The Open Dentistry Journal* 4(1):223–29.

Christiansen, Blaine A. 2016. “Effect of Micro-Computed Tomography Voxel Size and Segmentation Method on Trabecular Bone Microstructure Measures in Mice.” *Bone Reports* 5:136–40.

Clarke, Bart. 2008. “Normal Bone Anatomy and Physiology.” *Clinical journal of the American Society of Nephrology : CJASN* 3 Suppl 3:S131–39.

Clarkin, Claire E., Elena Garonna, Andrew a. Pitsillides, and C. P. D. Wheeler-Jones. 2008. “Heterotypic Contact Reveals a COX-2-Mediated Suppression of Osteoblast Differentiation by Endothelial Cells: A Negative Modulatory Role for Prostanoids in VEGF-Mediated Cell: Cell Communication?” *Experimental Cell Research* 314(17):3152–61.

Clarkin, Claire E., and Louis C. Gerstenfeld. 2013. “VEGF and Bone Cell Signalling: An Essential Vessel for Communication?” *Cell Biochemistry and Function* 31(1):1–11.

Coconi, Maria Teresa et al. 2005. “Angiogenic Response Induced by Acellular Aorta Matrix in Vivo.” *Journal of Anatomy* 207(1):79–83.

Cooley, Lindsay S. et al. 2010. “Reversible Transdifferentiation of Blood Vascular Endothelial Cells to a Lymphatic-like Phenotype in Vitro.” *Journal of cell science* 123(Pt 21):3808–16.

Cruz, Amauri, Charles Parnot, Domenico Ribatti, Pierre Corvol, and Jean Marie Gasc. 2001. “Endothelin-1, a Regulator of Angiogenesis in the Chick Chorioallantoic Membrane.” *Journal of Vascular Research* 38(6):536–45.

Cunningham, C. D., B. a Schulte, L. M. Bianchi, P. C. Weber, and B. N. Schmiedt. 2001. “Microwave Decalcification of Human Temporal Bones.” *The Laryngoscope* 111(2):278–82.

Czekanska, E. M., M. J. Stoddart, J. R. Ralphs, R. G. Richards, and J. S. Hayes. 2014. “A Phenotypic Comparison of Osteoblast Cell Lines versus Human Primary Osteoblasts for Biomaterials Testing.” *Journal of Biomedical Materials Research - Part A* 102(8):2636–43.

Damien, C. J., and J. R. Parsons. 1991. “Bone Graft and Bone Graft Substitutes: A Review of Current Technology and Applications.” *Journal of applied biomaterials : an official journal of the Society for Biomaterials* 2(3):187–208.

David M. Webber, David Menton and Philip Osdoby. 1990. “An in Vivo Model System for the Study of Avian Osteoclast Recruitment and Activity.” *Bone and Mineral* 11:127–40.

David, Valentin et al. 2008. “Ex Vivo Bone Formation in Bovine Trabecular Bone Cultured in a Dynamic 3D Bioreactor Is Enhanced by Compressive Mechanical Strain.” *Tissue engineering. Part A* 14(1):117–26.

Davies, CM. et al. 2006. “Mechanically Loaded Ex Vivo Bone Culture System ‘ Zetos ’: Systems and Culture Preparation.” *European cells & materials* 11(0):57–75.

Davies, Neil et al. 2008. “The Dosage Dependence of VEGF Stimulation on Scaffold Neovascularisation.” *Biomaterials* 29(26):3531–38.

Dawson, Jonathan I., Janos M. Kanczler, Xuebin B. Yang, George S. Attard, and Richard O. C. Oreffo. 2011. “Clay Gels for the Delivery of Regenerative Microenvironments.” *Advanced Materials* 23(29):3304–8.

Dawson, Jonathan I., Emmajayne Kingham, Nicholas R. Evans, Edward Tayton, and Richard O. C. Oreffo. 2012. “Skeletal Regeneration : Application of Nanoto- Pography and Biomaterials for Skeletal Stem Cell Based Bone Repair.” *Inflammation and regeneration* 32(3):72–89.

Dawson, Jonathan I., and Richard O. C. Oreffo. 2013. “Clay: New Opportunities for Tissue Regeneration and Biomaterial Design.” *Advanced Materials* 25(30):4069–86.

Debbasch, Caroline et al. 2005. “Eye Irritation of Low-Irritant Cosmetic Formulations: Correlation of in Vitro Results with Clinical Data and Product Composition.” *Food and Chemical Toxicology* 43(1):155–65.

Delalande, Jean Marie et al. 2014. “Vascularisation Is Not Necessary for Gut Colonisation by Enteric Neural Crest Cells.” *Developmental Biology* 385(2):220–29.

Deng, Yuan et al. 2014. "In Vitro Osteogenic Induction of Bone Marrow Stromal Cells with Encapsulated Gene-Modified Bone Marrow Stromal Cells and in Vivo Implantation for Orbital Bone Repair." *Tissue engineering. Part A* 20(13-14):2019–29.

Depan, Dilip, Annamalai Pratheep Kumar, and Raj Pal Singh. 2009. "Cell Proliferation and Controlled Drug Release Studies of Nanohybrids Based on Chitosan-G-Lactic Acid and Montmorillonite." *Acta Biomaterialia* 5(1):93–100.

DeRose, Yoko S. et al. 2011. "Tumor Grafts Derived from Women with Breast Cancer Authentically Reflect Tumor Pathology, Growth, Metastasis and Disease Outcomes." *Nature medicine* 17(11):1514–20.

Deryugina, Elena I., and James P. Quigley. 2008. "Chick Embryo Chorioallantoic Membrane Models to Quantify Angiogenesis Induced by Inflammatory and Tumor Cells or Purified Effector Molecules." *Methods Enzymology* 6879(08).

Devin, J. E., M. a Attawia, and C. T. Laurencin. 1996. "Three-Dimensional Degradable Porous Polymer-Ceramic Matrices for Use in Bone Repair." *Journal of biomaterials science. Polymer edition* 7(8):661–69.

DeVolder, Ross J., Andrew T. Zill, Jae H. Jeong, and Hyunjoon Kong. 2012. "Microfabrication of Proangiogenic Cell-Laden Alginate-G-Pyrrole Hydrogels." *Biomaterials* 33(31):7718–26.

Diaz-Gomez, Luis et al. 2014. "Biodegradable Electrospun Nanofibers Coated with Platelet-Rich Plasma for Cell Adhesion and Proliferation." *Materials Science and Engineering C* 40:180–88.

Dimitriou, Rozalia, Eleftherios Tsiridis, and Peter V. Giannoudis. 2005. "Current Concepts of Molecular Aspects of Bone Healing." *Injury* 36(12):1392–1404.

Ding, Wen-Ge, Zhao-Xiang Wei, and Jin-Bo Liu. 2011. "Reduced Local Blood Supply to the Tibial Metaphysis Is Associated with Ovariectomy-Induced Osteoporosis in Mice." *Connective tissue research* 52(1):25–29.

Durupt, F. et al. 2012. "The Chicken Chorioallantoic Membrane Tumor Assay as Model for Qualitative Testing of Oncolytic Adenoviruses." *Cancer Gene Therapy* 19(1):58–68.

Eckardt, Henrik et al. 2003. "Effects of Locally Applied Vascular Endothelial Growth Factor (VEGF) and VEGF-Inhibitor to the Rabbit Tibia during Distraction Osteogenesis." *Journal of Orthopaedic Research* 21(2):335–40.

Edwards, Sandra S. et al. 2014. "Functional Analysis Reveals Angiogenic Potential of Human Mesenchymal Stem Cells from Wharton's Jelly in Dermal Regeneration." *Angiogenesis* 17(4):851–66.

Einhorn, Thomas a, and Louis C. Gerstenfeld. 2015. "Fracture Healing: Mechanisms and Interventions." *Nature reviews. Rheumatology* 11(1):45–54.

El-Serafi, Ahmed T., David I. Wilson, Helmtrud I. Roach, and Richard O. C. Oreffo. 2011. "Developmental Plasticity of Human Foetal Femur-Derived Cells in Pellet Culture: Self Assembly of an Osteoid Shell around a Cartilaginous Core." *European Cells and Materials* 21:558–67.

Enomoto-Iwamoto, M. et al. 1998. "Bone Morphogenetic Protein Signaling Is Required for Maintenance of Differentiated Phenotype, Control of Proliferation, and Hypertrophy in Chondroctyes." *J. Cell Biol.* 140(2):409–18.

Fages, Jacques et al. 1998. "Bone Allografts and Supercritical Processing: Effects on Osteointegration and Viral Safety." *Journal of Supercritical Fluids* 13(1-3):351–56.

Fang, Tony D. et al. 2005. "Angiogenesis Is Required for Successful Bone Induction During Distraction Osteogenesis." *Journal of Bone and Mineral Research* 20(7):1114–24.

Ferrara, N. et al. 1996. "Heterozygous Embryonic Lethality Induced by Targeted Inactivation of the VEGF Gene." *Nature* 380(6573):439–42.

Ferrara, Napoleone, Hans-Peter Gerber, and Jennifer LeCouter. 2003. "The Biology of VEGF and Its Receptors." *Nature medicine* 9(6):669–76.

Fisichella, Matthieu et al. 2009. "Mesoporous Silica Nanoparticles Enhance MTT Formazan Exocytosis in HeLa Cells and Astrocytes." *Toxicology in Vitro* 23(4):697–703.

Friend, J. V., R. W. R. Crevel, T. C. Williams, and W. E. Parish. 1990. "Immaturity of the Inflammatory Response of the Chick Chorioallantoic Membrane." *Toxicology in Vitro* 4(4-5):324–26.

Fu, Rongwei et al. 2013. "Effectiveness and Harms of Recombinant Human Bone Morphogenetic." *Annals of Internal Medicine* 158:890–902.

Gabrielli, Maria Gabriella, and Daniela Accili. 2010. “The Chick Chorioallantoic Membrane: A Model of Molecular, Structural, and Functional Adaptation to Transepithelial Ion Transport and Barrier Function during Embryonic Development.” *Journal of Biomedicine and Biotechnology* 2010:940741.

Geiger, M., R. H. Li, and W. Friess. 2003. “Collagen Sponges for Bone Regeneration with rhBMP-2.” *Advanced Drug Delivery Reviews* 55(12):1613–29.

Georgi, Nicole et al. 2015. “MicroRNA Levels as Prognostic Markers for the Differentiation Potential of Human Mesenchymal Stromal Cell Donors.” *Stem cells and development* 24(16):1946–55.

Giannoudis, Peter V., Thomas a. Einhorn, and David Marsh. 2007. “Fracture Healing: The Diamond Concept.” *Injury* 38(4 SUPPL.):S3–6.

Gibbs, D. M. R. et al. 2016. “Bone Induction at Physiological Doses of BMP through Localization by Clay Nanoparticle Gels.” *Biomaterials* 99:16–23.

Govender, Shunmugam et al. 2002. “Recombinant Human Bone Morphogenetic Protein-2 for Treatment of Open Tibial Fractures.” *The Journal of bone and joint surgery American volume* 84(12):2123–34.

Greek, Ray, and Andre Menache. 2013. “Systematic Reviews of Animal Models: Methodology versus Epistemology.” *International Journal of Medical Sciences* 10(3):206–21.

Greenberg, Joshua I. et al. 2009. “A Role of VEGF as a Negative Regulator of Perycite Function and Vessel Maturation.” *Nature* 456(7223):809–13.

Hadjizadeh, Afra, and Charles J. Doillon. 2010. “Directional Migration of Endothelial Cells towards Angiogenesis Using Polymer Fibres in a 3D Co-Culture System.” *Journal of tissue engineering and regenerative medicine* 4(7):524–31.

V. Hamburger, H. L. Hamilton. 1951. “A Series of Normal Stages in the Development of the Chick Embryo.” *Journal of Morphology* 88(1):49–92.

Hancox, N. M. 1946. “The Survival of Transplanted Embryo Bone Grafted to CAM and Subsequent Osteogenesis.” *Journal of physiology* 106(1923):279–85.

Hankenson, Kurt D., Michael Dishowitz, Chancellor Gray, and Mara Schenker. 2011. “Angiogenesis in Bone Regeneration.” *Injury* 42(6):556–61.

Hara, T., E. Tanck, J. Homminga, and R. Huiskes. 2002. “The Influence of Microcomputed Tomography Threshold Variations on the Assessment of Structural and Mechanical Trabecular Bone Properties.” *Bone* 31(1):107–9.

Hardy, Charles T., Sarah A. Young, Robert G. Webster, Clayton W. Naeve, and Randall J. Owens. 1995. “Egg Fluids and Cells of the Chorioallantoic Membrane of Embryonated Chicken Eggs Can Select Different Variants of Influenza A (H3N2) Viruses.” *Virology* 211(1):302–6.

Haycock, John. 2011. “3D Cell Culture” edited by John W. Haycock. *Image (Rochester, N.Y.)* 695(2):261–80.

Hayden, J. M., S. Mohan, and D. J. Baylink. 1995. “The Insulin-like Growth Factor System and the Coupling of Formation to Resorption.” *Bone* 17(2 Suppl):93S – 98S.

Helmrich, Uta et al. 2013. “Osteogenic Graft Vascularization and Bone Resorption by VEGF-Expressing Human Mesenchymal Progenitors.” *Biomaterials* 34(21):5025–35.

Hofstaedter, Ferdinand, and Reinhard Ebner. 2004. “The Use of 3-D Cultures for High-Throughput Screening :” *Journal of biomolecular screening* 9(4):273–85.

Hoke, N., a. Grigat, G. Grupe, and M. Harbeck. 2013. “Reconsideration of Bone Postmortem Interval Estimation by UV-Induced Autofluorescence.” *Forensic Science International* 228(1-3):176.e1–6.

Holzmann, Philipp et al. 2010. “Investigation of Bone Allografts Representing Different Steps of the Bone Bank Procedure Using the CAM-Model.” *Altex* 27(2):97–103.

Hopkins, Delana R., Sunduz Keles, and Daniel S. Greenspan. 2007. “The Bone Morphogenetic Protein 1/Tolloid-like Metalloproteinases.” *Matrix Biology* 26(7):508–23.

Huang, Wenjing, Fumihito Arai, and Tomohiro Kawahara. 2015. “Egg-in-Cube: Design and Fabrication of a Novel Artificial Eggshell with Functionalized Surface.” *PLoS ONE* 10(3):e0118624.

Hughes, Francis J., Wendy Turner, Georgios Belibasakis, and Gianluca Martuscelli. 2006. “Effects of Growth Factors and

Cytokines on Osteoblast Differentiation." *Periodontology 2000* 41(1):48–72.

Hulsart-Billström, G. et al. 2016. "A Surprisingly Poor Correlation between in Vitro and in Vivo Testing of Biomaterials for Bone Regeneration: Results of a Multicentre Analysis." *European cells & materials* 31:312–22.

Hutmacher, Dietmar W., and Jan. T. Schantz. 2007. "State of the Art and Future Directions of Scaffold-Base Bone Engineering from a Biomaterials Perspective." *Journal of tissue engineering and regenerative medicine* 1(7):245–60.

Jaffray, D. A., and J. H. Siewerdsen. 2000. "Cone-Beam Computed Tomography with a Flat-Panel Imager: Initial Performance Characterization." *Medical Physics* 27(6):1311.

Jiang, Xi. 2005. "Histological Analysis of GFP Expression in Murine Bone." *Journal of Histochemistry and Cytochemistry* 53(5):593–602.

Johnell, Olof, and John Kanis. 2005. "Epidemiology of Osteoporotic Fractures." *Osteoporosis International* 16(SUPPL. 2):S3–7.

Kalfas, I. H. 2001. "Principles of Bone Healing." *Neurosurgical focus* 10(4):E1.

Kamiya, Nobuhiro et al. 2016. "Targeted Disruption of BMP Signaling through Type IA Receptor (BMPR1A) in Osteocyte Suppresses SOST and RANKL, Leading to Dramatic Increase in Bone Mass, Bone Mineral Density and Mechanical Strength." *Bone* 91:53–63.

Kanczler, J. M. et al. 2007. "Supercritical Carbon Dioxide Generated Vascular Endothelial Growth Factor Encapsulated Poly(dl-Lactic Acid) Scaffolds Induce Angiogenesis in Vitro." *Biochemical and Biophysical Research Communications* 352(1):135–41.

Kanczler, J. M., and R. O. C. Oreffo. 2008. "Osteogenesis and Angiogenesis: The Potential for Engineering Bone." *European Cells and Materials* 15:100–114.

Kanczler, Janos M. et al. 2008. "The Effect of Mesenchymal Populations and Vascular Endothelial Growth Factor Delivered from Biodegradable Polymer Scaffolds on Bone Formation." *Biomaterials* 29(12):1892–1900.

Kanczler, Janos M. et al. 2010. "The Effect of the Delivery of Vascular Endothelial Growth Factor and Bone Morphogenic Protein-2 to Osteoprogenitor Cell Populations on Bone Formation." *Biomaterials* 31(6):1242–50.

Kanczler, Janos M., Emma L. Smith, Carol a Roberts, and Richard O. C. Oreffo. 2012. "A Novel Approach for Studying the Temporal Modulation of Embryonic Skeletal Development Using Organotypic Bone Cultures and Microcomputed Tomography." *Tissue engineering. Part C, Methods* 18(10):747–60.

Kanno, Shohei, Keita Utsunomiya, Yumiko Kono, Noboru Tanigawa, and Satoshi Sawada. 2015. "The Effect of Radiation Exposure on Multidrug Resistance: In Vitro and in Vivo Studies Using Non-Small Lung Cancer Cells." *EJNMMI Research* 5(1):11.

Kaplan, Frederick S. et al. 2008. "Skeletal Metamorphosis in Fibrodysplasia Ossificans Progressiva (FOP)." *Journal of Bone and Mineral Metabolism* 26(6):521–30.

Kempen, Diederik H. R. et al. 2009. "Effect of Local Sequential VEGF and BMP-2 Delivery on Ectopic and Orthotopic Bone Regeneration." *Biomaterials* 30(14):2816–25.

Keramaris, N. C., G. M. Calori, V. S. Nikolaou, E. H. Schemitsch, and P. V. Giannoudis. 2008. "Fracture Vascularity and Bone Healing: A Systematic Review of the Role of VEGF." *Injury* 39(SUPPL.2):S45–57.

Kern, Susanne, Hermann Eichler, Johannes Stoeve, Harald Klüter, and Karen Bieback. 2006. "Comparative Analysis of Mesenchymal Stem Cells from Bone Marrow, Umbilical Cord Blood, or Adipose Tissue." *Stem cells (Dayton, Ohio)* 24(5):1294–1301.

Keshaw, Hussila et al. 2010. "Microporous Collagen Spheres Produced via Thermally Induced Phase Separation for Tissue Regeneration." *Acta Biomaterialia* 6(3):1158–66.

Kilarski, Witold W., Ludvig Petersson, Peder Fredlund Fuchs, Marcin S. Zielinski, and P??r Gerwins. 2012. "An in Vivo Neovascularization Assay for Screening Regulators of Angiogenesis and Assessing Their Effects on Pre-Existing Vessels." *Angiogenesis* 15(4):643–55.

Kilarski, Witold W., Branka Samolov, Ludvig Petersson, Anders Kvanta, and Pär Gerwins. 2009. "Biomechanical Regulation of Blood Vessel Growth during Tissue Vascularization." *Nature Medicine* 15(6):657–64.

Kilkenny, Carol, William Browne, Innes C. Cuthill, Michael Emerson, and Douglas G. Altman. 2010. “Animal Research: Reporting in Vivo Experiments: The ARRIVE Guidelines.” *British Journal of Pharmacology* 160(7):1577–79.

Kilkenny, Carol, William J. Browne, Innes C. Cuthill, Michael Emerson, and Douglas G. Altman. 2013. “Improving Bioscience Research Reporting: The Arrive Guidelines for Reporting Animal Research.” *Animals* 4(1):35–44.

Kitamura, Kei et al. 2002. “Registration Accuracy and Possible Migration of Internal Fiducial Gold Marker Implanted in Prostate and Liver Treated with Real-Time Tumor-Tracking Radiation Therapy (RTRT).” *Radiotherapy and Oncology* 62(3):275–81.

Klueh, U., D. Dorskty, and F. Moussy. 2003. “Ex Ova Chick Chorioallantoic Membrane as a Novel Model for Evaluation of Tissue Responses to Biomaterials and Implants.” *Journal of biomedical materials research. Part A* 67(1):215–23.

Klueh, Ulrike, David I. Dorsky, and Don L. Kreutzer. 2005. “Enhancement of Implantable Glucose Sensor Function in Vivo Using Gene Transfer-Induced Neovascularization.” *Biomaterials* 26(10):1155–63.

Kolk, Andreas et al. 2012. “Current Trends and Future Perspectives of Bone Substitute Materials - From Space Holders to Innovative Biomaterials.” *Journal of Cranio-Maxillofacial Surgery* 40(8):706–18.

Kothari, M. et al. 1998. “Impact of Spatial Resolution on the Prediction of Trabecular Architecture Parameters.” *Bone* 22(5):437–43.

Kue, Chin Siang, Kae Yi Tan, May Lynn Lam, and Hong Boon Lee. 2015. “Chick Embryo Chorioallantoic Membrane (CAM): An Alternative Predictive Model in Acute Toxicological Studies for Anti-Cancer Drugs.” *Experimental Animals* 64(October 2014):129–38.

Kular, Jasreen, Jennifer Tickner, Shek Man Chim, and Jiake Xu. 2012. “An Overview of the Regulation of Bone Remodelling at the Cellular Level.” *Clinical Biochemistry* 45(12):863–73.

Kunzi-Rapp, K., a Rück, and R. Kaufmann. 1999. “Characterization of the Chick Chorioallantoic Membrane Model as a Short-Term in Vivo System for Human Skin.” *Archives of dermatological research* 291(5):290–95.

De la Riva, Beatriz et al. 2010. “Local Controlled Release of VEGF and PDGF from a Combined Brushite-Chitosan System Enhances Bone Regeneration.” *Journal of Controlled Release* 143(1):45–52.

Lafferty, K. J., and M. a Jones. 1969. “Reactions of the Graft versus Host in the CAM.” *The Australian journal of experimental biology and medical science* 47(1):17–54.

Lambers, Floor M. et al. 2015. “Bone Adaptation to Cyclic Loading in Murine Caudal Vertebrae Is Maintained with Age and Directly Correlated to the Local Micromechanical Environment.” *Journal of Biomechanics* 48(6):1179–87.

Lambers, Floor M., Friederike a. Schulte, Gisela Kuhn, Duncan J. Webster, and Ralph Müller. 2011. “Mouse Tail Vertebrae Adapt to Cyclic Mechanical Loading by Increasing Bone Formation Rate and Decreasing Bone Resorption Rate as Shown by Time-Lapsed in Vivo Imaging of Dynamic Bone Morphometry.” *Bone* 49(6):1340–50.

Langford, Dale J. et al. 2010. “Coding of Facial Expressions of Pain in the Laboratory Mouse.” *Nature Methods* 7(6):447–49.

Larger, Etienne, Michel Marre, Pierre Corvol, and Jean Marie Gasc. 2004. “Hyperglycemia-Induced Defects in Angiogenesis in the Chicken Chorioallantoic Membrane Model.” *Diabetes* 53(3):752–61.

Largo, Ra, Vm Ramakrishnan, and Martin Ehrbar. 2010. “Angiogenesis and Vascularity for Tissue Engineering Applications.” *Cdn.Intechweb.Org*.

Lawrence, Thomas M., Christopher T. White, Russell Wenn, and Christopher G. Moran. 2005. “The Current Hospital Costs of Treating Hip Fractures.” *Injury* 36(1):88–91.

Leaman, John, Jerry Latter, and Michael Clemence. 2014. “Attitudes to Animal Research in 2014.” (September):1–54.

Lee, Min Kyung, Max H. Rich, Jonghwi Lee, and Hyunjoon Kong. 2015. “A Bio-Inspired, Microchanneled Hydrogel with Controlled Spacing of Cell Adhesion Ligands Regulates 3D Spatial Organization of Cells Andtissue.” *Biomaterials* 58:26–34.

Leng, Theodore et al. 2004. “The Chick Chorioallantoic Membrane as a Model Tissue for Surgical Retinal Research and Simulation.” *Retina (Philadelphia, Pa.)* 24(3):427–34.

van Lenthe, G. Harry et al. 2007. “Nondestructive Micro-Computed Tomography for Biological Imaging and Quantification of Scaffold-Bone Interaction in Vivo.” *Biomaterials* 28(15):2479–90.

Lenze, Ulrich et al. 2014. “Influence of Osteogenic Stimulation and VEGF Treatment on in Vivo Bone Formation in hMSC-Seeded Cancellous Bone Scaffolds.” *BMC musculoskeletal disorders* 15(1):350.

Lienemann, Philipp S. et al. 2015. “Longitudinal in Vivo Evaluation of Bone Regeneration by Combined Measurement of Multi-Pinhole SPECT and Micro-CT for Tissue Engineering.” *Scientific reports* 5(April):10238.

Ling, Thai Yen et al. 2014. “Differentiation of Lung Stem/progenitor Cells into Alveolar Pneumocytes and Induction of Angiogenesis within a 3D Gelatin - Microbubble Scaffold.” *Biomaterials* 35(22):5660–69.

Liu, Xi et al. 2012. “In Vivo Studies on Angiogenic Activity of Two Designer Self-Assembling Peptide Scaffold Hydrogels in the Chicken Embryo Chorioallantoic Membrane.” *Nanoscale* 4(8):2720–27.

Liu, Yuchun et al. 2013. “Contrasting Effects of Vasculogenic Induction Upon Biaxial Bioreactor Stimulation of Mesenchymal Stem Cells and Endothelial Progenitor Cells Cocultures in 3D Scaffolds Under In Vitro and In Vivo Paradigms for Vascularized Bone Tissue Engineering.” *Tissue Engineering Part A* 19(7-8):121026093833004.

Lokman, Noor a., Alison S. F. Elder, Carmela Ricciardelli, and Martin K. Oehler. 2012. “Chick Chorioallantoic Membrane (CAM) Assay as an in Vivo Model to Study the Effect of Newly Identified Molecules on Ovarian Cancer Invasion and Metastasis.” *International Journal of Molecular Sciences* 13(8):9959–70.

Long, Fanxin. 2011. “Building Strong Bones: Molecular Regulation of the Osteoblast Lineage.” *Nature Reviews Molecular Cell Biology* 13(1):27–38.

Luca, Ludmila et al. 2011. “Injectable rhBMP-2-Loaded Chitosan Hydrogel Composite: Osteoinduction at Ectopic Site and in Segmental Long Bone Defect.” *Journal of Biomedical Materials Research - Part A* 96 A(1):66–74.

Luepke, N. P. 1985. “Hen’s Egg Chorioallantoic Membrane Test for Irritation Potential.” *Food and Chemical Toxicology* 23(2):287–91.

Lutolf, M. P. et al. 2003. “Repair of Bone Defects Using Synthetic Mimetics of Collagenous Extracellular Matrices.” *Nat Biotechnol* 21(5):513–18.

Macey, L. R. et al. 1989. “Defects of Early Fracture-Healing in Experimental Diabetes.” *The Journal of bone and joint surgery. American volume* 71(5):722–33.

Maeda, Y., and M. Noda. 2003. “Coordinated Development of Embryonic Long Bone on Chorioallantoic Membrane in Ovo Prevents Perichondrium-Derived Suppressive Signals against Cartilage Growth.” *Bone* 32(1):27–34.

Makanya, Andrew Ndegwa, Ivanka Dimova, and Tobias Koller. 2016. “Dynamics of the Developing Chick Chorioallantoic Membrane Assessed by Immunohistochemistry and Molecular Analysis.” *PloS one* 5:1–23.

Marieb, Elaine N., and Katja Hoehn. 2013. *Human Anatomy & Physiology*. 7th ed. edited by publishing as Benjamin Cummings Copyright © 2006 Pearson Education, Inc. Boston, Pearson.

Marsell, Richard et al. 2014. “Skeletal Trauma Generates Systemic BMP2 Activation That Is Temporally Related to the Mobilization of CD73+ Cells.” *Journal of Orthopaedic Research* 32(1):17–23.

Marsell, Richard, and Thomas a. Einhorn. 2011. “The Biology of Fracture Healing.” *Injury* 42(6):551–55.

Martinez-Madrid, Belen et al. 2009. “Chick Embryo Chorioallantoic Membrane (CAM) Model: A Useful Tool to Study Short-Term Transplantation of Cryopreserved Human Ovarian Tissue.” *Fertility and sterility* 91(1):285–92.

McGonigle, Paul, and Bruce Ruggeri. 2014. “Animal Models of Human Disease: Challenges in Enabling Translation.” *Biochemical Pharmacology* 87(1):162–71.

McGrew, Michael J., Adrian Sherman, Simon G. Lillico, Lorna Taylor, and Helen Sang. 2010. “Functional Conservation between Rodents and Chicken of Regulatory Sequences Driving Skeletal Muscle Gene Expression in Transgenic Chickens.” *BMC developmental biology* 10:26.

McKay, William F., Steven M. Peckham, and Jeffrey M. Badura. 2007. “A Comprehensive Clinical Review of Recombinant Human Bone Morphogenetic Protein-2 (INFUSE?? Bone Graft).” *International Orthopaedics* 31(6):729–34.

Mehta, M. et al. 2010. “Influences of Age and Mechanical Stability on Volume, Microstructure, and Mineralization of the Fracture Callus during Bone Healing: Is Osteoclast Activity the Key to Age-Related Impaired Healing?” *Bone* 47(2):219–28.

Meneghin, Alessia, and Cm Hogaboam. 2007. “Infectious Disease, the Innate Immune Response, and Fibrosis.” *Journal of Clinical Investigation* 117(3).

Mihaila, Silvia M. et al. 2014. “The Osteogenic Differentiation of SSEA-4 Sub-Population of Human Adipose Derived Stem Cells Using Silicate Nanoplatelets.” *Biomaterials* 35(33):9087–99.

Miki, Toshio, Thomas Lehmann, Hongbo Cai, Donna B. Stolz, and Stephen C. Strom. 2005. “Stem Cell Characteristics of Amniotic Epithelial Cells.” *Stem cells (Dayton, Ohio)* 23(10):1549–59.

Mirmalek-Sani, Sayed-Hadi et al. 2006. “Characterization and Multipotentiality of Human Fetal Femur-Derived Cells: Implications for Skeletal Tissue Regeneration.” *Stem cells (Dayton, Ohio)* 24(4):1042–53.

Mitchel, R. 2007. “Low Doses of Radiation Reduce Risk in Vivo.” *Dose-Response* 5(1):1–10.

Murphy, J. B. 1913. “TRANSPLANTABILITY OF TISSUES TO THE EMBRYO OF FOREIGN SPECIES: ITS BEARING ON QUESTIONS OF TISSUE SPECIFICITY AND TUMOR IMMUNITY.” *Journal of Experimental Medicine* 17(4):482–93.

Murphy, J. B. 1914a. “FACTORS OF RESISTANCE TO HETEROPLASTIC TISSUE-GRAFTING: STUDIES IN TISSUE SPECIFICITY. III.” *Journal of Experimental Medicine* 19(5):513–22.

Murphy, J. B. 1914b. “STUDIES IN TISSUE SPECIFICITY: II. THE ULTIMATE FATE OF MAMMALIAN TISSUE IMPLANTED IN THE CHICK EMBRYO.” *Journal of Experimental Medicine* 19(2):181–86.

Muschler, George F., Vivek P. Raut, Thomas E. Patterson, Joseph C. Wenke, and Jeffrey O. Hollinger. 2010. “The Design and Use of Animal Models for Translational Research in Bone Tissue Engineering and Regenerative Medicine.” *Tissue Engineering: part B* 16(1):123–45.

Neve, Anna et al. 2013. “In Vitro and in Vivo Angiogenic Activity of Osteoarthritic and Osteoporotic Osteoblasts Is Modulated by VEGF and Vitamin D3 Treatment.” *Regulatory Peptides* 184:81–84.

Norfleet, Andrea M., John S. Bergmann, and Darrell H. Carney. 2000. “Thrombin Peptide, TP508, Stimulates Angiogenic Responses in Animal Models of Dermal Wound Healing, in Chick Chorioallantoic Membranes, and in Cultured Human Aortic and Microvascular Endothelial Cells.” *General Pharmacology: Vascular System* 35(5):249–54.

Nowak-Sliwinska, Patrycja, Tatiana Segura, and M. Luisa Iruela-Arispe. 2014. “The Chicken Chorioallantoic Membrane Model in Biology, Medicine and Bioengineering.” *Angiogenesis* 17(4):779–804.

O’Loughlin, Padhraig F. 2008. “Selection and Development of Preclinical Models in Fracture-Healing Research.” *The Journal of Bone and Joint Surgery (American)* 90(Supplement_1):79.

Odom, Duncan T. et al. 2007. “Tissue-Specific Transcriptional Regulation Has Diverged Significantly between Human and Mouse.” *Nature genetics* 39(6):730–32.

Okamoto, Mina, Junko Murai, Hideki Yoshikawa, and Noriyuki Tsumaki. 2006. “Bone Morphogenetic Proteins in Bone Stimulate Osteoclasts and Osteoblasts during Bone Development.” *Journal of bone and mineral research : the official journal of the American Society for Bone and Mineral Research* 21(7):1022–33.

Olson, H. et al. 2000. “Concordance of the Toxicity of Pharmaceuticals in Humans and in Animals.” *Regulatory toxicology and pharmacology : RTP* 32(1):56–67.

Oryan, Ahmad, Soodeh Alidadi, Ali Moshiri, and Nicola Maffulli. 2014. “Bone Regenerative Medicine: Classic Options, Novel Strategies, and Future Directions.” *Journal of orthopaedic surgery and research* 9(1):18.

P. Thévenaz, U.E. Ruttimann, M. Unser. 1998. “A Pyramid Approach to Subpixel Registration Based on Intensity.” *IEEE Transactions on Image Processing* 7(1):27–41.

Patel, Zarana S. et al. 2008. “Dual Delivery of an Angiogenic and an Osteogenic Growth Factor for Bone Regeneration in a Critical Size Defect Model.” *Bone* 43(5):931–40.

Pedersen, T. O. et al. 2012. “Osteogenic Stimulatory Conditions Enhance Growth and Maturation of Endothelial Cell Microvascular Networks in Culture with Mesenchymal Stem Cells.” *J Tissue Eng* 3(1):2041731412443236.

Peng, Hairong et al. 2002. “Synergistic Enhancement of Bone Formation and Healing by Stem Cell-Expressed VEGF and Bone Morphogenetic Protein-4.” *Journal of Clinical Investigation* 110(6):751–59.

Peng, Hairong et al. 2005. “VEGF Improves, Whereas sFlt1 Inhibits, BMP2-Induced Bone Formation and Bone Healing through Modulation of Angiogenesis.” *Journal of bone and mineral research : the official journal of the American Society for Bone and Mineral Research* 20(11):2017–27.

Polytarchou, C., T. Gligoris, D. Kardamakis, and E. Papadimitriou. 2004. “X-Rays Affect the Expression of Genes Involved in Angiogenesis.” *Anticancer Research* 24:2941–45.

Pountos, Ippokratis, Michalis Panteli, Elias Panagiotopoulos, Elena Jones, and Peter V. Giannoudis. 2014. “Can We Enhance Fracture Vascularity: What Is the Evidence?” *Injury* 45(SUPPL. 2):S49–57.

Poynton, Ashley R., and Joseph M. Lane. 2002. “Safety Profile for the Clinical Use of Bone Morphogenetic Proteins in the Spine.” *Spine* 27(16 Suppl 1):S40–48.

Proff, Peter, and Piero Römer. 2009. “The Molecular Mechanism behind Bone Remodelling: A Review.” *Clinical Oral Investigations* 13(4):355–62.

Ralis, Z. A., and G. Watkins. 1992. “Modified Tetrachrome Method for Osteoid and Defectively Mineralized Bone in Paraffin Sections.” *Biotechnic & Histochemistry* 67(6):339–45.

Ramazanoglu, Mustafa et al. 2013. “Bone Response to Biomimetic Implants Delivering BMP-2 and VEGF: An Immunohistochemical Study.” *Journal of Cranio-Maxillofacial Surgery* 41(8):826–35.

Ramoshebi, L. N., and U. Ripamonti. 2000. “Osteogenic Protein-1, a Bone Morphogenetic Protein, Induces Angiogenesis in the Chick Chorioallantoic Membrane and Synergizes with Basic Fibroblast Growth Factor and Transforming Growth Factor-beta1.” *The Anatomical record* 259(1):97–107.

Ramos-Vara, J. a., and M. a. Miller. 2014. “When Tissue Antigens and Antibodies Get Along: Revisiting the Technical Aspects of Immunohistochemistry--The Red, Brown, and Blue Technique.” *Veterinary Pathology* 51(1):42–87.

Rao, Rameshwar R. et al. 2014. “Effects of Hydroxyapatite on Endothelial Network Formation in Collagen/fibrin Composite Hydrogels in Vitro and in Vivo.” *Acta Biomaterialia* 10(7):3091–97.

Rao, Rameshwar R., and Jan P. Stegemann. 2013. “Cell-Based Approaches to the Engineering of Vascularized Bone Tissue.” *Cytotherapy* 15(11):1309–22.

Reichert, Johannes C. et al. 2009. “The Challenge of Establishing Preclinical Models for Segmental Bone Defect Research.” *Biomaterials* 30(12):2149–63.

Resnick, Daniel, and Kevin J. Bozic. 2013. “Meta-Analysis of Trials of Recombinant Human Bone Morphogenetic Protein-2: What Should Spine Surgeons and Their Patients Do with This Information?” *Annals of Internal Medicine* 158(12):912–13.

Ribatti, Domenico et al. 2001. “Cell-Mediated Delivery of Fibroblast Growth Factor-2 and Vascular Endothelial Growth Factor onto the Chick Chorioallantoic Membrane: Endothelial Fenestration and Angiogenesis.” *Journal of Vascular Research* 38(4):389–97.

Ribatti, Domenico et al. 2003. “Angiogenic Response Induced by Acellular Brain Scaffolds Grafted onto the Chick Embryo Chorioallantoic Membrane.” *Brain Research* 989(1):9–15.

Ribatti, Domenico. 2010. “The Chick Embryo Chorioallantoic Membrane as an in Vivo Assay to Study Antiangiogenesis.” *Pharmaceuticals* 3(3):482–513.

Ribatti, Domenico, Beatrice Nico, Angelo Vacca, and Marco Presta. 2006. “The Gelatin Sponge-Chorioallantoic Membrane Assay.” *Nature protocols* 1(1):85–91.

Ribeiro, Frederico O., María José Gómez-Benito, João Folgado, Paulo R. Fernandes, and José Manuel García-Aznar. 2015. “In Silico Mechano-Chemical Model of Bone Healing for the Regeneration of Critical Defects: The Effect of BMP-2.” *PloS one* 10(6):e0127722.

Richardson, Mary, David Wong, Samantha Lacroix, Jolanta Stanisz, and Gurmit Singh. 2005. “Inhibition by Doxycycline of Angiogenesis in the Chicken Chorioallantoic Membrane (CAM).” *Cancer Chemotherapy and Pharmacology* 56(1):1–9.

Roach, H. I., J. E. Baker, and N. M. Clarke. 1998. “Initiation of the Bony Epiphysis in Long Bones: Chronology of Interactions between the Vascular System and the Chondrocytes.” *Journal of bone and mineral research : the official journal of the American Society for Bone and Mineral Research* 13(6):950–61.

Robinson, R. 2011. “Three Rs of Animal Testing for Regenerative Medicine Products.” *Science Translational Medicine* 3(112):1–4.

Rosen, Vicki. 2009. “BMP2 Signaling in Bone Development and Repair.” *Cytokine and Growth Factor Reviews* 20(5-6):475–80.

Rountree, Ryan B. et al. 2004. “BMP Receptor Signaling Is Required for Postnatal Maintenance of Articular Cartilage.”

PLoS Biology 2(11).

Rous, P., and J. Murphy. 1911. “Tumor Implantation in the Developing Embryo.” P. 740 in *Journal of the American Medical Association*, vol. LVI. American Philosophical Society.

Russel, W. M. S and Burch, R. .. 1959. *The Principles of Humane Experimental Technique*. 18th ed. London, Methuen: Harvard.

Saleh, F. a, M. Whyte, and P. G. Genever. 2011. “Effects of Endothelial Cells on Human Mesenchymal Stem Cell Activity in a Three-Dimensional in Vitro Model.” *European cells & materials* 22(Area 9):242–57; discussion 257.

Salgado, Ant??nio J., Olga P. Coutinho, and Rui L. Reis. 2004. “Bone Tissue Engineering: State of the Art and Future Trends.” *Macromolecular Bioscience* 4(8):743–65.

Saul, Justin M., and David F. Williams. 2013. “Hydrogels in Regenerative Medicine.” *Handbook of Polymer Applications in Medicine and Medical Devices* 21(32-33):279–302.

Saunders, Marnie M., Linda a. Simmerman, Gretchen L. Reed, Neil a. Sharkey, and Amanda F. Taylor. 2010. “Biomimetic Bone Mechanotransduction Modeling in Neonatal Rat Femur Organ Cultures: Structural Verification of Proof of Concept.” *Biomechanics and Modeling in Mechanobiology* 9(5):539–50.

Schmidt-Bleek, Katharina, Brian J. Kwee, David J. Mooney, and Georg N. Duda. 2015. “Boon and Bane of Inflammation in Bone Tissue Regeneration and Its Link with Angiogenesis.” *Tissue engineering. Part B, Reviews* 21(4):354–64.

Schönmeyr, Björn H. et al. 2010. “Vascular Endothelial Growth Factor Inhibits Bone Morphogenetic Protein 2 Expression in Rat Mesenchymal Stem Cells.” *Tissue engineering. Part A* 16(2):653–62.

Schulte, Friederike A., Floor M. Lambers, Gisela. Kuhn, and Ralph. Müller. 2011. “In Vivo Micro-Computed Tomography Allows Direct Three-Dimensional Quantification of Both Bone Formation and Bone Resorption Parameters Using Time-Lapsed Imaging.” *Bone* 48(3):433–42.

Scott, Michelle A. et al. 2012. “Brief Review of Models of Ectopic Bone Formation.” *Stem cells and development* 21(5):655–67.

Seeherman, Howard J. 2010. “rhBMP2 Induces Transient Bone Resorption Followed by Bone Formation in a Nonhuman Primate Core-Defect Model.” *The Journal of Bone and Joint Surgery (American)* 92(2):411.

Seo, Bo Bae, Hyuck Choi, Jeong Tae Koh, and Soo Chang Song. 2015. “Sustained BMP-2 Delivery and Injectable Bone Regeneration Using Thermosensitive Polymeric Nanoparticle Hydrogel Bearing Dual Interactions with BMP-2.” *Journal of Controlled Release* 209:67–76.

Shah, Nisarg J. et al. 2014. “Adaptive Growth Factor Delivery from a Polyelectrolyte Coating Promotes Synergistic Bone Tissue Repair and Reconstruction.” *Proceedings of the National Academy of Sciences of the United States of America* 111(6):1–6.

Sharifi, Shahriar, Sebastien B. G. Blanquer, Theo G. Van Kooten, and Dirk W. Grijpma. 2012. “Biodegradable Nanocomposite Hydrogel Structures with Enhanced Mechanical Properties Prepared by Photo-Crosslinking Solutions of Poly(trimethylene Carbonate)-Poly(ethylene Glycol)-Poly(trimethylene Carbonate) Macromonomers and Nanoclay Particles.” *Acta Biomaterialia* 8(12):4233–43.

Shivani., Singh. 2013. “Delivery of VEGF Using Collagen-Coated Polycaprolactone Scaffolds Stimulate Angiogenesis.” *Journal of biomedical materials research A* 100(3):720–27.

Shore, Eileen M. et al. 2006. “A Recurrent Mutation in the BMP Type I Receptor ACVR1 Causes Inherited and Sporadic Fibrodysplasia Ossificans Progressiva.” *Nature genetics* 38(5):525–27.

Shrivats, Arun R., Michael C. McDermott, and Jeffrey O. Hollinger. 2014. “Bone Tissue Engineering: State of the Union.” *Drug Discovery Today* 19(6):781–86.

Simmonds, Mark C. et al. 2013. “Safety and Effectiveness of Recombinant Human Bone Morphogenetic Protein-2 for Spinal Fusion.” *Annals of Internal Medicine* 158(12):877.

Simon G. Lillico, Michael J. McGrew, Adrian Sherman and Helen M. Sang. 2005. “Transgenic Chickens as Bioreactors for Protein Based Drugs.” *Drug discovery today* 3(10):1–9.

Sims, Natalie a, and T. John Martin. 2014. “Coupling the Activities of Bone Formation and Resorption: A Multitude of Signals within the Basic Multicellular Unit.” *BoneKEy reports* 3(August 2013):481.

Smith, E. L. et al. 2014a. “Evaluation of Skeletal Tissue Repair, Part 1: Assessment of Novel Growth-Factor-Releasing Hydrogels in an Ex Vivo Chick Femur Defect Model.” *Acta Biomaterialia* 10(10):4186–96.

Smith, E. L. et al. 2014b. “Evaluation of Skeletal Tissue Repair, Part 2: Enhancement of Skeletal Tissue Repair through Dual-Growth-Factor-Releasing Hydrogels within an Ex Vivo Chick Femur Defect Model.” *Acta Biomaterialia* 10(10):4197–4205.

Smith, Emma L., Janos M. Kanczler, and Richard O. C. Oreffo. 2013. “A New Take on an Old Story: Chick Limb Organ Culture for Skeletal Niche Development and Regenerative Medicine Evaluation.” *European Cells and Materials* 26:91–106.

Smith, J. D., M. E. Melhem, K. T. Magge, a. S. Waggoner, and P. G. Campbell. 2007. “Improved Growth Factor Directed Vascularization into Fibrin Constructs through Inclusion of Additional Extracellular Molecules.” *Microvascular Research* 73(2):84–94.

Smitsmans, Monique H. P. et al. 2005. “Automatic Prostate Localization on Cone-Beam CT Scans for High Precision Image-Guided Radiotherapy.” *International Journal of Radiation Oncology*Biology*Physics* 63(4):975–84.

Sommerfeldt, D., and C. Rubin. 2001. “Biology of Bone and How It Orchestrates the Form and Function of the Skeleton.” *European Spine Journal* 10(SUPPL. 2):S86–95.

Song, F. et al. 2010. “Dissemination and Publication of Research Findings: An Updated Review of Related Biases.” *Health Technology Assessment* 14(8):1–220.

Van Staa, T. P., E. M. Dennison, H. G. M. Leufkens, and C. Cooper. 2001. “Epidemiology of Fractures in England and Wales.” *Bone* 29(6):517–22.

Stallmach, Thomas et al. 2001. “Feto-Maternal Interface of Human Placenta Inhibits Angiogenesis in the Chick Chorioallantoic Membrane (CAM) Assay.” *Angiogenesis* 4(1):79–84.

Steffens, Lilian, Andreas Wenger, G. Björn Stark, and Günter Finkenzeller. 2009. “In Vivo Engineering of a Human Vasculature for Bone Tissue Engineering Applications.” *Journal of Cellular and Molecular Medicine* 13(9 B):3380–86.

Steiner, Dominik, Florian Lampert, G. Björn Stark, and Günter Finkenzeller. 2012. “Effects of Endothelial Cells on Proliferation and Survival of Human Mesenchymal Stem Cells and Primary Osteoblasts.” *Journal of Orthopaedic Research* 30(10):1682–89.

Stevens, Molly M. et al. 2005. “In Vivo Engineering of Organs: The Bone Bioreactor.” *Proceedings of the National Academy of Sciences of the United States of America* 102(32):11450–55.

Stoddart, M. J., P. I. Furlong, a. Simpson, C. M. Davies, and R. G. Richards. 2006. “A Comparison of Non-Radioactive Methods for Assessing Viability in Ex Vivo Cultured Cancellous Bone: Technical Note.” *European Cells and Materials* 12(0):16–25.

Street, J. et al. 2000. “Is Human Fracture Hematoma Inherently Angiogenic?” *Clinical orthopaedics and related research* (378):224–37.

Street, John et al. 2002. “Vascular Endothelial Growth Factor Stimulates Bone Repair by Promoting Angiogenesis and Bone Turnover.” *Proceedings of the National Academy of Sciences of the United States of America* 99(15):9656–61.

Sukul, Mousumi, Thuy Ba Linh Nguyen, Young-Ki Min, Sun-Young Lee, and Byong-Taek Lee. 2015. “Effect of Local Sustainable Release of BMP2-VEGF from Nano-Cellulose Loaded in Sponge Biphasic Calcium Phosphate on Bone Regeneration.” *Tissue engineering. Part A* 21(11-12):1822–36.

Sulzbacher, Irene. 2013. “Osteoarthritis: Histology and Pathogenesis.” *Wiener Medizinische Wochenschrift* 163(9-10):212–19.

Suzuki, Yoshihisa et al. 2000. “Alginate Hydrogel Linked with Synthetic Oligopeptide Derived from BMP-2 Allows Ectopic Osteoinduction in Vivo.” *Journal of Biomedical Materials Research* 50(3):405–9.

Synthesis, Morphogenetic Protein-Evidence, and Data Sharing. 2013. “Closing in on the Truth About Recombinant Human Bone.” *Annals of Internal Medicine* 158:916–18.

Sys, Gwen et al. 2012. “Tumor Grafts Derived from Sarcoma Patients Retain Tumor Morphology, Viability, and Invasion Potential and Indicate Disease Outcomes in the Chick Chorioallantoic Membrane Model.” *Cancer Letters*

326(1):69–78.

Takahashi, K., M. D. Shanahan, L. a Coulton, and T. Duckworth. 1991. “Fracture Healing of Chick Femurs in Tissue Culture.” *Acta orthopaedica Scandinavica* 62(4):352–55.

Tan, Huaping, and Kacey G. Marra. 2010. “Injectable, Biodegradable Hydrogels for Tissue Engineering Applications.” *Materials* 3(3):1746–67.

Thompson, Dudley W., and James T. Butterworth. 1992. “The Nature of Laponite and Its Aqueous Dispersions.” *Journal of Colloid And Interface Science* 151(1):236–43.

Thompson, T. J., P. D. Owens, and D. J. Wilson. 1989. “Intramembranous Osteogenesis and Angiogenesis in the Chick Embryo.” *Journal of anatomy* 166:55–65.

Tomco, Marek et al. 2016. “In Vitro and in Vivo Study of Microporous Ceramics Using MC3T3 Cells, CAM Assay and a Pig Animal Model.” *Anatomical Science International*.

Tsuji, Kunikazu et al. 2006. “BMP2 Activity, Although Dispensable for Bone Formation, Is Required for the Initiation of Fracture Healing.” *Nature genetics* 38(12):1424–29.

Tuan, Rocky S. 1980. “Calcium Transport and Related Functions in the Chorioallantoic Membrane of Cultured Shell-Less Chick Embryos.” *Developmental Biology* 74(1):196–204.

Tuan, Rocky S., and Marion H. Lynch. 1983. “Effect of Experimentally Induced Calcium Deficiency on the Developmental Expression of Collagen Types in Chick Embryonic Skeleton.” *Developmental Biology* 100(2):374–86.

Tuli, Richard et al. 2003. “Characterization of Multipotential Mesenchymal Progenitor Cells Derived from Human Trabecular Bone.” *Stem cells* 21(6):681–93.

Udagawa, N. et al. 1990. “Origin of Osteoclasts: Mature Monocytes and Macrophages Are Capable of Differentiating into Osteoclasts under a Suitable Microenvironment Prepared by Bone Marrow-Derived Stromal Cells.” *Proceedings of the National Academy of Sciences of the United States of America* 87(18):7260–64.

Ulrich, Christine et al. 2013. “Low Osteogenic Differentiation Potential of Placenta-Derived Mesenchymal Stromal Cells Correlates with Low Expression of the Transcription Factors Runx2 and Twist2.” *Stem cells and development* 22(21):1–38.

Urist, MR R., and John Daly. 1965. “Bone Formation by Autoinduction.” *Science* 150(698):893–99.

Usami, Kazutada et al. 2009. “Composite Implantation of Mesenchymal Stem Cells with Endothelial Progenitor Cells Enhances Tissue-Engineered Bone Formation.” *Journal of biomedical materials research. Part A* 90(3):730–41.

Vacca, a et al. 1999. “Bone Marrow Neovascularization, Plasma Cell Angiogenic Potential, and Matrix Metalloproteinase-2 Secretion Parallel Progression of Human Multiple Myeloma.” *Blood* 93(9):3064–73.

Valdes, T. I., D. Kreutzer, and F. Moussy. 2002. “The Chick Chorioallantoic Membrane as a Novel in Vivo Model for the Testing of Biomaterials.” *Journal of Biomedical Materials Research* 62(2):273–82.

Vargas, Angelica, Magali Zeisser-Labouebe, Norbert Lange, Robert Gurny, and Florence Delie. 2007. “The Chick Embryo and Its Chorioallantoic Membrane (CAM) for the in Vivo Evaluation of Drug Delivery Systems.” *Advanced Drug Delivery Reviews* 59(11):1162–76.

Vargas, Gabriela E. et al. 2009. “Biocompatibility and Bone Mineralization Potential of 45S5 Bioglass®-Derived Glass-Ceramic Scaffolds in Chick Embryos.” *Acta Biomaterialia* 5(1):374–80.

Vargas, Gabriela E. et al. 2013. “Effect of Nano-Sized Bioactive Glass Particles on the Angiogenic Properties of Collagen Based Composites.” *Journal of Materials Science: Materials in Medicine* 24(5):1261–69.

Villars, F. et al. 2002. “Effect of HUVEC on Human Osteoprogenitor Cell Differentiation Needs Heterotypic Gap Junction Communication.” *American journal of physiology. Cell physiology* 282(4):C775–85.

Vivanco, Juan et al. 2013. “Apparent Elastic Modulus of Ex Vivo Trabecular Bovine Bone Increases with Dynamic Loading.” *Proceedings of the Institution of Mechanical Engineers. Part H, Journal of engineering in medicine* 227(8):904–12.

Waarsing, J. H. et al. 2004. “Detecting and Tracking Local Changes in the Tibiae of Individual Rats: A Novel Method to Analyse Longitudinal in Vivo Micro-CT Data.” *Bone* 34(1):163–69.

Waarsing, Jan H., Judd S. Day, and Harrie Weinans. 2004. “An Improved Segmentation Method for In Vivo μCT Imaging.” *Journal of Bone and Mineral Research* 19(10):1640–50.

Wall, R. J., and M. Shani. 2008. “Are Animal Models as Good as We Think?” *Theriogenology* 69(1):2–9.

Wang, Chuanshun et al. 2014. “Preparation of Laponite Bioceramics for Potential Bone Tissue Engineering Applications.” *PLoS ONE* 9(6):e99585.

Wang, E. a et al. 1990. “Recombinant Human Bone Morphogenetic Protein Induces Bone Formation.” *Proceedings of the National Academy of Sciences of the United States of America* 87(6):2220–24.

Wang, Ji et al. 2015. “Trabecular Plates and Rods Determine Elastic Modulus and Yield Strength of Human Trabecular Bone.” *Bone* 72:71–80.

Wang, Shige, Rita Castro, et al. 2012. “Electrospun Laponite-Doped Poly(lactic-Co-Glycolic Acid) Nanofibers for Osteogenic Differentiation of Human Mesenchymal Stem Cells.” *Journal of Materials Chemistry* 22(44):23357.

Wang, Shige, Fuyin Zheng, et al. 2012. “Encapsulation of Amoxicillin within Laponite-Doped Poly(lactic-Coglycolic Acid Nanofibers Preparation, Characterization 2012.pdf.” *Applied maerials and interfaces* 4(63):6393–6401.

Wozney, J. M. et al. 1988. “Novel Regulators of Bone Formation: Molecular Clones and Activities.” *Science* 242:1528–34.

Yang, R. et al. 2003. “Immunohistochemistry of Matrix Markers in Technovit 9100 New??-Embedded Undecalcified Bone Sections.” *European Cells and Materials* 6:57–71.

Yang, Xuebin B. et al. 2004. “Human Osteoprogenitor Bone Formation Using Encapsulated Bone Morphogenetic Protein 2 in Porous Polymer Scaffolds.” *Tissue engineering* 10(7):1037–47.

Yu, Yan Yiu, Shirley Lieu, Chuanyong Lu, and C??line Colnot. 2010. “Bone Morphogenetic Protein 2 Stimulates Endochondral Ossification by Regulating Periosteal Cell Fate during Bone Repair.” *Bone* 47(1):65–73.

Yuasa, Masato et al. 2014. “The Temporal and Spatial Development of Vascularity in a Healing Displaced Fracture.” *Bone* 67:208–21.

Zelzer, Elazar et al. 2002. “Skeletal Defects in VEGF(120/120) Mice Reveal Multiple Roles for VEGF in Skeletogenesis.” *Development (Cambridge, England)* 129(8):1893–1904.

Zhang, Licheng et al. 2014. “Improvement in Angiogenesis and Osteogenesis with Modified Cannulated Screws Combined with VEGF/PLGA/fibrin Glue in Femoral Neck Fractures.” *Journal of Materials Science: Materials in Medicine* 25(4):1165–72.

Zhang, Zhi Yong et al. 2010. “Neo-Vascularization and Bone Formation Mediated by Fetal Mesenchymal Stem Cell Tissue-Engineered Bone Grafts in Critical-Size Femoral Defects.” *Biomaterials* 31(4):608–20.

Zuo, Zhi et al. 2015. “High-Resolution MRI Analysis of Breast Cancer Xenograft on the Chick Chorioallantoic Membrane.” *NMR in biomedicine* 28(4):440–47.

List of publications

Part of the results from Chapter 4 Results Part II were recently published: Moreno-Jimenez, I. *et al.* The chorioallantoic membrane (CAM) assay for the study of human bone regeneration: a refinement animal model in tissue engineering. Sci. Rep. 6, 32168; doi: 10.1038/ srep32168 (2016). See full text in the next page.

Lists of abstracts selected for podium oral presentation

- Micro computed tomography user meeting – May 2015, Bruges. Abstract published in Abstract book 2015 Micro-CT User Meeting. "Examination of human bone regeneration using a replacement model for animal research"
- Faculty of Medicine Conference, University of Southampton, UK – June 2015. "Examination of human bone tissue regeneration using the chorioallantoic membrane (CAM): an ex vivo replacement model for animal research"
- Tissue and Cell Engineering Society (TCES) – Southampton, UK July 2015. European Cells and Materials Vol. 29. Suppl. 3, 2015 (page 20), ISSN 1473-2262. "Examination of human bone tissue regeneration using the chorioallantoic membrane (CAM): an ex vivo replacement model for animal research"
- European Congresses on Alternatives to Animal Testing (EUSAAT) – Linz, Austria Sept 2015. "Examination of human bone tissue regeneration using the chorioallantoic membrane (CAM): an ex vivo replacement model for animal research"
- South West Regional Regenerative Medicine Meeting – Bristol, UK Sept 2015. "Examination of human bone tissue regeneration using the chorioallantoic membrane (CAM): an ex vivo replacement model for animal research"

Lists of abstracts selected for poster presentation

- Tissue Engineering and Regenerative Medicine Society (TERMIS) – Boston, EEUU Sept 2015. TISSUE ENGINEERING: Part A, Volume 21, Supplement 1, 2015, DOI: 10.1089/ten.tea.2015.5000.abstracts "The Use Of A Novel Clay Hydrogel For VEGF Delivery In An Ex Vivo Human Bone Injury Model"

www.nature.com/scientificreports

SCIENTIFIC REPORTS

OPEN

The chorioallantoic membrane (CAM) assay for the study of human bone regeneration: a refinement animal model for tissue engineering

Received: 21 April 2016
Accepted: 02 August 2016
Published: 31 August 2016

Inés Moreno-Jiménez[1], Gry Hulsart-Billstrom[1], Stuart A. Lanham[1], Agnieszka A. Janeczek[1], Nasia Kontouli[2], Janos M. Kanczler[1], Nicholas D. Evans[1] & Richard OC Oreffo[1]

Biomaterial development for tissue engineering applications is rapidly increasing but necessitates efficacy and safety testing prior to clinical application. Current *in vitro* and *in vivo* models hold a number of limitations, including expense, lack of correlation between animal models and human outcomes and the need to perform invasive procedures on animals; hence requiring new predictive screening methods. In the present study we tested the hypothesis that the chick embryo chorioallantoic membrane (CAM) can be used as a bioreactor to culture and study the regeneration of human living bone. We extracted bone cylinders from human femoral heads, simulated an injury using a drill-hole defect, and implanted the bone on CAM or *in vitro* control-culture. Micro-computed tomography (μCT) was used to quantify the magnitude and location of bone volume changes followed by histological analyses to assess bone repair. CAM blood vessels were observed to infiltrate the human bone cylinder and maintain human cell viability. Histological evaluation revealed extensive extracellular matrix deposition in proximity to endochondral condensations (Sox9+) on the CAM-implanted bone cylinders, correlating with a significant increase in bone volume by μCT analysis ($p < 0.01$). This human-avian system offers a simple refinement model for animal research and a step towards a humanized *in vivo* model for tissue engineering.

Bone fracture is a major socio-economic burden that is set to rise as a consequence of current additional health issues including smoking, diabetes as well as an increasing ageing population[1,2]. Currently, approximately 10% of fractures fail to heal properly resulting in delayed union or non-union[3–5]. Poor vascularisation is frequently a contributing factor in impaired healing[6] and thus a central challenge in bone tissue engineering is the design and development of biomaterials which can promote vascularization and aid bone repair.

To achieve this, a number of strategies have focussed on functionalised biomaterial scaffolds. These may harness growth factors, cells and small peptides, providing an osteogenic environment together with appropriate mechanical support to promote and guide tissue growth[7]. As a consequence the number of biomaterial combinations has increased significantly in the field of bone tissue engineering, evidenced by the increase in publications from 60 to over 600 per year in the last 15 years. However, the efficacy and safety of these biomaterials still requires extensive assessment prior to Food and Drug Administration (FDA) approval for clinical applications.

Biomaterial preclinical testing involves an initial evaluation of the cytotoxicity, function and proliferative effects of the biomaterial on cells, followed by further studies using animal models[8]. *In vitro* systems are often limited as predictors of clinical function as such models cannot fully reproduce the complexity of biological systems (blood supply, immune function, inflammatory and hormonal response), nor the complex interactions of different cell types. Therefore, the application of animal models to determine the efficacy of a material and the generation of safety/toxicity data prior to clinical evaluation is still required. However, discrepancies in experimental design (animal age, physiology, injury location and size, and bone composition) have resulted in the lack

[1]Bone and Joint Research Group, Centre for Human Development, Stem Cells and Regeneration, Human Development and Health, Institute of Developmental Sciences University of Southampton, Tremona Road, Southampton, SO16 6YD, UK. [2]Cancer Sciences Unit, Somers Cancer Research, University of Southampton, Tremona Road, Southampton, SO16 6YD, UK. Correspondence and requests for materials should be addressed to R.O.O. (email: richard.oreffo@soton.ac.uk)

of reproducible standard animal models for bone tissue engineering. Furthermore, the inconsistent response of animals to drugs and devices in comparison to humans remains a concern[9,10]. For instance, bisphosphonates (inhibitors of bone resorption) increase bone mineral density in post-menopausal women, while the effects in animal models were reported to be bone site-dependent[11]. Such limitations, combined with a need to meet the ethical obligations to reduce, refine and replace (3Rs) animal usage in animal research[12], underline the importance of the development of new models that avoid the need for animal experimentation and recapitulate robustly species-specific effects.

One potential approach to refinement animal experimentation is the use of the chorioallantoic membrane (CAM) assay, which involves the implantation of a material or compound on the extraembryonic membrane of the developing chick egg. Critically the CAM is not innervated and thus no pain is experienced by the chick. The chick embryo develops over 21 days and from day 4 the CAM forms, growing exponentially until day 14 ($6\,cm^2$ up to $65\,cm^2$) to serve as a respiratory organ with a rapidly developing vascular system[13]. The CAM assay is commonly used to perform angiogenic (or anti-angiogenic)[14–16] studies as well as multi-species graft transplantation[17–19], given the partial immune-deficiency of the CAM. Studies indicate the production of immune cells (lymphocytes T and B) commences at day 11, however, the immune cells do not become fully mature until the embryo hatches (day 21)[18,20,21].

The CAM assay has been used in tissue engineering for over 40 years as a non-innervated vascular bed[21] and, thereby, as an intermediate step in between *in vitro* and the *in vivo* models. Unlike other *in vivo* models, such as the murine subcutaneous implant, the CAM assay is minimally invasive to the chick embryo and hence is a refinement model for animal research[12]. A number of studies have evaluated material constructs on the CAM not only to examine the angiogenic response but also as an indicator of the material-tissue biocompatibility. A plethora of materials have been examined, including collagen, silk and alginate[22–26], as well as polymer-based constructs such as polycaprolactone (PCL), polylactic acid (PLA) and poly(lactic-co-glycolic acid) (PLGA) with and without factors or cells[27–29]. Despite these studies, there remain few examples that have attempted to measure the tissue repair process *ex vivo* on the CAM. In 2004, Yang *et al.* demonstrated the potential of a BMP-2-loaded PLA scaffold to fill a chick femur segmental defect using the CAM assay[30]. The authors showed new cartilage and matrix deposition, proving the capability of the femur to grow *ex vivo* using the CAM[30]. Similar results, achieved from experiments conducted on human tissue, would validate the CAM assay as a clinically relevant platform to study bone regeneration.

In the present study, we have tested the hypothesis that the CAM model can support the incubation of living human bone and provide a bioreactor for the study and understanding of bone regeneration *in vivo*. We used femoral head bone samples from human subjects undergoing orthopaedic surgery and developed a bone repair model by introduction of a small drill defect in the bone cylinders. The implantation of bone cylinders on the innervated CAM provides a system to mimic the vascular contribution to human bone healing – something not achievable with current *in vitro* models, and hence an alternative model for animal research. Moreover, the CAM offers a step towards the development of a humanised, predictive preclinical model. A pictorial overview of the experimental approach adopted is shown in Fig. 1.

Results

The CAM blood vessels integrate and infiltrate throughout the implanted human bone cylinders.

We first examined whether freshly isolated human bone, implanted on the CAM of the chick egg as described in the methods section, integrated within the tissue of the CAM. Bone cylinders were incubated on the CAM or at the air-liquid interface of growth medium (*in vitro;* Fig. 2A) for 7 days. The chick embryo survival rate was 72.5% ± 20.61 SD at the end of the implantation period ($n = 8–10$, 4 independent experiments, Supplementary Table S1). The gross appearance of bone cylinders was not altered following 7 days culture *in vitro* (Fig. 2B,C) while the CAM-implanted bone cylinders were extensively surrounded by CAM tissue after 7 days implantation (Fig. 2I,J) with evidence of chick blood circulation around the graft site at the time of harvest (Supplementary Video S1).

Human and avian erythrocytes displayed different histological features, which facilitated the distinction of blood vessel origin: avian cells displayed a fusiform shape and nuclei (Supplementary Fig. S1B,D) compared to enucleated and biconcave mammalian red blood cells (Supplementary Fig. S1A,C). As expected, only human blood vessels containing enucleated erythrocytes were present in bone cylinders cultivated *in vitro* (see dashed arrow Fig. 2F). CAM blood vessels were clearly distinguishable macroscopically during harvest (Fig. 2H–J), as well as microscopically during histological evaluation. The CAM capillaries were apparent at the periphery of the bone cylinder, throughout the trabeculae and in close proximity to the central defect region of the human tissue (see arrows Fig. 2K–N). Thus, extensive CAM integration with the bone cylinders was evident by the infiltration of the surrogate blood supply into the human tissue.

Human tissue remains viable following culture on the chick CAM.

To determine whether human cells remained viable following CAM implantation or *in vitro* culture, primary cultures of human cells were derived from bone cylinders incubated for 7 days on the CAM, *in vitro* or maintained at 4 °C (negative control). To achieve this, chick embryos that constitutively expressed green fluorescent protein (GFP) were used in order to distinguish between host (GFP-CAM) and human cell outgrowths. Initial cell outgrowth from explanted bone samples was evident both in the *in vitro* and CAM-implanted group after 9 days and 4 days, respectively; however, no cells were detected from the bone cylinders maintained at 4 °C. No green fluorescence was observed in cells derived from the bone cylinders cultured *in vitro* (Fig. 3A–D).

Both GFP+ and GFP− cells were evident in the CAM-implanted group, indicating differences in the origin of the cells: avian and human (Fig. 3E,F). There were morphological differences in the appearance of GFP+ compared to GFP− cells. The GFP− cells displayed a fibroblastic, spindle-like morphology both in

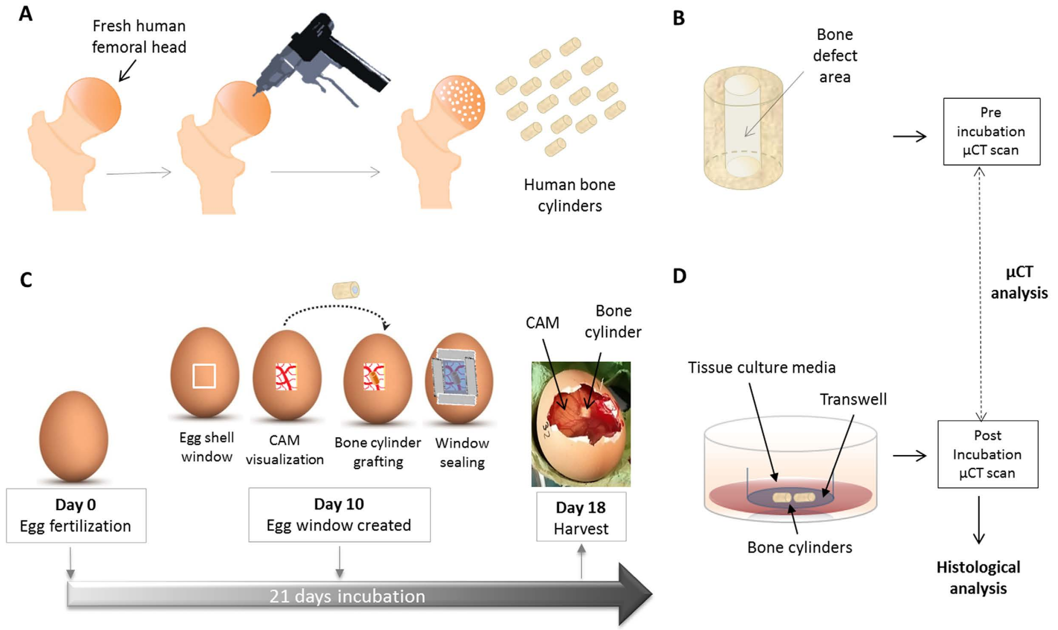

Figure 1. Experimental design. (**A**) Bone cylinder extraction. Human femoral heads were collected following total hip replacement surgery and bone cylinders (6 mm outer diameter, 4–6 mm length) were extracted using a surgical drill. (**B**) Engineered bone cylinders. Standard size bone cylinders were created with an empty core of 2 mm in diameter (bone defect) to facilitate CAM ingrowth and induce bone regeneration. (**C**) CAM-implantation. Fertile eggs were incubated for 10 days before removing a minimal amount of eggshell to access the CAM beneath. Bone cylinders were placed on the CAM and the eggshell was sealed to prevent infection. Incubation was resumed for an additional week before harvesting of the bone grafts. (**D**) *In vitro* incubation: organotypic culture. Bone cylinders were incubated at the air-liquid interface using a transwell membrane over one week. **Analysis**: Bone cylinders were µCT scanned before and after incubation (**C,D**), followed by (immuno) histochemical analysis. Chorioallantoic membrane of the chick embryo (CAM), micro computed tomography (µCT).

CAM-implanted and *in vitro* culture (Fig. 3A,E), as well as in the bone control explanted at day 0 (Fig. 3M,N). In contrast, chick GFP+ cells displayed variable morphology and size (Fig. 3E,F,I,J). The number of GFP+ cells in the CAM-implanted group was observed to decrease towards the end of the incubation period with a majority of GFP− cells growing in the well. Flow cytometry analysis indicated the presence of a mixture of GFP+ cells and GFP− cells in the CAM-implanted samples after 20 days in culture, with 29.75% GFP+ and 69.35% HLA+ (Fig. 3G,H). In all cases, GFP− cells stained positively for HLA, confirming their human origin. Bone control and *in vitro* culture groups showed over 99.7% of GFP− and over 99% HLA+ cells (Fig. 3A–D,M–P). In summary, these results indicate that human cells from the bone cylinder remained viable after 7 days incubation on the CAM, supporting the notion that CAM incubation promotes the continued survival of explanted cells.

CAM-implantation induces the deposition of extracellular matrix (ECM) and endochondral condensations within human bone tissue. Histological examination of the CAM-implanted bone cylinders demonstrated close interaction between human and avian tissues (Fig. 4A–D). CAM infiltration was evident in the marrow space of the bone, as evidenced by the deposition of ECM (Fig. 4A) and the presence of avian blood vessels (arrows Fig. 4B). Alcian Blue and Sirius Red staining (Fig. 4A) showed deposition of matrix rich in proteoglycans, within which trabecular bone was encapsulated. To interrogate further the origin of the cells laying down the new extracellular matrix in the bone tissue, GFP immunostaining was used to identify the avian cells (Fig. 4C). GFP+ cells were ubiquitously present in the CAM and were observed in the bone marrow space, further validating the invasion of the avian membrane into the human tissue. Furthermore, the GFP+ cells were observed to be co-localized with areas of ECM deposition in the bone marrow (Fig. 4A,C). *In vitro* cultured bone cylinders did not show any evidence of ECM deposition or GFP staining (Supplementary Fig. S2).

In addition to the close association of human and CAM tissue, cell condensations were found within CAM tissue in close proximity to the human tissue (Fig. 5A). These condensations were composed of layers of tightly packed cells located between the avian and human tissue (Fig. 5B–E). Antibodies specific to GFP demonstrated the avian origin of the cell nodule (Fig. 5C). In addition, the GFP+ cells located within the nodule specifically stained for Sox9, a transcription factor expressed by chondroprogenitors (Fig. 5E). Another marker of cartilage matrix, collagen type II, was found in the surrounding ECM of the cell condensation nodule (Fig. 5D. These results indicate the invasion of avian cells (GFP+) into the bone cylinder, which co-localised with new matrix deposition and cell condensations expressing chondrogenic mesenchymal condensations.

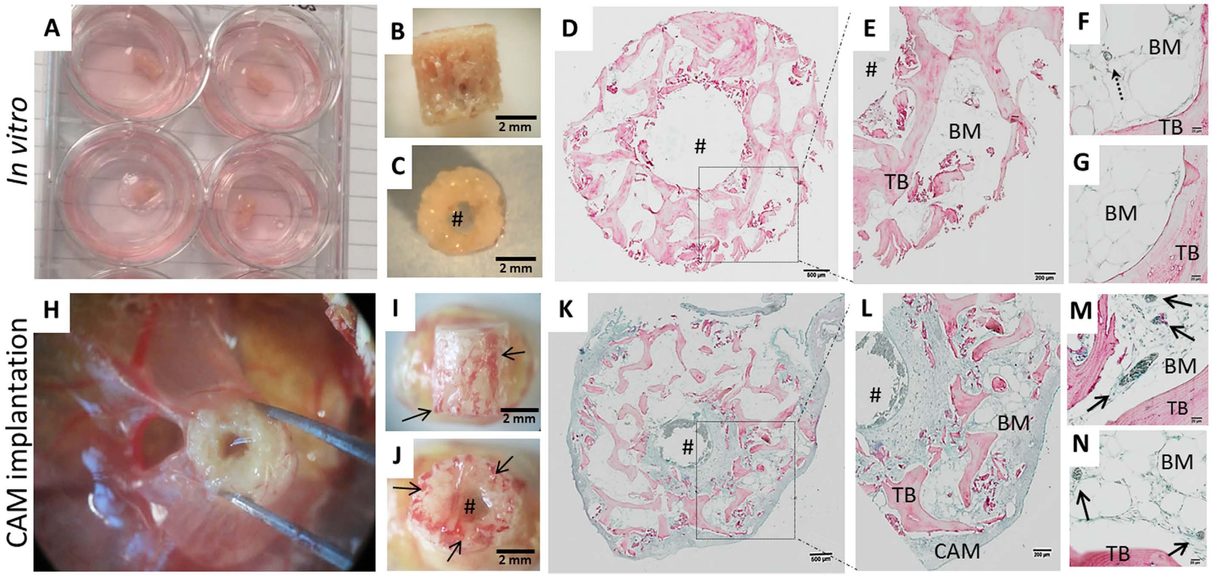

Figure 2. Avian blood vessels perfuse and infiltrate human bone tissue following implantation on the chorioallantoic membrane. Bone cylinders were extracted from the same femoral head immediately after surgery and incubated *in vitro* (**A**–**G**) or CAM-implanted (**G**–**N**) for 7 days. Macroscopic evaluation was performed upon harvesting of the bone cylinders (**A**–**C**,**H**–**J**), followed by histological examination (**D**–**G**, **K**–**N**). Representative paraffin-embedded cross-sections of the bone cylinders following Alcian Blue (proteoglycans) and Sirius Red staining (collagen) (**D**–**G**, **K**–**N**). Solid arrows indicate avian blood vessels. Dashed arrow indicate human blood vessel, #bone defect area. Chorioallantoic membrane (CAM), bone marrow (BM), trabecular bone (TB). Scale bars detailed equivalent to 500 μm (**D**,**K**), 200 μm (**E**,**L**) and 20 μm (**E**,**G**,**M**,**N**).

Mineral dense tissue is deposited in CAM-implanted human bone cylinders. Next, to determine if the incubation of human bone on the CAM facilitated bone mineral deposition, we measured changes in density using μCT. Bone cylinders were scanned pre and post incubation under identical scanning conditions. As an internal standard control, bone cylinders were kept at 4 °C and scanned at the same time points as the experimental groups. Bone cylinders implanted on the CAM for 7 days exhibited a significant increase in bone volume (6.9% ± 1.6 SD; $p < 0.01$) compared to the *in vitro* group (−1.5% ± 1.7 SD) and control (0.008% ± 1.3 SD) (Fig. 6C). Data representative of four independent experiments, using both osteoarthritic (OA) and osteoporotic (OP) femoral heads (Supplementary Fig. S3).

To determine the nature of the tissue driving the change in the bone volume measurements, the μCT cross-sections were further analysed applying a multi-level segmentation technique (see methods for more detail) instead of a standard binarisation (*i.e.* global thresholding) (Fig. 6). Multi-level Otsu thresholding allowed the differentiation between low (light grey) and high-density tissue (dark grey) and background (black; Fig. 6E). The relative bone volume change of each segment (low *versus* high density bone) was quantified in the CAM-implanted and *in vitro*-cultured bone cylinders as shown in Fig. 6F. A significant increase in the low density tissue (12.72% ± 5.4 SD; $p < 0.001$) was observed, with negligible changes in the higher density tissue (−0.26% ± 4.2 SD). In contrast to the effect shown in the CAM group, the *in vitro* treated bone cylinders displayed a decrease in the low density tissue (−3.02% ± 2.3 SD) and a negligible variation in high dense tissue (0.345% ± 1.9 SD). When comparing the global and multi-level methods of analysis, there was almost a two-fold difference between low density (12.72% ± 5.4 SD, Fig. 6F) and global (6.9% ± 1.6 SD, Fig. 6C) changes in bone volume in the CAM-implanted cylinders. Both methods (global and multi-level), reflected similar results in the *in vitro* cultured bone cylinders: negligible or negative change (Fig. 6C,F). These results indicate that low density material deposition drove the bone volume changes in the CAM-implanted bone cylinders.

Three dimensional registration software was used to visualise structural changes from μCT analysis of bone cylinders pre and post incubation. Co-registration paired images delineated matched (grey) and mismatched tissue (white and black) of the pre and post scans, respectively. On overlay, correct alignment of the bone cylinder was shown in most of the structure (grey colour in Fig. 7C,F,I). An example of divergence, resulting from actual physical change of the bone cylinder in the pre with respect to the post scan, is shown in the area highlighted by the green circle (Fig. 7G–I). Thus, the software was able to detect movement due to the location change of the trabecular bone spicule (Fig. 7I). One other structure was identified in the co-registered image as divergence in the bone cylinder defect area (see area highlighted in red in Fig. 7C,F,I). The overlay software displayed the structure in black colour (Fig. 7I), absent on the pre scan (Fig. 7G) and present in the post scan (Fig. 7H). Three independent observers assessed the overlay scan in 3D rendering to give an objective view, indicating the ability to visualise changes in the bone cylinder following incubation and, in particular, the deposition of new mineral-dense structures.

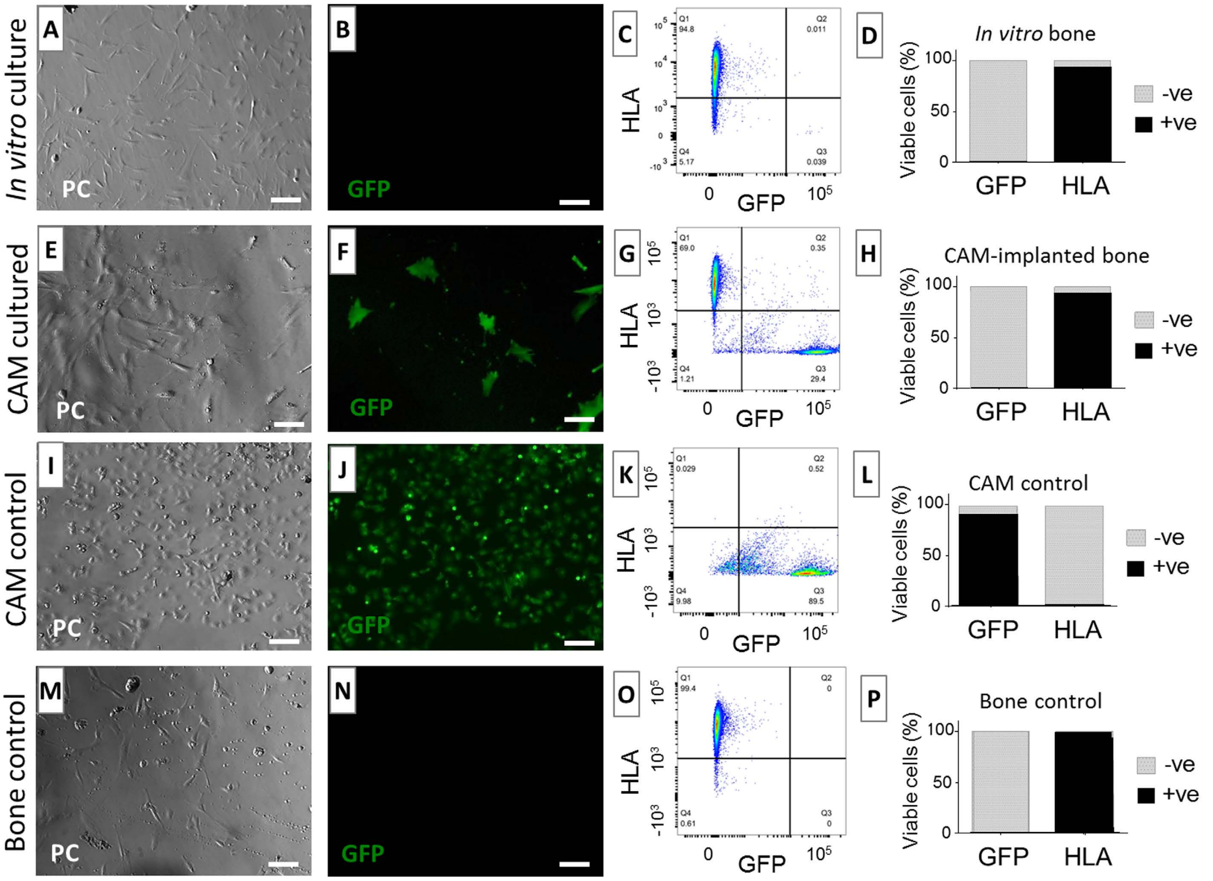

Figure 3. Human bone tissue remains viable following 7 days implantation on the CAM. Bone cylinders were excised and explanted in tissue culture plastic at day 0 (bone control) (**M**–**P**), day 7 of *in vitro* culture (**A**–**D**) or day 7 of GFP-CAM implantation (**E**,**F**). Data collected from two independent experiments, n = 3 cylinders per experiment. CAM only tissue was also explanted as GFP control (**I**–**L**). All conditions were imaged following 15 days culture using phase contrast (**A**,**E**,**I**,**M**) and fluorescence (**B**,**F**,**J**,**L**) to localize GFP+ cells. On confluence, cells were stained for a human specific marker (human leukocyte antigen, HLA). FACS analysis was used to interrogate for HLA+ and GFP+ cell populations (**C**,**G**,**K**,**O**). The relative number of HLA+ and GFP+ from each treatment was quantified with respect to the number of all viable cells (**D**,**H**,**L**,**P**). Phase contrast (PC), green fluorescent protein (GFP); Scale bars equivalent to 100 μm.

Discussion

The current study has demonstrated the potential of the CAM as an *ex vivo* bioreactor for the culture of human bone tissue providing a surrogate blood supply. Integration of the human bone tissue with the CAM was evident by macroscopic and microscopic evaluation, with extensive penetration of avian capillaries into the human bone tissue. The human tissue was observed to remain viable after 7 days cultivation on the CAM membrane, similar to human bone cultured *in vitro*. CAM-culture of human bone cylinders elicited new extracellular matrix deposition and formation of endochondral cell condensations in the human tissue. The histological changes were further validated using μCT, which showed a significant and consistent increase in the bone volume ($p < 0.01$) after 7 days of incubation on the CAM.

To our knowledge, this is the first report of the culture of viable human bone tissue on the CAM in combination with a sophisticated μCT analysis to examine tissue regeneration. A previous study has implanted human bone on the CAM and examined the angiogenic response of the bone chips after each stage of the allograft banking procedure[31]. The authors did not report invasion of avian blood vessels in the graft and showed minimal CAM-integration of isolated bone debris[31]. In comparison, here we demonstrated infiltration of CAM capillaries through the human tissue with extensive CAM-integration of the entire bone graft. These striking differences could be explained by i) the length of the CAM-implantation period (2 days by Holzmann *et al.*[31] compared to 7 days in the present report) and, ii) dissimilarities in the methodology (*i.e.* bone extraction, CAM assay).

The potential of this human-avian system to study bone regeneration was evidenced by the viability of human cells following GFP-CAM implantation. Human (GFP−/HLA+) cell outgrowths displayed a spindle-like and elongated shape morphology, typical of skeletal cells[32]. *In vitro* treated bone cylinders demonstrated a similar cell morphology after explant culture. Interestingly, cell outgrowth from the bone tissue was slower (9 days) compared to cell outgrowth from CAM-implanted cylinders (4 days). We hypothesise that the CAM growth impacted on

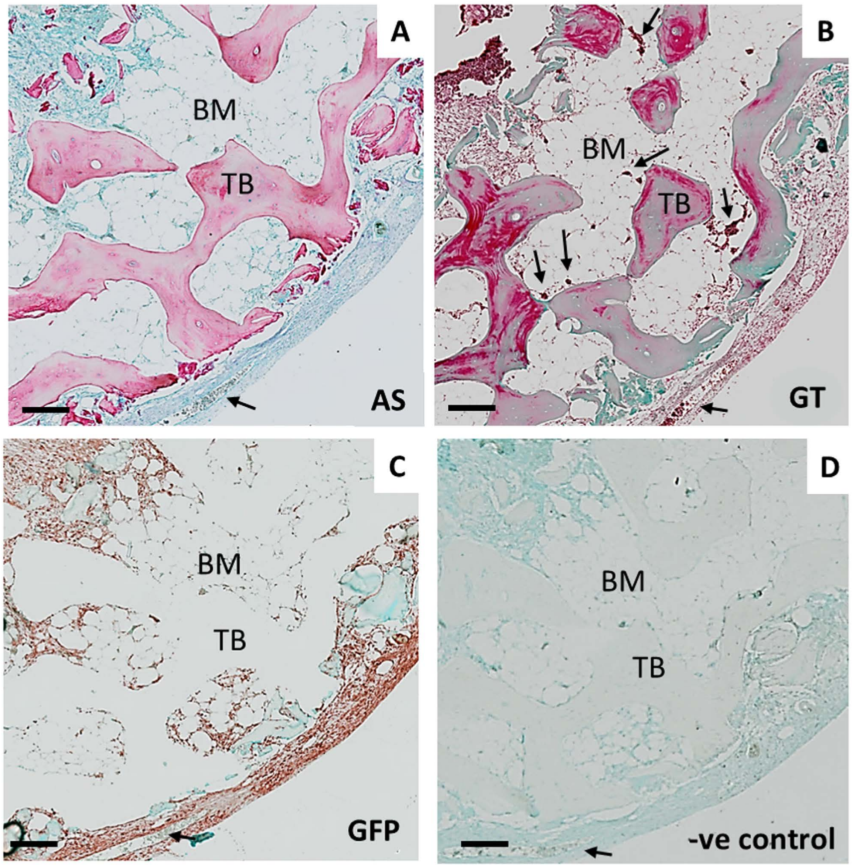

Figure 4. Extracellular matrix deposition localises with avian cells (GFP+) following CAM implantation. Representative images of bone cylinders implanted on the CAM for one week and then processed for paraffin histology. Consecutive sections were prepared for histochemistry; AS staining demarks proteoglycans in blue and collagen as a pink colouration (**A**), GT detects osteoid in pink, collagen in green (**B**), GFP positive immunostaining in brown-red colour, counterstained with Alcian Blue to visualize the matrix content (**C**) and isotype control (**D**). Arrows indicate blood vessels in the CAM. Human bone marrow (BM), human trabecular bone (TB), Alcian Blue and Sirius Red (AS), Goldner's Trichrome (GT). Scale bar equivalent to 200 μm.

the autologous human tissue, resulting in i) enhanced cell survival as a consequence of increased nutrient supply and ii) enhanced cell outgrowth as a consequence of matrix remodelling, which was not seen *in vitro*. Thus, the cell response from the human bone grafts was enhanced following CAM-implantation in comparison to *in vitro* culture.

Despite the use of xenograft material on CAM, embryo viability was reduced by only 27.5% compared to approximately 30% in other CAM studies[33,34], supporting the concept that the CAM offers a biocompatible model for explant culture[22,33]. Moreover, a number of studies have shown the chick embryo is able to elicit a primitive immune response[20,21,35], further highlighting the potential of the CAM assay as a tool to evaluate graft biocompatibility. Valdes *et al.* reported the presence of heterophils, leukocytes and giant cells as well as compact fibre deposition following 1, 7 and 11 days implantation of cotton threads, which the authors described as a chronic fibrotic response[22]. In contrast, our study showed loose matrix deposition, rich in proteoglycan and collagenous content, strongly associated with the presence of the avian cells (GFP+). The retention of embryo viability and the absence of a sustained fibrotic response support the conclusion that the human bone tissue can integrate with and is nourished by the CAM membrane.

Interestingly, we found evidence of cell condensations strongly expressing Sox9, an essential transcription factor expressed by chondroprogenitors[36], in the CAM tissue in proximity to the human bone cylinder. Moreover, these cells also co-stained with GFP, confirming their avian origin. Similar cell condensations were shown by Hancox, who implanted chick embryo calvaria fragments on CAM for 10 days[37]. In accordance with our findings, cell condensations (named by Hancox 'ectodermal pearls') were located in proximity to the bone tissue[37]. These findings are not surprising given the clinical gold standard biomaterial is bone autograft[38], which provides a unique osteogenic microenvironment as a consequence of the plethora of growth factors within the bone matrix (*i.e.* BMP, PDGF, FGF) as well as the presence of viable osteogenic cells[38]. Hence, it is likely that the implantation of such an osteoinductive material (*i.e.* living human bone cylinder) on the CAM can result in ectopic bone formation; indeed, it is well known that BMP proteins have significant structural similarity and function across species[39].

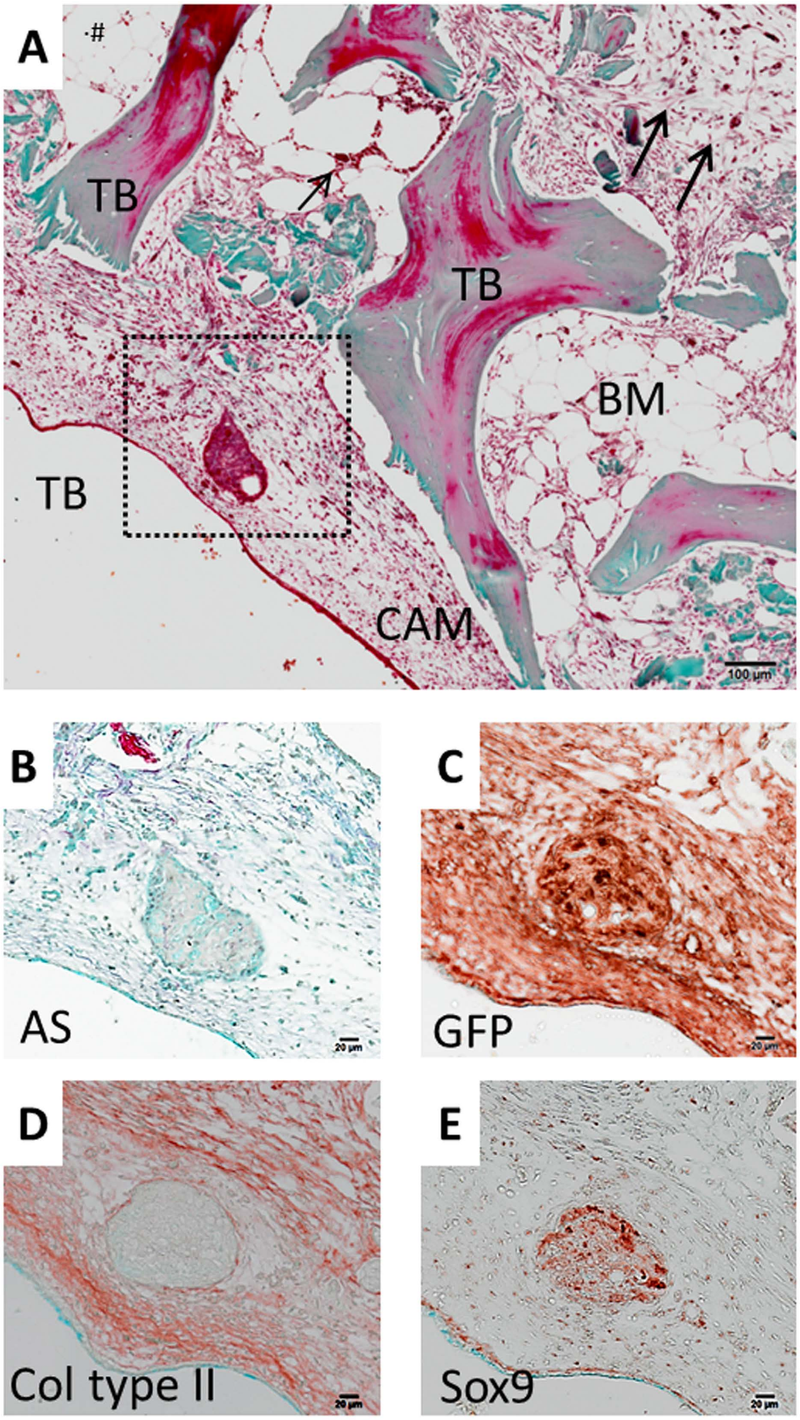

Figure 5. Endochondral cell condensation forms in the CAM after human bone cylinder implantation. Representative images of bone cylinders implanted on the CAM for one week and then processed for paraffin histology. Low magnification image shows the peripheral location of cell condensation in the CAM stained for GT (**A**). Cell condensation images at higher magnification stained for AS (**B**) and immunohistochemistry for GFP (**C**), Collagen type II (**D**) and Sox9 transcription factor (**E**). Arrows indicate blood vessels in the CAM. Chorioallantoic membrane (CAM), human bone marrow (BM), human trabecular bone (TB), Alcian Blue and Sirius Red (AS), Goldner's Trichrome (GT). Representative images of CAM-implanted bone cylinders. Scale bar equivalent to 100 µm (**A**) and 20 µm (**B–E**).

The observation of new bone or cartilage formation occurring on the CAM is supported by our µCT data, which showed significant increases in the bone volume ($p < 0.01$) over the 7 day incubation period. We hypothesise that the changes in bone volume were driven by: i) the deposition of new low density matrix, possibly through

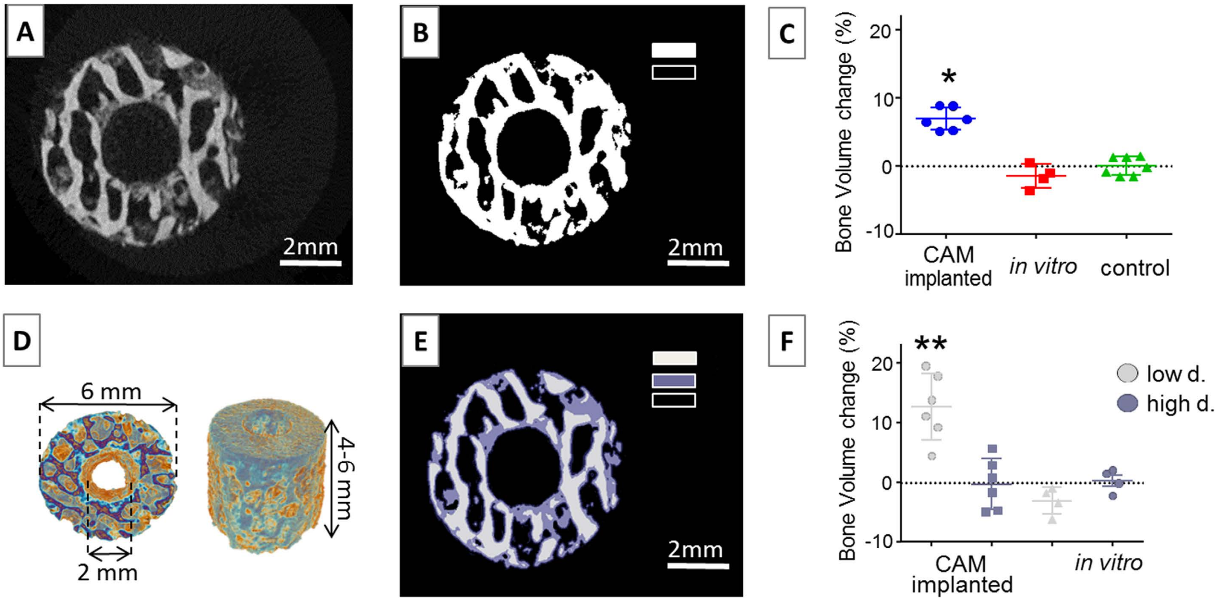

Figure 6. Bone volume is significantly increased following CAM implantation. Bone cylinders were scanned using the same µCT parameters before and after CAM-implantation (n = 6) or *in vitro* incubation (n = 4), or kept at 4 °C as control (n = 8). (**A**) Raw image (grayscale) of a bone cylinder µCT scan. (**B**) Standard method for image segmentation using a threshold value to differentiate mineralised tissue (white) and background (black). (**C**) Bone volume was quantified using standard binarisation method. (**D**) Three dimensional model of a bone cylinder µCT scan. (**E**) Image following the application of a three-level segmentation Otsu threshold: low dense tissue in light grey, high dense tissue in dark grey and background in black. (**F**) Bone volume was quantified following Otsu thresholding method, as previously described. Data points indicate the relative bone volume change following incubation of each individual bone cylinder. Error bars indicate mean value ± SD, $^*p < 0.01$, $^{**}p < 0.001$.

CAM-derived ectopic bone formation, as evidenced by the histology; and ii) mineralisation of the pre-existing trabecular bone. Segmentation of the grayscale datasets into three levels (multi-level thresholding)[40,41] showed a greater increase in the low density tissue ($p < 0.001$) compared to global thresholding ($p < 0.01$). It is worth considering that, even if bone volume was calculated as a relative change, multi-level thresholding was different for each bone cylinder, whereas global thresholding was applied equally to all bone cylinders. Critically, multi-level analysis allowed adaption to the subtle differences amongst the bone cylinders (structure, mineral content, composition: cortical *versus* trabecular) and thus, enhanced sensitivity when measuring specific regions of the grayscale histogram (*i.e.* low *versus* high density). Together, this data indicates that Multi-level Otsu thresholding allowed quantification of subtle changes in poorly mineralised tissue and that this less dense mineral tissue may be the main contributor to the increased bone volume measured using standard global thresholding.

In contrast to the increase in bone volume observed on the CAM-implanted bone cylinders, *in vitro* cultured samples showed a reduction in bone volume. This was despite the observation of a similar level of cell outgrowth and cell viability after 7 days incubation. In contrast, Kanczler *et al.* reported substantial mineralisation of early stage chick femurs following 10 days organotypic culture[42]. This mineralisation process occurred in the absence of angiogenesis due to it being a healthy and rapidly growing embryo organ. The present study evaluated bone from elderly patients with either osteoarthritis or osteoporosis, which is likely to grow significantly more slowly than embryonic bone and in all probability display an altered metabolic (catabolic) profile. These results support the conclusion that the CAM assay provides a unique vascular component in which bone tissue formation can be evaluated *in vivo*.

Given that most *in vivo* studies start to observe mineral deposition 14 days post-fracture[43,44], extended incubation periods would be required to shed more light on this CAM-human model. The limitation of the short incubation period was addressed in the present study by implementing high resolution computed tomography, which allowed quantifying the subtle changes resulting of the early stages in bone regeneration. In addition, previous studies have shown that it is possible to observe bone formation within a 7 day timeframe when implanted on CAM[30]. It is important to note that the fetal chick skeleton becomes mineralised in the time period of 10 days[45,42], thus, it is unsurprising that in our studies we observe mineralisation during the 7 day period of experimental measurement. The rapid and aggressive growth of the extraembryonic membrane has been previously demonstrated by Steffens *et al.*, who compared the vasoproliferative response of the CAM model with the subcutaneous mouse implant[46]. Interestingly, the authors reported micro-vessel density was higher in the 7 day CAM assay (50.4 ± 17.3 SD), compared to the 21 days implantation in the murine model (43.5 ± 16.3 SD)[46]. Thus, even a short-term CAM assay, limited to 7–10 days incubation, offers a strong angiogenic response from a rapidly developing embryo.

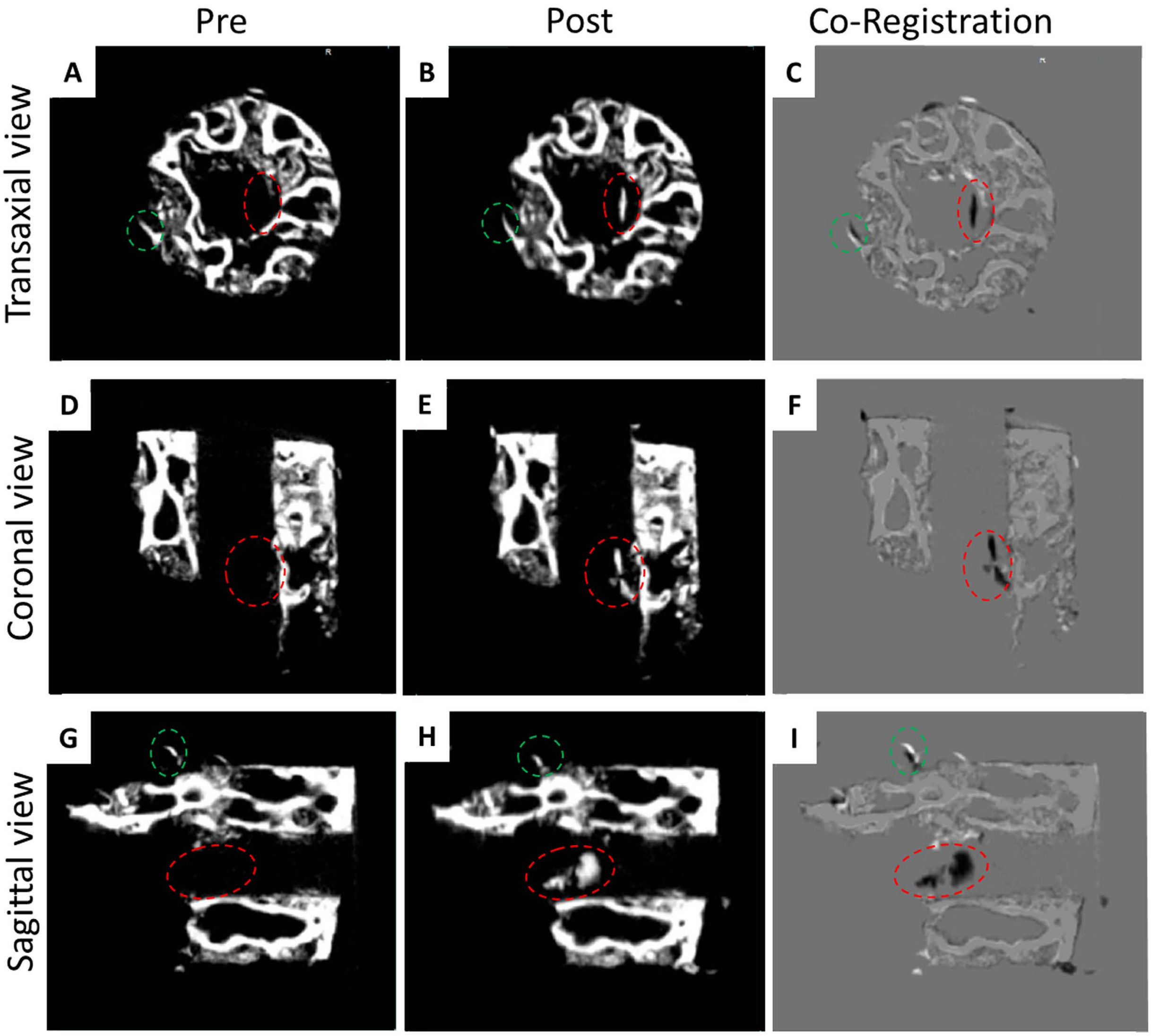

Figure 7. Overlay scans of the bone cylinders pre and post CAM implantation allow detection of new material deposition. Transaxial, coronal and sagittal scan images representative of bone graft before implantation on the CAM (**A**,**D**,**G**) and after (**B**,**E**,**H**), respectively. Corresponding structures in the *pre* and *post* scan are displayed in grey colour (**C**,**F**,**I**) while non-matching structures appear in white (pre) or black (post). Discontinuous circle highlight areas of interest: green indicates non-aligned structure and red indicates new deposited material.

The current study has a number of limitations including an inability to monitor bone cylinder vascularisation throughout the incubation process. One solution would be to introduce an *ex ovo* (shell-less) approach, although this method implies a viability drop down to 20–30% by the end of the gestational process[23]. It is worth noting that in the absence of the eggshell, the CAM can take up mineral from other sources (*i.e.* biomaterials) to restore calcium levels for skeletal development[47]. The bone resorptive potential of the CAM has been known for more than 30 years; in 1990 Webber *et al.* implanted bovine cortical bone on CAM and showed striking bone resorption following 8 days implantation[48]. In support of those findings, CAM-implanted bone cylinders resulted in a modest decrease of high densisty bone and a significant increase of low density bone, although whether this is related to any bone remodelling process, remains speculative. Future studies will include immune-detection of osteoclast markers to examine bone resorption.

Conclusion

In summary, the present study describes a novel method to study human bone regeneration *ex vivo* using an animal model; the CAM assay. The relevance of this methodology lies in the use of human bone tissue, freshly derived from patients and hence a more clinically relevant situation to study bone healing. We suggest this human-avian platform offers an alternative animal model to test novel biomaterials and constructs for tissue engineering. This cost-effective, rapid and simple method will have a critical impact on the reduction and replacement of the number of animals used in classical *in vivo* bioengineering models. On-going studies are focusing on utilising this model for biomaterial screening, applying biomaterials in the cylindrical defect area to deliver angiogenic and osteogenic growth factors and evaluation of cell-material constructs to augment skeletal tissue formation with exciting implications for skeletal regenerative medicine.

Materials and Methods

Human bone cylinder extraction. Bone cylinders were extracted from adult femoral heads collected from haematologically normal patients undergoing routine elective hip replacement surgery. Only tissue samples that would have been discarded were used following informed consent from the patients. All protocols were conducted in accordance to the Southampton & South West Hampshire Local Research Ethics Committee (Ref: 194/99/w). All experimental protocols were approved by the Southampton & South West Hampshire Local Research Ethics Committee (Ref: 194/99/w). A dentist's surgical drill (Osteomed, Glendale, USA) attached to a 2 mm drill bit was used to make an initial perforation. An empty-core saw (6 mm outer diameter) bound to a pilot drill (2 mm) guided the perforation of the bone cylinder outer diameter (Fig. 1A). Afterwards, forceps were used to rescue the bone cylinder (6 mm outer diameter, 2 mm empty core and 4–6 mm in length, Fig. 1B) and saline solution was perfused through its empty core to wash off any debris. A scalpel was used to remove the articular cartilage and standardize bone cylinder length. The entire protocol was conducted under aseptic conditions.

CAM assay. All animal procedures were carried out in accordance with the guidelines and regulations laid down in the Animals (Scientific Procedures) Act 1986, UK and chick embryo chorioallantoic membrane experimental protocols were approved and conducted under Home Office Approval UK (Project licence – PPL 30/2762) approved at the University of Southampton. Assays were carried out according to fertilised green fluorescent protein (GFP) transfected eggs were kindly provided by the Transgenic Chicken Facility of the Roslin Institute[49]. The eggs were incubated horizontally for 10 days at 37 °C in a 60% humidified atmosphere, using a Hatchmaster incubator (Brinsea, UK) with one hour scheduled rotation. At day 10-post fertilisation, a fine-toothed hacksaw blade was used to make an approximate 0.5 cm^2 square incision on the eggshell under sterile conditions and the eggshell window fragment was removed to access the CAM beneath. Bone cylinders were randomly distributed ($n = 8$–10 per experimental group) and individually placed on the CAM of the chicken embryo (Fig. 1C). Sterile parafilm tape was used to seal back the window and the eggs were further incubated without the rotation setting. Embryos were inspected daily by candling. After one week of incubation the bone cylinders were harvested; the CAM integration was assessed by visual inspection and photographed with a stereomicroscope attached to a digital camera (Canon Powershot G2). The number of fully developed chick embryos according to Hamburger and Hamilton[50] was recorded and the gestational process was terminated following Home Office specific guidelines.

Organotypic culture. Bone cylinders were placed on Millicell inserts (0.4 μm pore size, 30 mm diameter, Millipore, UK) in 6-well tissue culture plates containing serum-free basal media (αMEM, Lonza, Switzerland, with 100 U/ml 100 μg/ml of Pennicilin G and Streptomycin, PAA, USA). Bone cylinders were incubated at 37 °C and 5% CO_2 for a week; medium was replaced every other day during that period (Fig. 1D).

Bone viability assessment post incubation (I): cell outgrowth from explant culture. After incubation, bone cylinders and CAM tissue were collected under sterile conditions and sliced into small fragments (2–3 mm) using a scalpel. Bone fragments were evenly distributed through the surface area of a well of a 6-well-plate containing minimum amount of basal media with 10% serum to cover the surface. The plate was maintained at 5% CO_2 at 37 °C, and the media were replaced every 5 days for the first 10 days. After 10 days, the tissue fragments were removed from the well using sterile forceps, followed by repeated 1x PBS washing steps to remove any remaining tissue. The cultures were further incubated for 10 more days with media changes every other day. Cells were trypsinised at 90% confluence and prepared for fluorescence-activated cell sorting (FACS) analysis.

Bone viability assessment post incubation (II): Human Leukocyte Antigen (HLA) detection by FACS. Cells suspensions were washed (2x) in FACS buffer (2% foetal bovine serum and 0.1% sodium azide in PBS) before incubating with W6/32 mouse anti-human HLA-A-B-C monoclonal antibody (kindly provided by Prof. Tim Elliot, CSU, University of Southampton, UK) at 10 μg/ml, for 30 minutes at 4 °C. Following FACS buffer washes (2x), goat anti-mouse IgG (H + L)-AF647 (A-21237, Life Technologies, UK) was used for the secondary antibody incubation (1:2000 dilution) at 4 °C for 30 minutes and the cells were further washed (2x) with FACS buffer. Cells stained with secondary antibody only and non-stained cells were used as controls for non-specific antibody binding and autofluorecence, respectively; using these controls, gating for each sample was applied accordingly. A FACS Canto I Flow cytometer (BD Biosciences, San Jose, USA) was used to run the samples and data were analysed using FlowJo v10 software (Ashland, USA).

Micro computed tomography (μCT) analysis. Bone cylinders were scanned before and after incubation using the same parameters. The bone fragments were scanned individually in sterile microcentrifuge tubes using SkyScan 1176 (Bruker, Kontich, Belgium). Bone cylinders were scanned using the following settings: X-ray source 50 kV, 500 μA, 496 ms exposure time and a voxel size of 18 μm. Once the scans were completed, the raw data was reconstructed using NRecon software with correction for misalignment, ring artefacts and beam hardening (30%). The pre- and post-implantation reconstructed datasets of the same bone graft were orientated in the same position using DataViewer software for consistent analysis. 3D registration tool of DataViewer was used to match pixels of the same density on the same location of sequential scans. Global thresholding was applied on the pre and post scans. CTAn software was employed to quantify the bone volume of each individual cylinder pre and post incubation and the relative change was calculated as a percentage of the pre scan. CTvox was implemented to create and visualise the 3D models of the bone cylinders. All the software was from SkyScan, Bruker, Kontich, Belgium.

Multi-level Otsu thresholding was applied to the scan datasets in addition to the standard analysis (global thresholding). Otsu's algorithm consists of clustering pixels into different classes such that the variance between each class is maximal[40]. The Otsu algorithm is commonly used for image binarisation (two classes) and the same principle can be used to segment into additional classes. The present study used Otsu segmentation into two levels, separating pixels into three classes: high density, low density and background (Fig. 6E). To apply Otsu multi-level thresholding, pre and post scans of each bone cylinder were orientated on the same transaxial plane and an automated region of interest (ROI) was designed to select the full diameter. These segmented images were saved as a new dataset (Fig. 6E). Bone volume was calculated for the high density and low density classes as well as the relative change between pre and post incubation (%).

Histology and immunohistochemistry analysis. Bone cylinders were fixed in 4% paraformaldehyde in PBS at 4 °C for 24 hours and decalcified by incubating in Histoline (Histoline, Milan, Italy) for 24 hours in rotation at 4 °C. Complete demineralisation was confirmed using flat X-rays (Faxitron). Samples were then processed for paraffin sectioning (5 μm) and stained as described by Smith *et al.*[51] for Alcian Blue (proteoglycans) and Sirius Red (collagen) and Goldner's Trichrome (collagen in green, osteoid in red/pink and bright red for cell cytosol). Immunohistochemistry for Sox9 and collagen type II was performed as described by Kanczler *et al.*[42], positive staining identified in red-brown colour. GFP detection was performed using a rabbit polyclonal anti-GFP (2555, Cell Signalling, New England Biolabs, UK) at a 1:100 dilution in combination with SignalStain® Boost (8114P, Cell Signalling, New England Biolabs, UK) following the manufacturer's protocol. All immunostaining was matrix-counterstained with Alcian Blue (proteoclycans) and IgG isotype antibody was used for controls. Images were captured with an Olympus BX-51/22 dotSlide digital virtual microscope.

Statistical analysis. All experimental data were analysed using Statistical Analysis SPSS Base 16.0 software for Windows. Results were expressed as the mean ± SD and plotted using GraphPad Prism. Normal distribution of the data was confirmed by the Kolmogorov-Smirnov test. Comparisons between treatments were performed using the one-way ANOVA test including Tukey post-hoc test. Values of $p < 0.01$ were considered statistically significant.

References

1. Cobb, T. K. *et al.* Cigarette smoking and nonunion after ankle arthrodesis. *Foot Ankle Int.* **15,** 64–67 (1994).
2. Macey, L. R. *et al.* Defects of early fracture-healing in experimental diabetes. *J. Bone Joint Surg. Am.* **71,** 722–733 (1989).
3. Robinson, C. M. *et al.* Estimating the risk of nonunion following nonoperative treatment of a clavicular fracture. *J Bone Jt. Surg Am* **86-A,** 1359–1365 (2004).
4. Ebraheim, N. a. *et al.* Nonunion of distal femoral fractures: a systematic review. *Orthop. Surg.* **5,** 46–50 (2013).
5. Gruber, R. *et al.* Fracture healing in the elderly patient. *Exp. Gerontol.* **41,** 1080–1093 (2006).
6. Hankenson, K. D. *et al.* Angiogenesis in bone regeneration. *Injury* **42,** 556–561 (2011).
7. Giannoudis, P. V., Einhorn, T. a. & Marsh, D. Fracture healing: The diamond concept. *Injury* **38,** S3–S6 (2007).
8. Tuli, R. *et al.* Characterization of multipotential mesenchymal progenitor cells derived from human trabecular bone. *Stem Cells* **21,** 681–693 (2003).
9. Wall, R. J. & Shani, M. Are animal models as good as we think? *Theriogenology* **69,** 2–9 (2008).
10. Greek, R. & Menache, A. Systematic reviews of animal models: Methodology versus epistemology. *Int. J. Med. Sci.* **10,** 206–221 (2013).
11. Perel, P. *et al.* Comparison of treatment effects between animal experiments and clinical trials: systematic review. *BMJ* **334,** 197 (2007).
12. Russel, W. M. S. & Burch, R. *The Principles of Humane Experimental Technique*. London, Methuen, (1959).
13. Nowak-Sliwinska, P. *et al.* The chicken chorioallantoic membrane model in biology, medicine and bioengineering. *Angiogenesis* **17,** 779–804 (2014).
14. Ribatti, D. *et al.* The chick embryo chorioallantoic membrane as a model for *in vivo* research on anti-angiogenesis. *Curr. Pharm. Biotechnol.* **1,** 73–82 (1996).
15. Cantatore, F. P. *et al.* Osteocalcin is angiogenic *in vivo*. *Cell Biol. Int.* **29,** 583–585 (2005).
16. Ribatti, D., N. *et al.* The gelatin sponge-chorioallantoic membrane assay. *Nat. Protoc.* **1,** 85–91 (2006).
17. Kunzi-Rapp, K. *et al.* Characterization of the chick chorioallantoic membrane model as a short-term *in vivo* system for human skin. *Arch. Dermatol. Res.* **291,** 290–295 (1999).
18. Sys, G. *et al.* Tumor grafts derived from sarcoma patients retain tumor morphology, viability, and invasion potential and indicate disease outcomes in the chick chorioallantoic membrane model. *Cancer Lett.* **326,** 69–78 (2012).
19. Ribatti, D. *et al.* Angiogenic response induced by acellular brain scaffolds grafted onto the chick embryo chorioallantoic membrane. *Brain Res.* **989,** 9–15 (2003).
20. Friend, J. V. *et al.* Immaturity of the inflammatory response of the chick chorioallantoic membrane. *Toxicol. Vitr.* **4,** 324–326 (1990).
21. Lafferty, K. J. *et al.* Reactions of the graft versus host in the CAM. *Aust. J. Exp. Biol. Med. Sci.* **47,** 17–54 (1969).
22. Valdes, T. I. *et al.* The chick chorioallantoic membrane as a novel *in vivo* model for the testing of biomaterials. *J. Biomed. Mater. Res.* **62,** 273–282 (2002).
23. Valdes, T. I. *et al.* Ex ova chick chorioallantoic membrane as a novel *in vivo* model for testing biosensors. *J. Biomed. Mater. Res. A* **67,** 215–223 (2003).
24. Keshaw, H. *et al.* Microporous collagen spheres produced via thermally induced phase separation for tissue regeneration. *Acta Biomater.* **6,** 1158–1166 (2010).
25. DeVolder, R. J. *et al.* Microfabrication of proangiogenic cell-Laden alginate-g-Pyrrole hydrogels. *Biomaterials* **33,** 7718–7726 (2012).
26. Hadjizadeh, A. *et al.* Directional migration of endothelial cells towards angiogenesis using polymer fibres in a 3D co-culture system. *J. Tissue Eng. Regen. Med.* **4,** 524–531 (2010).
27. Diaz-Gomez, L. *et al.* Biodegradable electrospun nanofibers coated with platelet-rich plasma for cell adhesion and proliferation. *Mater. Sci. Eng. C* **40,** 180–188 (2014).
28. Kanczler, J. M. *et al.* Supercritical carbon dioxide generated vascular endothelial growth factor encapsulated poly(dl-lactic acid) scaffolds induce angiogenesis *in vitro*. *Biochem. Biophys. Res. Commun.* **352,** 135–141 (2007).
29. Buschmann, J. *et al.* Tissue engineered bone grafts based on biomimetic nanocomposite PLGA/amorphous calcium phosphate scaffold and human adipose-derived stem cells. *Injury* **43,** 1689–1697 (2012).

30. Yang, X. B. *et al.* Human osteoprogenitor bone formation using encapsulated bone morphogenetic protein 2 in porous polymer scaffolds. *Tissue Eng.* **10,** 1037–1047 (2004).
31. Holzmann, P. *et al.* Investigation of bone allografts representing different steps of the bone bank procedure using the CAM-model. *ALTEX* **27,** 97–103 (2010).
32. Kern, S. *et al.* Comparative analysis of mesenchymal stem cells from bone marrow, umbilical cord blood, or adipose tissue. *Stem Cells* **24,** 1294–1301 (2006).
33. Borges, J. *et al.* Chorioallantoic membrane angiogenesis model for tissue engineering: a new twist on a classic model. *Tissue Eng.* **9,** 441–450 (2003).
34. Martinez-Madrid, B. *et al.* Chick embryo chorioallantoic membrane (CAM) model: a useful tool to study short-term transplantation of cryopreserved human ovarian tissue. *Fertil. Steril.* **91,** 285–292 (2009).
35. Bellairs, R. & Osmond, M. *Atlas of Chick Development*. *Atlas Chick Dev.* (2014).
36. Akiyama, H. *et al.* The transcription factor *Sox9* has essential roles in successive steps of the chondrocyte differentiation pathway and is required for expression of *Sox5* and *Sox6*. *Genes Dev.* **16,** 2813–2828 (2002).
37. Hancox, N. M. The survival of transplanted embryo bone grafted to CAM and subsequent osteogenesis. *J. Physiol.* **106,** 279–285 (1946).
38. Oryan, A. *et al.* Bone regenerative medicine: classic options, novel strategies, and future directions. *J. Orthop. Surg. Res.* **9,** 18 (2014).
39. Hopkins, D. R. *et al.* The bone morphogenetic protein 1/Tolloid-like metalloproteinases. *Matrix Biol.* **26,** 508–523 (2007).
40. Otsu, N. *et al.* A Tlreshold Selection Method from Gray-Level Histograms. *IEEE Trans. Syst. man Cybern*. **20,** 62–66 (1979).
41. Diyana, W. M. *et al.* Multi-level segmentation method for serial computed tomography brain images. *Signal Image Process. Appl. (ICSIPA), 2009 IEEE Int. Conf.* 107–112 (2009).
42. Kanczler, J. M. *et al.* A novel approach for studying the temporal modulation of embryonic skeletal development using organotypic bone cultures and microcomputed tomography. *Tissue Eng. Part C. Methods* **18,** 747–760 (2012).
43. Shah, N. J. *et al.* Adaptive growth factor delivery from a polyelectrolyte coating promotes synergistic bone tissue repair and reconstruction. *Proc. Natl. Acad. Sci. USA* **111,** 1–6 (2014).
44. Yuasa, M. *et al.* The temporal and spatial development of vascularity in a healing displaced fracture. *Bone* **67,** 208–221 (2014).
45. Thompson, T. J. *et al.* Intramembranous osteogenesis and angiogenesis in the chick embryo. *J. Anat.* **166,** 55–65 (1989).
46. Steffens, L. *et al.* *In vivo* engineering of a human vasculature for bone tissue engineering applications. *J. Cell. Mol. Med.* **13,** 3380–3386 (2009).
47. Vargas, G. E. *et al.* Biocompatibility and bone mineralization potential of 45S5 Bioglass®-derived glass-ceramic scaffolds in chick embryos. *Acta Biomater.* **5,** 374–380 (2009).
48. Webber, D. M. *et al.* An *in vivo* model system for the study of avian osteoclast recruitment and activity. *Bone Miner.* **11,** 127–140 (1990).
49. Simon G. *et al.* Transgenic chickens as bioreactors for protein based drugs. *Drug Discov. Today* **3,** 1–9 (2005).
50. V. Hamburger, H. L. H. A series of normal stages in the development of the chick embryo. *J. Morphol.* **88,** 49–92 (1951).
51. Smith, E. L. *et al.* Evaluation of skeletal tissue repair, Part 1: Assessment of novel growth-factor-releasing hydrogels in an *ex vivo* chick femur defect model. *Acta Biomater.* **10,** 4186–4196 (2014).

Acknowledgements

This study was supported by the National Centre for the Replacement, Reduction and Refinement of Animals in Research (NC3Rs) (NC/K500380/1; studentship for IMJ). Funding to ROCO from the Medical Research Council, the Engineering and Physical Sciences Research Council and Biotechnology and Biological Sciences Research Council UK Regenerative Medicine Platform Hub Acellular Approaches for Therapeutic Delivery (MR/K026682/1) is gratefully acknowledged as well as the European Union Seventh Framework Programme under grant agreement n° [318553]—SkelGEN and Programme Grant, BioDesign (262948). The authors would like to express their gratitude to Julia Wells and Carol Roberts for their technical support, Dr. Jeroen Hostens and Dr Phil Salmon from Bruker MicroCT, Belgium, for their advice in μCT analysis, Dr Adrian Sherman for kindly providing the GFP-eggs for the experiments, Edoardo Scarpa and Dr. Ismael Suarez Falcón and for their constructive comments on the manuscripts, and Dr. David Gibbs, Dr. Jon I. Dawson, Dr. Vitali Goriainov, Juan A. Núñez and Cameron Black for helpful discussions.

Author Contributions

Study design: I.M.J., J.M.K., N.D.E. and R.O.C.O. Experimental work: I.M.-J. microCT analysis I.M.-J., G.H.-B. and S.A.L. FACS analysis I.M.-J., N.K. and A.A.J. Data analysis and interpretation: I.M.-J., J.M.K., N.D.E. and R.O.C.O. Drafting manuscript: I.M.-J. Revising manuscript content: I.M.-J., J.M.K., G.H.-B., S.A.L., N.K., A.A.J., N.D.E. and R.O.C.O. Approving final version of manuscript: I.M.-J., J.M.K., G.H.-B., S.A.L., N.K., A.A.J., N.D.E. and R.O.C.O. R.O.C.O. takes responsibility for the integrity of the data analysis.

Additional Information

Supplementary information accompanies this paper at http://www.nature.com/srep

Competing financial interests: The authors declare no competing financial interests.

How to cite this article: Moreno-Jimenez, I. *et al.* The chorioallantoic membrane (CAM) assay for the study of human bone regeneration: a refinement animal model in tissue engineering. *Sci. Rep.* **6**, 32168; doi: 10.1038/srep32168 (2016).